

Copyright
by
Mohammad Lotfollahi Sohi
2015

The Dissertation Committee for Mohammad Lotfollahi Sohi Certifies that this is the approved version of the following dissertation:

Development of a Four-Phase Flow Simulator to Model Hybrid Gas/Chemical EOR Processes

Committee:

Gary A. Pope, Supervisor

Mojdeh Delshad, Co-Supervisor

Kamy Sepehrnoori

Kishore K. Mohanty

Keith P. Johnston

**Development of a Four-Phase Flow Simulator to Model Hybrid
Gas/Chemical EOR Processes**

by

Mohammad Lotfollahi Sohi, B.E.; M.E.

Dissertation

Presented to the Faculty of the Graduate School of

The University of Texas at Austin

in Partial Fulfillment

of the Requirements

for the Degree of

Doctor of Philosophy

The University of Texas at Austin

May 2015

Dedication

To my beloved parents

Sedigheh & Ali

and my sister

Mahsa

for their endless love, support, and encouragement

Acknowledgements

The completion of this dissertation would not have been possible without the support and contribution of many people. I would like to thank all those who inspired and helped me throughout this journey.

It is a great honor for me to express my sincere gratitude to my supervisors, Dr. Mojdeh Delshad and Dr. Gary A. Pope, for their support, guidance, patience, and encouragement. I have learned a great deal from their keen observations, scientific intuition, and vast knowledge base. It has been a privilege to have the opportunity to work with them.

I appreciate invaluable comments and feedback from my committee members, Dr. Kamy Sepehrnoori, Dr. Kishore Mohanty, and Dr. Keith P. Johnston, who have further enriched this dissertation with their suggestions and comments.

I would like to specially thank Dr. Abdoljalil Varavei for his continuous help, patience and kindness. Dr. Varavei was always available for my questions and gave generously of his time and knowledge along with positive encouragement. I learned a great deal from him throughout my time at UT Austin.

Also, it is with immense gratitude that I acknowledge the support and help of Dr. Rouhi Farajzadeh, Dr. William R. Rossen, and Dr. George J. Hirasaki. The collaboration with them on the foam modeling project is one of the greatest privileges that I have had during my Ph.D. study.

I would like to acknowledge the staff of Petroleum and Geosystems Engineering Department, Frankie Hart, Joanna Castillo, Esther Barrientes, Roger Terzian, and Cheryl Kruzic for their technical and administrative assistance.

I am deeply grateful to be surrounded by many peers and friends who have been both helpful and supportive. I would like to thank my friends Mohammad Reza Beygi, Reza Tavakoli, Amir Reza Shahmohammad, Iman Mohammad, Morteaz Elahi Naraghi, Masoud Alfi, Hamid Lashgari, Seyyed Abolfazl Hosseini, Mohammad Omidvar Eshkalak, Mojtaba Ghasemi Doroh, Hosein Yousefpour, Amir Reza Rahmani, Ali Aboii, Zhitao Li, Hariharan Ramachandran, Soheil Ghanbarzadeh, Abolghasem Kazeminia, Mohsen Rezaveisi, Reza Parsi, Arjang Shahriari, Babak Nasouri, Reza Nasouri, Amir Khalighi, Rouzbeh Ghanbarnezhad, Meghdad Roshanfekar, Javad Behseresht, Saeedeh Mohebbinia, Amir Frooqnia, Shaina Kelly, Mahmood Shakiba, Venkat Sriram Pudugramam, Ali Goudarzi, Shayan Tavassoli, Saeid Enayatpour, Amir Kianinejad, Behzad Eftekhari, Ali Moinfar, Peter Wang, Neil Rodrigues, Alireza Sanaei, Ali Farhadinia, Gazal Dashti, Haishan Luo, Dean Alen Checkai, Luis Lamas, and Ali Naderi as well as many other friends whom I did not name explicitly.

The work presented in this dissertation was funded by the sponsors of the Chemical EOR Joint Industry Project (CEORJIP) at the Center for Petroleum and Geosystems Engineering at The University of Texas at Austin.

Above all, I would like to express my deepest gratitude to my beloved parents, Sedigheh and Ali, my sister Mahsa, and my grandparents Mohtaram and Abbas Lotfollahi and Zahra and Abbas Esmaili for their endless love and support through my entire life. I would like to remember my grandfather Abbas Lotfollahi whose memory gave me strength along the way.

May 2015

Development of a Four-Phase Flow Simulator to Model Hybrid Gas/Chemical EOR Processes

Mohammad Lotfollahi Sohi, Ph.D.

The University of Texas at Austin, 2015

Supervisors: Gary A. Pope

Mojdeh Delshad

Hybrid gas/chemical Enhanced Oil Recovery (EOR) methods are such novel techniques to increase oil production and oil recovery efficiency. Gas flooding using carbon dioxide, nitrogen, flue gas, and enriched natural gas produce more oil from the reservoirs by channeling gas into previously by-passed areas. Surfactant flooding can recover trapped oil by reducing the interfacial tension between oil and water phases. Hybrid gas/chemical EOR methods benefit from using both chemical and gas flooding. In hybrid gas/chemical EOR processes, surfactant solution is injected with gas during low-tension-gas or foam flooding. Polymer solution can also be injected alternatively with gas to improve the gas volumetric sweep efficiency.

Most fundamentally, wide applications of hybrid gas/chemical processes are limited due to uncertainties in reservoir characterization and heterogeneity, due to the lack of understanding of the process and consequently lack of a predictive reservoir simulator to mechanistically model the process. Without a reliable simulator, built on mechanisms determined in the laboratory, promising field candidates cannot be identified in advance nor can process performance be optimized.

In this research, UTCHEM was modified to model four-phase water, oil, microemulsion, and gas phases to simulate and interpret chemical EOR processes including free and/or solution gas. We coupled the black-oil model for water/oil/gas equilibrium with microemulsion phase behavior model through a new approach. Four-phase fluid properties, relative permeability, and capillary pressure were developed and implemented. The mass conservation equation was solved for total volumetric concentration of each component at standard conditions and pressure equation was derived for both saturated and undersaturated PVT conditions.

To model foam flow in porous media, comprehensive research was performed comparing capabilities and limitations of implicit texture (IT) and population-balance (PB) foam models. Dimensionless foam bubble density was defined in IT models to derive explicitly the foam-coalescence-rate function in these models. Results showed that each of the IT models examined was equivalent to the LE formulation of a population-balance model with a lamella-destruction function that increased abruptly in the vicinity of the limiting capillary pressure, as in current population-balance models. Foam models were incorporated in UTCHEM to model low-tension-gas and foam flow processes in laboratory and field scales.

The modified UTCHEM reservoir simulator was used to history match published low-tension-gas and foam coreflood experiments. The simulations were also extended to model and evaluate hybrid gas/chemical EOR methods in field scales. Simulation results indicated a well-designed low-tension-gas flooding has the potential to recover the trapped oil where foam provides mobility control during surfactant and surfactant-alkaline flooding in reservoirs with very low permeability.

Table of Contents

| | |
|---|------|
| List of Tables | xiv |
| List of Figures | xvii |
| Chapter 1: Introduction | 1 |
| 1.1 Problem Statement | 1 |
| 1.1.1 Four-Phase Flow Simulation | 1 |
| 1.1.2 Foam Modeling in Porous Media | 2 |
| 1.2 Research Objectives | 4 |
| 1.3 Review of Chapters | 5 |
| Chapter 2: Background and Literature Review | 7 |
| 2.1 Background | 7 |
| 2.2 Black-Oil Model History | 8 |
| 2.3 Introduction to UTCHEM | 11 |
| 2.4 Chemical EOR with Gas | 13 |
| 2.5 Effect of Solution Gas and Pressure on Surfactant Phase Behavior .. | 15 |
| 2.6 Foam Flow in Porous Media | 18 |
| 2.7 Foam Generation Mechanism ins Porous Media | 22 |
| 2.8 Foam Influences on Phase Mobility | 24 |
| 2.9 Foam Models | 24 |
| 2.9.1 Implicit-Texture (IT) Models | 25 |
| 2.9.1.1 UT Foam Model | 25 |
| 2.9.1.2 STARS Model | 26 |
| 2.9.1.3 Vassenden and Holt Model | 28 |
| 2.9.2 Population Balance (PB) Models | 31 |
| 2.9.2.1 Kovsky et al. (1994) Model | 32 |
| 2.9.2.2 Kam et al. (2007) and Kam (2008) Models | 34 |
| Nomenclature | 37 |

| | |
|---|----|
| Chapter 3: Black Oil Model in UTCHEM..... | 40 |
| 3.1 Assumptions..... | 40 |
| 3.2 Bubble Point..... | 41 |
| 3.3 Fluid Properties..... | 41 |
| 3.3.1 Solution Gas Ratio..... | 41 |
| 3.3.2 Formation Volume Factor (FVF)..... | 43 |
| 3.3.3 Fluid Viscosity..... | 47 |
| 3.4 Three Phase Relative Permeability..... | 50 |
| 3.4.1 Corey-Type Model..... | 50 |
| 3.4.2 Parker <i>et al.</i> Model..... | 51 |
| 3.4.3 Stone's II Model..... | 51 |
| 3.5 Three Phase Capillary Pressure..... | 51 |
| 3.5.1 Brooks-Corey Model..... | 52 |
| 3.5.2 van Genuchten Model..... | 52 |
| 3.6 Mass Conservation Equations..... | 52 |
| 3.7 Pressure Equation..... | 56 |
| 3.7.1 Pressure Equation for Saturated Reservoirs..... | 57 |
| 3.7.2 Pressure Equation for Undersaturated Reservoirs..... | 60 |
| 3.8 Transmissibility..... | 63 |
| 3.8.1 Finite Difference Equation for Saturation..... | 67 |
| 3.8.2 Finite Difference Form of Pressure Equation for Saturated Gridblocks..... | 68 |
| 3.8.3 Finite Difference Form of Pressure Equation for Undersaturated Gridblocks..... | 70 |
| 3.9 Bubble Point Tracking..... | 72 |
| 3.9.1 Variable-Substitution Method..... | 72 |
| 3.9.2 Pseudo-solution Method..... | 72 |
| 3.9.3 Bubble Point Tracking in UTCHEM..... | 73 |
| 3.9.3.1 Bubble Point Tracking for Saturated Gridblocks..... | 73 |
| 3.9.3.2 Bubble Point Tracking for Undersaturated Gridblocks..... | 74 |
| Nomenclature..... | 75 |

| | |
|--|-----|
| Chapter 4: Four-Phase Flow Model to Simulate Chemical EOR with Gas..... | 77 |
| 4.1 Model Description | 77 |
| 4.2 Gas Phase Properties..... | 78 |
| 4.3 Liquid Phase Properties | 79 |
| 4.3.1 Viscosity..... | 79 |
| 4.3.2 Formation Volume Factor | 79 |
| 4.3.3 Solution Gas Ratio..... | 80 |
| 4.3.4 Density..... | 80 |
| 4.3.5 Compressibility..... | 81 |
| 4.4 Relative Permeability..... | 81 |
| 4.5 Capillary Pressure | 83 |
| 4.6 Mass Conservation Equation | 84 |
| 4.7 Pressure Equation..... | 88 |
| 4.7.1 Pressure Equation for Saturated Gridblocks..... | 89 |
| 4.7.2 Pressure Equation for Undersaturated Gridblocks | 92 |
| 4.8 Finite Difference Equation for Mass Conservation | 96 |
| 4.9 Finite Difference Form of Pressure Equation for Saturated Gridblocks..... | 99 |
| 4.10 Finite Difference Form of Pressure Equation for Undersaturated Gridblocks..... | 102 |
| 4.11 Bubble Point Tracking | 104 |
| 4.12 Surfactant Phase Behavior | 106 |
| 4.13 Effect of Solution Gas and Pressure on Surfactant Phase Behavior | 108 |
| 4.14 Phase Saturations | 109 |
| Nomenclature | 110 |
| Chapter 5: Comparison of Implicit Texture and Population Balance Models..... | 112 |
| 5.1 Introduction..... | 112 |
| 5.2 Foam Models | 114 |
| 5.2.1 Implicit-Texture Models..... | 115 |
| 5.2.1.1 UT Model | 115 |
| 5.2.1.2 STARS Model..... | 115 |

| | | |
|------------|--|-----|
| 5.2.1.3 | Vassenden-Holt model | 116 |
| 5.2.2 | Population-Balance Models..... | 118 |
| 5.2.2.1 | Kovscek et al. (1994) Model, Modified by Chen et al. (2010)..... | 119 |
| 5.2.2.2 | Kam et al. Model (2007) | 120 |
| 5.2.2.3 | Kam (2008) | 120 |
| 5.3 | Corresponding Foam Model Parameters..... | 122 |
| 5.4 | Fitting Foam Models to Experimental Data..... | 123 |
| 5.4.1 | Experimental Data | 123 |
| 5.4.2 | Data Fitting Procedure..... | 126 |
| 5.4.3 | Steady-State Foam Simulation Results..... | 126 |
| 5.5 | Coalescence Function in Implicit-Texture Models..... | 129 |
| 5.6 | Numerical Simulation of Transient Foam Experiments | 133 |
| 5.6.1 | Chen <i>et al.</i> Experiment (2010) | 133 |
| 5.6.2 | Effect of Foam Injection on Oil Recovery (Farajzadeh <i>et al.</i> 2010)..... | 134 |
| 5.7 | Summary and Conclusions | 137 |
| | Nomenclature..... | 139 |
| Chapter 6: | Simulation Results | 163 |
| 6.1 | Comparison of Black-Oil Model with IMEX-CMG..... | 163 |
| 6.1.1 | Case 1 – Water Injection | 169 |
| 6.1.2 | Case 2 – Gas Injection in Saturated Reservoir | 173 |
| 6.1.3 | Case 3 – Gas Injection in Undersaturated Reservoir | 177 |
| 6.2 | Verification of New UTCHEM Formulation Against Original UTCHEM..... | 181 |
| 6.2.1 | Case 4- Surfactant-Polymer Flood | 184 |
| 6.2.2 | Case 5- Surfactant Flood Assisted with Foam Drive | 188 |
| 6.3 | Grid Refinement Study | 192 |
| 6.3.1 | Case 6- Foam Injection as a Drive in the Surfactant-Polymer Process | 192 |
| 6.4 | Simulation of Low-Tension-Gas Flooding | 202 |

| | | |
|---|---|-----|
| 6.4.1 | Case 7 – Base Case (Surfactant Flooding without Mobility Control)..... | 206 |
| 6.4.2 | Case 8 – Surfactant Alternating Gas (SAG) with Foam..... | 208 |
| 6.4.3 | Case 9 – Co-injection of Surfactant and Gas..... | 209 |
| 6.4.4 | Results and Discussions..... | 210 |
| 6.5 | Mobility Control for Gas Flooding..... | 214 |
| 6.5.1 | Case 10 – Gas Injection..... | 219 |
| 6.5.2 | Case 11 – Water Alternating Gas..... | 222 |
| 6.5.3 | Case 12 – Polymer Alternating Gas (PAG)..... | 225 |
| 6.5.4 | Case 13 – Surfactant Alternating GAS (SAG)..... | 228 |
| 6.5.5 | Results and Discussions..... | 231 |
| 6.6 | Coreflood Simulation of Low-Tension-Gas Flooding in Tight Formations (Case 14)..... | 236 |
| Chapter 7: Summary, Conclusions, and Recommendations..... | | 242 |
| 7.1 | Summary and Conclusions..... | 242 |
| 7.2 | Recommendations for Future Work..... | 246 |
| Appendix A: Gas/surfactant simulation in UTCHEM-2011-9..... | | 248 |
| Appendix B: Sample Input Files..... | | 252 |
| Bibliography..... | | 273 |

List of Tables

| | |
|---|-----|
| Table 4.1: Possible phases and their constituent components in new model..... | 78 |
| Table 5.1: A summary of IT models used in this study | 117 |
| Table 5.2: A summary of PB models used in this study | 121 |
| Table 5.3: Rock and fluid properties for experimental data | 142 |
| Table 5.4: UT model parameters to match experimental data | 142 |
| Table 5.5: STARS model parameters to match experimental data | 142 |
| Table 5.6: Vassenden-Holt model parameters to match experimental data..... | 143 |
| Table 5.7: Chen <i>et al.</i> (2010) Model Parameters to Fit Experimental Data | 143 |
| Table 5.8: Kam <i>et al.</i> (2007) parameters to fit experimental data | 143 |
| Table 5.9: Kam (2008) model parameters to fit experimental data | 144 |
| Table 5.10: The Value of Limiting Water Saturation at Different Model | 144 |
| Table 5.11: Rock and fluid properties in Chen <i>et al.</i> experiment..... | 144 |
| Table 5.12: Population-balance foam model parameters for Chen <i>et al.</i> experiment. | 145 |
| Table 5.13: UT foam model parameters for Chen <i>et al.</i> experiment | 145 |
| Table 5.14: Rock and fluid properties in Farajzadeh <i>et al.</i> experiment..... | 145 |
| Table 5.15: Chen <i>et al.</i> foam model parameters to history match Farajzadeh <i>et al.</i> experiment..... | 146 |
| Table 5.16: UT foam model parameters to history match Farajzadeh <i>et al.</i> experiment..... | 146 |
| Table 6.1: Reservoir model and fluid properties (Cases 1 to 3) | 164 |
| Table 6.2: Saturated oil and gas PVT properties (Cases 1 to 3 and 6) | 166 |
| Table 6.3: Water and oil relative permeability (Cases 1 to 3) | 168 |
| Table 6.4: Oil and gas relative permeability (Cases 1 to 3)..... | 168 |

| | |
|---|-----|
| Table 6.5: Model description (Cases 4 and 5) | 182 |
| Table 6.6: Relative permeability parameters (Cases 4 and 5) | 182 |
| Table 6.7: Surfactant and microemulsion parameters (Cases 4 and 5)..... | 183 |
| Table 6.8: Polymer properties (Cases 4 and 5)..... | 184 |
| Table 6.9: Case 4- Injection scenario..... | 185 |
| Table 6.10: Case 5- Injection scenario..... | 189 |
| Table 6.11: UT foam model parameters (Case 5)..... | 189 |
| Table 6.12: Model description (Case 6)..... | 193 |
| Table 6.13: Relative permeability data (Case 6)..... | 194 |
| Table 6.14: Surfactant adsorption, microemulsion phase behavior and viscosity parameters (Case 6)..... | 195 |
| Table 6.15: Polymer properties (Cases 6)..... | 196 |
| Table 6.16: Case 6 – Injection schedule | 196 |
| Table 6.17: UT foam model parameters (Case 6)..... | 197 |
| Table 6.18: Case 6- Number of gridblocks in different runs | 197 |
| Table 6.19: Reservoir and fluid properties for four-phase simulations (Cases 7 to 9)..... | 203 |
| Table 6.20: Gas phase properties (Cases 7 to 9)..... | 204 |
| Table 6.21: Relative permeability for four-phase simulations (Cases 7 to 9) | 204 |
| Table 6.22: Surfactant adsorption, microemulsion phase behavior and viscosity parameters (Cases 7 to 9)..... | 205 |
| Table 6.23: UT foam model parameters (Cases 8 and 9) | 206 |
| Table 6.24: Case 7 – Injection Schedule..... | 207 |
| Table 6.25: Case 8 – Injection Schedule..... | 208 |
| Table 6.26: Case 9 – Injection Schedule..... | 210 |

| | |
|---|-----|
| Table 6.27: Reservoir and fluid properties (Cases 10 to 13) | 216 |
| Table 6.28: Oil-Gas PVT properties (Cases 10 to 13) | 218 |
| Table 6.29: Corey-relative permeability parameters (Lim 1993) (Cases 10 to 13) | 219 |
| Table 6.30: UT Foam model parameters (Case 13) | 228 |
| Table 6.31: Model fit parameters for microemulsion phase behavior in Figure 6.75 (Case 14) | 237 |
| Table 6.32: Case 14 – Injection strategy and species concentration (LTG_Tert_#1) | 238 |
| Table 6.33: Corey relative permeability parameters (Cases 14)..... | 239 |
| Table 6.34: UT foam model parameters (Case 14)..... | 239 |
| Table A.1: Model parameters for synthetic one-dimensional case..... | 248 |

List of Figures

| | |
|---|----|
| Figure 1.1: Schematic illustrating the increased vertical sweep using foam (right image) compared to gas (left image) | 3 |
| Figure 2.1: Optimum salinity of live-oil, dead-oil, and surrogate-oil for different oil samples (Jang <i>et al.</i> 2014)..... | 16 |
| Figure 2.2: Solubilization ratios of live-oil, dead-oil, and surrogate-oil for different oil samples (Jang <i>et al.</i> 2014)..... | 17 |
| Figure 2.3: Effect of pressure on microemulsion phase behavior at 980 and 2000 psi (Jang <i>et al.</i> 2014)..... | 18 |
| Figure 2.4: Limiting capillary pressure concept: In a porous medium capillary pressure is a function of water saturation and the gas fractional-flow function depends on bubble size. At the limiting capillary pressure P_c^* foam breaks. At this fixed water saturation $S_w^* = S_w(P_c^*)$ foam becomes coarser, mean bubble size increases, and gas fractional flow increases (Adapted from Khatib <i>et al.</i> , 1988.) The LE behavior of foam would follow the red curve at small S_w , then the dotted line, and then the green curve at large S_w on the right plot. | 21 |
| Figure 2.5: Pressure-gradient contours as a function of superficial velocities of gas and liquid calculated from the foam model presented (a) abrupt transition between regimes (b) less abrupt transition. Dotted line is a hypothetical scan of foam quality at a fixed superficial velocity of 15 ft/day (Farajzadeh <i>et al.</i> , 2015)..... | 21 |
| Figure 2.6: Snap-off mechanism showing (A) gas enters to constriction (B) new bubble is formed (adopted from: Ransohoff and Radke, 1988)..... | 23 |

| | |
|--|-----|
| Figure 2.7: Lamella division mechanism (A) lamellae is approaching the branch point (B) divided gas bubbles formed (adopted from: Ransohoff and Radke, 1988) | 23 |
| Figure 2.8: Leave behind mechanism (A) gas invasion (B) forming lens (adopted from: Ransohoff and Radke, 1988)..... | 23 |
| Figure 2.9: Relative permeability expected from Vassenden-Holt foam model | 30 |
| Figure 2.10: Characteristics of foam relative permeability equation..... | 30 |
| Figure 2.11: Comparison of generation function [Kam <i>et al.</i> (2007) and Kam (2008)]..... | 36 |
| Figure 3.1: Solution gas/oil ratio versus pressure for constant bubble point pressure. | 42 |
| Figure 3.2: Solution gas/oil ratio versus pressure for variable bubble point pressure. | 43 |
| Figure 3.3: Water formation volume factor versus pressure..... | 44 |
| Figure 3.4: Gas formation volume factor versus pressure. | 45 |
| Figure 3.5: Oil formation volume factor versus pressure for constant bubble point. | 46 |
| Figure 3.6: Oil formation volume factor versus pressure for variable bubble point..... | 46 |
| Figure 3.7: Water viscosity versus pressure. | 47 |
| Figure 3.8: Gas viscosity versus pressure. | 48 |
| Figure 3.9: Oil viscosity versus pressure in saturated and undersaturated regions. | 49 |
| Figure 3.10: Oil viscosity versus pressure for variable bubble point. | 49 |
| Figure 5.1: Capillary-pressure curves used to model CO ₂ and N ₂ foam experiments | 147 |
| Figure 5.2: UT model fit to experimental data using the parameters in Table 5.4 | 148 |
| Figure 5.3: STARS model fit to experimental data using the parameters in Table 5.5..... | 148 |

| | |
|--|-----|
| Figure 5.4: a) Vassenden-Holt model fit to experimental data using the parameters in Table 5.6, assuming $a = 1$ in Equation (5-8) b) Vassenden-Holt model fit to experimental data using the parameters in Table 5.6, including a | 149 |
| Figure 5.5: Chen <i>et al.</i> model fit to experimental data using the parameters in Table 5.7..... | 150 |
| Figure 5.6: Kam <i>et al.</i> model fit to experimental data using the parameters in Table 5.8..... | 150 |
| Figure 5.7: Kam model fit to experimental data using the parameters in Table 5.9... | 151 |
| Figure 5.8: Lamella-destruction function f in different population balance models plotted as a function of water saturation. Vertical dotted line represents S_w^* | 151 |
| Figure 5.9: Lamella-destruction function f in different population-balance models plotted as a function of capillary pressure. Vertical dotted line represents P_c^* | 152 |
| Figure 5.10: Lamella-destruction function f implied by the UT foam model plotted as a function of water saturation. Vertical dotted lines represent $S_w^* - \varepsilon$ | 152 |
| Figure 5.11: Lamella-destruction function f implied by the UT foam model plotted as a function of capillary pressure. Vertical dotted lines represent the capillary pressure at $S_w^* - \varepsilon$ | 153 |
| Figure 5.12: Lamella-destruction function f implied by the Vassenden-Holt foam model plotted as a function of water saturation. The vertical dotted lines is S_f | 153 |
| Figure 5.13: Lamella-destruction function f implied by the Vassenden-Holt foam model plotted as a function of capillary pressure. The vertical dotted lines represent the capillary pressure at S_f | 154 |

| | |
|---|-----|
| Figure 5.14: Lamella-destruction function f implied by the STARS foam model plotted as a function of water saturation. The vertical dotted lines represent f_{mdry} | 154 |
| Figure 5.15: Lamella-destruction function f implied by the STARS foam model plotted as a function of capillary pressure. The vertical dotted lines represent capillary pressure at f_{mdry} | 155 |
| Figure 5.16: Dimensional foam texture obtained in population-balance models to fit Moradi-Araghi <i>et al.</i> experiment. | 155 |
| Figure 5.17: Explicit dimensionless foam texture defined in implicit texture models to fit Moradi-Araghi <i>et al.</i> experiment..... | 156 |
| Figure 5.18: Dimensional foam texture obtained in population-balance models to fit Alvarez <i>et al.</i> experiment..... | 156 |
| Figure 5.19: Explicit dimensionless foam texture defined in implicit texture models to fit Alvarez <i>et al.</i> experiment. | 157 |
| Figure 5.20: Transient aqueous phase saturation (experimental data from Chen <i>et al.</i> 2010 vs. simulation results using LE Chen <i>et al.</i> model in this work) .. | 157 |
| Figure 5.21: Transient pressure drop (experimental data from Chen <i>et al.</i> 2010 vs. simulation results using LE Chen <i>et al.</i> model in this work)..... | 158 |
| Figure 5.22: Simulation of transient flowing foam texture using LE Chen <i>et al.</i> model in this work | 158 |
| Figure 5.23: Transient aqueous phase saturation (experimental data from Chen <i>et al.</i> 2010 vs. simulation results using UT foam model in this work)..... | 159 |
| Figure 5.24: Transient pressure drop (experimental data from Chen <i>et al.</i> 2010 vs. simulation results using UT foam model in this work)..... | 159 |

| | |
|---|-----|
| Figure 5.25: Cumulative oil production (experimental data from Farajzadeh <i>et al.</i> 2010 experiment vs. simulation results using Chen <i>et al.</i> model in this work) | 160 |
| Figure 5.26: Pressure drop (experimental data from Farajzadeh <i>et al.</i> 2010 experiment vs. simulation results using Chen <i>et al.</i> model in this work) | 160 |
| Figure 5.27: Cumulative oil production (experimental data from Farajzadeh <i>et al.</i> 2010 experiment vs. simulation results using UT foam model in this work) | 161 |
| Figure 5.28: Pressure drop (experimental data from Farajzadeh <i>et al.</i> 2010 experiment vs. simulation results using UT foam model in this work) | 161 |
| Figure 5.29: Effect of oil on foam resistance factor in UT foam model simulation... | 162 |
| Figure 6.1: Reservoir model for UTCHEM and IMEX-CMG (Cases 1 to 3) | 164 |
| Figure 6.2: Oil and gas formation volume factor in UTCHEM and IMEX-CMG (Cases 1 to 3) | 165 |
| Figure 6.3: Oil and gas viscosity in UTCHEM and IMEX-CMG (Cases 1 to 3)..... | 165 |
| Figure 6.4: Solution gas/oil ratio in UTCHEM and IMEX-CMG (Cases 1 to 3)..... | 166 |
| Figure 6.5: Oil/water relative permeability in UTCHEM and IMEX-CMG (Cases 1 to 3) | 167 |
| Figure 6.6: Oil/gas relative permeability in UTCHEM and IMEX-CMG (Cases 1 to 3)..... | 167 |
| Figure 6.7: Case 1- Pressure map (psi) after 30 days (UTCHEM vs. IMEX-CMG).. | 169 |
| Figure 6.8: Case 1- Oil saturation map after 30 days (UTCHEM vs. IMEX-CMG).. | 170 |
| Figure 6.9: Case 1- Cumulative oil recovery (UTCHEM vs. IMEX-CMG) | 170 |
| Figure 6.10: Case 1- Oil rate (UTCHEM vs. IMEX-CMG)..... | 171 |
| Figure 6.11: Case 1- Water rate (UTCHEM vs. IMEX-CMG)..... | 171 |

| | |
|--|-----|
| Figure 6.12: Case 1- Gas rate (UTCHEM vs. IMEX-CMG) | 172 |
| Figure 6.13: Case 1- Average pressure (UTCHEM vs. IMEX-CMG)..... | 172 |
| Figure 6.14: Case 2- Pressure map (psi) after 30 days (UTCHEM vs. IMEX-CMG) | 173 |
| Figure 6.15: Case 2- Oil saturation map after 30 days (UTCHEM vs. IMEX-CMG) | 174 |
| Figure 6.16: Case 2- Oil recovery (UTCHEM vs. IMEX-CMG)..... | 174 |
| Figure 6.17: Case 2- Oil rate (UTCHEM vs. IMEX-CMG)..... | 175 |
| Figure 6.18: Case 2- Water rate (UTCHEM vs. IMEX-CMG)..... | 175 |
| Figure 6.19: Case 2- Gas rate (UTCHEM vs. IMEX-CMG) | 176 |
| Figure 6.20: Case 2- Average pressure (UTCHEM vs. IMEX-CMG)..... | 176 |
| Figure 6.21: Case 3- Pressure map (psi) after 30 days (UTCHEM vs. IMEX-CMG) | 177 |
| Figure 6.22: Case 3- Oil saturation after 30 days (UTCHEM vs. IMEX-CMG) | 178 |
| Figure 6.23: Case 3- Oil recovery (UTCHEM vs. IMEX-CMG) - two curves coincide..... | 178 |
| Figure 6.24: Case 3- Oil rate (UTCHEM vs. IMEX-CMG) - two curves coincide ... | 179 |
| Figure 6.25: Case 3- Water rate (UTCHEM vs. CMG) - two curves coincide | 179 |
| Figure 6.26: Case 3- Gas rate (UTCHEM vs. IMEX-CMG) - two curves coincide .. | 180 |
| Figure 6.27: Case 3- Average pressure (UTCHEM vs. IMEX-CMG)..... | 180 |
| Figure 6.28: Oil/water solubilization ratio for surfactant formulation (Cases 4 and 5)..... | 183 |
| Figure 6.29: Polymer viscosity curve (Cases 4 and 5)..... | 184 |
| Figure 6.30: Case 4- Oil cut and cumulative oil recovery (New UTCHEM vs. Original UTCHEM)..... | 185 |
| Figure 6.31: Case 4- Average phase saturations inside the core versus injected PV (New UTCHEM vs. Original UTCHEM)..... | 186 |

| | |
|---|-----|
| Figure 6.32: Case 4- Phase saturations versus dimensionless distance at 0.5 PV (New UTCHEM vs. Original UTCHEM)..... | 186 |
| Figure 6.33: Case 4- Effluent total surfactant concentration (New UTCHEM vs. Original UTCHEM)..... | 187 |
| Figure 6.34: Case 4- Pressure drop across the core (New UTCHEM vs. Original UTCHEM) | 187 |
| Figure 6.35: Case 5- Oil cut and cumulative oil recovery (New UTCHEM vs. Original UTCHEM)..... | 190 |
| Figure 6.36: Case 5- Average phase saturations inside the core versus injected PV (New UTCHEM vs. Original UTCHEM)..... | 190 |
| Figure 6.37: Case 5- Phase saturations versus dimensionless distance at 0.5 PV (New UTCHEM vs. Original UTCHEM)..... | 191 |
| Figure 6.38: Case 5- Effluent total surfactant concentration (New UTCHEM vs. Original UTCHEM)..... | 191 |
| Figure 6.39: Case 5- Pressure drop across the core (New UTCHEM vs. Original UTCHEM) | 192 |
| Figure 6.40: Oil/water solubilization ratio for surfactant formulation (Cases 6)..... | 194 |
| Figure 6.41: Polymer viscosity curve (Cases 6) | 195 |
| Figure 6.42: Case 6- Reservoir model and gridblock sizes for different simulations runs..... | 198 |
| Figure 6.43: Case 6 - Cumulative Oil recovery (Runs 4, 5 and Runs 2, 6, 7, 8, 9 coincide)..... | 199 |
| Figure 6.44: Case 6 – Final oil recovery versus dimensionless gridblock size in areal direction | 199 |

| | |
|--|-----|
| Figure 6.45: Case 6 – Final oil recovery versus dimensionless gridblock size in vertical direction | 200 |
| Figure 6.46: Case 6– Oil concentration after 1200 days a) full field and b) a quarter of the field | 201 |
| Figure 6.47: Case 6– Gas saturation after 1200 days a) full field and b) a quarter of the field | 201 |
| Figure 6.48: Reservoir model and permeability distribution (Cases 7 to 9)..... | 202 |
| Figure 6.49: Oil/water solubilization ratio for surfactant formulation (Cases 7 to 9) | 205 |
| Figure 6.50: Case 7 - Cumulative oil recovery and oil rate..... | 207 |
| Figure 6.51: Case 8 - Cumulative oil recovery and oil rate | 209 |
| Figure 6.52: Case 9 - Cumulative oil recovery and oil rate..... | 210 |
| Figure 6.53: Comparison of recovery factor between Cases 7 to 9..... | 211 |
| Figure 6.54: Remaining oil saturation (after 360 days) a) Case 7- Base case b) Case 8- SAG c) Case 9– Co-injection (surfactant/gas) | 212 |
| Figure 6.55: Salinity limits and effluent salinity for Cases 7 to 9 | 213 |
| Figure 6.56: Injector bottomhole pressure for Cases 7 to 9 | 213 |
| Figure 6.57: Reservoir model, well locations and permeability distribution ($L_x = L_y = 150$ ft, $L_z = 40$ ft)..... | 215 |
| Figure 6.58: Oil and gas formation volume factor (Cases 10 to 13)..... | 217 |
| Figure 6.59: Oil and gas viscosity (Cases 10 to 13) | 217 |
| Figure 6.60: Solution gas/oil ratio (Cases 10 to 13) | 218 |
| Figure 6.61: Case 10 - Cumulative oil recovery and oil rate..... | 220 |
| Figure 6.62: Case 10 - Remaining oil saturation at the end of the gas flood (700 days) a) full field and b) across-section between injector and producer | 221 |
| Figure 6.63: Case 11 - Cumulative oil recovery and oil rate..... | 223 |

| | |
|--|-----|
| Figure 6.64: Case 11 - Remaining oil saturation after seven cycle of WAG a) full field and b) across-section between injector and producer | 224 |
| Figure 6.65: Case 12 - Cumulative oil recovery and oil rate..... | 226 |
| Figure 6.66: Case 12 - Remaining oil saturation after seven cycle of PAG a) full field and b) across-section between injector and producer | 227 |
| Figure 6.67: Case 13 - Cumulative oil recovery and oil rate..... | 229 |
| Figure 6.68: Case 13 - Remaining oil saturation after gas injection with foam a) full field and b) across-section between injector and producer | 230 |
| Figure 6.69: Oil recovery factor for Cases 10 through 13..... | 232 |
| Figure 6.70: Oil rate for Cases 10 through 13 | 232 |
| Figure 6.71: Oil concentration for Cases 10 through 13 | 233 |
| Figure 6.72: Injector bottomhole-pressure for Cases 10 through 13..... | 233 |
| Figure 6.73: Average reservoir pressure for Cases 10 through 13 | 234 |
| Figure 6.74: Gas saturation (after 370 days) a) Case 10- Gas injection b) Case 11- WAG c) Case 12– PAG d) Case 13- Foam..... | 235 |
| Figure 6.75: Case 14- Oil and water solubilization ratio for selected surfactant formulation (symbols are experimental data and lines are model fit) ... | 237 |
| Figure 6.76: Case 14 - Oil cut and cumulative oil recovery (experimental data from the work by Szlendak <i>et al.</i> 2013 vs. simulation results in this work) .. | 240 |
| Figure 6.77: Case 14 - Pressure drop over the entire core (experimental data from the work by Szlendak <i>et al.</i> 2013 vs. simulation results in this work) | 241 |
| Figure A.1: Oil recovery and oil cut for the co-injection of surfactant and gas using UTCHEM-2011-9. Simulation failed after 0.751 PV..... | 249 |
| Figure A.2: Gas saturation at 0.751 PV. Gas saturation in second gridblock close to the injector is -0.681 (UTCHEM-2011-9) | 249 |

| | |
|---|-----|
| Figure A.3: Oil recovery and oil cut for the co-injection of surfactant and gas using new improved UTCHEM code. | 250 |
| Figure A.4: Gas saturation at 0.751 PV using new improved UTCHEM code. | 250 |
| Figure A.5: Comparison of oil recovery between UTCHEM-2011-9 and new improved UTCHEM code. | 251 |
| Figure A.6: Comparison of oil cut between UTCHEM-2011-9 and new improved UTCHEM code. | 251 |

Chapter 1: Introduction

This chapter presents the problem statement and describes the main objectives of the research. The dissertation chapters are also briefly summarized.

1.1 PROBLEM STATEMENT

1.1.1 Four-Phase Flow Simulation

The need for improved models to simulate chemical enhanced oil recovery (CEOR) methods involving either free gas or solution gas has increased in recent years as it has become more common to inject surfactants to recover live oils using surfactant-polymer or alkaline-surfactant-polymer flooding, or to inject gas with the surfactant solution (low-tension gas flooding or foam). A four-phase flow and transport formulation is needed to accurately model these EOR methods. New experimental data are now available to help in the development and validation of such models. In particular, the effect of pressure and solution gas on microemulsion phase behavior is now much better understood because of new and much more systematic experimental data. New low-tension gas or alkali surfactant foam experiments have also recently been published.

The UTCHEM simulator was used in this research. UTCHEM is a three-dimensional chemical flooding reservoir simulator developed at The University of Texas at Austin to model chemical EOR processes such as polymer flooding, polymer/gel, surfactant-polymer flooding, alkaline-surfactant-polymer flooding and low-tension-gas flooding. The solution scheme is analogous to IMPES, where pressure is solved for implicitly and concentrations (rather than saturations) are solved for explicitly. Phase saturations and species concentrations in each phase are then solved in chemical phase

behavior routines. An energy balance equation is solved explicitly for reservoir temperature. The energy balance equation includes heat flow between the reservoir and over- and under-burden rocks.

Gas is modeled as a single component. All components are assumed to be slightly compressible. The previous implementation of gas in UTCHEM was often the source of numerical instability problems. Srivastava (2010) reported large computational time and numerical instability in UTCHEM during the simulation of gas and surfactant in Winsor Type III. Appendix A presents an example case in which UTCHEM-2011-9 fails to simulate simultaneous injection of gas and surfactant.

As part of this research, UTCHEM was modified to include capillary pressure and relative permeability models for four-phase flow and to add a black-oil model.

1.1.2 Foam Modeling in Porous Media

Enhanced oil recovery (EOR) techniques such as miscible-gas, thermal, and chemical methods have the potential to increase oil production and oil recovery efficiency (Lake *et al.*, 2014). The development, optimization, and implementation of EOR methods require accurate and robust reservoir simulators. Gas EOR projects often suffer from low volumetric sweep efficiency due to low gas density and viscosity. As shown in Figure 1.1, the use of foam in gas EOR applications has the potential to improve oil recovery by reducing gas mobility (Schramm, 1994; Kovscek and Radke 1994; Rossen, 1996; Farajzadeh *et al.*, 2011; Andrianov *et al.* 2012, Lashgari *et al.* 2014).

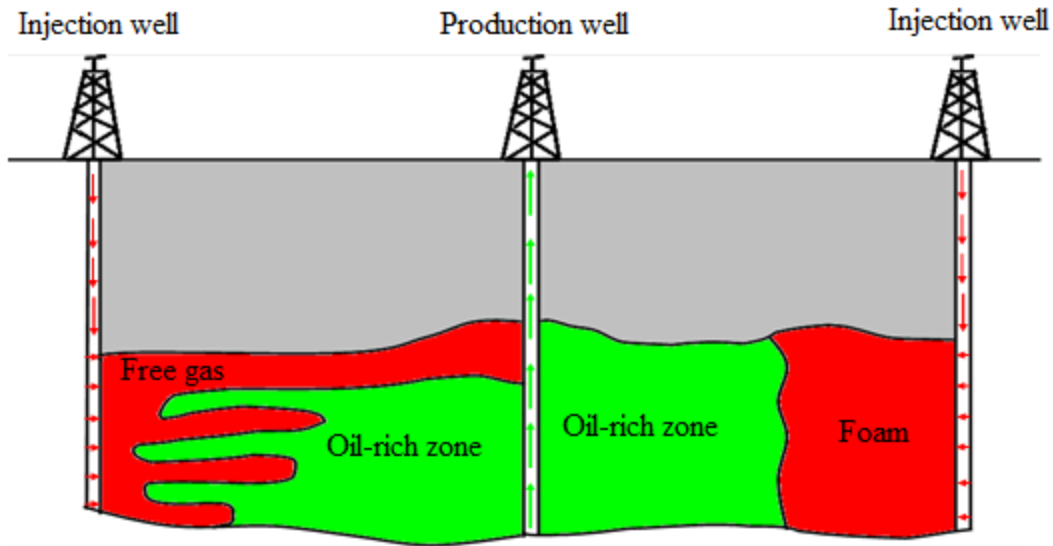


Figure 1.1: Schematic illustrating the increased vertical sweep using foam (right image) compared to gas (left image)

Design of foam EOR processes for field applications requires accurate simulation models. A reliable simulator can be used to help identify promising reservoirs for EOR and to optimize performance of the EOR process among other beneficial uses.

Two types of foam models have been developed. Population-balance (PB) models attempt to represent all the dynamic processes of lamella creation and destruction as well as the effect of bubble size on gas mobility. These models can be set to assume local equilibrium (LE) between the processes of lamella creation and destruction. The second type of foam model reflects the effects of foam texture implicitly through a gas mobility-reduction factor that depends on saturations, superficial velocities and other factors. These models all assume LE. To avoid confusion with the LE version of PB models we refer to the second group here as implicit-texture (IT) models. PB models are often assumed to be better because they are based on "first principles," and the dynamic version of the models are sometimes called "full physics" models (Chen *et al.*, 2010; Ma

et al., 2014b). The IT models are often referred to as "empirical" or "semi-empirical" and lacking in essential physics (Kovscek *et al.*, 1995; Rossen *et al.*, 1999; Chen *et al.*, 2010; Skoreyko *et al.*, 2012; Ma *et al.*, 2014b). However, the ultimate test of a model is its ability to represent and explain a variety of data using different model parameters.

1.2 RESEARCH OBJECTIVES

The objective of this research was to develop a four-phase flow model to simulate hybrid chemical/gas EOR processes including low-tension-gas flooding, foam, and polymer alternating gas. A black-oil model for water/oil/gas was coupled with the surfactant/oil/water phase behavior through a new formulation implemented in the UTCHEM reservoir simulator. The resulting flow equations are discretized and solved using a block-centered finite-difference method.

A comprehensive evaluation of available foam models was performed to study the capabilities and limitations of each model. UT (P_c^*), and local-equilibrium Chen's population balance model were implemented and coupled with the new four-phase simulator to study foam flow in porous media. The new version of the UTCHEM simulator was used to evaluate chemical EOR methods involving solution gas and/or free gas.

1.3 REVIEW OF CHAPTERS

This dissertation describes the development and application of four-phase flow model coupled with existing foam models. This research has been organized in seven chapters.

Chapter 2 contains a review on the related topics to this research. This chapter provides a background on black-oil and compositional simulators, foam flow behavior in porous media, and existing foam models. It includes a literature review on the hybrid chemical/gas laboratory experiments.

Chapter 3 includes assumptions, equations and initial framework for black-oil formulation in UTCHEM. The pressure dependence of fluid properties, and available three-phase relative permeability and capillary pressure models will be discussed.

Chapter 4 presents four-phase flow formulation and its implementation method in chemical simulator UTCHEM. The discretized form of mass and pressure equations are discussed in details. Fluid properties, relative permeabilities, and capillary pressures are defined for the four-phase flow.

Chapter 5 compares population-balance and implicit-texture (IT) models in two ways. First, it shows the equivalence of the two approaches by deriving explicitly the foam-coalescence-rate function implicit in the IT models, and showing its similarity to that in population-balance models. Second, the models are compared based on their ability to represent a set of N_2 and CO_2 steady-state foam experiments. It also discusses the corresponding parameters of the different methods.

Chapter 6 presents simulation results with new developed four-phase flow simulator UTCHEM. This chapter starts with verification of black-oil model with IMEX. The new formulation is checked for convergence with grid refinement tests. The model is also compared with original UTCHEM in absence of gas phase. After verification tests,

the simulator is used to history match a low-tension-gas coreflood experiment and model low-tension-gas flooding with different injection schemes in field scales. The impact of Water Alternating Gas (WAG), Polymer Alternating Gas (PAG), and foam on gas mobility control are also investigated.

Chapter 7 provides the key findings and conclusions remarks of this research. Finally recommendations are made for further studies and developments.

Chapter 2: Background and Literature Review

This chapter provides a literature review of black-oil and compositional reservoir simulators including UTCHEM, hybrid chemical/gas EOR processes including low-tension-gas flooding (surfactant/gas, or alkali/surfactant/gas), foam flow in porous media, and foam models that will be used later in Chapter 5.

2.1 BACKGROUND

Reservoir simulation is a software tool for predicting hydrocarbon reservoir performance based on relevant physics, chemistry, geology, reservoir engineering and numerical and computational sciences. The need for reservoir simulation stems from the requirement for petroleum engineers to obtain accurate performance predictions for a hydrocarbon reservoir under different operating conditions. This need arises from the fact that in a hydrocarbon recovery project (which may involve a capital investment of hundreds of millions of dollars), the risk associated with the selected development plan must be assessed and minimized. Factors contributing to this risk include the complexity of the reservoir because of heterogeneous and anisotropic rock properties, regional variations of fluid properties and relative permeability characteristics, the complexity of the hydrocarbon-recovery mechanisms, and the limitations of the predictive methods that may make them inappropriate among other factors. The first three factors are beyond the engineer's control, and they are taken into consideration in reservoir simulation through the generality of input data built into reservoir-simulation models and the availability of simulators for various enhanced oil recovery (EOR) techniques. The fourth factor can be controlled through proper use of sound engineering practices and judicious use of reservoir simulation.

Reservoir simulators can be classified in several ways (Ertekin *et al.* 2001). The most common criteria for classifying reservoir simulators are the type of reservoir and reservoir fluids to be simulated and the recovery processes occurring in the subject reservoir. Reservoir simulators can also be classified according to the coordinate system used in the model, the number of dimensions in space, and the number of phases.

Reservoir simulators based on reservoir and fluid descriptions fall into two categories: black-oil and compositional simulators. Black oil simulators are used in situations where recovery processes are insensitive to compositional changes in the reservoir fluids. In black-oil simulators, mass transfer is assumed to be strictly pressure dependent and the fluid properties are modeled using B_o , B_g , and R_s .

Compositional simulators are used when recovery processes are sensitive to compositional changes. These situations include primary depletion of volatile-oil and gas-condensate reservoirs, pressure-maintenance operations in these reservoirs among other processes. Also, multiple-contact-miscible processes are generally modeled with compositional simulators. In compositional simulators, an equation of state is used to model the hydrocarbon phase behavior.

2.2 BLACK-OIL MODEL HISTORY

Some part of this literature review on black-oil model history is from the work by Lu (2008).

Early computing technology in the 1960's facilitated both the development of the black oil model and mathematical research into solvers for large systems of equation. Numerous workers contributed to the pioneering work on reservoir simulation (Douglas and Peaceman, 1955; Peaceman, 1977; Aziz and Settari, 1979; Coats, 1982; Peaceman

and Rachford, 1995). The three-phase black oil fluid treatment has remained the standard for reservoir simulators (Coats, 1982).

The 1970's, the conventional formulation of the black oil model was derived and was used in the simulation field (Aziz and Settari, 1979; Breit *et al.*, 1973; Kazemi *et al.*, 1978; Peaceman, 1977; Wong *et al.*, 1987). The main attraction of the black oil model at that time was that it accounted for the four basic oil recovery mechanisms: (1) fluid expansion, (2) displacement, (3) gravity drainage, and (4) capillary imbibition (Coats, 1982). Cook *et al.* (1974) proposed a method for extending the black oil model to include gas injection with non-equilibrium gases for represent into more complex compositional effects, including when three or more components are required; Spivak and Dixon (1973) then made modifications to the black oil formulation to account for volatile oil and gas condensate fluids, where the oil component may exist in the gas phase.

In the 1980s, the black oil model was applied to more complicated geological conditions. Dimitrie *et al.* (1985) described an approach for simulating three-phase flow in a fractured reservoir that was based on the dual porosity concept with certain modifications to the 3D black oil model. Whitson *et al.* (1988) modified the black oil model with simplified compositional PVT formulations to solve the full-field simulation problems of several North Sea reservoirs that contained near-critical fluids with compositions that varied areally and with depth. The modified black oil model included four components: non-volatile surface oil, volatile surface oil, surface hydrocarbon gas, and injection gas. Simulation of a heavy oil reservoir with the black oil model had been addressed by Huan (1985, 1986), in which he proposed the flash approach. Several papers treated black oil simulation as a special case of compositional simulation (Gjerde *et al.*, 1988; Norvik , 1985; Watts, 1985, Young and a Stephenson, 1983) and the behavior of the gas phase was investigated specifically (Fanchi, 1987, Forsythe and

Sammon, 1984). In particular, Trangenstein and Bell (1989) provided a detailed mathematical structure of the black oil model, including thermodynamic equilibrium, an equation of state (EOS) and component conservation equations. It should be noted that the black oil models developed during this decade were beginning to realize their potential to simulate full-field reservoir problems.

Since the 1990s, most research has focused on the various black oil model solution methodologies (Buchwalter and Miller, 1993; Coats, 1999; Collins *et al.* 1992). Several general purpose black oil models have been developed to handle comprehensive reservoir problems (Ganzer and Heinemann, 1997; Coats, 1998; Tan and Kaiogerakis, 1991). Tan and Kaiogerakis described a reservoir simulator with an automatic history matching capability. Ganzer and Heinemann (1997) developed a multipurpose reservoir simulator to solve a wide range of reservoir problems, including three-phase black oil depletion, miscible displacement of multi-component fluids. The black oil model has also been used together with other models, such as the compositional model, to deal with particular reservoir conditions. Fevang *et al.* (2000) discussed the guidelines for choosing different models for volatile oil and gas-condensate reservoirs. They discovered that the black oil model can be used for most depletion cases with proper PVT data; however, it is not suitable in most cases of gas injection. In recent decades, much effort has also been expended in solving the black oil problem using powerful parallel computation technologies (Agarwal *et al.*, 2001; Kendall *et al.*, 1983; Ma *et al.*, 1995)

The black oil model with thermal functionality is another developing topic in reservoir simulation. It is becoming more and more important together with the enhancement of oil recovery, especially with regard to steam injection (Behie *et al.*, 1987; Chen *et al.*, 2000).

2.3 INTRODUCTION TO UTCHEM

UTCHEM is a 3-D, multicomponent, multiphase, compositional model of chemical flooding processes which accounts for microemulsion phase behavior, chemical and physical transformations and heterogeneous porous media properties. It uses advanced concepts in high-order numerical accuracy and dispersion control and vector and parallel processing. A one-dimensional version of the simulator was originally developed by Pope and Nelson (1978) to simulate enhanced recovery oil using surfactant and polymer processes. Thus, the microemulsion phase behavior as a function of surfactant, alcohol, oil, and aqueous components was developed early and has been extensively verified against experiments. Generalizations by Bhuyan *et al.* (1990) have extended the model to include other chemical processes and a variety of geochemical reactions between the aqueous and solid phases. The non-equilibrium dissolution of organic components from a non-aqueous phase liquid into a flowing aqueous or microemulsion phase is modeled using a linear mass-transfer model. In this simulator, the flow and mass-transport equations are solved for any number of user-specified chemical components (water, organic contaminants, surfactant, alcohols, polymer, chloride, calcium, other electrolytes, microbiological species, electron acceptors, etc.). These components can form up to four fluid phases (water, oil, microemulsion, and gas) and any number of solid minerals depending on the overall composition. The microemulsion forms only above the critical micelle concentration of the surfactant and is a thermodynamically stable mixture of water, surfactant and one or more organic components. All of these features taken together, but especially the transport and flow of multiple-phases with multiple-species and multiple-chemical and biological reactions make UTCHEM unique. A multiphase and multicomponent dual porosity model has also

been implemented in UTCHEM to evaluate the use of chemical methods in naturally fractured oil reservoirs.

UTCHEM can be used to simulate a wide range of displacement processes at both the field and laboratory scales. The number of components is variable depending on the application. When electrolytes, tracers, co-solvents, polymer, and other commonly needed components are included, the number of components may be on the order of twenty or more. When the geochemical option is used, a large number of additional aqueous components and solid phases may be used.

Surfactant phase behavior modeling is based in part on the Hand representation of the ternary phase diagram (Hand, 1939). A pseudo-phase theory (Prouvost *et al.*, 1984, 1985) reduces the water, oil, surfactant, and co-surfactant fluid mixtures to a pseudo-ternary composition space. The major physical phenomena modeled are microemulsion phase behavior, density, viscosity, velocity-dependent dispersion, molecular diffusion, adsorption, interfacial tension, relative permeability, capillary pressure, capillary trapping of residual phases, cation-exchange, and polymer, microemulsion and foam rheology, gel reactions and properties such as permeability reduction, polymer inaccessible pore volume, various geochemical and microbial reactions and heat losses (Hirasaki and Pope, 1974; Bear, 1979; Satoh, 1984; Datta Gupta *et al.* 1986; Delshad *et al.*, 1986; Pope *et al.*, 1987; Saad, 1989; Jin, 1995; Delshad *et al.*, 2008, Mohammadi, 2008).

The reaction chemistry includes aqueous electrolyte chemistry, precipitation and dissolution of minerals, ion exchange reactions with the matrix (the geochemical option), reactions of acidic components of oil with the bases in the aqueous solution (Bhuyan, 1989; Bhuyan *et al.*, 1990 and 1991) and polymer reactions with crosslinking agents to form gel (Garver *et al.*, 1989; Kim, 1995).

The balance equations are the mass conservation equations, an overall balance that determines the pressure for up to four fluid phases, and an energy balance equation to determine the temperature. Flow equations are solved using a block-centered finite-difference scheme. The solution scheme is IMPEC, analogous to IMPES, where pressure is solved for implicitly and concentrations are solved for explicitly. One- and two-point upstream weighting and a third-order spatial discretization are available as options in the code. To increase the stability and robustness of the third-order method, a flux limiter that is total-variation-diminishing (TVD) has been added (Liu, 1993; Liu *et al.*, 1994). The third-order TVD method gives the most accurate solution.

2.4 CHEMICAL EOR WITH GAS

Recently chemical enhanced oil recovery has increased due to significant advances in the technology, a better understanding of the processes and additional field projects, especially commercial polymer flooding projects. A very large number of candidate oil reservoirs for CEOR contain live oil. Therefore, the gas phase may disappear or reappear under certain conditions. When the reservoir is depressurized (below bubble point pressure) and oil contains gas, the dissolved gas is liberated from the oil. However, the gas phase may re-dissolve if the pressure increases.

The gas can be also injected along with an aqueous surfactant solution to create foam, now sometimes called in low-tension gas flooding (Kamal and Marsden, 1973; Lawson and Reisberg, 1980; Wang, 2006; Srivastava *et al.*, 2009; Li *et al.*, 2010, Szlendak *et al.* 2013; Farajzadeh *et al.* 2013). Kamal and Marsden (1973) conducted alkaline/surfactant/gas (ASG) experiments using high permeability sandpacks in both secondary and tertiary recovery modes. In their experiments, the injected chemical slug

was displaced with a foam drive. Lawson and Reisberg (1980) studied the alternate injection of gas and aqueous surfactant solution in both sandstone and tight carbonate rocks. In their experiments, the chemical slug was displaced by alternating slugs of gas and surfactant solution to provide mobility control behind the chemical slug.

Wang (2006) conducted ASG experiments using both micro-models and sandpacks. Micro-model experiments helped to provide visual observation of the process. He observed that the co-injection of chemical slug and gas is more efficient for lower saturation of oil, which is due to lower stability of foam in presence of oil. He also found that the foam was more effective when alkali was added in the slug.

Srivastava *et al.* (2009) conducted ASG floods using low to medium permeability sandstone and dolomite cores. In their experiments, foam was effective in providing mobility control in presence of low IFT. They concluded the presence of alkali assists in increasing the efficiency of the process by reducing surfactant adsorption and in-situ soap generation. They also showed the negative salinity gradient employed in their chemical floods improves foam stability by mobilizing trapped surfactant. Trapped surfactant is mobilized as salinity changes from Winsor Type II to Type III to Type I. Foam strength is increased in Type I environment due to surfactant mobilization. Thus, they concluded, the design of ASG process should be such that the drive salinity stays in Type I region.

Li *et al.* (2010) carried out alternating injection of surfactant solution and gas in 1-D homogeneous and 2-D layered sandpacks with 19:1 permeability contrast. They showed a foam drive with surfactant alternating gas (SAG) can be used as an alternative for polymer drive in ASP EOR. In their experiments, a viscous oil (226 cp) was displaced successfully with ASP slug and SAG drive. In 2-D experiments the vertical sweep was greatly enhanced with SAG compared to waterflood or WAG.

Szlendak *et al.* (2013) studied the impact of low-tension-gas flooding in tight formations. In their experiments the low tension chemical solution was co-injected with nitrogen gas at 50% gas fraction as a slug and then followed with a drive of surfactant and nitrogen designed to foam at the same rate and gas quality. They showed a low quality, low rate co-injection of gas and surfactant was effective in mobilizing and displacing residual oil in 10 md carbonate cores.

Farajzadeh *et al.* (2013) investigate the impact of the presence of gas on recovery efficiency of surfactant flooding process. They designed several experiments to represent different situations in the reservoir, where gas can be continuous, trapped, or flowing.

In terms of modeling, there have been very limited attempts to model chemical EOR in the presence of gas. Moncorgé *et al.* (2012) presented a framework aimed at integration of new physics for improved recovery process with black-oil and K-value models. Trouillaud *et al.* (2014) simulated the effect of pressure and oil composition on microemulsion phase behavior by coupling a gas/oil/water phase behavior model with a microemulsion phase behavior model.

2.5 EFFECT OF SOLUTION GAS AND PRESSURE ON SURFACTANT PHASE BEHAVIOR

The effect of solution gas and pressure on microemulsion phase behavior is important to develop a successful chemical formulation for enhanced oil recovery. The effect of solution gas and pressure on microemulsion phase behavior has been reported by different authors. Puerto and Reed (1983), Roshanfekar *et al.* (2009), Southwick *et al.* (2012), Sagi *et al.* (2013), and Jang *et al.* (2014) all reported a reduction in the optimum salinity when methane is added to crude oil. Southwick *et al.* (2012) also discussed that pressurizing of oil with nitrogen rather than methane did not show enhanced relative

surfactant solubility in the oil phase. Salager *et al.* (1979a, 1979b) proposed equivalent alkane carbon number (EACN) as a physical characteristic relating to surfactant solubility and optimum salinity. Roshanfekar *et al.* (2009) used the EACN concept to account for the methane content of live oil. In their experiments for the surrogate oil, the logarithm of optimum salinity shows a linear increase with increasing EACN. Later, Jang *et al.* (2014) used sapphire cells to measure the microemulsion phase behavior for different live oil samples over a wide range of pressure, temperature and solution gas. They found that the optimum salinity is closer to the dead oil than expected and higher than the value for surrogate oils made based on EACN, as shown in Figure 2.1.

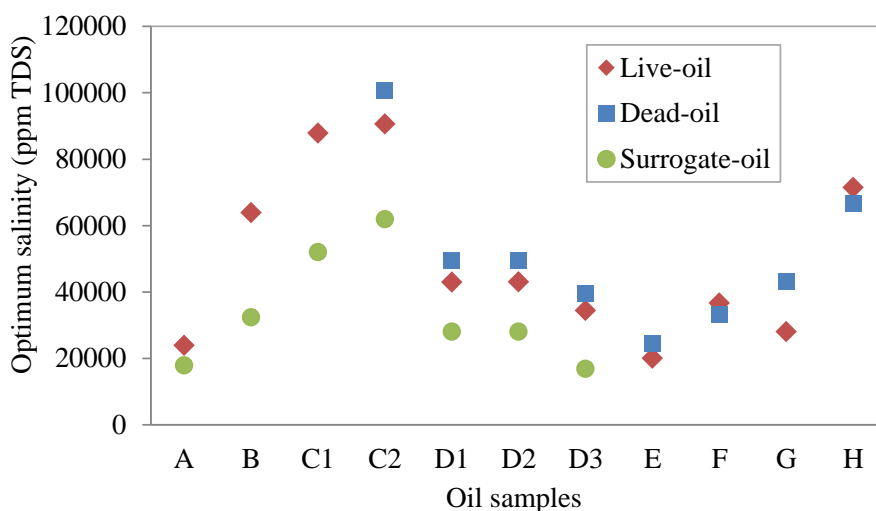


Figure 2.1: Optimum salinity of live-oil, dead-oil, and surrogate-oil for different oil samples (Jang *et al.* 2014)

Roshanfekar *et al.* (2009), Southwick *et al.* (2012) and Jang *et al.* (2014) all reported an increase in solubilization ratio for the live oils compared to dead oil. Jang also observed that the solubilization ratio for live oil samples are similar to the surrogate oil samples with one exception. More importantly, he observed for all the live-oil

samples, the solubilization ratios were above 10, which corresponds to the ultra-low interfacial tension, as shown in Figure 2.2. Roshanfekar *et al.* (2009) showed for the surrogate oil samples, the solubilization ratio at optimum salinity decreases with increasing EACN.

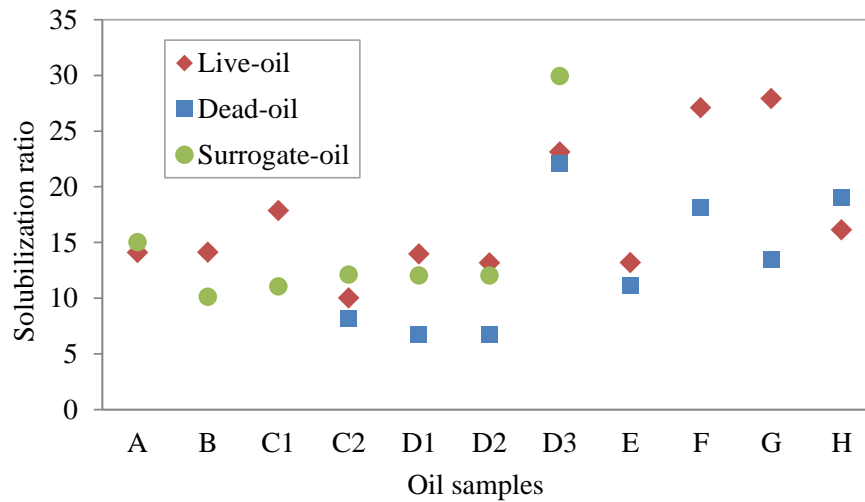


Figure 2.2: Solubilization ratios of live-oil, dead-oil, and surrogate-oil for different oil samples (Jang *et al.* 2014)

Kim *et al.* (1985, 1988), Austad *et al.* (1990), Austad and Strand (1996), Austad *et al.* (1996), Skauge and Fortland (1990), Sanderson *et al.* (2012), and Jang *et al.* (2014) consistently report that for both pure hydrocarbons and crude oils the optimum salinity increases as the pressure increases. However, the shift in optimum salinity with pressure up to several thousand psi is small. Figure 2.3 shows the effect of pressure on microemulsion phase behavior in Jang’s experiment was negligible.

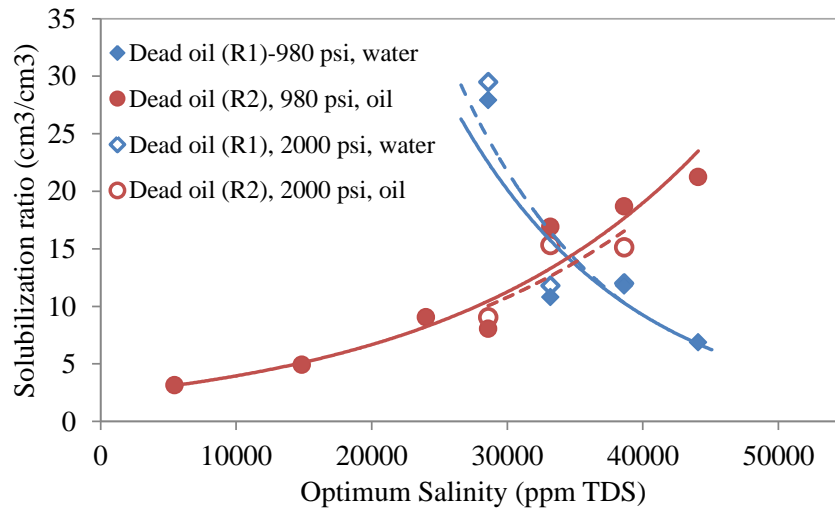


Figure 2.3: Effect of pressure on microemulsion phase behavior at 980 and 2000 psi (Jang *et al.* 2014)

2.6 FOAM FLOW IN POROUS MEDIA

Foam in porous media can be defined as a dispersion of gas in liquid such that the liquid is connected and at least some gas paths are blocked by thin liquid films, called lamellae (Falls *et al.*, 1988). In reservoir rock, an individual bubble occupies one or several pore bodies (Ettinger and Radke, 1992). This means foam cannot be treated as a homogeneous phase in porous media (Dong, 2001). Foam can be classified as continuous-gas foam and discontinuous-gas foam depending on whether there are free pathways for gas to flow. Continuous-gas foam is obtained when there is at least one free path for gas to flow. In discontinuous-gas foam, on the other hand, all the pathways are blocked by lamellae (Falls, 1988). A strong and stable foam is thought to be a discontinuous foam while weak foam is associated with continuous-gas foam (Friedmann *et al.*, 1991).

Foam flow and stability in a porous medium is very complex and depends not only on the foam itself, but also on the petrophysical properties of the rock to some extent (Dong, 2001). Foam stability and behavior is closely related to the number of gas bubbles in a unit bulk volume, which is called bubble density or foam texture. The higher the bubble density, the finer the foam texture and the stronger the foam is.

It has been experimentally observed that when gas/water capillary pressure in a porous medium approaches a certain value, the foam coarsens abruptly; this value referred to as the “limiting capillary pressure”, and the corresponding saturation is called “limiting water saturation”, (Khatib *et al.*, 1988; Zhou and Rossen, 1995). The limiting-capillary-pressure concept is illustrated in Figure 2.4. The P_c^* concept is analogous to the concept of the critical disjoining pressure in bulk foam, above which a single foam lamella breaks (Aronson *et al.*, 1994; Exerowa and Kruglyakov, 1998; Farajzadeh *et al.*, 2008).

In the absence of oil, foam exhibits two steady-state flow regimes (Osterloh and Jante, 1992; Alvarez *et al.*, 2001). If foam collapse is abrupt the transition between regimes occurs at a single water saturation S_w^* (the water saturation corresponding to P_c^* , see Figure 2.4). In the “low quality” (i.e., low gas fractional flow) or “wet” regime, the foam bubble size remains near the average pore size and pressure gradient is nearly independent of liquid velocity. In the “high quality”, “dryout” or “coalescence” regime, bubble size increases and foam becomes coarser over a narrow range of water saturation. In the high-quality regime, pressure gradient is nearly independent of gas superficial velocity (Figure 2.5a). However, if foam collapse is not abrupt, there is a range of water saturations over which foam becomes coarser in texture. In this case, the contour plot of pressure gradient shows a rounded transition between regimes rather than a sharp corner (Figure 2.5b). For a constant total superficial velocity, the high-quality regime is the

range of foam quality where the pressure gradient decreases with increasing foam quality, whereas in the low-quality regime the pressure gradient increases with increasing foam quality.

The limiting capillary pressure is thought to regulate foam behavior in the high-quality regime as follows. Suppose foam is at local equilibrium in the high-quality regime. Capillary pressure is close to P_c^* . Then suppose gas velocity increases by a factor X . As a result, water saturation falls slightly. Capillary pressure P_c approaches P_c^* . The approach to P_c^* causes a large increase in coalescence rate, coarsening foam and raising gas mobility by the same factor X . The decrease in water saturation is slight, so water saturation is nearly unchanged. Therefore LE is restored with the same pressure gradient as before the increase in gas superficial velocity.

The limiting capillary pressure is a function of surfactant formulation and concentration, electrolyte concentration, formation properties such as permeability, and other factors (Khatib *et al.*, 1988; Farajzadeh *et al.*, 2015).

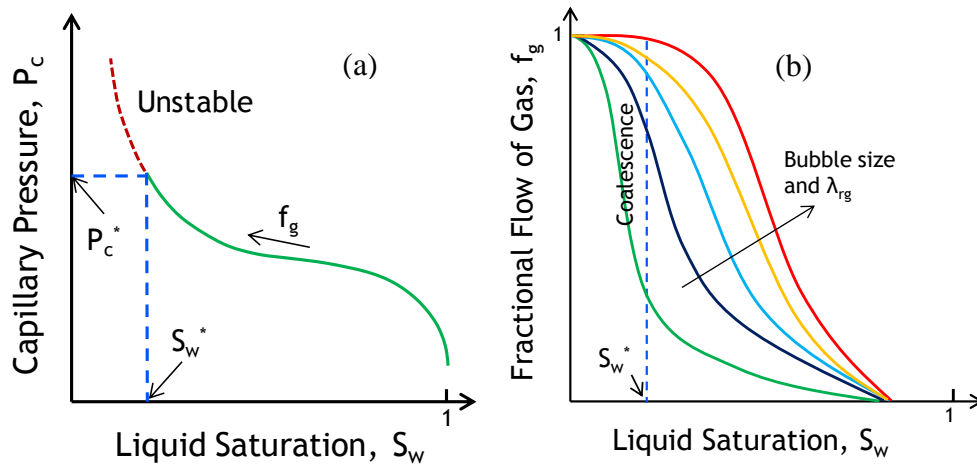


Figure 2.4: Limiting capillary pressure concept: In a porous medium capillary pressure is a function of water saturation and the gas fractional-flow function depends on bubble size. At the limiting capillary pressure P_c^* foam breaks. At this fixed water saturation $S_w^* = S_w(P_c^*)$ foam becomes coarser, mean bubble size increases, and gas fractional flow increases (Adapted from Khatib *et al.*, 1988.) The LE behavior of foam would follow the red curve at small S_w , then the dotted line, and then the green curve at large S_w on the right plot.

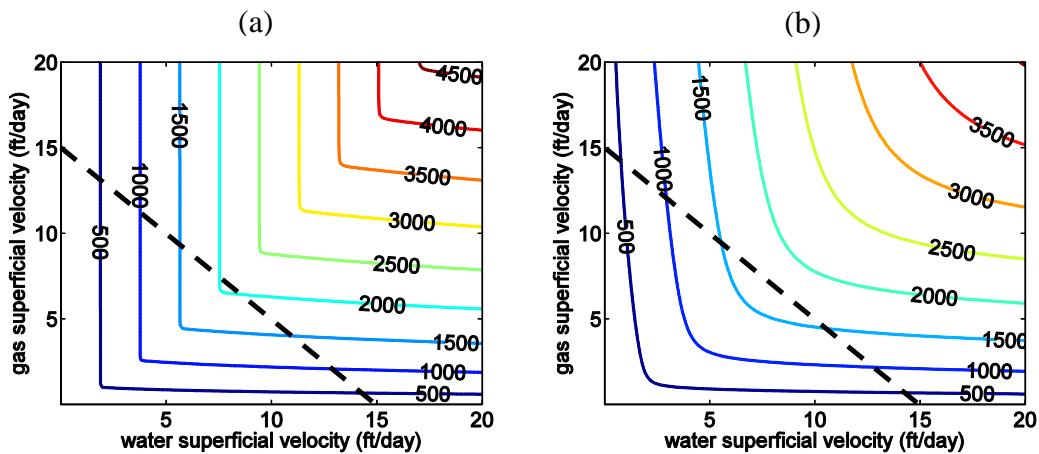


Figure 2.5: Pressure-gradient contours as a function of superficial velocities of gas and liquid calculated from the foam model presented (a) abrupt transition (b) less abrupt transition. Dotted line is a hypothetical scan of foam quality at a fixed superficial velocity of 15 ft/day (Farajzadeh *et al.*, 2015)

2.7 FOAM GENERATION MECHANISM INS POROUS MEDIA

Foam generation is caused by lamella creation in a porous medium. Capillary snap-off, lamella division, and leave-behind are the three main mechanisms for foam formation (Ransohoff and Radke, 1988).

Capillary snap-off is the most common mechanism for foam generation and is shown in Figure 2.6. At low capillary pressure, capillary forces drive water to accumulate in swollen film around each pore throat. If the capillary pressure is low enough, the film swells to bridge the throat and form a lens, which spans and block the throat. If capillary pressure rises again, the lens thins into a lamella. This mechanism can occur repeatedly at the same site, and can affect a relatively large portion of the flow field.

Lamella division occurs when a preformed lamella approaches a branch point so that the lamella is divided into two or more lamellae, as shown in Figure 2.7. Lamellae division is an effective foam generation mechanism if lamellae already exist and are stable enough to endure movement through pore bodies, and the pressure gradient is high enough for the lamellae to be displaced out of their static positions in the pore throat. Lamella division also occurs numerous times at one site. Snap-off and lamella division mechanisms are in effect at high flow velocities.

When two gas menisci enter a porous medium initially saturated with wetting phase from different directions, as shown in Figure 2.8, a lens is left behind as the two menisci converge downstream. This process is called leave-behind. This mechanism is non-repetitive process which is important at low velocities, and generates relatively weak foam.

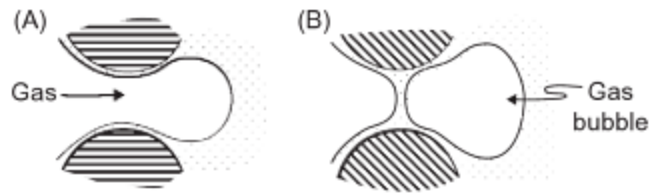


Figure 2.6: Snap-off mechanism showing (A) gas enters to constriction (B) new bubble is formed (adopted from: Ransohoff and Radke, 1988)

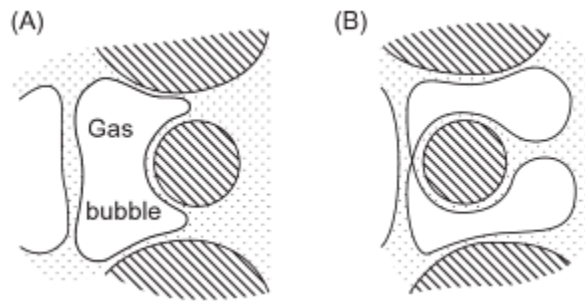


Figure 2.7: Lamella division mechanism (A) lamellae is approaching the branch point (B) divided gas bubbles formed (adopted from: Ransohoff and Radke, 1988)

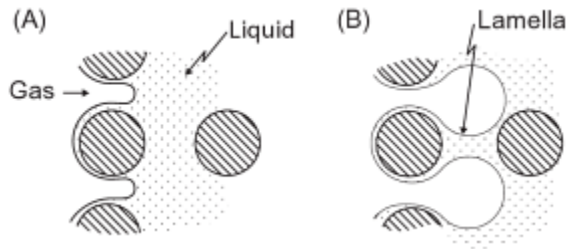


Figure 2.8: Leave behind mechanism (A) gas invasion (B) forming lens (adopted from: Ransohoff and Radke, 1988)

2.8 FOAM INFLUENCES ON PHASE MOBILITY

In a water-wet porous medium, the liquid-phase relative permeability does not depend on whether the gas exists in a foam. Most of the liquid resides either in smaller pores, which do not contain gas, or next to the solid in pores that are occupied by both phases. As long as the amount of liquid carried in lamellae is small compared with the total flux of liquid, the mobility of the liquid can be taken as the usual function of its saturation (Fall *et al.*, 1988)

The gas trapped by stationary lamella is immobilized, resulting in the reduction of mobile gas saturation. Stationary lamella blocks gas flow and alters gas flow paths, thus affecting the gas relative permeability. On the other hand, moving lamellae experience a drag force when they slide along the pore walls. The flowing fraction of gas experiences increased resistance to flow. This effect is similar to increasing gas viscosity, since it increases the resistance to flow of the flowing portion of the gas phase. Since the actual viscosity of gas is not increased by foam, the effect of increased resistance to gas flow due to the presence of lamellae is termed ‘increase in apparent gas viscosity’. Thus foam modifies gas mobility by reducing gas relative permeability and increasing apparent gas viscosity.

2.9 FOAM MODELS

Foam models should reflect the most relevant physics for foam flow in porous media (e.g. the effects of permeability, surfactant concentration, oil saturation and composition, wettability, etc.). Several models have been proposed for modeling foam flow in porous media (Farajzadeh *et al.*, 2012; Ma *et al.*, 2014; Lotfollahi *et al.*, 2015). These models can be divided into two main categories. Population-balance (PB) models (e.g. Falls *et al.*; 1988; Friedmann *et al.*; 1991; Kovsky *et al.*, 1995; Bertin *et al.*, 1998, Li *et al.*, 2006; Kam *et al.*, 2007; Chen *et al.*, 2010) attempt to describe the processes that

create and destroy the lamellae that separate gas bubbles, as well as the effect of bubble size on gas mobility. Implicit-texture (IT) models attempt to represent the effect of bubble size implicitly, through a mobility-reduction factor that depends on saturations, superficial velocities and other factors (e.g. Patzek *et al.*; 1989; Mohammadi *et al.*, 1993; Cheng *et al.*; 2000). PB models can be restructured to assume local equilibrium (LE) between the dynamics of lamella creation and destruction; all current IT models assume LE. These models contain adjustable parameters that are estimated by fitting the model to experiments (Cheng *et al.*, 2000; Boeije and Rossen, 2013; Rossen and Boeije, 2013; Ma *et al.*, 2013, 2014). Several different foam models can fit the steady-state mobility of strong foam in a given porous medium to a satisfactory degree. In this section we explain the foam models which later will be used in this research.

2.9.1 Implicit-Texture (IT) Models

In this section, the Rossen *et al.* (1999), STARS (Computer Modeling Group, 2012) and Vassenden-Holt (1998) IT models are described.

2.9.1.1 UT Foam Model

The UT foam model is based on a model developed by (Rossen *et al.*, 1999). This model gives a steep increase in gas mobility as water saturation decreases in the immediate vicinity of limiting water saturation (S_w^*) and a constant reduction in gas mobility for larger value of (S_w^*).

$$k_{rg}^f = \begin{cases} k_{rg} & S_w < S_w^* - \varepsilon \text{ or } C_s < C_s^* \text{ or } S_o \geq S_o^* \\ \frac{k_{rg}}{(1 + ((R-1)(S_w - S_w^* + \varepsilon)) / 2\varepsilon)} & S_w^* - \varepsilon \leq S_w \leq S_w^* + \varepsilon \text{ \& } C_s \geq C_s^* \text{ \& } S_o < S_o^* \\ \frac{k_{rg}}{R} & S_w > S_w^* + \varepsilon \text{ \& } C_s \geq C_s^* \text{ \& } S_o < S_o^* \end{cases} \quad (2-1)$$

where C_s is the surfactant concentration, C_s^* is threshold surfactant concentration for foam formation, S_w^* is the water saturation at which foam collapses, S_o^* is the maximum oil saturation at which foam remains stable, k_{rg} and k_{rg}^f are gas relative permeability in absence and presence of foam, respectively, ε determines the range of water saturation for high quality regime and finally R is foam resistance factor. The foam parameter R is modified according to gas flow rate to allow for shear thinning behavior of foam in low-quality regime as follows:

$$R = R_{ref} \left(\frac{u_g}{u_{g,ref}} \right)^{\sigma-1} \quad (2-2)$$

where u_g is gas velocity, R_{ref} is reference foam resistance factor at reference gas velocity ($u_{g,ref}$), and σ is the power-law exponent. For Newtonian foam behavior ($\sigma = 1$) and for shear thinning behavior ($\sigma < 1$).

We use this model for four-phase flow simulations in Chapter 6. Most of the surfactant is in the microemulsion phase when it is present. Therefore, water saturation needs to be replaced with microemulsion saturation in Equation (2-1). The foam also does not form in Winsor Type II, or when the oil concentration in the microemulsion phase is higher than foam tolerance.

2.9.1.2 STARS Model

STARS model was developed by Computer Modeling Group (CMG). In this model gas relative permeability is scaled by a function, FM , when foam is present:

$$k_{rg}^f = k_{rg} \cdot FM = \frac{k_{rg}}{1 + fmmob \prod_{i=1}^n F_i} \quad (2-3)$$

Parameter $fmmob$ is the maximum (or reference) mobility reduction factor that could be achieved by foam when all conditions are favorable. The “ F_i ” functions reflect the effects of different physical parameters such as surfactant concentration, water saturation, oil saturation (and composition), capillary number, etc., on foam behavior in porous media. In this dissertation we focus on the dry-out and shear-thinning functions. The dry-out function is defined in STARS as

$$F_2 = 0.5 + \frac{1}{\pi} \arctan(epdry(S_w - fmdry)) \quad (2-4)$$

Parameter $fmdry$ is the water saturation at which foam experiences significant coalescence and consequently in the limit of large $epdry$ it is equivalent to S_w^* . Parameter $epdry$ controls the sharpness of transition from the high-quality regime to the low-quality regime: when $epdry$ is very large the transition is sharp and foam collapses within a very narrow range of water saturation. When $epdry$ approaches infinity foam coalescence occurs at a single water saturation (S_w^*). In the most recent version of STARS, the parameter $fmdry$ is renamed $sfdry$, and $epdry$ is renamed $sfbet$. In that model $sfdry$ can be represented as a function of surfactant concentration, oil saturation, salt concentration, and capillary number. If one disables these other functionalities $sfdry$ is a constant and plays the same role as $fmdry$ does.

The shear-thinning function is defined as

$$F_5 = \begin{cases} 1 & N_{Ca} \left(= \frac{k\nabla P}{\sigma} \right) < fmcap \\ \left(\frac{fmcap}{N_{Ca}} \right)^{epcap} & N_{Ca} \left(= \frac{k\nabla P}{\sigma} \right) > fmcap \end{cases} \quad (2-5)$$

where, ∇P is the magnitude of pressure gradient, k is permeability, and σ is the surface tension. Parameter $fmcap$ should be set to the smallest capillary number expected to be encountered by foam in the simulation (Cheng *et al.*, 2000; Boeije and Rossen, 2013), and $epcap$ represents the extent of shear-thinning behavior. Newtonian behavior corresponds to $epcap = 0$ and positive $epcap$ to shear-thinning behavior.

2.9.1.3 Vassenden and Holt Model

Vassenden and Holt presented a foam flow model based on their lab experiments, field trial, and theoretical analysis (Vassenden and Holt, 2000; Martinsen and Vassenden, 1999; Blaker *et al.*, 1999; and Vassenden *et al.* 1999). In their model, they combined the limiting capillary pressure (P_c^*) model for the high-quality regime and the limiting pressure gradient model for low quality regime. Figure 2.9 shows how the resulting relative permeability curves for gas and water are expected to look like for foam, if foam transport is governed by the effects of a limiting capillary pressure and limiting pressure gradient. The water relative permeability curve is expected to be unchanged by the presence of foam. At limiting capillary pressure, the gas mobility varies dramatically with saturation. For higher water saturations, gas mobility is controlled by the limiting pressure gradient, which yields a rate-dependent gas mobility that does not vary with water saturation.

In this foam model, gas relative permeability is calculated by multiplication of the no-foam relative permeability function by a mobility factor F . This factor is given as a sum of two exponential functions, as

$$F = \begin{cases} e^{(S_f - S_w)s_1} + \left(\frac{u_g}{u_{go}} \right) F_o e^{(S_f - S_w)s_2} & S_w > S_f \\ 1 & S_w \leq S_f \end{cases} \quad (2-6)$$

The terms in this equation are illustrated in Figure 2.10. For water saturations below S_f (which is equivalent to S_w^*), there is no foam effect. For higher saturations, the gas mobility is reduced exponentially with the slope s_1 through the limiting capillary pressure region, until it reaches the limiting pressure gradient region, where the gas mobility is a factor $(F_o u_g / u_{go})$ lower than the gas mobility without foam. F_o is the reference mobility factor at the reference gas velocity u_{go} . Within the limiting pressure gradient region, the mobility factor may vary with a slope s_2 , which is presumably much smaller than the slope s_1 . Within each foam regime, the model gives nearly linear k_{rg} curves on semi-log plots, with a rounded transition region.

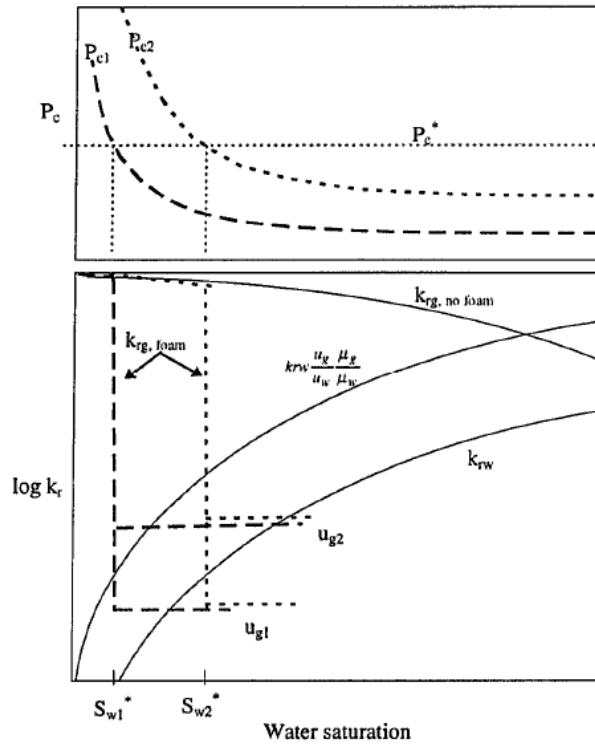


Figure 2.9: Relative permeability expected from Vassenden-Holt foam model

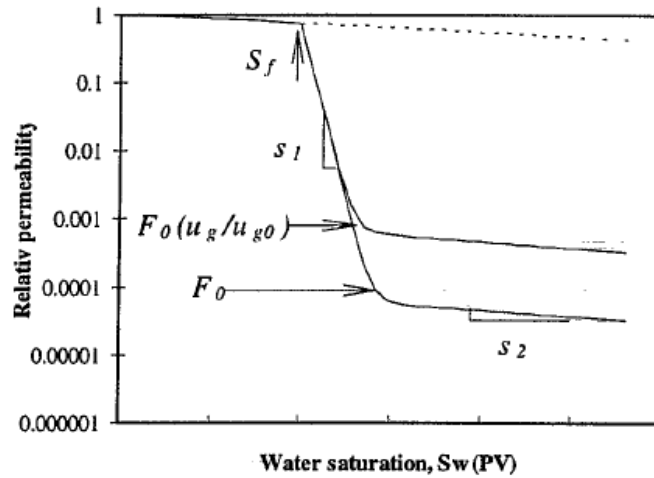


Figure 2.10: Characteristics of foam relative permeability equation

2.9.2 Population Balance (PB) Models

Foam mobility is influenced by its texture (Falls *et al.*, 1988). Foam texture is quantified as the number of lamellae per unit volume of gas. Foam with fine texture has more lamellae in a given volume of gas and therefore induces more resistance to gas flow. Population-balance models incorporate foam texture explicitly to predict flow properties. A balance equation for lamellae allows the simulator to track foam texture dynamically, i.e. without the local equilibrium assumption. The rates of accumulation, convection, generation, and coalescence of foam bubbles are incorporated into the bubble balance, and, if desired, rates of trapping and mobilization as well, as they are for other molecular species in a reservoir simulator.

The transient population balance for the average flowing and trapped bubble sizes is written as (Chen *et al.*, 2010):

$$\frac{\partial}{\partial t} [\phi(S_f n_f + S_t n_t)] + \nabla \cdot (u_f n_f) = q_f + Q_b \quad (2-7)$$

where S_f and S_t are flowing and trapped gas saturations, and n_f and n_t are number density of flowing and trapped foam lamellae, respectively. Q_b is a source/sink term, and q_f is the net rate of generation of lamellae and can be defined as

$$q_f = r_g - r_c \quad (2-8)$$

where, r_g and r_c represent generation and coalescence rates, respectively. The population balance model can be simplified by assuming local equilibrium if desired (Ettinger and Radke, 1992; Myers and Radke, 2000; Kam and Rossen, 2003; Chen *et al.*, 2010). In the LE version of the PB models, the rates of foam generation and coalescence are set equal to each other, which defines the LE value of foam texture n_f at each location. Equation (2-7) is eliminated from the set of governing equations.

In this section, the Chen *et al.* (2010), Kam *et al.* (2007), and Kam (2008) models are described. The population-balance models examined here use the shear-thinning expression for effective viscosity (Hirasaki and Lawson, 1985),

$$\mu_f = \mu_g + \frac{\alpha n_f}{|v_f|^{1/3}} \quad (2-9)$$

where μ_g and μ_f are the gas viscosity in the absence and presence of foam, n_f is the foam bubble density, v_f is local gas velocity and α is proportionality constant, which depends on the surfactant formulation and permeability.

2.9.2.1 Kavscek *et al.* (1994) Model

Kavscek *et al.* (1994) considered Roof snap-off as the mechanism of lamella creation. In this model, foam generation is taken as a power-law expression that is proportional to the magnitude of the flux of surfactant solution multiplied the 1/3 power of magnitude of interstitial velocity. The liquid-velocity dependence originates from the net imposed liquid flow through pores occupied by both gas and liquid, while the gas-velocity dependence arises from the time for newly formed lens to exit a pore. Therefore, the foam generation rate is defined as,

$$r_g = k_1 \left| \overline{v_w} \right| \left| \overline{v_f} \right|^{1/3} \quad (2-10)$$

where the proportionality constant k_1 reflects the number of foam generation sites. Later, Chen *et al.* (2010) discussed that foam generation rate reduces when the foam generation sites are occupied by pre-existing gas bubbles. They proposed

$$k_1 = k_1^o \left[1 - \left(n_f / n^* \right)^\omega \right] \quad (2-11)$$

where ω is a constant determining the shape of inverse proportionality of foam generation sites to pre-existing bubbles and n^* is an upper limit for the concentration of foam bubble, that is related to pore-size distribution. This model employs a capillary-pressure-dependent kinetic expression for lamella coalescence to reflect the limiting capillary pressure.

$$r_c = k_{-1} \left| \vec{v}_f \right| n_f \quad (2-12)$$

where

$$k_{-1} = k_{-1}^o \left(\frac{P_c}{P_c^* - P_c} \right)^2 \quad (2-13)$$

where k_{-1}^o is a constant and P_c^* is limiting capillary pressure for foam coalescence. It is experimentally observed that highly concentrated foamer solutions and robust surfactants lead to larger P_c^* . Aronson *et al.* (1994) suggested the following functional form for P_c^* versus surfactant concentration

$$P_c^* = P_{c,\max}^* \tanh\left(\frac{C_s}{C_s^o}\right) \quad (2-14)$$

where $P_{c,\max}^*$ is a limiting value for P_c^* and C_s^o is a reference surfactant concentration for strong net foam generation.

The LE version of this model based on equalizing the rates of foam generation and coalescence is written as (Chen *et al.*, 2010)

$$n_f^\omega + \frac{n^{*\omega} k_{-1} |v_f|^{2/3}}{k_1^\omega |v_w|} n_f - n^{*\omega} = 0 \quad (2-15)$$

The model also represents the trapped fraction of foam as

$$X_t = X_{t,\max} \left(\frac{\beta n_t}{1 + \beta n_t} \right) \quad (2-16)$$

where $X_{t,\max}$ is the maximum fraction of trapped foam and β is trapping parameter.

Therefore the gas relative permeability needs to be adjusted for the flowing fraction of the gas as

$$k_{rg} = k_{rg}^\circ \left((1 - X_t) S_{gD} \right)^{n_g} \quad (2-17)$$

where S_{gD} , k_{rg}° , and n_g are normalized gas saturation, gas endpoint relative permeability and gas Corey exponent, respectively.

2.9.2.2 *Kam et al. (2007) and Kam (2008) Models*

In a homogeneous porous medium, foam is created by mobilization of lamellae and subsequent division rather than primarily by Roof snap-off (Rossen and Gauglitz 1990; Tanzil *et al.* 2002; Gauglitz *et al.* 2002). The theory of Rossen and Gauglitz (1990) for foam generation implies that lamella creation depends on pressure gradient, but also on water saturation or capillary pressure, which governs the presence of lenses or lamellae available to be mobilized. Specifically, foam generation is easier at higher water saturation, because there are more liquid lenses on the pore network, and these lenses can be mobilized at lower pressure gradient because of their arrangement on the network. However, it is not clear from the theory how the rate of lamellae creation in porous media depends on pressure gradient and other factors. Kam *et al.* (2007) proposed the follow the following simple relationship for rate of lamellae creation:

$$r_g = c_g S_w (\nabla P)^m \quad (2-18)$$

where ∇P is pressure gradient and c_g and m are model parameters. For $m > 1$ the rate of generation increases steeply with increasing pressure gradient.

The foam coalescence is governed by limiting water saturation S_w^* (equivalent to limiting capillary pressure, P_c^*) according to following expression

$$r_c = c_c n_f \left(\frac{1}{S_w - S_w^*} \right)^n \quad (2-19)$$

where c_c and n are model parameters. $(S_w - S_w^*)$ in the denominator reflects the physical discontinuity of foam mechanism, and holds S_w near S_w^* with feedback mechanism (Kibodeaux, 1997).

The LE version of this model can be written as

$$n_f = \begin{cases} n_f = \frac{c_g}{c_c} S_w (S_w - S_w^*)^n (\nabla P)^m & , n_f < n_{\max} \\ n_{\max} & , n_f \geq n_{\max} \end{cases} \quad (2-20)$$

where n_{\max} is the maximum (limiting) bubble density.

Kam (2008) states that the division of foam films no longer increases once foams are already finely textured and individual bubbles becomes as small as the average pore size. Therefore, at high pressure gradients, the rate of lamella generation should reach a plateau. Then, he suggested the new lamella-creation function as follows:

$$r_g = \frac{c_g}{2} \left(\operatorname{erf} \left(\frac{\nabla P - \nabla P_o}{\sqrt{2}} \right) - \operatorname{erf} \left(\frac{-\nabla P_o}{\sqrt{2}} \right) \right) \quad (2-21)$$

∇P_o is model parameter. The value of ∇P_o is related to the minimum pressure gradient, ∇P_{min} , for lamella mobilization and division. Figure 2.11 compares the new lamella-creation function with old model by Kam *et al.* (2007).

Kam also defined the rate of breakage with a minor change to previous model by Kam *et al.* (2007).

$$r_c = c_c n_f \left(\frac{S_w}{S_w - S_w^*} \right)^n \quad (2-22)$$

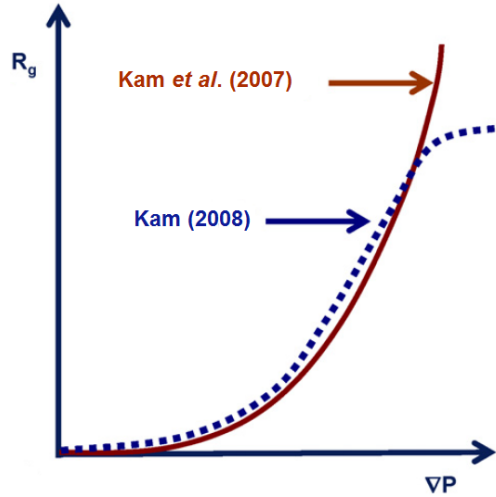


Figure 2.11: Comparison of generation function [Kam *et al.* (2007) and Kam (2008)]

The LE version of Kam (2008) model can be written as

$$n_f = \begin{cases} \frac{c_g}{2c_c} \left(\frac{S_w - S_w^*}{S_w} \right)^n \left(\operatorname{erf} \left(\frac{\nabla P - \nabla P_o}{\sqrt{2}} \right) - \operatorname{erf} \left(\frac{-\nabla P_o}{\sqrt{2}} \right) \right) & , n_f < n_{\max} \\ n_{\max} & , n_f \geq n_{\max} \end{cases} \quad (2-23)$$

NOMENCLATURE

| | |
|------------|---|
| c_c | = coalescence rate constant |
| c_g | = generation rate constant |
| C_s | = surfactant concentration |
| C_s^* | = threshold surfactant concentration in UT model |
| C_s^o | = reference surfactant concentration in Chen <i>et al.</i> model |
| $epcap$ | = exponent in factor (F_5) representing shear-thinning in STARS model |
| $epdry$ | = factor governing abruptness of dry-out calculation (F_2) in STARS model |
| F | = foam mobility multiplier in Vassenden- Holt model |
| F_o | = reference mobility multiplier at reference gas velocity u_{go} in Vassenden- Holt model |
| F_2 | = dry-out function in STARS model |
| F_5 | = shear-thinning function in STARS model |
| FM | = mobility reduction factor in STARS model |
| $fncap$ | = reference capillary number in STARS model |
| $fmdry$ | = reference water saturation in dry-out calculation (F_2) in STARS model |
| $fmmob$ | = maximum resistance factor in STARS model |
| F_o | = foam mobility constant in Vassenden-Holt model |
| k | = permeability |
| k_l | = generation rate coefficient in Chen <i>et al.</i> model |
| $k_{.l}$ | = coalescence coefficient in Chen <i>et al.</i> model |
| k_l^o | = model parameter in Chen <i>et al.</i> model |
| $k_{.l}^o$ | = model parameter in Chen <i>et al.</i> model |
| k_{rg} | = gas relative permeability in absence of foam |
| k_{rg}^f | = gas relative permeability in presence of foam |
| k_{rg}^o | = gas endpoint relative permeability |
| m | = model parameter Kam <i>et al.</i> Model |
| n | = coalescence exponent in Kam <i>et al.</i> Model |
| n^* | = limiting (maximum) lamella density in Chen <i>et al.</i> model |
| N_{ca} | = capillary number |
| n_f | = number density of flowing lamellae (lamellae/volume gas) |
| n_g | = gas exponent relative permeability |
| n_{max} | = Maximum foam lamella density in Kam model |

| | |
|--------------|---|
| n_t | = number density of trapped foam bubbles |
| P_c | = capillary pressure |
| P_c^* | = limiting capillary pressure |
| P_{cmax}^* | = limiting value of P_c^* in Chen <i>et al.</i> model |
| Q_b | = source/sink term for foam bubbles |
| q_f | = net rate of generation of foam bubbles |
| R | = foam resistance factor in UT model |
| r_c | = foam coalescence rate |
| r_g | = foam generation rate |
| R_{ref} | = reference foam resistance factor at reference gas velocity in UT model |
| s_1 | = slope of the gas relative permeability at high quality regime in Vassenden-Holt model |
| s_2 | = slope of the gas relative permeability at low quality regime in Vassenden-Holt model |
| S_f | = flowing gas saturation or lowest water saturation for foam effect in Vassenden-Holt model |
| S_{fD} | = dimensionless gas saturation in the presence of foam |
| S_{gD} | = dimensionless gas saturation |
| S_o | = oil saturation |
| S_o^* | = maximum oil saturation for foam stability |
| S_t | = trapped gas saturation |
| S_w | = water saturation |
| S_w^* | = limiting water saturation |
| S_{wc} | = connate water saturation |
| S_{wD} | = dimensionless water saturation |
| u_f | = Darcy velocity of gas in foam |
| u_g | = gas Darcy velocity |
| $u_{g,ref}$ | = reference gas Darcy velocity |
| u_w | = water Darcy velocity |
| v_f | = local gas velocity |
| v_w | = local water velocity |
| X_t | = trapping foam fraction Chen <i>et al.</i> model |
| $X_{t,max}$ | = maximum trapping fraction in Chen <i>et al.</i> model |
| α | = proportionality constant |

| | |
|------------------|--|
| β | = trapping parameter Chen <i>et al.</i> model |
| ε | = width of high-quality regime in UT model (in terms of S_w) |
| μ_f | = gas viscosity in the presence of foam |
| μ_g | = gas viscosity in the absence of foam |
| σ | = power-law exponent in UT model or surface tension |
| ω | = constant exponent in Chen <i>et al.</i> Model |
| ∇P | = pressure gradient |
| ∇P_{min} | = minimum pressure gradient for lamella mobilization and division |
| ∇P_o | = model parameters related to minimum pressure gradient for lamella mobilization and division in Kam model |

Chapter 3: Black Oil Model in UTCHEM

This chapter includes the assumptions and equations for the three-dimensional, three-phase black-oil model implemented in UTCHEM. The pressure dependence of fluid densities, viscosities, formation volume factors (FVF's), and solution-gas are presented. Three-phase relative permeability and capillary pressure options are discussed.

3.1 ASSUMPTIONS

The black-oil model includes three phases: water, oil and gas. The water and oil phases are assumed to be immiscible with no mass exchange. The reservoir oil is modeled with two pseudo components called stock tank oil and solution gas at standard conditions. The conventional *standard condition* in the oil field is 14.7 psi and 60° F. The solution gas can dissolved in both the oil phase and the water phase.

The following additional assumptions have been made in developing the mathematical model:

- Temperature is assumed to be constant (isothermal process).
- Local thermodynamic equilibrium
- No-flow Neumann boundary conditions apply on the external boundary
- The permeability tensor is diagonal and aligned with the coordinate system.
- Fluid flow is characterized by Darcy's law for multi-phase flow.
- No chemical reactions, precipitation or adsorption.
- Injection and production of fluids are treated as source and sink terms using wells.
- The rock formation is slightly compressible.

3.2 BUBBLE POINT

Reservoir oils often contain volatile components such as methane that are called solution gas. The pressure at which the first bubble of gas comes out of solution is called the bubble point pressure (P_b). The reservoir is called undersaturated when its pressure is greater than the bubble point pressure. For the pressures below the bubble point, the reservoir is called saturated.

3.3 FLUID PROPERTIES

In the isothermal black-oil model, formation volume factors, the gas solubility in oil and water, and viscosities are all functions of pressure. In this section the fluid properties for saturated and undersaturated conditions are discussed.

3.3.1 Solution Gas Ratio

Figure 3.1 shows an example of solution gas ratio as a function of pressure. For the primary depletion, when the reservoir is undersaturated, no gas evolves from the solution and R_s remains constant until the pressure reaches the bubble point pressure. When the pressure goes below bubble point, free gas saturation will form. When the gas saturation exceeds the residual gas saturation it becomes mobile.

In some cases the bubble point is not constant. For example, in thick formations, the bubble point varies vertically. Pressure maintenance schemes (water or gas injection) can also cause a change in the bubble point pressure. Considering an undersaturated reservoir, represented by point A in Figure 3.2, during the primary depletion, the reservoir declined below the original bubble point (point B) to point C. Due to vertical gas migration, the lower portion of the reservoir will have less free gas compared to upper portion. If the water is injected at point C, the reservoir pressure increases and gas goes into solution, giving new bubble points D and F for the lower and upper part of the

reservoir. Further pressurization may lead to the conditions indicated by points E and G for the lower and upper portion of the reservoir. Therefore, the variable bubble point formulation is the most standard formulation in commercial reservoir simulators. UTCHEM has both constant and variable bubble point options.

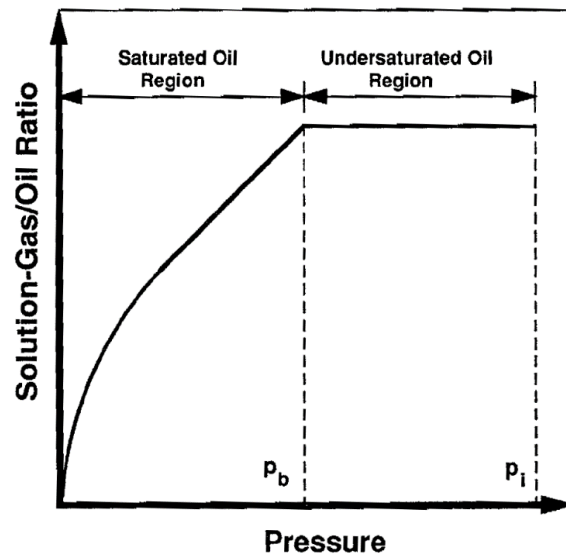


Figure 3.1: Solution gas/oil ratio versus pressure for constant bubble point pressure.

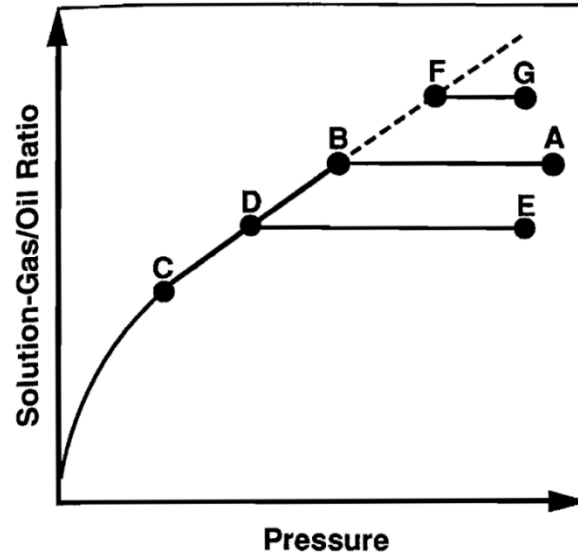


Figure 3.2: Solution gas/oil ratio versus pressure for variable bubble point pressure.

3.3.2 Formation Volume Factor (FVF)

A fixed mass of reservoir fluid occupies a different volume at different reservoir pressure. Formation volume factors are used to convert volumes at reservoir pressure and temperature to its equivalent volumes at standard conditions. Formation volume factors consider the volume changes due to fluid compressibility for the oil, water and gas phases and also changes due to mass transfer of solution gas for the oil phase. The formation volume factor B_l is defined as

$$B_l = \frac{V_{l,rc}}{V_{l,sc}} \quad (l = o, w, g) \quad (3-1)$$

For slightly compressible fluids, such as water and dead-oil, FVF at constant temperature can be written as

$$B_l = 1 - c_l (P - P_{sc}) \quad (j = w, \text{dead oil}) \quad (3-2)$$

where c_l is fluid compressibility and P_{sc} is standard condition pressure. For gas at reservoir condition, the FVF can be written as

$$B_g = \frac{P_{sc}}{T_{sc}} \frac{T}{P} Z \quad (3-3)$$

where Z is gas compressibility factor. Figure 3.3 and Figure 3.4 give the typical curves for water and gas phase FVF.

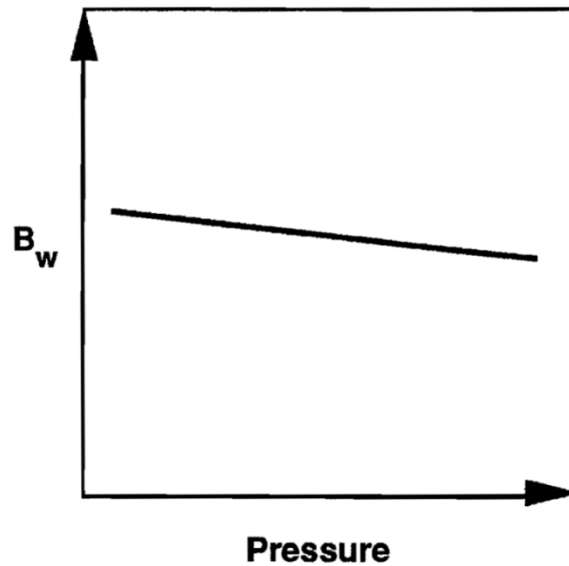


Figure 3.3: Water formation volume factor versus pressure.

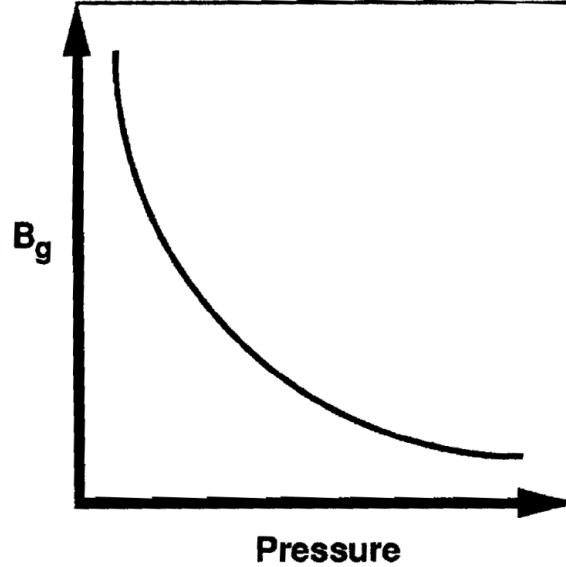


Figure 3.4: Gas formation volume factor versus pressure.

The formation volume factor of crude oil is different from gas and water because of the mass transfer between the gas and oil phase (Figure 3.5). The oil formation volume factor increases as pressure decreases in the undersaturated region ($P > P_b$) as a result of the expansion of the oil. The formation volume factor of undersaturated oil above the bubble point pressure can be calculated from

$$B_o = B_{ob} [1 - c_o (P - P_b)] \quad (3-4)$$

where B_{ob} is the FVF at the bubble point pressure.

As the pressure decreases in the saturated region ($P < P_b$), the oil phase shrinks because of gas evolution and formation volume factor decreases. In this region, the oil shrinkage as a result of gas evolution dominates oil expansion due to pressure drop.

For the variable bubble point pressure formulation, the oil formation volume factor follows the saturated curve (solid line) in Figure 3.6 when the oil pressure is below its bubble point pressure. For pressures greater than the bubble point pressure, the

formation volume factor follows the undersaturated dashed curve above the bubble point pressure.

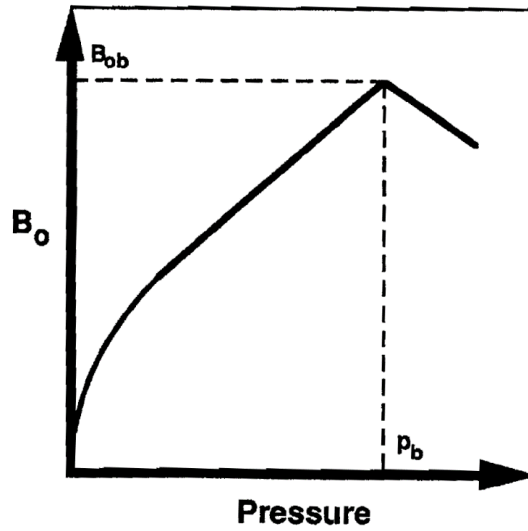


Figure 3.5: Oil formation volume factor versus pressure for constant bubble point.

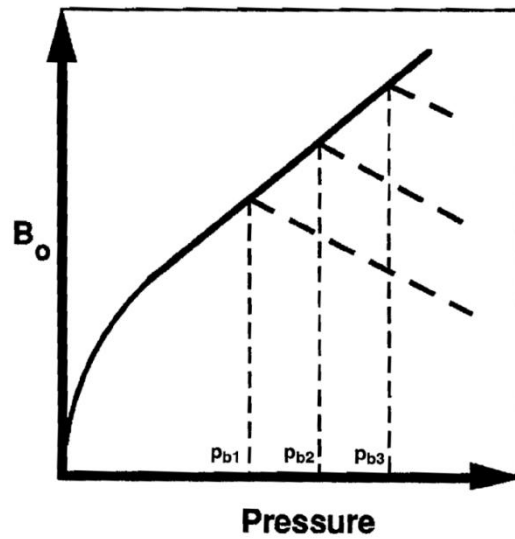


Figure 3.6: Oil formation volume factor versus pressure for variable bubble point.

3.3.3 Fluid Viscosity

Fluid viscosity is a function of pressure and temperature; however, we are only interested in the pressure dependency of viscosity for isothermal reservoir conditions. Water viscosity increases slightly with pressure (see Figure 3.7). Gas viscosity increases as pressure increases but the change is less at high pressure (see Figure 3.8).

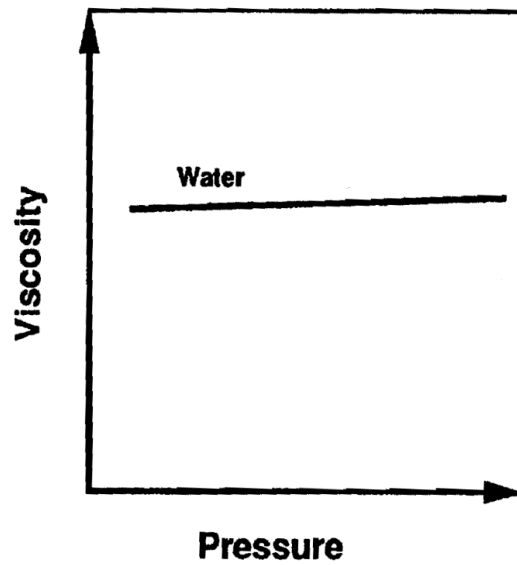


Figure 3.7: Water viscosity versus pressure.

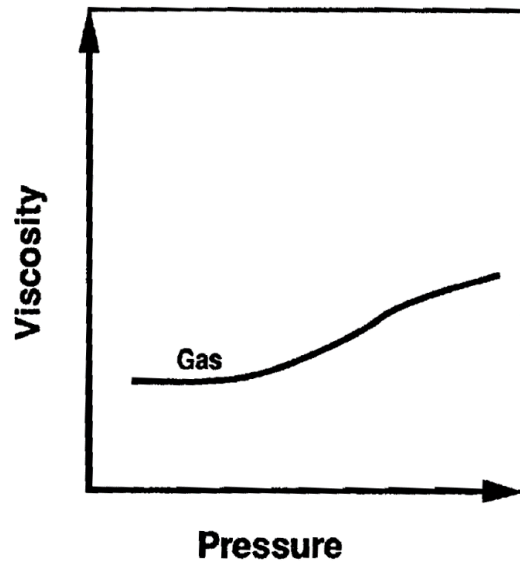


Figure 3.8: Gas viscosity versus pressure.

In the undersaturated region, solution gas ratio is constant and the oil viscosity increases with pressure as shown in Figure 3.9. As pressure decreases below the bubble point, the effect of gas liberation on oil viscosity dominates the effect of oil expansion and the oil phase becomes more viscous as the reservoir pressure drops.

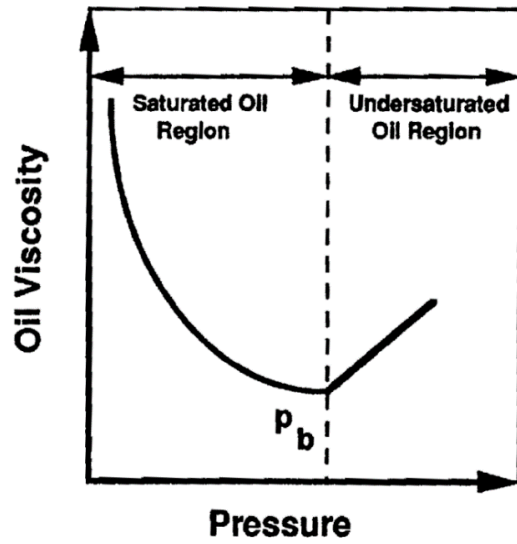


Figure 3.9: Oil viscosity versus pressure in saturated and undersaturated regions.

Figure 3.10 shows oil viscosity for variable bubble point formulation. Oil viscosity follows the solid line in the saturated region and dashed line in the undersaturated region.

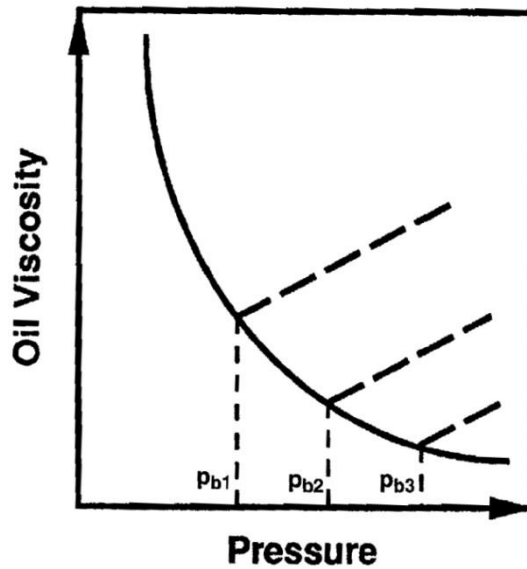


Figure 3.10: Oil viscosity versus pressure for variable bubble point.

3.4 THREE PHASE RELATIVE PERMEABILITY

This section includes a description of three-phase relative permeability models available in UTCHEM: Brooks and Corey (1966), Parker *et al.* (1987), and Stone's model II (1973).

3.4.1 Corey-Type Model

The Corey model (Brooks and Corey, 1966; Delshad and Pope, 1989) used in UTCHEM assumes the relative permeability of each phase l can be modeled as a function of the normalized saturation of the same phase l :

$$k_{rl} = k_{rl}^o (S_{nl})^{n_l} \quad (l = w, o, g) \quad (3-5)$$

where the normalized saturations are defined as

$$S_{nl} = \frac{S_l - S_{lr}}{1 - S_{wr} - S_{or} - S_{gr}} \quad (l = w, o, g) \quad (3-6)$$

where k_{rl}^o , n_l , and S_{lr} are the relative permeability endpoint, exponent, and residual saturation for phase l . The residual oil saturation for three-phase flow (S_{or}) is calculated based on a function by Fayers and Matthews (1982), which uses the two-phase residual saturations:

$$S_{or} = S_{orw} \left(1 - \frac{S_g}{1 - S_{wr} - S_{org}} \right) + S_{org} \left(\frac{S_g}{1 - S_{wr} - S_{org}} \right) \quad (3-7)$$

where S_{orw} and S_{org} are residual oil saturations to water and gas, respectively.

3.4.2 Parker *et al.* Model

Parker *et al.* (1987) derived three-phase water/oil/gas relative permeability as follows:

$$k_{rw} = \bar{S}_w^{1/2} \left[1 - \left(1 - \bar{S}_w^{1/m} \right)^m \right]^2 \quad (3-8)$$

$$k_{ro} = \left(\bar{S}_t - \bar{S}_w \right)^{1/2} \left[\left(1 - \bar{S}_w^{1/m} \right)^m - \left(1 - \bar{S}_t^{1/m} \right)^m \right]^2 \quad (3-9)$$

$$k_{rg} = \left(\bar{S}_g \right)^{1/2} \left(1 - \bar{S}_t^{1/m} \right)^{2m} \quad (3-10)$$

where S_t is total liquid saturation and \bar{S}_l is the effective saturation defined as

$$\bar{S}_l = \frac{S_l - S_{wr}}{1 - S_{wr}} \quad (l = w, o, g) \quad (3-11)$$

3.4.3 Stone's II Model

The normalized Stone's Model II is described as

$$k_{ro} = k_{row}^o \left[\left(\frac{k_{row}}{k_{row}^o} + k_{rw} \right) \left(\frac{k_{rog}}{k_{row}^o} + k_{rg} \right) - \left(k_{rw} + k_{rg} \right) \right] \quad (3-12)$$

Equation (3-12) can potentially give negative values for k_{ro} , which is physically meaningless. Therefore, negative values of k_{ro} are set to zero.

3.5 THREE PHASE CAPILLARY PRESSURE

The Parker *et al.* (1987) generalization of the van Genuchten (1980)) and the Brooks and Corey (1966) models are the two models used to calculate the capillary pressure in UTCHEM. A new table look up option for water/oil and oil/gas capillary pressure vs. saturation is implemented as part of black oil model option.

3.5.1 Brooks-Corey Model

This model assumes direction of descending wettability is water, oil and gas and that the water phase is always present. The capillary pressure between water and gas (no oil present) or between water and oil phase is calculated as

$$P_{c_{wj}} = C_{pc_i} \frac{\sigma_{wl}}{\sigma_{wo}} \sqrt{\frac{\phi}{k}} (1 - S_{nw})^{e_{pc}} \quad (l = o, g) \quad (3-13)$$

In the presence of oil phase, the capillary pressure between gas and oil phase is calculated as

$$P_{c_{og}} = C_{pc_i} \frac{\sigma_{og}}{\sigma_{wo}} \sqrt{\frac{\phi}{k}} \left(\frac{S_{ng}}{1 - S_{nw}} \right)^{e_{pc}} \quad (3-14)$$

3.5.2 van Genuchten Model

The three-phase capillary pressure-saturation function determined using the generalization of Parker *et al.* (1987) to the two-phase flow model of van Genuchten (1980) is represented by

$$\begin{cases} \bar{S}_l = [1 + (\alpha h^*)^n]^{-m} & h^* > 0 \\ \bar{S}_l = 1 & h^* \leq 0 \end{cases} \quad (3-15)$$

where h^* is scaled capillary pressure.

$$h^* = \beta_{ll'} P_{c_{ll'}} \quad (3-16)$$

$\beta_{ll'}$ is the scaling coefficient, α and n are the model parameters, and $m = 1 - \frac{1}{n}$.

3.6 MASS CONSERVATION EQUATIONS

A mass balance for component k can be written as follows:

$$-\nabla \cdot \vec{J}_k + q_k = \frac{\partial C_k}{\partial t} \quad (3-17)$$

where \vec{J}_k is mass flux, q_k is sink/source term and C_k is total mass concentration of pseudo-component k . The mass flux of each pseudo-component is

$$\vec{J}_w = \frac{\rho_{wsc}}{B_w} \vec{u}_w \quad (3-18)$$

$$\vec{J}_o = \frac{\rho_{osc}}{B_o} \vec{u}_o \quad (3-19)$$

$$\vec{J}_g = \frac{\rho_{gsc}}{B_g} \vec{u}_g + \frac{R_{so} \rho_{gsc}}{B_o} \vec{u}_o + \frac{R_{sw} \rho_{gsc}}{B_w} \vec{u}_w \quad (3-20)$$

where R_{so} and R_{sw} are solution gas ratio in oil and water, respectively and B_w , B_o and B_g are formation volume factors and the Darcy velocities and they can be written as below:

$$\vec{u}_l = -\vec{k} \cdot \lambda_{rl} \nabla \Phi_l \quad (l = o, w, g) \quad (3-21)$$

where Φ_l and λ_{rl} are phase potential and phase relative mobility, respectively.

$$\nabla \Phi_l = \nabla P_l - \rho_l \nabla z \quad (3-22)$$

$$\lambda_{rl} = \frac{k_{rl}}{\mu_l} \quad (3-23)$$

The phase densities are calculated as below:

$$\rho_w = \frac{1}{B_w} [\rho_{wsc} + R_{sw} \rho_{gsc}] \quad (3-24)$$

$$\rho_o = \frac{1}{B_o} [\rho_{osc} + R_{so} \rho_{gsc}] \quad (3-25)$$

$$\rho_g = \frac{\rho_{gsc}}{B_g} \quad (3-26)$$

Total mass concentration of the water, oil and gas pseudo-components in each gridblock is given by,

$$C_w = \phi \rho_{wsc} S_w / B_w \quad (3-27)$$

$$C_o = \phi \rho_{osc} S_o / B_o \quad (3-28)$$

$$C_g = \phi \rho_{gsc} \left[\frac{S_g}{B_g} + \frac{R_{so} S_o}{B_o} + \frac{R_{sw} S_w}{B_w} \right] \quad (3-29)$$

Combining Equations (3-17) through (3-20) and (3-27) through (3-29) and dividing by the density at standard conditions, the mass conservation equations can be written as

$$-\left[\frac{\partial}{\partial x} \left(\frac{u_{xw}}{B_w} \right) + \frac{\partial}{\partial y} \left(\frac{u_{yw}}{B_w} \right) + \frac{\partial}{\partial z} \left(\frac{u_{zw}}{B_w} \right) \right] - \frac{q_w}{\rho_{wsc}} = \frac{\partial}{\partial t} (\phi S_w / B_w) \quad (3-30)$$

$$-\left[\frac{\partial}{\partial x} \left(\frac{u_{xo}}{B_o} \right) + \frac{\partial}{\partial y} \left(\frac{u_{yo}}{B_o} \right) + \frac{\partial}{\partial z} \left(\frac{u_{zo}}{B_o} \right) \right] - \frac{q_o}{\rho_{osc}} = \frac{\partial}{\partial t} (\phi S_o / B_o) \quad (3-31)$$

$$\begin{aligned} & -\frac{\partial}{\partial x} \left(\frac{u_{xg}}{B_g} + \frac{R_{so}}{B_o} u_{xo} + \frac{R_{sw}}{B_w} u_{xw} \right) - \frac{\partial}{\partial y} \left(\frac{u_{yg}}{B_g} + \frac{R_{so}}{B_o} u_{yo} + \frac{R_{sw}}{B_w} u_{yw} \right) \\ & - \frac{\partial}{\partial z} \left(\frac{u_{zg}}{B_g} + \frac{R_{so}}{B_o} u_{zo} + \frac{R_{sw}}{B_w} u_{zw} \right) - \frac{q_g}{\rho_{gsc}} = \frac{\partial}{\partial t} \left[\phi \left(\frac{S_g}{B_g} + \frac{R_{so} S_o}{B_o} + \frac{R_{sw} S_w}{B_w} \right) \right] \end{aligned} \quad (3-32)$$

Equations (3-30) to (3-32) can be written in an abbreviated but simpler form as

$$-\nabla \cdot \frac{\vec{u}_w}{B_w} - \frac{q_w}{\rho_{wsc}} = \frac{\partial}{\partial t} (\phi S_w / B_w) \quad (3-33)$$

$$-\nabla \cdot \frac{\vec{u}_o}{B_o} - \frac{q_o}{\rho_{osc}} = \frac{\partial}{\partial t} (\phi S_o / B_o) \quad (3-34)$$

$$-\nabla \cdot \left(\frac{\vec{u}_g}{B_g} + \frac{R_{so}}{B_o} \vec{u}_o + \frac{R_{sw}}{B_w} \vec{u}_w \right) - \frac{q_g}{\rho_{gsc}} = \frac{\partial}{\partial t} \left[\phi \left(\frac{S_g}{B_g} + \frac{R_{so} S_o}{B_o} + \frac{R_{sw} S_w}{B_w} \right) \right] \quad (3-35)$$

where

$$\nabla \cdot \vec{u} = \frac{\partial}{\partial x} u_x + \frac{\partial}{\partial y} u_y + \frac{\partial}{\partial z} u_z \quad (3-36)$$

Replacing velocities from Equation (3-21) in Equations (3-33) to (3-35) gives

$$\frac{\nabla \cdot \vec{k} \cdot \lambda_{rw} \nabla \Phi_w}{B_w} - \frac{q_w}{\rho_{wsc}} = \frac{\partial}{\partial t} \left(\frac{\phi S_w}{B_w} \right) \quad (3-37)$$

$$\frac{\nabla \cdot \vec{k} \cdot \lambda_{ro} \nabla \Phi_o}{B_o} - \frac{q_o}{\rho_{osc}} = \frac{\partial}{\partial t} \left(\frac{\phi S_o}{B_o} \right) \quad (3-38)$$

$$\nabla \cdot \vec{k} \cdot \left[\frac{\lambda_{rg} \nabla \Phi_g}{B_g} + \frac{R_{so} \lambda_{ro} \nabla \Phi_o}{B_o} + \frac{R_{sw} \lambda_{rw} \nabla \Phi_w}{B_w} \right] - \frac{q_g}{\rho_{gsc}} = \frac{\partial}{\partial t} \left[\phi \left(\frac{S_g}{B_g} + \frac{R_{so} S_o}{B_o} + \frac{R_{sw} S_w}{B_w} \right) \right] \quad (3-39)$$

The presence of oil, water and gas phase pressures in flow equations complicates solving the problem. Capillary pressure is used to solve the equations,

$$P_{cow} = P_o - P_w \quad (3-40)$$

$$P_{cgw} = P_g - P_w \quad (3-41)$$

Rewriting Equations (3-37), (3-38), and (3-39) using capillary pressure gives

$$\nabla \cdot \vec{k} \cdot \left(\frac{\lambda_{rw}}{B_w} \right) \nabla P_w + CG_w - \frac{q_w}{\rho_{wsc}} = \frac{\partial}{\partial t} \left(\phi \frac{S_w}{B_w} \right) \quad (3-42)$$

$$\nabla \cdot \vec{k} \cdot \left(\frac{\lambda_{ro}}{B_o} \right) \nabla P_w + CG_o - \frac{q_o}{\rho_{osc}} = \frac{\partial}{\partial t} \left(\phi \frac{S_o}{B_o} \right) \quad (3-43)$$

$$\nabla \cdot \left[\vec{k} \cdot \left(\frac{\lambda_{rg}}{B_g} + \frac{R_{so}\lambda_{ro}}{B_o} + \frac{R_{sw}\lambda_{rw}}{B_w} \right) \right] \nabla P_w + CG_g - \frac{q_g}{\rho_{gsw}} = \frac{\partial}{\partial t} \left[\phi \left(\frac{S_g}{B_g} + \frac{R_{so}S_o}{B_o} + \frac{R_{sw}S_w}{B_w} \right) \right] \quad (3-44)$$

where CG_w , CG_o and CG_g are capillary-gravity contribution terms.

$$CG_w = -\nabla \cdot \vec{k} \cdot \left(\frac{\lambda_{rw}}{B_w} \right) \nabla (\rho_w z) \quad (3-45)$$

$$CG_o = -\nabla \cdot \vec{k} \cdot \left(\frac{\lambda_{ro}}{B_o} \right) \nabla (\rho_o z - P_{cow}) \quad (3-46)$$

$$CG_g = -\nabla \cdot \vec{k} \cdot \left[\left(\frac{\lambda_{rg}}{B_g} \right) \nabla (\rho_g z - P_{cgw}) + \frac{R_{so}\lambda_{ro}}{B_o} \nabla (\rho_o z - P_{cow}) + \frac{R_{sw}\lambda_{rw}}{B_w} \nabla (\rho_w z) \right] \quad (3-47)$$

From now on, the subscript w is not used for the aqueous phase pressure. P is the aqueous phase pressure unless it is otherwise stated.

3.7 PRESSURE EQUATION

To get the pressure equation, mass conservation equations require to be combined such that subsequent equation remains with just one unknown of P .

For pressures less than bubble point pressure (saturated reservoirs), P , S_w , and S_g are unknowns, while S_o is calculated from volume constraint equation ($S_o = 1 - S_w - S_g$). Therefore, the mass conservation equations need to be combined to cancel saturation derivatives with respect to time ($\partial S_l / \partial t$ $l = w, o, g$).

For pressures greater than bubble point pressure, P_b is independent of oil pressure. P , P_b , and S_w are unknowns and S_o is calculated from volume constraint equation ($S_o = 1 - S_w$). Then, the mass conservation equations combine to cancel the saturation derivatives ($\partial S_l / \partial t$ $l = w, o$) and bubble point pressure derivative with respect to time ($\partial P_b / \partial t$).

3.7.1 Pressure Equation for Saturated Reservoirs

Equations (3-42), (3-43), and (3-44) can be written in short form where L_w , L_o and L_g are the left hand sides of these equations.

$$L_w = \frac{\partial}{\partial t} \left(\phi \frac{S_w}{B_w} \right) \quad (3-48)$$

$$L_o = \frac{\partial}{\partial t} \left(\phi \frac{S_o}{B_o} \right) \quad (3-49)$$

$$L_g = \frac{\partial}{\partial t} \left[\phi \left(\frac{S_g}{B_g} + \frac{R_{so} S_o}{B_o} + \frac{R_{sw} S_w}{B_w} \right) \right] \quad (3-50)$$

where

$$L_w = \nabla \cdot \vec{k} \cdot \left(\frac{\lambda_{rw}}{B_w} \right) \nabla P + CG_w - \frac{q_w}{\rho_{wsc}} \quad (3-51)$$

$$L_o = \nabla \cdot \vec{k} \cdot \left(\frac{\lambda_{ro}}{B_o} \right) \nabla P + CG_o - \frac{q_o}{\rho_{osc}} \quad (3-52)$$

$$L_g = \nabla \cdot \left[\bar{k} \cdot \left(\frac{\lambda_{rg}}{B_g} + \frac{R_{so} \lambda_{ro}}{B_o} + \frac{R_{sw} \lambda_{rw}}{B_w} \right) \right] \nabla P + CG_g - \frac{q_g}{\rho_{gsw}} \quad (3-53)$$

Formation volume factor, solution gas ratio and porosity are functions of pressure. Chain rule is used to expand the accumulation terms of Equations (3-48), (3-49), and (3-50).

$$L_w = \frac{\phi}{B_w} \frac{\partial S_w}{\partial t} + \left[\frac{S_w}{B_w} \frac{\partial \phi}{\partial P} - \frac{S_w \phi}{B_w^2} \frac{\partial B_w}{\partial P} \right] \frac{\partial P}{\partial t} \quad (3-54)$$

$$L_o = \frac{\phi}{B_o} \frac{\partial S_o}{\partial t} + \left[\frac{S_o}{B_o} \frac{\partial \phi}{\partial P} - \frac{S_o \phi}{B_o^2} \frac{\partial B_o}{\partial P} \right] \frac{\partial P}{\partial t} \quad (3-55)$$

$$\begin{aligned} L_g &= \frac{\phi}{B_g} \frac{\partial S_g}{\partial t} + \left[\frac{S_g}{B_g} \frac{\partial \phi}{\partial P} - \frac{S_g \phi}{B_g^2} \frac{\partial B_g}{\partial P} \right] \frac{\partial P}{\partial t} \\ &+ \frac{\phi R_{so}}{B_o} \frac{\partial S_o}{\partial t} + \left[\frac{S_o R_{so}}{B_o} \frac{\partial \phi}{\partial P} + \frac{\phi S_o}{B_o} \frac{\partial R_{so}}{\partial P} - \frac{\phi S_o R_{so}}{B_o^2} \frac{\partial B_o}{\partial P} \right] \frac{\partial P}{\partial t} \\ &+ \frac{\phi R_{sw}}{B_w} \frac{\partial S_w}{\partial t} + \left[\frac{S_w R_{sw}}{B_w} \frac{\partial \phi}{\partial P} + \frac{\phi S_w}{B_w} \frac{\partial R_{sw}}{\partial P} - \frac{\phi S_w R_{sw}}{B_w^2} \frac{\partial B_w}{\partial P} \right] \frac{\partial P}{\partial t} \end{aligned} \quad (3-56)$$

Then the saturation volume constraint equation is used to remove $\partial S_g / \partial t$ from Equation (3-56), where

$$\frac{\partial S_g}{\partial t} = -\frac{\partial S_o}{\partial t} - \frac{\partial S_w}{\partial t} \quad (3-57)$$

Substituting $\partial S_g / \partial t$ in Equation (3-56) and rearranging gives

$$\begin{aligned}
L_g = & \left(\frac{\phi R_{so}}{B_o} - \frac{\phi}{B_g} \right) \frac{\partial S_o}{\partial t} + \left(\frac{\phi R_{sw}}{B_w} - \frac{\phi}{B_g} \right) \frac{\partial S_w}{\partial t} + \\
& \left(\frac{S_g}{B_g} \frac{\partial \phi}{\partial P} - \frac{S_g \phi}{B_g^2} \frac{\partial B_g}{\partial P} + \frac{S_o R_{so}}{B_o} \frac{\partial \phi}{\partial P} + \frac{\phi S_o}{B_o} \frac{\partial R_{so}}{\partial P} - \frac{\phi S_o R_{so}}{B_o^2} \frac{\partial B_o}{\partial P} \right. \\
& \left. + \frac{S_w R_{sw}}{B_w} \frac{\partial \phi}{\partial P} + \frac{\phi S_w}{B_w} \frac{\partial R_{sw}}{\partial P} - \frac{\phi S_w R_{sw}}{B_w^2} \frac{\partial B_w}{\partial P} \right) \frac{\partial P}{\partial t}
\end{aligned} \tag{3-58}$$

Equations (3-54), (3-55), and (3-58) are multiplied by $(B_w - R_{sw} B_g)$, $(B_o - R_{so} B_g)$ and B_g , respectively and then are added together to remove all the terms containing saturation derivatives with time. The remaining results are

$$\begin{aligned}
& (B_o - R_{so} B_g) L_o + (B_w - R_{sw} B_g) L_w + B_g L_g = \\
& \left[\frac{\partial \phi}{\partial P} - \phi S_g \frac{1}{B_g} \frac{\partial B_g}{\partial P} + \phi S_o \left(\frac{B_g}{B_o} \frac{\partial R_{so}}{\partial P} - \frac{1}{B_o} \frac{\partial B_o}{\partial P} \right) + \phi S_w \left(\frac{B_g}{B_w} \frac{\partial R_{sw}}{\partial P} - \frac{1}{B_w} \frac{\partial B_w}{\partial P} \right) \right] \frac{\partial P}{\partial t}
\end{aligned} \tag{3-59}$$

The water, oil, gas and rock compressibilities are introduced as follow:

$$c_w = -\frac{1}{B_w} \frac{\partial B_w}{\partial P} + \frac{B_g}{B_w} \frac{\partial R_{sw}}{\partial P} \tag{3-60}$$

$$c_o = -\frac{1}{B_o} \frac{\partial B_o}{\partial P} + \frac{B_g}{B_o} \frac{\partial R_{so}}{\partial P} \tag{3-61}$$

$$c_g = -\frac{1}{B_g} \frac{\partial B_g}{\partial P} \tag{3-62}$$

$$c_r = \frac{1}{\phi} \frac{\partial \phi}{\partial P} \tag{3-63}$$

The total compressibility can be written as

$$c_t = c_r + S_w c_w + S_o c_o + S_g c_g \tag{3-64}$$

Combining Equations (3-51) through (3-53) and (3-59) through (3-64) the final form of pressure equation for saturated gridblocks can be written as

$$\begin{aligned}
& (B_o - R_{so} B_g) \left[\nabla \cdot \vec{k} \cdot \frac{\lambda_{ro}}{B_o} \nabla P + CG_o - \frac{q_o}{\rho_{osc}} \right] + \\
& (B_w - R_{sw} B_g) \left[\nabla \cdot \vec{k} \cdot \frac{\lambda_{rw}}{B_w} \nabla P + CG_w - \frac{q_w}{\rho_{wsc}} \right] + \\
& B_g \left[\nabla \cdot \vec{k} \cdot \left(\frac{\lambda_{rg}}{B_g} + \frac{R_{so} \lambda_{ro}}{B_o} + \frac{R_{sw} \lambda_{rw}}{B_w} \right) \nabla P + CG_g - \frac{q_g}{\rho_{gsc}} \right] = \phi c_t \frac{\partial P}{\partial t}
\end{aligned} \tag{3-65}$$

3.7.2 Pressure Equation for Undersaturated Reservoirs

For pressures greater than bubble point pressure, porosity, water and gas formation volume factor, and water solution gas ratio are functions of pressure. Oil formation volume factor is both function of pressure and bubble point pressure (see Equation (3-4)) and oil solution gas ratio is a function of bubble point pressure (see Figure 3.2).

$$B_o = B_o(P, P_b) \tag{3-66}$$

$$R_{so} = R_{so}(P_b) \tag{3-67}$$

Then, the chain rule was used to expand the accumulation terms of Equations (3-48), (3-49), and (3-50) for above bubble point pressure.

$$L_w = \frac{\phi}{B_w} \frac{\partial S_w}{\partial t} + \left[\frac{S_w}{B_w} \frac{\partial \phi}{\partial P} - \frac{S_w \phi}{B_w^2} \frac{\partial B_w}{\partial P} \right] \frac{\partial P}{\partial t} \tag{3-68}$$

$$L_o = \frac{\phi}{B_o} \frac{\partial S_o}{\partial t} + \left[\frac{S_o}{B_o} \frac{\partial \phi}{\partial P} - \frac{S_o \phi}{B_o^2} \frac{\partial B_o}{\partial P} \right] \frac{\partial P}{\partial t} - \frac{S_o \phi}{B_o^2} \frac{\partial B_o}{\partial P_b} \frac{\partial P_b}{\partial t} \tag{3-69}$$

For pressures above bubble point pressure $S_g = 0$, then

$$\begin{aligned}
 L_g = & \frac{\phi R_{so}}{B_o} \frac{\partial S_o}{\partial t} + \left[\frac{S_o R_{so}}{B_o} \frac{\partial \phi}{\partial P} - \frac{\phi S_o R_{so}}{B_o^2} \frac{\partial B_o}{\partial P} \right] \frac{\partial P}{\partial t} + \left[\frac{\phi S_o}{B_o} \frac{\partial R_{so}}{\partial P_b} - \frac{\phi S_o R_{so}}{B_o^2} \frac{\partial B_o}{\partial P_b} \right] \frac{\partial P_b}{\partial t} \\
 & + \frac{\phi R_{sw}}{B_w} \frac{\partial S_w}{\partial t} + \left[\frac{S_w R_{sw}}{B_w} \frac{\partial \phi}{\partial P} + \frac{\phi S_w}{B_w} \frac{\partial R_{sw}}{\partial P} - \frac{\phi S_w R_{sw}}{B_w^2} \frac{\partial B_w}{\partial P} \right] \frac{\partial P}{\partial t}
 \end{aligned} \tag{3-70}$$

Coefficients C_1 and C_2 are defined as

$$C_1 = - \frac{\frac{d}{dP_b} \left(\frac{1}{B_o} \right)}{\frac{d}{dP_b} \left(\frac{R_{so}}{B_o} \right)} = \frac{\frac{1}{B_o^2} \frac{\partial B_o}{\partial P_b}}{\frac{1}{B_o} \frac{\partial R_{so}}{\partial P_b} - \frac{R_{so}}{B_o^2} \frac{\partial B_o}{\partial P_b}} \tag{3-71}$$

$$C_2 = \frac{C_1 \times \frac{\phi R_{so}}{B_o} + \frac{\phi}{B_o} - C_1 \times \frac{\phi R_{sw}}{B_w}}{\frac{\phi}{B_w}} \tag{3-72}$$

Equations (3-68), (3-69) and (3-70) are multiplied by C_2 , one, and C_1 , respectively and then added together to remove all terms containing saturation derivative and bubble point pressure derivative with respect to time.

$$\begin{aligned}
& C_2 \times L_w + L_o + C_1 \times L_g = \\
& \left[C_1 \times \frac{\phi R_{so}}{B_o} + \frac{\phi}{B_o} - C_1 \times \frac{\phi R_{sw}}{B_w} \right] \frac{\partial S_w}{\partial t} + C_2 \times \left[\frac{S_w}{B_w} \frac{\partial \phi}{\partial P} - \frac{S_w \phi}{B_w^2} \frac{\partial B_w}{\partial P} \right] \frac{\partial P}{\partial t} \\
& + \frac{\phi}{B_o} \frac{\partial S_o}{\partial t} + \left[\frac{S_o}{B_o} \frac{\partial \phi}{\partial P} - \frac{S_o \phi}{B_o^2} \frac{\partial B_o}{\partial P} \right] \frac{\partial P}{\partial t} - \frac{S_o \phi}{B_o^2} \frac{\partial B_o}{\partial P_b} \frac{\partial P_b}{\partial t} \\
& + C_1 \times \frac{\phi R_{so}}{B_o} \frac{\partial S_o}{\partial t} + C_1 \times \left[\frac{S_o R_{so}}{B_o} \frac{\partial \phi}{\partial P} - \frac{\phi S_o R_{so}}{B_o^2} \frac{\partial B_o}{\partial P} \right] \frac{\partial P}{\partial t} + \frac{\phi S_o}{B_o^2} \frac{\partial B_o}{\partial P_b} \frac{\partial P_b}{\partial t} \\
& + C_1 \times \frac{\phi R_{sw}}{B_w} \frac{\partial S_w}{\partial t} + C_1 \times \left[\frac{S_w R_{sw}}{B_w} \frac{\partial \phi}{\partial P} + \frac{\phi S_w}{B_w} \frac{\partial R_{sw}}{\partial P} - \frac{\phi S_w R_{sw}}{B_w^2} \frac{\partial B_w}{\partial P} \right] \frac{\partial P}{\partial t}
\end{aligned} \tag{3-73}$$

where

$$\frac{\partial S_w}{\partial t} + \frac{\partial S_o}{\partial t} = 0 \tag{3-74}$$

The remaining results are

$$\begin{aligned}
& C_2 \times L_w + L_o + C_1 \times L_g = \\
& \phi S_w \left[\left(\frac{C_2}{B_w} + \frac{C_1 R_{sw}}{B_w} \right) \frac{1}{\phi} \frac{\partial \phi}{\partial P} - \left(\frac{C_2}{B_w} + \frac{C_1 R_{sw}}{B_w} \right) \frac{1}{B_w} \frac{\partial B_w}{\partial P} + \frac{C_1}{B_w} \frac{\partial R_{sw}}{\partial P} \right] \frac{\partial P}{\partial t} \\
& \phi S_o \left[\left(\frac{1}{B_o} + \frac{C_1 R_{so}}{B_o} \right) \frac{1}{\phi} \frac{\partial \phi}{\partial P} - \left(\frac{1}{B_o} + \frac{C_1 R_{so}}{B_o} \right) \frac{1}{B_o} \frac{\partial B_o}{\partial P} \right] \frac{\partial P}{\partial t}
\end{aligned} \tag{3-75}$$

From equation (3-72) ,

$$\frac{C_2}{B_w} + \frac{C_1 R_{sw}}{B_w} = \frac{1}{B_o} + \frac{C_1 R_{so}}{B_o} \tag{3-76}$$

Assuming $\partial R_{sw} / \partial P_w \approx 0$, equation (3-75) can be written as

$$C_2 \times L_w + L_o + C_1 \times L_g = \left(\frac{1}{B_o} + \frac{C_1 R_{so}}{B_o} \right) \phi c_t \frac{\partial P}{\partial t} \tag{3-77}$$

where the total compressibility for pressures greater than bubble point pressure is defined as

$$c_t = c_r + S_w c_w + S_o c_o \quad (3-78)$$

Combining Equations (3-51) through (3-53) and (3-75) and (3-78) the final form of pressure equation for undersaturated reservoir can be written as

$$\begin{aligned} & C_2 \left[\nabla \cdot \vec{k} \cdot \frac{\lambda_{rw}}{B_w} \nabla P + CG_w - \frac{q_w}{\rho_{wsc}} \right] + \left[\nabla \cdot \vec{k} \cdot \frac{\lambda_{ro}}{B_o} \nabla P + CG_o - \frac{q_o}{\rho_{osc}} \right] + \\ & C_1 \left[\nabla \cdot \vec{k} \cdot \left(\frac{\lambda_{rg}}{B_g} + \frac{R_{so} \lambda_{ro}}{B_o} + \frac{R_{sw} \lambda_{rw}}{B_w} \right) \nabla P + CG_g - \frac{q_g}{\rho_{gsc}} \right] = \left(\frac{1}{B_o} + \frac{C_1 R_{so}}{B_o} \right) \phi c_t \frac{\partial P}{\partial t} \end{aligned} \quad (3-79)$$

3.8 TRANSMISSIBILITY

The fluid flow of phase l between two gridblocks i and $i+1$ in x -direction can be written as

$$Q_l = T_{l,i+1/2} (P_i - P_{i+1}) \quad (3-80)$$

where $T_{l,i+1/2}$ is Darcy phase transmissibility between two gridblocks i and $i+1$ in x -direction and can be defined as below:

$$T_{l,i+1/2} = \left(\frac{k_{rl}}{\mu_l B_l} \right)_{(upstream)} \left(\frac{2(kA_c)_i (kA_c)_{i+1}}{\Delta x_i (kA_c)_{i+1} + \Delta x_{i+1} (kA_c)_i} \right) \quad (l = w, o, g) \quad (3-81)$$

where k_{rl} , μ_l and B_l are relative permeability, viscosity, and formation volume factor of phase l , respectively. k is absolute permeability, Δx is the gridblock length in x -direction and A_c is flow cross sectional area.

For a rectangular gridblock system, cross-sectional area remains constant from block to block. Then the Darcy phase transmissibility can be simplified as below:

$$T_{l,i+1/2} = \left(\frac{k_{rl}}{\mu_l B_l} \right)_{(upstream)} \left(\frac{2k_i k_{i+1} A_c}{\Delta x_i k_{i+1} + \Delta x_{i+1} k_i} \right) \quad (l = w, o, g) \quad (3-82)$$

The first term of mass equation for each component can be expanded as below:

$$\nabla \cdot \vec{k} \cdot \frac{\lambda_{rl}}{B_l} \nabla P = \frac{\partial}{\partial x} \left(k_x \frac{\lambda_{rl}}{B_l} \frac{\partial P}{\partial x} \right) + \frac{\partial}{\partial y} \left(k_y \frac{\lambda_{rl}}{B_l} \frac{\partial P}{\partial y} \right) + \frac{\partial}{\partial z} \left(k_z \frac{\lambda_{rl}}{B_l} \frac{\partial P}{\partial z} \right) \quad (3-83)$$

Expanding the first part in terms of phase transmissibilities gives,

$$\begin{aligned} \frac{\partial}{\partial x} \left(k_x \frac{\lambda_{rl}}{B_l} \frac{\partial P}{\partial x} \right)_i &\approx \frac{\frac{T_{l,i+1/2}}{\Delta y_i \Delta z_i} (P_{i+1} - P_i) - \frac{T_{l,i-1/2}}{\Delta y_i \Delta z_i} (P_i - P_{i-1})}{x_{i+1/2} - x_{i-1/2}} \equiv \\ &\frac{\left(k_x \frac{\lambda_{rl}}{B_l} \right)_{i+1/2} \left(\frac{P_{i+1} - P_i}{x_{i+1} - x_i} \right) - \left(k_x \frac{\lambda_{rl}}{B_l} \right)_{i-1/2} \left(\frac{P_i - P_{i-1}}{x_i - x_{i-1}} \right)}{x_{i+1/2} - x_{i-1/2}} \end{aligned} \quad (3-84)$$

Multiplying Equation (3-84) by the volume of gridblock i (V_{B_i}) gives,

$$V_{B_i} \frac{\partial}{\partial x} \left(k_x \frac{\lambda_{rl}}{B_l} \frac{\partial P}{\partial x} \right)_i \approx T_{l,i+1/2} (P_{i+1} - P_i) - T_{l,i-1/2} (P_i - P_{i-1}) \quad (3-85)$$

Similarly transmissibility can be written for other directions. Using transmissibility definition, the left hand sides of mass and pressure equations can be written in the finite difference form. These equations need to be multiplied by the bulk volume of the gridblock (V_B). The following linear difference operators is introduced for writing in simpler form,

$$\Delta T \Delta P = \Delta_x T_x \Delta P_x + \Delta_y T_y \Delta P_y + \Delta_z T_z \Delta P_z \quad (3-86)$$

where

$$\Delta_x T_x \Delta P_x = T_{x_{i+1/2}} (P_{i+1} - P_i) + T_{x_{i-1/2}} (P_{i-1} - P_i) \quad (3-87)$$

$$\Delta_t x = x^{n+1} - x^n \quad (3-88)$$

The mass balance and pressure equations in terms of transmissibility can be written as

Mass conservation for water

$$\Delta T_w^n \Delta P^{n+1} + CG_w - \frac{q_w V_B}{\rho_{wsc}} = \frac{V_B}{\Delta t} \Delta_t \left(\phi \frac{S_w}{B_w} \right) \quad (3-89)$$

Mass conservation for oil

$$\Delta T_o^n \Delta P^{n+1} + CG_o - \frac{q_o V_B}{\rho_{osc}} = \frac{V_B}{\Delta t} \Delta_t \left(\phi \frac{S_o}{B_o} \right) \quad (3-90)$$

Mass conservation for gas

$$\begin{aligned} & \Delta T_g^n \Delta P^{n+1} + \Delta R_{so}^n T_o^n \Delta P^{n+1} + \Delta R_{sw}^n T_w^n \Delta P^{n+1} + CG_g - \frac{q_g V_B}{\rho_{gsc}} \\ & = \frac{V_B}{\Delta t} \Delta_t \left[\phi \left(\frac{S_g}{B_g} + \frac{R_{so} S_o}{B_o} + \frac{R_{sw} S_w}{B_w} \right) \right] \end{aligned} \quad (3-91)$$

Pressure equation for saturated gridblocks ($P < P_{bp}$)

$$\begin{aligned}
& \left(B_o^n - B_g^n R_{so}^n \right) \left(\Delta T_o^n \Delta P^{n+1} + CG_o - \frac{q_o V_B}{\rho_{osc}} \right) + \\
& \left(B_w^n - B_g^n R_{sw}^n \right) \left(\Delta T_w^n \Delta P^{n+1} + CG_w - \frac{q_w V_B}{\rho_{wsc}} \right) + \\
& \left(B_g^n \right) \left(\Delta T_g^n \Delta P^{n+1} + \Delta R_{so}^n T_o^n \Delta P^{n+1} + \Delta R_{sw}^n T_w^n \Delta P^{n+1} + CG_g - \frac{q_g V_B}{\rho_{gsc}} \right) \\
& = \frac{V_B \phi c_t}{\Delta t} (P^{n+1} - P^n)
\end{aligned} \tag{3-92}$$

Pressure equation for undersaturated gridblocks ($P > P_{bp}$)

$$\begin{aligned}
& \left(\Delta T_o^n \Delta P^{n+1} + CG_o - \frac{q_o V_B}{\rho_{osc}} \right) + C_2 \left(\Delta T_w^n \Delta P^{n+1} + CG_w - \frac{q_w V_B}{\rho_{wsc}} \right) + \\
& C_1 \left(\Delta T_g^n \Delta P^{n+1} + \Delta R_{so}^n T_o^n \Delta P^{n+1} + \Delta R_{sw}^n T_w^n \Delta P^{n+1} + CG_g - \frac{q_g V_B}{\rho_{gsc}} \right) \\
& = \left(\frac{1}{B_o} + \frac{C_1 R_{so}}{B_o} \right)^n \frac{V_B \phi c_t}{\Delta t} (P^{n+1} - P^n)
\end{aligned} \tag{3-93}$$

where C_1 and C_2 are calculated from Equations (3-71) and (3-72), respectively. Total compressibility c_t is calculated from Equation (3-64) and Equation (3-78) for saturated and undersaturated gridblocks, respectively. Capillary pressure and gravity effects in terms of transmissibility are defined as

$$CG_w = -\Delta T_w^n \Delta (\rho_w z)^n \tag{3-94}$$

$$CG_o = -\Delta T_o^n \Delta (\rho_o z - P_{cow})^n \tag{3-95}$$

$$CG_g = -\Delta \left[T_g^n \Delta (\rho_g z - P_{cgw})^n + R_{so}^n T_o^n \Delta (\rho_o z - P_{cow})^n + R_{sw}^n T_w^n \Delta (\rho_w z)^n \right] \quad (3-96)$$

3.8.1 Finite Difference Equation for Saturation

Once the pressure equation is solved for a new time step, it is used to calculate the new saturation at time $n+1$. For saturated gridblocks the mass equation is solved for water and oil phase, then gas saturation is obtained from volume constraint equation ($S_g = 1 - S_w - S_o$). For undersaturated gridblocks, the free gas saturation is zero ($S_g = 0$), then mass equation is only solved for water phase, and then the oil phase saturation is obtained from volume constraint equation ($S_o = 1 - S_w$).

Equations (3-89) and (3-90) can be written in short form where L_w and L_o are the left hand sides of these equations.

$$L_w = \frac{V_B}{\Delta t} \Delta_t \left(\phi \frac{S_w}{B_w} \right) \quad (3-97)$$

$$L_o = \frac{V_B}{\Delta t} \Delta_t \left(\phi \frac{S_o}{B_o} \right) \quad (3-98)$$

Formation volume factor and porosity at the right hand side of Equations (3-97) and (3-98) are functions of pressure. Chain rule is used to expand the right hand side of mass equations. Chain rule in general form can be written as

$$\Delta_t(xy) = x^{n+1} \Delta_t y + y^n \Delta_t x \quad (3-99)$$

Using the chain rule, Equation (3-97) can be expanded as below:

$$L_w^{n+1} = \frac{V_B}{\Delta t} \left[\left(\frac{\phi}{B_w} \right)^{n+1} \Delta_t S_w + S_w^n \Delta_t \left(\frac{\phi}{B_w} \right) \right] \quad (3-100)$$

$$L_w^{n+1} = \frac{V_B}{\Delta t} \left[\left(\frac{\phi}{B_w} \right)^{n+1} (S_w^{n+1} - S_w^n) + S_w^n \left(\phi^{n+1} \Delta_t \left(\frac{1}{B_w} \right) + \left(\frac{1}{B_w} \right)^n \Delta_t \phi \right) \right] \quad (3-101)$$

$$\frac{\Delta t}{V_B} L_w^{n+1} = \left(\frac{\phi}{B_w} \right)^{n+1} (S_w^{n+1} - S_w^n) + S_w^n \left[\phi^{n+1} \frac{d}{dP} \left(\frac{1}{B_w} \right) + \left(\frac{1}{B_w} \right)^n \frac{d\phi}{dP} \right] \Delta_t P \quad (3-102)$$

All the variables are known, so water saturation in the new time step is computed as

$$S_w^{n+1} = \frac{\frac{\Delta t}{V_B} L_w^{n+1} + S_w^n \left[\left(\frac{\phi}{B_w^2} \right)^{n+1} \frac{dB_w}{dP} - \left(\frac{1}{B_w} \right)^n \frac{d\phi}{dP} \right] (P^{n+1} - P^n) + \left(\frac{\phi}{B_w} \right)^{n+1} S_w^n}{\left(\frac{\phi}{B_w} \right)^{n+1}} \quad (3-103)$$

or

$$S_w^{n+1} = \frac{\Delta t}{V_B \phi^{n+1}} B_w^{n+1} L_w^{n+1} + S_w^n \left[1 - \left(\frac{B_w^{n+1}}{B_w^n} \frac{1}{\phi^{n+1}} \frac{d\phi}{dP} - \frac{1}{B_w^{n+1}} \frac{dB_w}{dP} \right) (P^{n+1} - P^n) \right] \quad (3-104)$$

For saturated gridblocks, mass equation also needs to be solved for the oil phase. Using the same solution approach oil saturation in the new time step is computed as

$$S_o^{n+1} = \frac{\Delta t}{V_B \phi^{n+1}} B_o^{n+1} L_o^{n+1} + S_o^n \left[1 - \left(\frac{B_o^{n+1}}{B_o^n} \frac{1}{\phi^{n+1}} \frac{d\phi}{dP} - \frac{1}{B_o^{n+1}} \frac{dB_o}{dP} \right) (P^{n+1} - P^n) \right] \quad (3-105)$$

3.8.2 Finite Difference Form of Pressure Equation for Saturated Gridblocks

It is useful to combine capillary, gravity and source/sink terms to simplify the notation in the pressure equation.

$$\begin{aligned}
Q_{WOG} = & \left(B_o^n - B_g^n R_{so}^n \right) \left(CG_o - \frac{q_o V_B}{\rho_{osc}} \right)^n + \left(B_w^n - B_g^n R_{sw}^n \right) \left(CG_w - \frac{q_w V_B}{\rho_{wsc}} \right)^n \\
& + \left(B_g^n \right) \left(CG_g - \frac{q_g V_B}{\rho_{gsc}} \right)^n
\end{aligned} \tag{3-106}$$

Therefore, Equation (3-92) can be written in short form as

$$\begin{aligned}
& \left(B_o^n - B_g^n R_{so}^n \right) \Delta T_o^n \Delta P^{n+1} + \left(B_w^n - B_g^n R_{sw}^n \right) \Delta T_w^n \Delta P^{n+1} + \\
& B_g^n \left(\Delta T_g^n + \Delta \left(R_{so}^n T_o^n \right) + \Delta \left(R_{sw}^n T_w^n \right) \right) \Delta P^{n+1} + Q_{WOG} = \frac{V_B \phi^n c_t^n}{\Delta t} \left(P^{n+1} - P^n \right)
\end{aligned} \tag{3-107}$$

The pressure equation for gridblock i is

$$AT_k P_{k-1}^{n+1} + AN_j P_{j-1}^{n+1} + AW_i P_{i-1}^{n+1} + AC_i^{n+1} P_i^{n+1} + AE_i P_{i+1}^{n+1} + AS_j P_{j+1}^{n+1} + AB_k P_{k+1}^{n+1} = B_i \tag{3-108}$$

where $AT_k, AN_j, AW_i, AC_i, AE_i, AS_j, AB_k$ and B_i are all known values.

Writing for all the gridblocks, pressure equation can be stated using matrix format as follows:

$$AP^{n+1} = B \tag{3-109}$$

where A is the matrix of coefficient, P is pressure vector at time $n+1$, and B is a known given vector. All the coefficients of the pressure equation at time $n+1$ are all known and Equation (3-109) can be solved for the pressure at new time step. The pressure coefficients and given vector B for saturated gridblocks are defined as below:

$$AE_i = \left[B_{o_i} + B_{g_i} \left(R_{so_{i+1/2}} - R_{so_i} \right) \right] T_{o_{i+1/2}} + \left[B_{w_i} + B_{g_i} \left(R_{sw_{i+1/2}} - R_{sw_i} \right) \right] T_{w_{i+1/2}} + B_{g_i} T_{g_{i+1/2}} \tag{3-110}$$

$$AW_i = \left[B_{o_i} + B_{g_i} \left(R_{so_{i-1/2}} - R_{so_i} \right) \right] T_{o_{i-1/2}} + \left[B_{w_i} + B_{g_i} \left(R_{sw_{i-1/2}} - R_{sw_i} \right) \right] T_{w_{i-1/2}} + B_{g_i} T_{g_{i-1/2}} \tag{3-111}$$

$$AS_j = \left[B_{o_j} + B_{g_j} \left(R_{so_{j+1/2}} - R_{so_j} \right) \right] T_{o_{j+1/2}} + \left[B_{w_j} + B_{g_j} \left(R_{sw_{j+1/2}} - R_{sw_j} \right) \right] T_{w_{j+1/2}} + B_{g_j} T_{g_{j+1/2}} \quad (3-112)$$

$$AN_j = \left[B_{o_j} + B_{g_j} \left(R_{so_{j-1/2}} - R_{so_j} \right) \right] T_{o_{j-1/2}} + \left[B_{w_j} + B_{g_j} \left(R_{sw_{j-1/2}} - R_{sw_j} \right) \right] T_{w_{j-1/2}} + B_{g_j} T_{g_{j-1/2}} \quad (3-113)$$

$$AB_k = \left[B_{o_k} + B_{g_k} \left(R_{so_{k+1/2}} - R_{so_k} \right) \right] T_{o_{k+1/2}} + \left[B_{w_k} + B_{g_k} \left(R_{sw_{k+1/2}} - R_{sw_k} \right) \right] T_{w_{k+1/2}} + B_{g_k} T_{g_{k+1/2}} \quad (3-114)$$

$$AT_k = \left[B_{o_k} + B_{g_k} \left(R_{so_{k-1/2}} - R_{so_k} \right) \right] T_{o_{k-1/2}} + \left[B_{w_k} + B_{g_k} \left(R_{sw_{k-1/2}} - R_{sw_k} \right) \right] T_{w_{k-1/2}} + B_{g_k} T_{g_{k-1/2}} \quad (3-115)$$

$$AC_i = - \left[AT_k + AS_j + AE_i + AW_i + AN_j + AB_k + \frac{V_B \phi^n c_t^n}{\Delta t} \right] \quad (3-116)$$

$$B_i = - \left[Q_{OWG} + \frac{V_B \phi^n c_t^n P^n}{\Delta t} \right] \quad (3-117)$$

3.8.3 Finite Difference Form of Pressure Equation for Undersaturated Gridblocks

Pressure equation for undersaturated gridblocks (Equation (3-93)) in terms of transmissibility can be written as

$$\begin{aligned} & \Delta T_o^n \Delta P^{n+1} + C_2 \Delta T_w^n \Delta P^{n+1} + C_1 \left(\Delta T_g^n + \Delta R_{so}^n T_o^n + \Delta R_{sw}^n T_w^n \right) \Delta P^{n+1} + Q'_{WOG} \\ & = \frac{V_B \phi^n c_t^n}{\Delta t} (P^{n+1} - P^n) \end{aligned} \quad (3-118)$$

where

$$Q'_{WOG} = \left(CG_o - \frac{q_o V_B}{\rho_{osc}} \right)^n + C_2 \left(CG_w - \frac{q_w V_B}{\rho_{wsc}} \right)^n + C_1 \left(CG_g - \frac{q_g V_B}{\rho_{gsc}} \right)^n \quad (3-119)$$

The general form of pressure equation in matrix format is the same as saturated gridblocks

$$A'P^{n+1} = B' \quad (3-120)$$

The pressure coefficients and given vector B' for undersaturated gridblocks are defined as below (all the coefficients are calculated at time step n):

$$AE'_i = (C_2 + C_1 \times R_{sw_{i+1/2}})T_{w_{i+1/2}} + (1 + C_1 \times R_{so_{i+1/2}})T_{o_{i+1/2}} + C_1 \times T_{g_{i+1/2}} \quad (3-121)$$

$$AW'_i = (C_2 + C_1 \times R_{sw_{i-1/2}})T_{w_{i-1/2}} + (1 + C_1 \times R_{so_{i-1/2}})T_{o_{i-1/2}} + C_1 \times T_{g_{i-1/2}} \quad (3-122)$$

$$AS'_j = (C_2 + C_1 \times R_{sw_{j+1/2}})T_{w_{j+1/2}} + (1 + C_1 \times R_{so_{j+1/2}})T_{o_{j+1/2}} + C_1 \times T_{g_{j+1/2}} \quad (3-123)$$

$$AN'_j = (C_2 + C_1 \times R_{sw_{j-1/2}})T_{w_{j-1/2}} + (1 + C_1 \times R_{so_{j-1/2}})T_{o_{j-1/2}} + C_1 \times T_{g_{j-1/2}} \quad (3-124)$$

$$AB'_k = (C_2 + C_1 \times R_{sw_{k+1/2}})T_{w_{k+1/2}} + (1 + C_1 \times R_{so_{k+1/2}})T_{o_{k+1/2}} + C_1 \times T_{g_{k+1/2}} \quad (3-125)$$

$$AT'_k = (C_2 + C_1 \times R_{sw_{k-1/2}})T_{w_{k-1/2}} + (1 + C_1 \times R_{so_{k-1/2}})T_{o_{k-1/2}} + C_1 \times T_{g_{k-1/2}} \quad (3-126)$$

$$AC'_i = - \left[AT'_k + AS'_j + AE'_i + AW'_i + AN'_j + AB'_k + \left(\frac{1}{B_o} + \frac{C_1 R_{so}}{B_o} \right)^n \frac{V_B \phi^n c_t^n}{\Delta t} \right] \quad (3-127)$$

$$B'_i = - \left[Q'_{OWG} + \left(\frac{1}{B_o} + \frac{C_1 R_{so}}{B_o} \right) \frac{V_B \phi^n c_t^n P^n}{\Delta t} \right] \quad (3-128)$$

3.9 BUBBLE POINT TRACKING

In multiphase flow, the gas phase may disappear or reappear under certain conditions. The gas phase may not exist initially in an undersaturated oil reservoir but appears under primary depletion as the reservoir pressure drops below the bubble point pressure. Also the gas phase may disappear in saturated oil reservoir undergoing repressurizing by i.e. water injection. Likewise, it may appear if gas is injected into an undersaturated reservoir. Also, gas may appear locally because of the pressure drawdown near a well. This section will discuss two most common methods for handling gas-phase change: variable substitution method and the pseudo-solution GOR method. The bubble point tracking in UTCHEM is also discussed.

3.9.1 Variable-Substitution Method

In this method the main idea is to identify the prevailing conditions in a given gridblock and then determine the appropriate unknowns and the constraint equation to be used. The variable-substitution method uses the $(P-S_w-S_g)$ and the $(P-S_w-R_s)$ formulations. A gridblock in a reservoir exhibits one of these two cases.

- Case1: for $P < P_b$ implies the saturated gridblock, R_s is known. P , S_w and S_o are unknowns, and volume constraint equation is $S_g = 1 - S_w - S_o$.
- Case2: for $P \geq P_b$ implies the undersaturated gridblock, where R_s is independent of oil pressure. P , S_w , and R_s are unknowns and the volume constraint equation is $S_o = 1 - S_w$.

3.9.2 Pseudo-solution Method

In this method, the appearance and reappearance of the gas phase is handled without resorting to the variable-substitution logic in the numerical-solution procedure of a black-oil simulator. In this method, the saturated condition of the gridblock is

determined at the beginning of the iteration step by comparing oil phase pressure and bubble point pressure. At the end of the iteration step, saturated gridblocks are tested for a change of state. If gas saturation is positive in the saturated gridblock, bubble point pressure is set equal to gridblock pressure. If gas saturation is negative, gas saturation is set to zero and bubble point pressure is set slightly below the oil phase pressure. This makes the gridblock slightly undersaturated as it enters the next iteration. Undersaturated gridblocks do not require any special treatment. The next iteration is then performed.

3.9.3 Bubble Point Tracking in UTCHEM

UTCHEM has both options for classical constant bubble point and variable bubble point pressure approach. The variable bubble point pressure approach for saturated and undersaturated gridblocks is discussed in the next two sections.

3.9.3.1 Bubble Point Tracking for Saturated Gridblocks

For saturated gridblocks ($P < P_b$), R_{so} is known. Therefore, the new gridblock bubble point pressure is the pressure at which all the gas dissolves into the oil phase. The new solubility of gas in oil is estimated as the sum of the dissolved gas and the free gas in the gridblock divided by the stock tank oil in the gridblock,

$$R_{so}^{n+1} = \frac{(R_{so}^n S_o V_B \phi / B_o + S_g V_B \phi / B_g)}{S_o V_B \phi / B_o} \quad (3-129)$$

$$R_{so}^{n+1} = R_{so}^n + \frac{S_g B_o}{S_o B_g} \quad (3-130)$$

The saturation pressure corresponding to R_{so}^{n+1} is the new bubble point pressure (P_b^{n+1}).

3.9.3.2 Bubble Point Tracking for Undersaturated Gridblocks

For undersaturated gridblocks ($P > P_b$), R_{so} is unknown and independent of oil pressure. Therefore, R_{so} needs to be computed through the mass balance equations.

Equation (3-91) can be written in short form where L_g is the left hand side of the equation.

$$L_g = \frac{V_B}{\Delta t} \Delta_t \left[\phi \left(\frac{S_g}{B_g} + \frac{R_{so} S_o}{B_o} + \frac{R_{sw} S_w}{B_w} \right) \right] \quad (3-131)$$

For undersaturated conditions, there is no free gas. The solution gas ratio in water is also negligible compared to oil. Therefore, Equation (3-131) can be simplified as

$$L_g = \frac{V_B}{\Delta t} \Delta_t \left(\frac{\phi R_{so} S_o}{B_o} \right) \quad (3-132)$$

Using the chain rule, Equation (3-132) can be expanded as

$$L_g^{n+1} = \frac{V_B}{\Delta t} \left[\left(\frac{\phi S_o}{B_o} \right)^{n+1} \Delta_t R_{so} + R_{so}^n \Delta_t \left(\frac{\phi S_o}{B_o} \right) \right] \quad (3-133)$$

Combining Equations (3-98) and (3-133) gives

$$\frac{L_g^{n+1} \Delta t}{V_B} = \left(\frac{\phi S_o}{B_o} \right)^{n+1} \Delta_t R_{so} + R_{so}^n \frac{L_o^{n+1} \Delta t}{V_B} \quad (3-134)$$

Then

$$R_{so}^{n+1} = R_{so}^n + \frac{\frac{\Delta t}{V_B} (L_g^{n+1} - R_{so}^n L_o^{n+1})}{\left(\frac{\phi S_o}{B_o} \right)^{n+1}} \quad (3-135)$$

The saturation pressure corresponding to R_{so}^{n+1} is the new bubble point pressure (P_b^{n+1}).

NOMENCLATURE

| | |
|---|--|
| A_c | = flow cross sectional area (L^2) |
| $\overline{\overline{A}}, \overline{\overline{A}}'$ | = matrix of pressure coefficients ($M^{-1}L^4 t$) |
| $\overline{\overline{B}}, \overline{\overline{B}}'$ | = known vectors for pressure equation ($L^3 t^{-1}$) |
| B_l | = formation volume factor (L^3/L^3) |
| c_k | = compressibility ($ML^{-1}t^{-2})^{-1}$ |
| C_k | = total mass concentration (ML^{-3}) |
| C_{pci} | = capillary pressure model parameter (Mt-2) |
| e_{pc} | = capillary pressure model parameter |
| g | = gravitational force (Lt^{-2}) |
| h_c^* | = scaled capillary pressure (Van Genuchten model) ($ML^{-1}t^{-2}$) |
| J_k | = mass flux of component k ($ML^3 t^{-1}$) |
| k | = absolute permeability (L^2) |
| k_r | = relative permeability |
| k_{rl}^o | = endpoint relative permeability |
| m | = relative permeability/capillary pressure model parameter (Parker <i>et al.</i>) |
| n | = capillary pressure model parameter (Van Genuchten model) |
| n_l | = Corey relative permeability exponent |
| P | = pressure ($ML^{-1}t^{-2}$) |
| P_b | = bubble point pressure ($ML^{-1}t^{-2}$) |
| P_{cjl} | = capillary pressure between phase l and l ($ML^{-1}t^{-2}$) |
| q_k | = source/sink term ($ML^3 t^{-1}$) |
| R_{sl} | = solution gas ratio in phase l (L^3/L^3) |
| S_l | = saturation of phase l (L^3/L^3 PV) |
| \overline{S}_l | = effective saturation of phase l |
| S_{lr} | = residual saturation of phase l (L^3/L^3 PV) |
| $S_{lrl'}$ | = residual saturation of phase l respect to phase l' (L^3/L^3 PV) |

| | |
|----------------|--|
| S_{nl} | = normalized saturation of phase l |
| t | = time (t) |
| T | = temperature (T) |
| T_l | = phase transmissibility ($M^{-1}L^4 t$) |
| V_B | = grid volume (L^3) |
| V_l | = phase volume (L^3) |
| u_l | = Darcy phase velocity of phase l (Lt^{-1}) |
| z | = depth (L) |
| Z | = gas compressibility factor |
| α | = capillary pressure model parameter (Van Genuchten model) |
| $\beta_{ll'}$ | = Capillary pressure scaling coefficient (Van Genuchten model) |
| λ_{rl} | = phase relative mobility ($M^{-1}Lt$) |
| μ_l | = phase viscosity ($ML^{-1}t^{-1}$) |
| ρ | = density (ML^{-3}) |
| $\sigma_{ll'}$ | = interfacial tension between phase l and l' (Mt^{-2}) |
| ϕ | = porosity |
| Φ_l | = phase potential ($ML^{-1}t^{-2}$) |

Chapter 4: Four-Phase Flow Model to Simulate Chemical EOR with Gas

In this chapter, the four-phase flow formulation implemented in UTCHEM is described. The black-oil model described in Chapter 3 was coupled with the surfactant/oil/water (microemulsion) phase behavior model through a new formulation to model chemical EOR with gas. The new formulation includes water, oil, gas, surfactant, polymer and electrolytes components in the aqueous, oleic, microemulsion and gas phases. The PVT properties are calculated for each phase. The impact of pressure and solution gas on the optimum salinity and interfacial tension will also be discussed.

4.1 MODEL DESCRIPTION

The new four-phase formulation includes aqueous, oleic, and microemulsion liquid phases. The single pseudo-component gas can be either free gas or gas dissolved in one of the three liquid phases corresponding to PVT data. Table 4.1 summarizes possible components that may exist in each phase. An important and valid assumption is the solubilized oil and water components in the microemulsion phase have the same properties as the excess oil and water phases (Lotfollahi *et al.* 2014). We ignore co-solvent in this new formulation. However, the model can be easily extended to include co-solvent.

The assumptions imposed when developing the flow and transport equations are local thermodynamic equilibrium, ideal mixing, and Darcy's law. The mass balance equation is solved for each pseudo component. The aqueous pressure equation is obtained by an overall mass balance on volume-occupying components of water, oil, gas and surfactant. The other phase pressures are computed by adding the capillary pressure between phases. The microemulsion phase behavior depends on the effective salinity.

The resulting flow equations are solved using a block-centered finite-difference method. The solution scheme is IMPEC - analogous to IMPES - where pressure is solved for implicitly, but concentrations are solved for explicitly. To increase the stability and robustness of the higher order finite-difference methods, a flux limiter that is total-variation-diminishing (TVD) has been added (Liu, 1993; Liu *et al.*, 1994). The third-order TVD method gives the most accurate solution by reducing the numerical dispersion.

In this chapter, all the necessary equations are separately written for the gas phase to show how to couple the black-oil formulation with the microemulsion phase behavior.

Table 4.1: Possible phases and their constituent components in new model

| Component Phase | Water | Stock tank Oil | Surfactant | Polymer | Anion | Divalent cation | Gas |
|--------------------|-------|-------------------|------------|---------|-------|--------------------|-----|
| Water (Aqueous) | ✓ | | | ✓ | ✓ | ✓ | ✓ |
| Oil (Oleic) | | ✓ | | | | | ✓ |
| Microemulsion | ✓ | ✓ | ✓ | ✓ | ✓ | ✓ | ✓ |
| Gas | | | | | | | ✓ |

4.2 GAS PHASE PROPERTIES

The gas phase consists of a single pseudo component, existing as either free gas or solution gas in liquid phases. The gas phase properties, including solution gas ratio, formation volume factor and viscosity can be either read from the input PVT table or calculated from correlations.

4.3 LIQUID PHASE PROPERTIES

Liquid phase properties are computed based on pure component properties and the composition of each phase including water, oil, gas, surfactant, polymer and electrolyte components (Lotfollahi *et al.* 2014).

4.3.1 Viscosity

Liquid phase viscosities are modeled in terms of pure water and oil component viscosities and the phase concentrations of the oil, water, and surfactant in each phase.

$$\mu_l = \bar{C}_{wl} \mu_w e^{\alpha_1(\bar{C}_{ol} + \bar{C}_{sl})} + \bar{C}_{ol} \mu_o e^{\alpha_2(\bar{C}_{wl} + \bar{C}_{sl})} + \bar{C}_{sl} \alpha_3 e^{(\alpha_4 \bar{C}_{wl} + \alpha_5 \bar{C}_{ol})} \quad (l = w, o, me) \quad (4-1)$$

where \bar{C}_{kl} is the volumetric concentration of component k in phase l at “*reservoir conditions*”. Then, \bar{C}_{wl} , \bar{C}_{ol} , and \bar{C}_{sl} are water, oil and surfactant concentrations in phase l at reservoir conditions. μ_w and μ_o are water and oil viscosities at reservoir conditions, respectively. The effect of solution gas on microemulsion phase viscosity is reflected in water and oil viscosities. When polymer is present, μ_w is replaced by polymer viscosity (μ_p). The α parameters are determined by matching laboratory viscosity data at several compositions. In the absence of surfactant and polymer, water and oil viscosities reduce to pure water and pure oil viscosities.

4.3.2 Formation Volume Factor

The formation volume factor (B_l), which is the fluid volume at reservoir pressure and temperature divided by its volume at standard conditions, in terms of constituent volume-occupying components is computed as

$$B_l = C_{wl} B_w + C_{ol} B_o + C_{sl} B_s \quad (l = w, o, me) \quad (4-2)$$

where C_{kl} is volumetric concentration of component k in phase l at “*standard conditions*”. Then, C_{wl} , C_{ol} , and C_{sl} are water, oil and surfactant concentrations in phase l at standard conditions. Note that, the solubilized oil and water components have the same formation volume factor as the pure oil and water phases.

4.3.3 Solution Gas Ratio

The solution gas ratio in each liquid phase (R_{sl}) is written as

$$R_{sl} = C_{wl} R_{sw} + C_{ol} R_{so} \quad (l = w, o, me) \quad (4-3)$$

where R_{sw} and R_{so} are the values of the solution gas ratios at reservoir pressure and temperature. The solubilized water and oil components have the same solution gas ratios as the pure oil and water phases.

4.3.4 Density

Liquid density at standard conditions ($\rho_{l_{sc}}$) in terms of its components is written as

$$\rho_{l_{sc}} = \sum_{k=1}^{n_k} C_{kl} \rho_{k_{sc}} \quad (l = w, o, me) \quad (4-4)$$

where $\rho_{k_{sc}}$ is component density at standard conditions, and n_k is the total number of components. Then, the phase density at reservoir conditions is computed as

$$\rho_l = \frac{1}{B_l} (\rho_{l_{sc}} + R_{sl} \rho_{g_{sc}}) \quad (l = w, o, me) \quad (4-5)$$

where $\rho_{g_{sc}}$ is gas density at standard conditions.

4.3.5 Compressibility

The liquid phase compressibility at reservoir conditions is written as a linear combination of constituent components,

$$c_l = \sum \bar{C}_{kl} c_k \quad (l = w, o, me \quad k = w, o, s) \quad (4-6)$$

where c_k is the compressibility of each component k at reservoir conditions. c_k is later defined in Equations (4-51) through (4-54).

For the surfactant phase behavior with plait points located at the corners of ternary diagram, the excess aqueous and oleic phases are essentially pure water and pure oil ($C_{wo} = C_{ow} = 0, C_{ww} = C_{oo} = 1$). Then, the aqueous and oleic phase properties reduce to water and oil properties.

4.4 RELATIVE PERMEABILITY

Four-phase relative permeabilities are modeled using Corey-type functions. The relative permeabilities are assumed to be unique functions of their respective saturations only.

$$k_{rl} = k_{rl}^o (S_{nl})^{n_l} \quad (l = w, o, me, g) \quad (4-7)$$

where normalized saturations are defined as

$$S_{nl} = \frac{S_l - S_{lr}}{1 - \sum_{l=1}^{n_p} S_{lr}} \quad (l = w, o, me, g) \quad (4-8)$$

and k_{rl}^o , n_l , and S_{lr} are the end-point relative permeability, Corey exponent, and residual saturation for phase l , which are a function of the trapping number, and n_p is the number

of phases. The derivation of trapping number for three-dimensional heterogeneous, anisotropic porous media is given by Jin (1995) and Pope *et al.* (2000). The trapping number of phase l is defined as

$$N_{T_l} = \frac{\left| \vec{k} \cdot \vec{\nabla} \Phi_{l'} + \vec{k} \cdot \left[g (\rho_{l'} - \rho_l) \vec{\nabla} D \right] \right|}{\sigma_{ll'}} \quad (l = w, o, me, g) \quad (4-9)$$

where l and l' subscripts stand for the displaced and displacing phases. \vec{k} is permeability tensor, g is gravitational force, ρ is fluid density, σ is interfacial tension, $\vec{\nabla} \Phi$ and $\vec{\nabla} D$ are the gradients of potential and depth, respectively.

The residual saturations, end-points and exponents are computed as a function of trapping number as (Delshad *et al.*, 1986)

$$S_{lr} = \min \left(S_l, S_{lr}^{high} + \frac{S_{lr}^{low} - S_{lr}^{high}}{1 + T_{DCI} N_{T_l}} \right) \quad (l = w, o, me, g) \quad (4-10)$$

$$k_{rl}^o = k_{rl}^{o^{low}} + \frac{S_{l'r}^{low} - S_{l'r}^{high}}{S_{l'r}^{low} - S_{l'r}^{high}} \left(k_{rl}^{o^{high}} - k_{rl}^{o^{low}} \right) \quad (l = w, o, me, g) \quad (4-11)$$

$$n_l = n_l^{low} + \frac{S_{l'r}^{low} - S_{l'r}^{high}}{S_{l'r}^{low} - S_{l'r}^{high}} \left(n_l^{high} - n_l^{low} \right) \quad (l = w, o, me, g) \quad (4-12)$$

where *low* and *high* superscripts stand for the values at low and high trapping numbers, respectively. T_{DCI} is a positive input parameter based on the experimental observation of the relationship between residual saturations and trapping number.

4.5 CAPILLARY PRESSURE

When four phases exist, Corey-type function can be extended to account for presence of microemulsion phase. The direction of descending wettability is assumed to be water, microemulsion, oil, and gas for strongly water-wet conditions. For both three-phase oil/microemulsion/gas (Winsor Type I) or water/microemulsion/ gas (Winsor Type II) the imbibition capillary pressure using Corey-function is

$$P_{c_{me/l}} = C_{pc_i} \frac{\sigma_{me/l}}{\sigma_{w/o}} \sqrt{\frac{\phi}{k}} (1 - S_{nl'})^{e_{pc}} \quad (4-13)$$

where C_{pc_i} and e_{pc} are model parameters, ϕ is porosity, k is permeability, and σ is interfacial tension. For $l = o$, $l' = me$ (Winsor Type I) while $l = w$, $l' = w$ (Winsor Type II). If free gas exists, the capillary pressure between gas and non-wet liquid is calculated as

$$P_{c_{l/g}} = C_{pc_i} \frac{\sigma_{l/g}}{\sigma_{w/o}} \sqrt{\frac{\phi}{k}} \left(\frac{S_{ng}}{1 - S_{nl'}} \right)^{e_{pc}} \quad (4-14)$$

For $l = o$, $l' = me$ (Winsor Type I) while $l = me$, $l' = w$ (Winsor Type II). For four-phase water/microemulsion/oil/gas (Winsor Type III), the capillary pressure between the oil and microemulsion is calculated as

$$P_{c_{me/o}} = C_{pc_i} \frac{\sigma_{me/o}}{\sigma_{w/o}} \sqrt{\frac{\phi}{k}} \left(\frac{S_{no}}{1 - S_{nw}} \right)^{e_{pc}} \quad (4-15)$$

The capillary pressure between water and microemulsion phase is calculated from Equation (4-13) for $l = w$ and $l' = w$. If gas is present, then the capillary pressure between oil and gas is calculated from Equation (4-14) for $l = o$ and $l' = w$. However, for

ultra-low IFT the capillary pressure between microemulsion phase and excess phases of water and oil is typically small and negligible.

4.6 MASS CONSERVATION EQUATION

The general mass conservation equation for component k can be written as

$$-\nabla \cdot \vec{J}_k + q_k = \frac{\partial(\phi \tilde{C}_k \rho_{k_{sc}})}{\partial t} \quad (4-16)$$

J_k is mass flux of component k , and q_k is the sink/source term. \tilde{C}_k is overall volume of component k at “*standard conditions*” per unit pore volume and is the summation over all phases including the adsorbed phases. For components except gas

$$\tilde{C}_k = (1 - \sum_{k=1}^{n_{cv}} \hat{C}_k) \sum_{l=1}^{n_p} \frac{S_l C_{kl}}{B_l} + \hat{C}_k \quad (k \neq g) \quad (4-17)$$

C_{kl} is volumetric concentration of component k in phase l at standard conditions, \hat{C}_k is the adsorbed concentration of species k (surfactant or polymer), and n_{cv} is the total number of volume-occupying components. These components are water, oil, surfactant, and gas.

UTCHEM uses a Langmuir-type isotherm to describe the adsorption of surfactant and polymer which takes into account the salinity, surfactant concentration, and rock permeability (Hirasaki and Pope, 1974). The adsorption is irreversible with concentration and reversible with salinity. The adsorbed concentrations of surfactant and polymer is given by

$$\hat{C}_k = \min \left(\tilde{C}_k, \frac{a_k (\tilde{C}_k - \hat{C}_k)}{1 + b_k (\tilde{C}_k - \hat{C}_k)} \right) \quad (4-18)$$

where

$$a_k = (a_{k_1} + a_{k_2} C_{SE}) \left(\frac{k_{ref}}{k} \right)^{0.5} \quad (4-19)$$

a_{k_1} , a_{k_2} , and b_k are model input parameters, C_{SE} is the effective salinity, and k_{ref} is the permeability at which the input adsorption parameters are specified. The ratio of a_k/b_k represents the maximum level of adsorption.

The effective salinity for surfactant increases with divalent cations bound to micelles (Camilleri *et al.*, 1987a,b,c), and is a function of temperature.

$$C_{SE} = C_{anion/w} \left(1 - \beta_s f_{cation^{++}}^s \right)^{-1} \left[1 + \beta_T (T - T_{ref}) \right]^{-1} \quad (4-20)$$

where $C_{anion/w}$ is total anion concentration in aqueous phase, β_s is a positive constant, $f_{cation^{++}}^s$ is the fraction of total divalent cations bound to surfactant micelles and β_T is the temperature coefficient.

The effective salinity for polymer adsorption (C_{SEP}) is defined as

$$C_{SEP} = \frac{C_{anion/w} + (\beta_p - 1) C_{cation^{++}/w}}{C_{ww}} \quad (4-21)$$

where $C_{anion/w}$, $C_{cation^{++}/w}$ and C_{ww} are the total anion, divalent cations, and water concentrations in the aqueous phase and β_p is measured in the laboratory and is an input parameter to the model.

The overall concentration of gas at standard conditions can be written as the summation of free gas and solution gas.

$$\tilde{C}_g = \tilde{C}_g^f + \tilde{C}_w R_{sw} + \tilde{C}_o R_{so} = \frac{S_g}{B_g} + \left(\sum_{l=1}^{n_p} \frac{S_l C_{wl}}{B_l} \right) R_{sw} + \left(\sum_{l=1}^{n_p} \frac{S_l C_{ol}}{B_l} \right) R_{so} \quad (4-22)$$

where \tilde{C}_g^f is free gas concentration at the standard conditions.

The mass flux of component k in each direction is written as

$$\vec{J}_k = \sum_{l=1}^{n_p} \frac{C_{kl} \rho_{k_{sc}} \vec{u}_l}{B_l} \quad (k \neq g) \quad (4-23)$$

and for the gas component

$$\vec{J}_g = \frac{\rho_{g_{sc}}}{B_g} \vec{u}_g + \left(\sum_{l=1}^{n_p} \frac{C_{ol}}{B_l} \vec{u}_l \right) R_{so} \rho_{g_{sc}} + \left(\sum_{l=1}^{n_p} \frac{C_{wl}}{B_l} \vec{u}_l \right) R_{sw} \rho_{g_{sc}} \quad (4-24)$$

where \vec{v}_l is phase Darcy velocity.

Combining Equations (4-16) through (4-31) and canceling the densities at standard condition mass conservation equation for each component can be written as

$$-\left[\frac{\partial}{\partial x} \left(\sum_{l=1}^{n_p} \frac{C_{kl} u_{xl}}{B_l} \right) + \frac{\partial}{\partial y} \left(\sum_{l=1}^{n_p} \frac{C_{kl} u_{yl}}{B_l} \right) + \frac{\partial}{\partial z} \left(\sum_{l=1}^{n_p} \frac{C_{kl} u_{zl}}{B_l} \right) \right] - \frac{q_k}{\rho_{k_{sc}}} = \frac{\partial(\phi \tilde{C}_k)}{\partial t} \quad (k \neq g) \quad (4-25)$$

and for the gas component,

$$\begin{aligned} & -\frac{\partial}{\partial x} \left(\frac{u_{xg}}{B_g} + \left(\sum_{l=1}^{n_p} \frac{C_{ol}}{B_l} u_{xl} \right) R_{so} + \left(\sum_{l=1}^{n_p} \frac{C_{wl}}{B_l} u_{xl} \right) R_{sw} \right) - \frac{\partial}{\partial y} \left(\frac{u_{yg}}{B_g} + \left(\sum_{l=1}^{n_p} \frac{C_{ol}}{B_l} u_{yl} \right) R_{so} + \left(\sum_{l=1}^{n_p} \frac{C_{wl}}{B_l} u_{yl} \right) R_{sw} \right) \\ & - \frac{\partial}{\partial z} \left(\frac{u_{zg}}{B_g} + \left(\sum_{l=1}^{n_p} \frac{C_{ol}}{B_l} u_{zl} \right) R_{so} + \left(\sum_{l=1}^{n_p} \frac{C_{wl}}{B_l} u_{zl} \right) R_{sw} \right) - \frac{q_g}{\rho_{g_{sc}}} = \frac{\partial(\phi \tilde{C}_k)}{\partial t} \end{aligned} \quad (4-26)$$

Equations (4-25) and (4-26) can be written in a shorter but simpler form as

$$-\nabla \cdot \left(\sum_{l=1}^{n_p} \frac{C_{kl} \vec{u}_l}{B_l} \right) - \frac{q_k}{\rho_{k_{sc}}} = \frac{\partial(\phi \tilde{C}_k)}{\partial t} \quad (k \neq g) \quad (4-27)$$

and for the gas component,

$$-\nabla \cdot \left(\frac{1}{B_g} \vec{u}_g + \left(\sum_{l=1}^{n_p} \frac{C_{ol}}{B_l} \vec{u}_l \right) R_{so} + \left(\sum_{l=1}^{n_p} \frac{C_{wl}}{B_l} \vec{u}_l \right) R_{sw} \right) - \frac{q_g}{\rho_{g_{sc}}} = \frac{\partial(\phi \tilde{C}_g)}{\partial t} \quad (4-28)$$

The Darcy velocity is defined as

$$\vec{u}_l = -\vec{k} \cdot \lambda_l \nabla \Phi_l \quad (4-29)$$

where Φ_l and λ_l are phase potential and phase relative mobility, respectively.

$$\nabla \Phi_l = \nabla P_l - \rho_l \nabla z \quad (4-30)$$

$$\lambda_{rl} = \frac{k_{rl}}{\mu_l} \quad (4-31)$$

Replacing Darcy velocity from Equation (4-29) in Equations (4-27) and (4-28)

gives

$$\nabla \cdot \vec{k} \cdot \left(\sum_{l=1}^{n_p} \frac{C_{kl} \lambda_{rl} \nabla \Phi_l}{B_l} \right) - \frac{q_k}{\rho_{k_{sc}}} = \frac{\partial(\phi \tilde{C}_k)}{\partial t} \quad (k \neq g) \quad (4-32)$$

and for the gas component

$$\nabla \cdot \vec{k} \cdot \left(\frac{\lambda_{rg} \nabla \Phi_g}{B_g} + \left(\sum_{l=1}^{n_p} \frac{C_{ol} \lambda_{rl} \nabla \Phi_l}{B_l} \right) R_{so} + \left(\sum_{l=1}^{n_p} \frac{C_{wl} \lambda_{rl} \nabla \Phi_l}{B_l} \right) R_{sw} \right) - \frac{q_g}{\rho_{g_{sc}}} = \frac{\partial(\phi \tilde{C}_g)}{\partial t} \quad (4-33)$$

Using the capillary pressure, the final form of the mass conservation equation is written as

$$\nabla \cdot \vec{k} \cdot \left(\sum_{l=1}^{n_p} \frac{C_{kl} \lambda_{rl}}{B_l} \right) \nabla P_w + CG_k - \frac{q_k}{\rho_{k_{sc}}} = \frac{\partial(\phi \tilde{C}_k)}{\partial t} \quad (k \neq g) \quad (4-34)$$

and for the gas pseudo component

$$\nabla \cdot \vec{k} \cdot \left(\frac{\lambda_{rg}}{B_g} + \left(\sum_{l=1}^{n_p} \frac{C_{ol} \lambda_{rl}}{B_l} \right) R_{so} + \left(\sum_{l=1}^{n_p} \frac{C_{wl} \lambda_{rl}}{B_l} \right) R_{sw} \right) \nabla P_w + CG_g - \frac{q_g}{\rho_{g_{sc}}} = \frac{\partial(\phi \tilde{C}_g)}{\partial t} \quad (4-35)$$

where CG_k is gravity-capillary contribution term and is defined as

$$CG_k = -\nabla \cdot \vec{k} \cdot \left(\sum_{l=1}^{n_p} \frac{C_{kl} \lambda_{rl}}{B_l} \right) \nabla (\rho_l z - P_{clw}) \quad (k \neq g) \quad (4-36)$$

$$CG_g = -\nabla \cdot \vec{k} \cdot \left[\left(\frac{\lambda_{rg}}{B_g} \right) \nabla (\rho_g z - P_{cgw}) + \left(\sum_{l=1}^{n_p} \frac{C_{ol} \lambda_{rl} \nabla (\rho_l z - P_{clw})}{B_l} \right) R_{so} + \left(\sum_{l=1}^{n_p} \frac{C_{wl} \lambda_{rl} \nabla (\rho_l z - P_{clw})}{B_l} \right) R_{sw} \right] \quad (4-37)$$

Aqueous phase pressure (P_w) is reference pressure and capillary pressure is defined as

$$P_{clw} = P_l - P_w \quad (4-38)$$

From now on, for simplicity we do not use subscript w for aqueous phase pressure. P is the aqueous phase pressure unless otherwise stated.

4.7 PRESSURE EQUATION

The pressure equation is obtained by summing up the mass balance equations for all volume-occupying components (water, oil, surfactant, and gas). Mass conservation

equations are combined so that the pressure will be the only unknown. The pressure equation is written separately for saturated and undersaturated conditions. For saturated gridblocks where pressure is below the bubble point pressure, free gas is in equilibrium with liquid phases. Then, bubble point pressure is known, P and \tilde{C}_k are unknowns. Therefore, the mass conservation equations need to be combined to cancel total concentration derivatives with respect to time. ($\partial\tilde{C}_k / \partial t$, $k = w, o, g, s$)

For undersaturated gridblocks, where the pressure is above the bubble point pressure and free gas does not exist, bubble point pressure is independent of oil pressure and is unknown. Then, the mass conservation equations combine in a way to cancel both total concentration derivatives and bubble point pressure derivative respect to time ($\partial\tilde{C}_k / \partial t$ $k = w, o, g, s$ and $\partial P_b / \partial t$). In next two sections, we will discuss the formulation of pressure equation for saturated and undersaturated phase behavior conditions.

4.7.1 Pressure Equation for Saturated Gridblocks

The mass balance in Equation (4-34) for water, oil, surfactant and Equation (4-35) for gas can be written in short form where L_k is the left hand side of these equations.

$$L_k = \frac{\partial}{\partial t} (\phi \tilde{C}_k) \quad (k = w, o, s) \quad (4-39)$$

$$L_g = \frac{\partial}{\partial t} \left[\phi \left(\tilde{C}_g^f + \tilde{C}_w R_{sw} + \tilde{C}_o R_{so} \right) \right] \quad (4-40)$$

where

$$L_k = \nabla \cdot \vec{k} \cdot \left(\sum_{l=1}^{n_p} \frac{C_{kl} \lambda_{rl}}{B_l} \right) \nabla P + C G_k - \frac{q_k}{\rho_{k_{sc}}} \quad (k = w, o, s) \quad (4-41)$$

$$L_g = \nabla \cdot \vec{k} \cdot \left(\frac{\lambda_{rg}}{B_g} + \left(\sum_{l=1}^{n_p} \frac{C_{ol} \lambda_{rl}}{B_l} \right) R_{so} + \left(\sum_{l=1}^{n_p} \frac{C_{wl} \lambda_{rl}}{B_l} \right) R_{sw} \right) \nabla P + CG_g - \frac{q_g}{\rho_{g_{sc}}} \quad (4-42)$$

Using the chain rule, accumulation term in the right hand side of equations (4-39) and (4-40) is expanded as follows:

$$L_k = \phi \frac{\partial \tilde{C}_k}{\partial t} + \tilde{C}_k \frac{\partial \phi}{\partial P} \frac{\partial P}{\partial t} \quad (k = w, o, s) \quad (4-43)$$

$$L_g = \phi \frac{\partial \tilde{C}_g^f}{\partial t} + \tilde{C}_g^f \frac{\partial \phi}{\partial P} \frac{\partial P}{\partial t} + \phi R_{so} \frac{\partial \tilde{C}_o}{\partial t} + \tilde{C}_o \left(R_{so} \frac{\partial \phi}{\partial P} + \phi \frac{\partial R_{so}}{\partial P} \right) \frac{\partial P}{\partial t} \\ + \phi R_{sw} \frac{\partial \tilde{C}_w}{\partial t} + \tilde{C}_w \left(R_{sw} \frac{\partial \phi}{\partial P} + \phi \frac{\partial R_{sw}}{\partial P} \right) \frac{\partial P}{\partial t} \quad (4-44)$$

From the volume constraint equation, the total concentration of volume occupying components at the reservoir condition is equal to one.

$$\tilde{C}_g^f B_g + \tilde{C}_w B_w + \tilde{C}_o B_o + \tilde{C}_s B_s = 1 \quad (4-45)$$

Surfactant formation volume factor (B_s) is defined as

$$B_s = 1 - c_s (P - P_{sc}) \quad (4-46)$$

where c_s is surfactant compressibility and P_{sc} is pressure at standard condition.

Therefore, the free gas concentration can be written as

$$\tilde{C}_g^f = \frac{1}{B_g} - \frac{\tilde{C}_o B_o}{B_g} - \frac{\tilde{C}_w B_w}{B_g} - \frac{\tilde{C}_s B_s}{B_g} \quad (4-47)$$

and

$$\begin{aligned}
\frac{\partial \tilde{C}_g^f}{\partial t} &= -\frac{1}{B_g^2} \frac{\partial B_g}{\partial t} - \frac{B_o}{B_g} \frac{\partial \tilde{C}_o}{\partial t} - \left(\frac{\tilde{C}_o}{B_g} \frac{\partial B_o}{\partial P} - \frac{\tilde{C}_o B_o}{B_g^2} \frac{\partial B_g}{\partial P} \right) \frac{\partial P}{\partial t} \\
&- \frac{B_w}{B_g} \frac{\partial \tilde{C}_w}{\partial t} - \left(\frac{\tilde{C}_w}{B_g} \frac{\partial B_w}{\partial P} - \frac{\tilde{C}_w B_w}{B_g^2} \frac{\partial B_g}{\partial P} \right) \frac{\partial P}{\partial t} \\
&- \frac{B_s}{B_g} \frac{\partial \tilde{C}_s}{\partial t} - \left(\frac{\tilde{C}_s}{B_g} \frac{\partial B_s}{\partial P} - \frac{\tilde{C}_s B_s}{B_g^2} \frac{\partial B_g}{\partial P} \right) \frac{\partial P}{\partial t}
\end{aligned} \tag{4-48}$$

Substituting $(\partial \tilde{C}_g^f / \partial t)$ from Equation (4-48) in Equation (4-44) and rearrangements give

$$\begin{aligned}
L_g &= -\frac{\phi}{B_g^2} \frac{\partial B_g}{\partial t} + \tilde{C}_g^f \frac{\partial \phi}{\partial P} \frac{\partial P}{\partial t} + \left(\phi R_{so} - \frac{\phi B_o}{B_g} \right) \frac{\partial \tilde{C}_o}{\partial t} + \left(\phi R_{sw} - \frac{\phi B_w}{B_g} \right) \frac{\partial \tilde{C}_w}{\partial t} - \frac{\phi B_s}{B_g} \frac{\partial \tilde{C}_s}{\partial t} \\
&+ \left(-\frac{\phi \tilde{C}_o}{B_g} \frac{\partial B_o}{\partial P} + \frac{\phi \tilde{C}_o B_o}{B_g^2} \frac{\partial B_g}{\partial P} - \frac{\phi \tilde{C}_w}{B_g} \frac{\partial B_w}{\partial P} + \frac{\phi \tilde{C}_w B_w}{B_g^2} \frac{\partial B_g}{\partial P} \right. \\
&\left. - \frac{\phi \tilde{C}_s}{B_g} \frac{\partial B_s}{\partial P} + \frac{\phi \tilde{C}_s B_s}{B_g^2} \frac{\partial B_g}{\partial P} + \tilde{C}_o R_{so} \frac{\partial \phi}{\partial P} + \tilde{C}_o \phi \frac{\partial R_{so}}{\partial P} + \tilde{C}_w R_{sw} \frac{\partial \phi}{\partial P} + \tilde{C}_w \phi \frac{\partial R_{sw}}{\partial P} \right) \frac{\partial P}{\partial t}
\end{aligned} \tag{4-49}$$

Equation (4-43) for water, oil and surfactant and Equation (4-49) for gas are multiplied by $(B_w - R_{sw} B_g)$, $(B_o - R_{so} B_g)$, B_s and B_g , respectively and then are added to cancel the terms containing saturation derivatives respect to time. The remaining results is

$$\begin{aligned}
&(B_w - R_{sw} B_g) L_w + (B_o - R_{so} B_g) L_o + B_s L_s + B_g L_g = \\
&\phi \left[\frac{1}{\phi} \frac{\partial \phi}{\partial t} + \tilde{C}_w B_w \left(-\frac{1}{B_w} \frac{\partial B_w}{\partial P} + \frac{B_g}{B_w} \frac{\partial R_{sw}}{\partial P} \right) + \tilde{C}_o B_o \left(-\frac{1}{B_o} \frac{\partial B_o}{\partial P} + \frac{B_g}{B_o} \frac{\partial R_{so}}{\partial P} \right) \right. \\
&\left. + \tilde{C}_s B_s \left(-\frac{1}{B_s} \frac{\partial B_s}{\partial P} \right) + \tilde{C}_g^f B_g \left(-\frac{1}{B_g} \frac{\partial B_g}{\partial P} \right) \right] \frac{\partial P}{\partial t}
\end{aligned} \tag{4-50}$$

Water, oil, surfactant, gas and rock compressibilities are introduced as follow:

$$c_w = -\frac{1}{B_w} \frac{\partial B_w}{\partial P} + \frac{B_g}{B_w} \frac{\partial R_{sw}}{\partial P} \quad (4-51)$$

$$c_o = -\frac{1}{B_o} \frac{\partial B_o}{\partial P} + \frac{B_g}{B_o} \frac{\partial R_{so}}{\partial P} \quad (4-52)$$

$$c_s = -\frac{1}{B_s} \frac{\partial B_s}{\partial P} \quad (4-53)$$

$$c_g = -\frac{1}{B_g} \frac{\partial B_g}{\partial P} \quad (4-54)$$

$$c_r = \frac{1}{\phi} \frac{\partial \phi}{\partial P} \quad (4-55)$$

Therefore, the total compressibility is defined as

$$c_t = c_r + (\tilde{C}_g^f B_g) c_g + (\tilde{C}_o B_o) c_o + (\tilde{C}_w B_w) c_w + (\tilde{C}_s B_s) c_s \quad (4-56)$$

Combining Equations (4-41), (4-42), and (4-50) through (4-56) the final form of the pressure equation for saturated conditions is

$$\begin{aligned} & (B_w - R_{sw} B_g) \left[\nabla \cdot \vec{k} \cdot \left(\sum_{l=1}^{n_p} \frac{C_{wl} \lambda_{rl}}{B_l} \right) \nabla P + CG_w - \frac{q_w}{\rho_{w_{sc}}} \right] + \\ & (B_o - R_{so} B_g) \left[\nabla \cdot \vec{k} \cdot \left(\sum_{l=1}^{n_p} \frac{C_{ol} \lambda_{rl}}{B_l} \right) \nabla P + CG_o - \frac{q_o}{\rho_{o_{sc}}} \right] + \\ & B_s \left[\nabla \cdot \vec{k} \cdot \left(\sum_{l=1}^{n_p} \frac{C_{sl} \lambda_{rl}}{B_l} \right) \nabla P + CG_s - \frac{q_s}{\rho_{s_{sc}}} \right] + \\ & B_g \left[\nabla \cdot \vec{k} \cdot \left(\frac{\lambda_{rg}}{B_g} + \left(\sum_{l=1}^{n_p} \frac{C_{ol} \lambda_{rl}}{B_l} \right) R_{so} + \left(\sum_{l=1}^{n_p} \frac{C_{wl} \lambda_{rl}}{B_l} \right) R_{sw} \right) \nabla P + CG_g - \frac{q_g}{\rho_{g_{sc}}} \right] = \phi c_t \frac{\partial P}{\partial t} \end{aligned} \quad (4-57)$$

4.7.2 Pressure Equation for Undersaturated Gridblocks

For undersaturated gridblocks, when pressure is above the bubble point pressure, the free gas concentration is zero ($\tilde{C}_g^f = 0$), and gas exists only as solution gas in the oil, water and microemulsion phases. The total gas concentration is

$$\tilde{C}_g = \tilde{C}_w R_{sw} + \tilde{C}_o R_{so} \quad (4-58)$$

For gridblocks with undersaturated conditions, oil formation volume factor and oil solution gas ratio are functions of bubble point pressure.

$$B_o = B_o(P, P_{bp}) \quad (4-59)$$

$$R_{so} = R_{so}(P_{bp}) \quad (4-60)$$

Then, the right hand sides of Equations (4-39) and (4-40) are expanded as

$$L_k = \phi \frac{\partial \tilde{C}_k}{\partial t} + \tilde{C}_k \frac{\partial \phi}{\partial P} \frac{\partial P}{\partial t} \quad (k = w, o, s) \quad (4-61)$$

$$\begin{aligned} L_g = & \phi R_{so} \frac{\partial \tilde{C}_o}{\partial t} + \tilde{C}_o R_{so} \frac{\partial \phi}{\partial P} \frac{\partial P}{\partial t} + \tilde{C}_o \phi \frac{\partial R_{so}}{\partial P_b} \frac{\partial P_b}{\partial t} \\ & + \phi R_{sw} \frac{\partial \tilde{C}_w}{\partial t} + \tilde{C}_w \left(R_{sw} \frac{\partial \phi}{\partial P} + \phi \frac{\partial R_{sw}}{\partial P} \right) \frac{\partial P}{\partial t} \end{aligned} \quad (4-62)$$

The volume constraint equation is used to remove $\partial \tilde{C}_o / \partial t$ from Equation (4-61) and (4-62). From the volume constraint equation,

$$\tilde{C}_o = \frac{1}{B_o} - \frac{\tilde{C}_w B_w}{B_o} - \frac{\tilde{C}_s B_s}{B_o} \quad (4-63)$$

therefore

$$\begin{aligned} \frac{\partial \tilde{C}_o}{\partial t} = & -\frac{B_w}{B_o} \frac{\partial \tilde{C}_w}{\partial t} - \frac{B_s}{B_o} \frac{\partial \tilde{C}_s}{\partial t} + \left[-\frac{\tilde{C}_w}{B_o} \frac{\partial B_w}{\partial P} - \frac{\tilde{C}_s}{B_o} \frac{\partial B_s}{\partial P} - \frac{\tilde{C}_o B_o}{B_o^2} \frac{\partial B_o}{\partial P} \right] \frac{\partial P}{\partial t} \\ & - \frac{\tilde{C}_o B_o}{B_o^2} \frac{\partial B_o}{\partial P_b} \frac{\partial P_b}{\partial t} \end{aligned} \quad (4-64)$$

Substituting (4-64) in Equations (4-61) for oil component and (4-62) gives

$$L_o = -\frac{\phi B_w}{B_o} \frac{\partial \tilde{C}_w}{\partial t} - \frac{\phi B_s}{B_o} \frac{\partial \tilde{C}_s}{\partial t} + \left[-\frac{\phi \tilde{C}_w}{B_o} \frac{\partial B_w}{\partial P} - \frac{\phi \tilde{C}_s}{B_o} \frac{\partial B_s}{\partial P} - \frac{\phi \tilde{C}_o B_o}{B_o^2} \frac{\partial B_o}{\partial P} \right] \frac{\partial P}{\partial t} - \frac{\phi \tilde{C}_o B_o}{B_o^2} \frac{\partial B_o}{\partial P_b} \frac{\partial P_b}{\partial t} + \tilde{C}_o \frac{\partial \phi}{\partial P} \frac{\partial P}{\partial t} \quad (4-65)$$

$$L_g = -\frac{\phi R_{so} B_w}{B_o} \frac{\partial \tilde{C}_w}{\partial t} - \frac{\phi R_{so} B_s}{B_o} \frac{\partial \tilde{C}_s}{\partial t} + \left[-\frac{\phi R_{so} \tilde{C}_w}{B_o} \frac{\partial B_w}{\partial P} - \frac{\phi R_{so} \tilde{C}_s}{B_o} \frac{\partial B_s}{\partial P} - \frac{\phi R_{so} \tilde{C}_o B_o}{B_o^2} \frac{\partial B_o}{\partial P} \right] \frac{\partial P}{\partial t} + \tilde{C}_o R_{so} \frac{\partial \phi}{\partial P} \frac{\partial P}{\partial t} + \tilde{C}_o B_o \phi \left(\frac{1}{B_o} \frac{\partial R_{so}}{\partial P_b} - \frac{R_{so}}{B_o^2} \frac{\partial B_o}{\partial P_b} \right) \frac{\partial P_b}{\partial t} + \phi R_{sw} \frac{\partial \tilde{C}_w}{\partial t} + \tilde{C}_w \left[R_{sw} \frac{\partial \phi}{\partial P} + \phi \frac{\partial R_{sw}}{\partial P} \right] \frac{\partial P}{\partial t} \quad (4-66)$$

Coefficients C_1 , C_2 and C_3 are defined as

$$C_1 = \frac{\frac{1}{B_o^2} \frac{\partial B_o}{\partial P_b}}{\frac{1}{B_o} \frac{\partial R_{so}}{\partial P_b} - \frac{R_{so}}{B_o^2} \frac{\partial B_o}{\partial P_b}} \quad (4-67)$$

$$C_2 = C_1 \frac{B_w R_{so}}{B_o} - C_1 R_{sw} + \frac{B_w}{B_o} \quad (4-68)$$

$$C_3 = C_1 \frac{B_s R_{so}}{B_o} + \frac{B_s}{B_o} \quad (4-69)$$

Equation (4-43) for water, Equation (4-65) for oil, Equation (4-43) for surfactant, and Equation (4-66) for gas are multiplied by C_2 , one, C_3 , and C_1 , respectively and then

added together to remove all the terms containing concentration and bubble point pressure derivatives with respect to time. The remaining results is

$$\begin{aligned}
& C_2 L_w + L_o + C_3 L_s + C_1 L_g = \\
& \phi \left[\tilde{C}_w B_w \left(\left(\frac{C_2}{B_w} + \frac{C_1 R_{sw}}{B_w} \right) \frac{1}{\phi} \frac{\partial \phi}{\partial P} - \left(\frac{1}{B_o} + \frac{C_1 R_{so}}{B_o} \right) \frac{1}{B_w} \frac{\partial B_w}{\partial P} + \frac{C_1}{B_w} \frac{\partial R_{sw}}{\partial P} \right) \right. \\
& + \tilde{C}_o B_o \left(\left(\frac{1}{B_o} + \frac{C_1 R_{so}}{B_o} \right) \frac{1}{\phi} \frac{\partial \phi}{\partial P} - \left(\frac{1}{B_o} + \frac{C_1 R_{so}}{B_o} \right) \frac{1}{B_o} \frac{\partial B_o}{\partial P} \right) \\
& \left. + \tilde{C}_s B_s \left(\left(\frac{C_1 R_{so}}{B_o} + \frac{1}{B_o} \right) \frac{1}{\phi} \frac{\partial \phi}{\partial P} - \left(\frac{C_1 R_{so}}{B_o} + \frac{1}{B_o} \right) \frac{1}{B_s} \frac{\partial B_s}{\partial P} \right) \right] \frac{\partial P}{\partial t}
\end{aligned} \tag{4-70}$$

From Equation (4-68)

$$\frac{C_2}{B_w} + \frac{C_1 R_{sw}}{B_w} = \frac{1}{B_o} + \frac{C_1 R_{so}}{B_o} \tag{4-71}$$

The remaining result is

$$C_2 L_w + L_o + C_3 L_s + C_1 L_g = \left(\frac{1}{B_o} + \frac{C_1 R_{so}}{B_o} \right) \phi c_t \frac{\partial P}{\partial t} \tag{4-72}$$

where c_t is total compressibility and defined as

$$c_t = c_r + (\tilde{C}_w B_w) c_w + (\tilde{C}_o B_o) c_o + (\tilde{C}_s B_s) c_s \tag{4-73}$$

and $\partial R_{sw} / \partial P$ was assumed to be negligible.

Combining Equations (4-41), (4-42), and (4-70) through (4-73) the final form of pressure equation for undersaturated reservoir can be written as

$$\begin{aligned}
& C_2 \left[\nabla \cdot \vec{k} \cdot \left(\sum_{l=1}^{n_p} \frac{C_{wl} \lambda_{rl}}{B_l} \right) \nabla P + CG_w - \frac{q_w}{\rho_{w_{sc}}} \right] + \\
& \left[\nabla \cdot \vec{k} \cdot \left(\sum_{l=1}^{n_p} \frac{C_{ol} \lambda_{rl}}{B_l} \right) \nabla P + CG_o - \frac{q_o}{\rho_{o_{sc}}} \right] + \\
& C_3 \left[\nabla \cdot \vec{k} \cdot \left(\sum_{l=1}^{n_p} \frac{C_{sl} \lambda_{rl}}{B_l} \right) \nabla P + CG_s - \frac{q_s}{\rho_{s_{sc}}} \right] + \\
& C_1 \left[\nabla \cdot \vec{k} \cdot \left(\frac{\lambda_{rg}}{B_g} + \left(\sum_{l=1}^{n_p} \frac{C_{ol} \lambda_{rl}}{B_l} \right) R_{so} + \left(\sum_{l=1}^{n_p} \frac{C_{wl} \lambda_{rl}}{B_l} \right) R_{sw} \right) \nabla P + CG_g - \frac{q_g}{\rho_{g_{sc}}} \right] \\
& = \left(\frac{1}{B_o} + \frac{C_1 R_{so}}{B_o} \right) \phi_{c_t} \frac{\partial P}{\partial t}
\end{aligned} \tag{4-74}$$

4.8 FINITE DIFFERENCE EQUATION FOR MASS CONSERVATION

Using the transmissibility definition (see Equation (3-81)), and linear difference operators (see Equations (3-86) through (3-88)) Equations (4-34) and (4-35) in terms of transmissibility can be written as

$$\sum_{l=1}^{n_p} \Delta (C_{kl} T_l)^n \Delta P^{n+1} + CG_k - \frac{q_k V_B}{\rho_{k_{sc}}} = \frac{V_B}{\Delta t} \Delta_t (\phi \tilde{C}_k) \quad (k \neq g) \tag{4-75}$$

and for the gas component

$$\begin{aligned}
& \Delta T_g^n \Delta P^{n+1} + \sum_{l=1}^{n_p} \Delta (R_{so} C_{ol} T_l)^n \Delta P^{n+1} + \sum_{l=1}^{n_p} \Delta (R_{sw} C_{wl} T_l)^n \Delta P^{n+1} + CG_g - \frac{q_g V_B}{\rho_{g_{sc}}} \\
& = \frac{V_B}{\Delta t} \Delta_t (\phi \tilde{C}_g)
\end{aligned} \tag{4-76}$$

where V_B is grid volume ($V_B = \Delta x \cdot \Delta y \cdot \Delta z$). Superscripts n and $n+1$ represent the old and new time step, respectively. The capillary-gravity contributions in terms of transmissibility can be written as

$$CG_k = - \sum_{l=1}^{n_p} \Delta (C_{kl} T_l)^n \Delta (\rho_l z - P_{clw})^n \quad (k \neq g) \quad (4-77)$$

and for the gas component

$$CG_g = - \left(\Delta T_g^n \Delta (\rho_g z - P_{cgw})^n + \sum_{l=1}^{n_p} \Delta (R_{so} C_{ol} T_l)^n \Delta (\rho_l z - P_{clw})^n + \sum_{l=1}^{n_p} \Delta (R_{sw} C_{wl} T_l)^n \Delta (\rho_l z - P_{clw})^n \right) \quad (4-78)$$

The source/sink term can be written as

$$\frac{q_k V_B}{\rho_{k_{sc}}} = \sum_{l=1}^{n_p} Q_{l_{sc}} C_{kl_{well}} \quad (k \neq g) \quad (4-79)$$

and for the gas component

$$\frac{q_g V_B}{\rho_{g_{sc}}} = Q_{g_{sc}} + \sum_{l=1}^{n_p} Q_{l_{sc}} C_{ol_{well}} R_{so} + \sum_{l=1}^{n_p} Q_{l_{sc}} C_{wl_{well}} R_{sw} \quad (4-80)$$

where $Q_{l_{sc}}$ is volumetric injection/production rate of phase l at standard conditions, and $C_{kl_{well}}$ is the concentration of component k in injection/production phase l at standard condition.

Equation (4-75) can be written in short form where L_k is the left hand side of this equation.

$$L_k = \frac{V_B}{\Delta t} \Delta_t (\phi \tilde{C}_k) \quad (k \neq g) \quad (4-81)$$

Assuming the change in pore volume due to surfactant adsorption is negligible, the overall standard concentration of non-adsorbing components can be written as

$$\tilde{C}_k = \sum_{l=1}^{n_p} \frac{S_l C_{kl}}{B_l} \quad (4-82)$$

Substituting Equation (4-82) into (4-81) gives

$$L_k = \frac{V_B}{\Delta t} \Delta_t \left(\phi \sum_{l=1}^{n_p} \frac{S_l C_{kl}}{B_l} \right) = \frac{V_B}{\Delta t} \sum_{l=1}^{n_p} \Delta_t \left(\phi \frac{S_l C_{kl}}{B_l} \right) \quad (k \neq g) \quad (4-83)$$

Using the mixing rule Equation (4-83) is written as

$$L_k = \frac{V_B}{\Delta t} \sum_{l=1}^{n_p} \left[\left(\frac{\phi}{B_l} \right)^{n+1} \Delta_t (C_{kl} S_l) + (C_{kl} S_l)^n \Delta_t \left(\frac{\phi}{B_l} \right) \right] \quad (k \neq g) \quad (4-84)$$

Writing the mixing rule for $\Delta_t (\phi/B_l)$ term gives

$$L_k = \frac{V_B}{\Delta t} \sum_{l=1}^{n_p} \left[\left(\frac{\phi}{B_l} \right)^{n+1} \Delta_t (C_{kl} S_l) + (C_{kl} S_l)^n \left(\phi^{n+1} \Delta_t \left(\frac{1}{B_l} \right) + \left(\frac{1}{B_l} \right)^n \Delta_t \phi \right) \right] \quad (k \neq g) \quad (4-85)$$

Writing the equation in terms of pressure and some arrangement gives

$$\begin{aligned} \frac{L_k \Delta t}{V_B} &= \phi^{n+1} \sum_{l=1}^{n_p} \left(\frac{S_l C_{kl}}{B_l} \right)^{n+1} - \phi^{n+1} \sum_{l=1}^{n_p} \frac{(C_{kl} S_l)^n}{B_l^{n+1}} \\ &+ \sum_{l=1}^{n_p} (C_{kl} S_l)^n \left(\phi^{n+1} \frac{d}{dP} \left(\frac{1}{B_l} \right) + \left(\frac{1}{B_l} \right)^n \frac{d\phi}{dP} \right) (P^{n+1} - P^n) \quad (k \neq g) \end{aligned} \quad (4-86)$$

The total concentration of non-adsorbing components k except gas at the new time step can be computed as

$$\tilde{C}_k^{n+1} = \frac{L_k \Delta t}{\phi^{n+1} V_B} - \sum_{l=1}^{n_p} (C_{kl} S_l)^n \left[-\frac{1}{B_l^{n+1}} + \left(-\frac{1}{(B_l^{n+1})^2} \left(\frac{dB_l}{dP} \right)^{n+1} + \left(\frac{1}{B_l} \right)^n \frac{1}{\phi^{n+1}} \frac{d\phi}{dP} \right) (P^{n+1} - P^n) \right] \quad (k \neq g) \quad (4-87)$$

For adsorbing components (surfactant, polymer or electrolyte) the right hand side of Equation (4-81) is expanded as follow:

$$L_k = \frac{V_B}{\Delta t} \left[\phi^{n+1} (\tilde{C}_k^{n+1} - \tilde{C}_k^n) + \tilde{C}_k^n \frac{d\phi}{dP} (P^{n+1} - P^n) \right] \quad (4-88)$$

Then the total concentration at new time step can be computed as

$$\tilde{C}_k^{n+1} = \frac{L_k \Delta t}{\phi^{n+1} V_B} + \tilde{C}_k^n \left[1 - \frac{1}{\phi^{n+1}} \frac{d\phi}{dP} (P^{n+1} - P^n) \right] \quad (4-89)$$

or

$$\tilde{C}_k^{n+1} = \frac{L_k \Delta t}{\phi^{n+1} V_B} + \tilde{C}_k^n \left[1 - c_r (P^{n+1} - P^n) \right] \quad (4-90)$$

where c_r is rock compressibility.

For saturated gridblocks, Equation (4-87) is solved for water and oil. Equation (4-90) is solved for surfactant, polymer and electrolyte. Then the free gas concentration is calculated from volume constraint Equation (4-47). For undersaturated gridblocks, Equation (4-87) is only solved for water. The oil concentration is calculated from equation (4-63).

4.9 FINITE DIFFERENCE FORM OF PRESSURE EQUATION FOR SATURATED GRIDBLOCKS

Pressure equation for saturated gridblocks (Equation (4-57)) in terms of transmissibility can be written as

$$\begin{aligned}
& (B_o^n - B_g^n R_{so}^n) \sum_{l=1}^{n_p} \Delta(C_{ol} T_l)^n \Delta P^{n+1} + (B_w^n - B_g^n R_{sw}^n) \sum_{l=1}^{n_p} \Delta(C_{wl} T_l)^n \Delta P^{n+1} \\
& + B_s^n \sum_{l=1}^{n_p} \Delta(C_{sl} T_l)^n \Delta P^{n+1} + B_g^n \left(\Delta T_g^n + \sum_{l=1}^{n_p} \Delta(R_{so} C_{ol} T_l)^n + \sum_{l=1}^{n_p} \Delta(R_{sw} C_{wl} T_l)^n \right) \Delta P^{n+1} \quad (4-91) \\
& + Q_{WOGS} = \frac{V_B \phi c_t}{\Delta t} (P^{n+1} - P^n)
\end{aligned}$$

where Q_{WOGS} is defined to simplify the notation in pressure equation as

$$\begin{aligned}
Q_{WOGS} &= (B_o^n - B_g^n R_{so}^n) \left(CG_o - \frac{q_o V_B}{\rho_{o_{sc}}} \right)^n + (B_w^n - B_g^n R_{sw}^n) \left(CG_w - \frac{q_w V_B}{\rho_{w_{sc}}} \right)^n \\
& + B_s^n \left(CG_s - \frac{q_s V_B}{\rho_{s_{sc}}} \right)^n + B_g^n \left(CG_g - \frac{q_g V_B}{\rho_{g_{sc}}} \right)^n \quad (4-92)
\end{aligned}$$

The pressure equation for gridblock i is written as

$$AT_k P_{k-1}^{n+1} + AN_j P_{j-1}^{n+1} + AW_i P_{i-1}^{n+1} + AC_i P_i^{n+1} + AE_i P_{i+1}^{n+1} + AS_j P_{j+1}^{n+1} + AB_k P_{k+1}^{n+1} = B_i \quad (4-93)$$

where AT_k , AN_j , AW_i , AC_i , AE_i , AS_j , AB_k and B_i are all known values. Writing for all the gridblocks, pressure equation can be stated using matrix format as follows:

$$AP^{n+1} = B \quad (4-94)$$

where A is the matrix of coefficient, P is pressure vector at time $n+1$, and B is a known given vector. All the coefficients of the pressure at time $n+1$ are all known and are defined as below:

$$\begin{aligned}
AE_i &= \left(B_{o_i} + B_{g_i} (R_{so_{i+1/2}} - R_{so_i}) \right) \left(\sum_{l=1}^{n_p} C_{ol} T_{x_l} \right)_{i+1/2} + \left(B_{w_i} + B_{g_i} (R_{sw_{i+1/2}} - R_{sw_i}) \right) \left(\sum_{l=1}^{n_p} C_{wl} T_{x_l} \right)_{i+1/2} \\
&+ B_{s_i} \left(\sum_{l=1}^{n_p} C_{sl} T_{x_l} \right)_{i+1/2} + B_{g_i} T_{x_{g_{i+1/2}}}
\end{aligned} \tag{4-95}$$

$$\begin{aligned}
AW_i &= \left(B_{o_i} + B_{g_i} (R_{so_{i-1/2}} - R_{so_i}) \right) \left(\sum_{l=1}^{n_p} C_{ol} T_{x_l} \right)_{i-1/2} + \left(B_{w_i} + B_{g_i} (R_{sw_{i-1/2}} - R_{sw_i}) \right) \left(\sum_{l=1}^{n_p} C_{wl} T_{x_l} \right)_{i-1/2} \\
&+ B_{s_i} \left(\sum_{l=1}^{n_p} C_{sl} T_{x_l} \right)_{i-1/2} + B_{g_i} T_{x_{g_{i-1/2}}}
\end{aligned} \tag{4-96}$$

$$\begin{aligned}
AS_j &= \left(B_{o_j} + B_{g_j} (R_{so_{j+1/2}} - R_{so_j}) \right) \left(\sum_{l=1}^{n_p} C_{ol} T_{y_l} \right)_{j+1/2} + \left(B_{w_j} + B_{g_j} (R_{sw_{j+1/2}} - R_{sw_j}) \right) \left(\sum_{l=1}^{n_p} C_{wl} T_{y_l} \right)_{j+1/2} \\
&+ B_{s_j} \left(\sum_{l=1}^{n_p} C_{sl} T_{y_l} \right)_{j+1/2} + B_{g_j} T_{y_{g_{j+1/2}}}
\end{aligned} \tag{4-97}$$

$$\begin{aligned}
AN_j &= \left(B_{o_j} + B_{g_j} (R_{so_{j-1/2}} - R_{so_j}) \right) \left(\sum_{l=1}^{n_p} C_{ol} T_{y_l} \right)_{j-1/2} + \left(B_{w_j} + B_{g_j} (R_{sw_{j-1/2}} - R_{sw_j}) \right) \left(\sum_{l=1}^{n_p} C_{wl} T_{y_l} \right)_{j-1/2} \\
&+ B_{s_j} \left(\sum_{l=1}^{n_p} C_{sl} T_{y_l} \right)_{j-1/2} + B_{g_j} T_{y_{g_{j-1/2}}}
\end{aligned} \tag{4-98}$$

$$\begin{aligned}
AB_k &= \left(B_{o_k} + B_{g_k} (R_{so_{k+1/2}} - R_{so_k}) \right) \left(\sum_{l=1}^{n_p} C_{ol} T_{z_l} \right)_{k+1/2} + \left(B_{w_k} + B_{g_k} (R_{sw_{k+1/2}} - R_{sw_k}) \right) \left(\sum_{l=1}^{n_p} C_{wl} T_{z_l} \right)_{k+1/2} \\
&+ B_{s_k} \left(\sum_{l=1}^{n_p} C_{sl} T_{z_l} \right)_{k+1/2} + B_{g_k} T_{z_{g_{k+1/2}}}
\end{aligned} \tag{4-99}$$

$$\begin{aligned}
AT_k = & \left(B_{o_k} + B_{g_k} (R_{so_{k-1/2}} - R_{so_k}) \right) \left(\sum_{l=1}^{n_p} C_{ol} T_{z_l} \right)_{k-1/2} + \left(B_{w_k} + B_{g_k} (R_{sw_{k-1/2}} - R_{sw_k}) \right) \left(\sum_{l=1}^{n_p} C_{wl} T_{z_l} \right)_{k-1/2} \\
& + B_{s_k} \left(\sum_{l=1}^{n_p} C_{sl} T_{z_l} \right)_{k-1/2} + B_{g_k} T_{z_{g_{k-1/2}}}
\end{aligned} \tag{4-100}$$

$$AC_i = - \left[AT_k + AS_j + AE_i + AW_i + AN_j + AB_k + \frac{V_B \phi^n c_t^n}{\Delta t} \right] \tag{4-101}$$

$$B_i = - \left(Q_{WOGS} + \frac{V_B \phi^n c_t^n P^n}{\Delta t} \right) \tag{4-102}$$

4.10 FINITE DIFFERENCE FORM OF PRESSURE EQUATION FOR UNDERSATURATED GRIDBLOCKS

Pressure equation for undersaturated gridblocks (Equation (4-74)) in terms of transmissibility can be written as

$$\begin{aligned}
& \sum_{l=1}^{n_p} \Delta (C_{ol} T_l)^n \Delta P^{n+1} + C_2 \sum_{l=1}^{n_p} \Delta (C_{wl} T_l)^n \Delta P^{n+1} + C_3 \sum_{l=1}^{n_p} \Delta (C_{sl} T_l)^n \Delta P^{n+1} \\
& + C_1 \left(\Delta T_g^n + \sum_{l=1}^{n_p} \Delta (R_{so} C_{ol} T_l)^n + \sum_{l=1}^{n_p} \Delta (R_{sw} C_{wl} T_l)^n \right) \Delta P^{n+1} \\
& + Q'_{WOGS} = \frac{V_B \phi^n c_t^n}{\Delta t} \left(\frac{1}{B_o} + \frac{C_1 R_{so}}{B_o} \right)^n (P^{n+1} - P^n)
\end{aligned} \tag{4-103}$$

where

$$\begin{aligned}
Q'_{WOGS} &= \left(CG_o - \frac{q_o V_B}{\rho_{o_{sc}}} \right)^n + C_2 \left(CG_w - \frac{q_w V_B}{\rho_{w_{sc}}} \right)^n + C_3 \left(CG_s - \frac{q_s V_B}{\rho_{s_{sc}}} \right)^n \\
&+ C_1 \left(CG_g - \frac{q_g V_B}{\rho_{g_{sc}}} \right)^n
\end{aligned} \tag{4-104}$$

The general form of pressure equation in matrix format is the same as saturated gridblocks

$$A'P^{n+1} = B' \tag{4-105}$$

The pressure coefficients and given vector B' for undersaturated gridblocks are defined as below (all the coefficients are calculated at time step n):

$$\begin{aligned}
AE'_i &= \left(1 + C_1 R_{so_{i+1/2}} \right) \left(\sum_{l=1}^{n_p} C_{ol} T_{x_l} \right)_{i+1/2} + \left(C_2 + C_1 R_{sw_{i+1/2}} \right) \left(\sum_{l=1}^{n_p} C_{wl} T_{x_l} \right)_{i+1/2} \\
&+ C_3 \left(\sum_{l=1}^{n_p} C_{sl} T_{x_l} \right)_{i+1/2} + C_1 T_{x_g_{i+1/2}}
\end{aligned} \tag{4-106}$$

$$\begin{aligned}
AW'_i &= \left(1 + C_1 R_{so_{i-1/2}} \right) \left(\sum_{l=1}^{n_p} C_{ol} T_{x_l} \right)_{i-1/2} + \left(C_2 + C_1 R_{sw_{i-1/2}} \right) \left(\sum_{l=1}^{n_p} C_{wl} T_{x_l} \right)_{i-1/2} \\
&+ C_3 \left(\sum_{l=1}^{n_p} C_{sl} T_{x_l} \right)_{i-1/2} + C_1 T_{x_g_{i-1/2}}
\end{aligned} \tag{4-107}$$

$$\begin{aligned}
AS'_j &= \left(1 + C_1 R_{so_{j+1/2}} \right) \left(\sum_{l=1}^{n_p} C_{ol} T_{y_l} \right)_{j+1/2} + \left(C_2 + C_1 R_{sw_{j+1/2}} \right) \left(\sum_{l=1}^{n_p} C_{wl} T_{y_l} \right)_{j+1/2} \\
&+ C_3 \left(\sum_{l=1}^{n_p} C_{sl} T_{y_l} \right)_{j+1/2} + C_1 T_{y_g_{j+1/2}}
\end{aligned} \tag{4-108}$$

$$\begin{aligned}
AN'_j &= \left(1 + C_1 R_{so_{j-1/2}}\right) \left(\sum_{l=1}^{n_p} C_{ol} T_{y_l} \right)_{j-1/2} + \left(C_2 + C_1 R_{sw_{j-1/2}}\right) \left(\sum_{l=1}^{n_p} C_{wl} T_{y_l} \right)_{j-1/2} \\
&+ C_3 \left(\sum_{l=1}^{n_p} C_{sl} T_{y_l} \right)_{j-1/2} + C_1 T_{y_{g_{j-1/2}}}
\end{aligned} \tag{4-109}$$

$$\begin{aligned}
AB'_k &= \left(1 + C_1 R_{so_{k+1/2}}\right) \left(\sum_{l=1}^{n_p} C_{ol} T_{z_l} \right)_{k+1/2} + \left(C_2 + C_1 R_{sw_{k+1/2}}\right) \left(\sum_{l=1}^{n_p} C_{wl} T_{z_l} \right)_{k+1/2} \\
&+ C_3 \left(\sum_{l=1}^{n_p} C_{sl} T_{z_l} \right)_{k+1/2} + C_1 T_{z_{g_{k+1/2}}}
\end{aligned} \tag{4-110}$$

$$\begin{aligned}
AT'_k &= \left(1 + C_1 R_{so_{k-1/2}}\right) \left(\sum_{l=1}^{n_p} C_{ol} T_{z_l} \right)_{k-1/2} + \left(C_2 + C_1 R_{sw_{k-1/2}}\right) \left(\sum_{l=1}^{n_p} C_{wl} T_{z_l} \right)_{k-1/2} \\
&+ C_3 \left(\sum_{l=1}^{n_p} C_{sl} T_{z_l} \right)_{k-1/2} + C_1 T_{z_{g_{k-1/2}}}
\end{aligned} \tag{4-111}$$

$$AC'_i = - \left(AT'_k + AS'_j + AE'_i + AW'_i + AN'_j + AB'_k + \left(\frac{1}{B_o} + \frac{C_1 R_{so}}{B_o} \right)^n \frac{V_B \phi^n c_t^n}{\Delta t} \right) \tag{4-112}$$

$$B'_i = - \left(Q'_{WOGS} + \left(\frac{1}{B_o} + \frac{C_1 R_{so}}{B_o} \right)^n \frac{V_B \phi^n c_t^n P^n}{\Delta t} \right) \tag{4-113}$$

4.11 BUBBLE POINT TRACKING

The bubble point tracking methods is described in Section 3.9. This section presents the bubble point calculation when four phases are present.

In saturated gridblocks ($P < P_b$), free gas is in equilibrium with liquid phases. Then, the new gridblock bubble point pressure is a pressure at which all the free gas and

solution gas in the oil component goes into solution. The new solubility of gas in oil is defined as

$$R_{so}^{n+1} = \frac{\frac{S_g}{B_g} + \left(\sum_{l=1}^{n_p} \frac{S_l C_{ol}}{B_l} \right) R_{so}}{\left(\sum_{l=1}^{n_p} \frac{S_l C_{ol}}{B_l} \right)} \quad (4-114)$$

In undersaturated gridblocks ($P > P_b$), solution gas ratio is unknown and bubble point pressure is independent of gridblock pressure. Therefore, the bubble point pressure needs to be calculated through the mass balance equation.

For undersaturated gridblocks, Equation (4-76) can be written in simplified form. The free gas concentration is zero and the water solution gas ratio is assumed to be negligible compared to oil solution gas ratio ($R_{sw} \ll R_{so}$).

$$L_g = \frac{V_B}{\Delta t} \Delta_t (\phi \tilde{C}_o R_{so}) \quad (4-115)$$

Using the mixing rule Equation (4-115) is expanded as

$$L_g^{n+1} = \frac{V_B}{\Delta t} \left[(\phi \tilde{C}_o)^{n+1} \Delta_t (R_{so}) + R_{so}^n \Delta_t (\phi \tilde{C}_o) \right] \quad (4-116)$$

where superscript n and $n+1$ represent old and new time step, respectively. Equation (4-75) for the oil component is written as

$$L_o = \frac{V_B}{\Delta t} \Delta_t (\phi \tilde{C}_o) \quad (4-117)$$

Combining Equations (4-116) and (4-117) gives

$$L_g^{n+1} = \frac{V_B}{\Delta t} (\phi \tilde{C}_o)^{n+1} \Delta_t (R_{so}) + R_{so}^n L_o^{n+1} \quad (4-118)$$

Therefore, the solution gas ratio for the new time step $n+1$ is computed as

$$R_{so}^{n+1} = R_{so}^n + \frac{\frac{\Delta t}{V_B} (L_g^{n+1} - R_{so}^n L_o^{n+1})}{(\phi \tilde{C}_o)^{n+1}} \quad (4-119)$$

The new time step bubble point pressure (P_{bp}^{n+1}) associated with R_{so}^{n+1} is then estimated from the PVT table.

4.12 SURFACTANT PHASE BEHAVIOR

Surfactant phase behavior considers up to four volumetric components (water, oil, surfactant and gas). The effect of gas on surfactant phase behavior will be discussed later. In absence of gas, only three components are modeled. The volumetric concentrations of these three components are used as the coordinates on a ternary diagram. Salinity and divalent cation concentrations have a strong influence on phase behavior. At low salinity, an excess oil phase that is essentially pure oil and a microemulsion phase that contains water plus electrolytes, surfactant, and some solubilized oil exist. This type of phase environment is called Winsor Type I, or alternatively Type II (-). If the surfactant concentration is below the critical micellar concentration (CMC), the two phases are an aqueous phase containing all the surfactant, electrolytes, and dissolved oil at the water solubility limit and a pure excess oil phase. For high salinity, an excess water phase and a microemulsion phase containing most of the surfactant and oil, and some solubilized water exist. This type of phase environment is called Winsor Type II, or alternatively Type II (+). An overall composition at intermediate salinity separates into three liquid phases. These phases are excess oil and water phases and a microemulsion phase whose

composition is represented by an invariant point. This phase environment is called Winsor Type III.

The surfactant/oil/water phase behavior can be represented as a function of effective salinity once the binodal curve and tie lines are described. The phase behavior model in UTCHEM is based on the work by Pope and Nelson (1978), Prouvost *et al.* (1984; 1985; 1986), Satoh (1984), and Camilleri *et al.* (1987a,b,c) simplified to not include the effects of co-solvent.

The formulation of the binodal curve using Hand's rule (Hand, 1939) is assumed to be the same in all phase environments. Hand's rule is based on the empirical observation that equilibrium phase concentration ratios are straight lines on a log-log scale. The binodal curve is computed from

$$\frac{\bar{C}_{sl}}{\bar{C}_{ol}} = A \left(\frac{\bar{C}_{sl}}{\bar{C}_{wl}} \right)^B \quad (l = w, o, me) \quad (4-120)$$

where A and B are empirical parameters. For a symmetric binodal curve where $B = -1$, which is the current formulation used in UTCHEM. All phase concentrations are calculated explicitly in terms of oil concentration (\bar{C}_{ol}).

$$\bar{C}_{sl} = \frac{1}{2} \left[-A\bar{C}_{ol} + \sqrt{(A\bar{C}_{ol})^2 + 4A\bar{C}_{ol}(1 - \bar{C}_{ol})} \right] \quad (l = w, o, me) \quad (4-121)$$

Parameter A is related to the height of the bimodal curve ($\bar{C}_{s,max}$) as follows:

$$A_m = \left(\frac{2\bar{C}_{s,max,m}}{1 - \bar{C}_{s,max,m}} \right)^2 \quad (m = 0, 1, \text{ and } 2) \quad (4-122)$$

where $m = 0, 1$, and 2 are corresponding to low (or zero), optimal, and high (twice optimum) salinities, respectively. A_m is linearly interpolated as

$$A = (A_0 - A_1) \left(1 - \frac{C_{SE}}{C_{SEOP}} \right) + A_1 \quad C_{SE} \leq C_{SEOP} \quad (4-123)$$

$$A = (A_2 - A_1) \left(\frac{C_{SE}}{C_{SEOP}} - 1 \right) + A_1 \quad C_{SE} > C_{SEOP} \quad (4-124)$$

where C_{SE} and C_{SEOP} are effective salinity and optimum effective salinity, respectively. The heights of binodal curve at three reference salinities are input parameters and are estimated based on laboratory phase behavior experiments.

In presence of free gas, its volume needs to be excluded from the phase behavior calculations and the overall volume concentrations of water, oil, and surfactant are normalized for the volume of free gas. At the end, saturations are re-normalized for the volume of the free gas.

4.13 EFFECT OF SOLUTION GAS AND PRESSURE ON SURFACTANT PHASE BEHAVIOR

The effect of pressure and solution gas was discussed in Section 2.5 Here we briefly review the results.

The effect of solution gas and pressure on microemulsion phase behavior has been studied by Nelson (1983), Puerto and Reed (1983), Roshanfekar *et al.* (2009), Southwick *et al.* (2012), Sagi *et al.* (2013) and Jang *et al.* (2014). Jang *et al.* (2014) used sapphire cells to measure the phase behavior for eight different oil samples over a wide range of pressure, temperature and solution gas and is the most complete set of data available at this time. Roshanfekar *et al.* (2009), Southwick *et al.* (2012) and Jang *et al.* (2014) all report an increase in the solubilization ratio and a small decrease in the optimum salinity for live oils compared to dead oils. Kim *et al.* (1985, 1988), Austad *et al.* (1990), Austad and Strand (1996), Austad *et al.* (1996), Skauge and Fortland (1990), Sanderson *et al.*

(2012) and Jang *et al.* (2014) observed that for both pure hydrocarbons and crude oils the optimum salinity increases slightly as the pressure increases. However, the shift in optimum salinity with pressure up to several thousand psi is small. The effect of pressure is much less than the effect of solution gas. Because the effect of solution gas and pressure on the optimum salinity is relatively small and a general correlation has not yet been well established (using EACN does not appear to be generally valid), it has been currently neglected in the four-phase flow model. However, it could be added to the model when a good correlation becomes available.

4.14 PHASE SATURATIONS

The phase saturations are calculated from the phase composition, overall composition and saturation constraint. The overall composition and the saturation constraint are

$$\tilde{C}_k = \sum_{l=1}^{n_p} \frac{S_l}{B_l} C_{kl} \quad (4-125)$$

$$\sum_{l=1}^{n_p} S_l = 1 \quad (4-126)$$

NOMENCLATURE

| | |
|---|--|
| A, A_0, A_1, A_2 | = empirical parameters for Hand's rule |
| $\overline{\overline{A}}, \overline{\overline{A}}'$ | = matrix of pressure coefficients ($M^{-1}L^4t$) |
| A_c | = flow cross sectional area (L^2) |
| a_k | = Langmuir adsorption model parameter |
| a_{kl} | = Langmuir adsorption model parameter (L^2) ^{0.5} |
| a_{k2} | = Langmuir adsorption model parameter (L^2) ^{0.5} (Eq/L^3) ⁻¹ |
| b_k | = Langmuir adsorption model parameter |
| B | = empirical parameters for Hand's rule |
| $\overline{B}, \overline{B}'$ | = known vectors for pressure equation (L^3t^{-1}) |
| B_l | = formation volume factor (L^3/L^3) |
| c_k | = compressibility ($ML^{-1}t^{-2}$) ⁻¹ |
| \tilde{C}_k | = total volume concentration of component k at standard conditions (L^3/L^3 PV) |
| \hat{C}_k | = adsorbed concentration of component k at standard conditions (L^3/L^3 PV) |
| C_{kl} | = volume concentration of component k in phase l at standard conditions (L^3/L^3) |
| \overline{C}_{kl} | = volume concentration of component k in phase l at reservoir conditions (L^3/L^3) |
| C_{pci} | = capillary pressure model parameter (Mt-2) |
| C_{SE} | = effective salinity (Eq/L^3) |
| C_{SEL} | = lower limit for Type III window (Eq/L^3) |
| C_{SEOP} | = optimum effective salinity (Eq/L^3) |
| C_{SEP} | = effective salinity for polymer (Eq/L^3) |
| C_{SEU} | = upper limit for Type III window (Eq/L^3) |
| $\overline{C}_{s,max,m}$ | = height of binodal curve (L^3/L^3) |
| E_g | = gas expansion factor (L^3/L^3) |
| e_{pc} | = capillary pressure model parameter |
| f_{cation}^{s++} | = fraction of divalent cation on surfactant |
| g | = gravitational force (Lt^{-2}) |
| J_k | = mass flux of component k (ML^3t^{-1}) |
| k | = absolute permeability (L^2) |
| k_r | = relative permeability |
| k_{rl}^o | = endpoint relative permeability |
| n_k | = number of components |

| | |
|----------------|---|
| n_l | = Corey relative permeability exponent |
| n_p | = number of phases |
| N_{Ti} | = trapping number |
| P | = pressure ($ML^{-1}t^{-2}$) |
| P_b | = bubble point pressure ($ML^{-1}t^{-2}$) |
| P_{cur} | = capillary pressure between phase l and l' ($ML^{-1}t^{-2}$) |
| q_k | = source/sink term (ML^3t^{-1}) |
| R_{sl} | = solution gas ratio in phase l (L^3/L^3) |
| S_l | = saturation of phase l (L^3/L^3 PV) |
| S_{lr} | = residual saturation of phase l (L^3/L^3 PV) |
| S_{nl} | = normalized saturation of phase l |
| t | = time (t) |
| T | = temperature (T) |
| T_{DCI} | = capillary desaturation curve parameter for phase l |
| T_l | = phase transmissibility ($M^{-1}L^4 t$) |
| V_B | = grid volume (L^3) |
| u_l | = Darcy phase velocity of phase l (Lt^{-1}) |
| z | = depth (L) |
| α_i | = phase viscosity parameters |
| β_p | = polymer effective salinity coefficient |
| β_s | = effective salinity parameter for divalent cations |
| β_T | = effective salinity temperature coefficient (T^{-1}) |
| λ_{rl} | = phase relative mobility ($M^{-1}Lt$) |
| μ_l | = Phase viscosity ($ML^{-1}t^{-1}$) |
| ρ | = density (ML^{-3}) |
| $\sigma_{ll'}$ | = interfacial tension between phase l and l' (Mt^{-2}) |
| ϕ | = porosity |
| Φ_l | = phase potential ($ML^{-1}t^{-2}$) |

Chapter 5: Comparison of Implicit Texture and Population Balance Models

In this chapter population-balance (PB) and implicit-texture (IT) models are compared. The equivalence of the two approaches is demonstrated by deriving explicitly the foam-coalescence-rate function implicit in the IT models, and showing its similarity to that in population-balance models. The models are compared and discussed based on their ability to represent a set of N₂ and CO₂ steady-state foam experiments and the corresponding parameters of the different methods.

5.1 INTRODUCTION

Simulation models for foam enhanced oil recovery are of two types: those that treat foam texture or bubble size explicitly (population-balance models) and those that treat the effects of foam texture implicitly through a gas mobility-reduction factor. The implicit-texture models assume local equilibrium (LE) between the processes of foam creation and destruction. In published studies most population-balance models predict rapid attainment of local-equilibrium as well, and some have been recast in LE versions. Population-balance models are credited with being based on first principles and are sometimes called "full physics" models, although of course all models incorporate only partial physics.

In all the foam models discussed here, foam coalescence is related to P_c^* . In the PB models, P_c^* , or its corresponding saturation, S_w^* , is explicitly specified as an input parameter to calculate the coalescence rate and bubble size. The IT models incorporate P_c^* implicitly by employing the limiting water saturation S_w^* as an input parameter. In PB models foam collapses as capillary pressure approaches P_c^* , while in IT models foam collapse occurs when foam becomes too dry i.e. in the vicinity of S_w^* . The IT models

differ in whether foam collapses completely, or degrades partially, in the vicinity of S_w^* (Cheng *et al.*, 2000).

Skoreyko *et al.* (2012) model represents foam generation, foam degradation and trapped foam by defining a set of first order, non-reversible reactions. They use Arrhenius-type equations to compute reaction rates. Their model makes no reference to foam coarsening at a limiting capillary pressure, which distinguishes it from the models described here. Likewise, the population-balance models of Falls *et al.* (1988), Friedmann *et al.* (1991) and Zitha (2006) do not include foam coalescence at a limiting capillary pressure. Therefore, we do not address these models further in this chapter.

This chapter investigates the limiting capillary pressure concept as applied in both IT and PB models. Specifically, it shows that the limiting water saturation in IT models can be expressed as a coalescence (destruction) term in an equivalent way to that in PB models. In other words, each IT model examined is equivalent to the LE formulation of a corresponding population-balance model: the physics of foam coalescence as represented in the two types of models is essentially the same.

In addition, the experimental data for steady-state apparent foam viscosity (without oil present) versus foam quality are matched with the different foam models and the corresponding parameters in each model are discussed. The results confirm that the steady-state flow of foam in porous media can be adequately represented equally well by the simpler IT models.

Only population-balance models can represent the dynamics of foam creation and propagation at a shock front, the creation of foam at the entrance of the porous medium or near an abrupt change in permeability. However, in published applications, PB models come to local equilibrium rapidly, suggesting that on the field scale LE applies, at least in relatively homogeneous formations (Rossen *et al.*, 1999; Chen *et al.*, 2010). The first step

in evaluating any foam model is to examine its ability to represent laboratory LE data, and this study focuses on that issue.

5.2 FOAM MODELS

Nearly all foam models alter the transport properties of gas only and assume that liquid mobility remains the same function of saturations as it is in the absence of foam, in accordance with laboratory observations (Bernard and Holm, 1964; Bernard *et al.*, 1965; Sanchez *et al.*, 1989; de Vries and Wit, 1990; Friedmann *et al.*, 1991; Vassenden and Holt, 2000). However, there are few experiments indicating the effect of foam on the water relative permeability (Arran *et al.*, 2014). In the presence of foam, gas trapped by stationary lamellae reduces mobile gas saturation, blocks gas flow and alters gas flow paths, and thus reduces gas relative permeability. The fraction of trapped gas is a function of pressure gradient, capillary pressure, aqueous phase saturation, pore geometry and bubble size (Kovscek *et al.*, 1995; Nguyen *et al.*, 2007; 2009). On the other hand, moving lamellae experience a drag force when they slide along the pore walls (Hirasaki and Lawson, 1985) that is complicated by capillary effects on the lamellae (Falls *et al.*, 1989; Xu and Rossen, 2003). This effect is similar to an increase in gas viscosity. Because the viscosity of gas itself is not increased by foam, the effect of increased resistance to gas flow due to the presence of lamellae is termed “apparent gas viscosity.” However, many models combine the effects of foam on gas relative permeability and apparent viscosity and reduce the gas mobility by a factor applied to either the gas viscosity or the gas relative permeability. In the following sections, IT and PB foam models are briefly discussed.

5.2.1 Implicit-Texture Models

In this section, the UT (Rossen *et al.*, 1999; Cheng *et al.*, 2000), STARS (Computer Modeling Group, 2012) and Vassenden-Holt (1998) IT models are described. A summary of these models is provided in Table 5.1.

5.2.1.1 UT Model

The UT model (Rossen *et al.*, 1999; Cheng, 2000) was originally based on data of Persoff *et al.* (1991), which lies entirely in the high-quality regime. At fixed gas superficial velocity, this model gives a steep, linear increase in gas mobility as water saturation decreases through a narrow interval in the immediate vicinity of S_w^* , and a constant reduction in gas mobility for larger values of S_w . The model allows for non-Newtonian behavior in the low-quality regime by making the mobility-reduction factor in the low-quality regime a power-law function of gas superficial velocity. This model is currently in use in compositional simulator UT-DOECO2 (Delshad *et al.*, 2013; Naderi Beni *et al.*, 2013) and UTCHEM (Delshad, 2013).

5.2.1.2 STARS Model

In the STARS model (Computer Modeling Group (CMG), 2012), when foam is present, the gas relative permeability is multiplied by a factor FM , which is function of several factors. The dry-out function F_2 and shear-thinning function F_5 , are defined in Table 5.1. As in the UT model, foam mobility increases as S_w decreases in the vicinity of S_w^* , which is given the name $fmdry$ in the STARS model. However, in the STARS model foam does not collapse completely at any water saturation. The function F_5 allows for shear-thinning in the low-quality regime by making the mobility-reduction factor dependent on capillary number (i.e., on pressure gradient).

5.2.1.3 Vassenden-Holt model

Vassenden and Holt (1998) proposed a foam simulation model in which the gas mobility reduction factor, F , is sum of two exponential functions of water saturation. For water saturation slightly greater than S_f (equivalent to S_w^*), foam mobility decreases steeply because of the first exponential function; this corresponds to foam dryout and the high-quality regime. The second function decreases more gradually for higher water saturation and controls foam behavior in the low-quality regime.

Table 5.1: A summary of IT models used in this study

| Model Description | Model parameters |
|---|--|
| <p><u>UT Model (1994)</u></p> $k_{rg}^f = \begin{cases} k_{rg} & ; S_w < S_w^* - \varepsilon \text{ or } C_s < C_s^* \\ \frac{k_{rg}}{(1 + ((R-1)(S_w - S_w^* + \varepsilon)) / 2\varepsilon)} & ; S_w^* - \varepsilon \leq S_w \leq S_w^* + \varepsilon \text{ \& } C_s \geq C_s^* \\ k_{rg}^f = \frac{k_{rg}}{R} & ; S_w > S_w^* + \varepsilon \text{ \& } C_s \geq C_s^* \end{cases} \quad (5-1)$ $R = R_{ref} \left(\frac{u_g}{u_{gref}} \right)^{\sigma-1} \quad (5-2)$ | <p>k_{rg}: gas relative permeability k_{rg}^f: foam relative permeability C_s: surfactant concentration C_s^*: threshold surfactant conc. S_w^*: limiting water saturation u_g: gas Darcy velocity u_{gref}: ref. gas Darcy velocity R: foam resistance factor ε: Water saturation tolerance σ: power-law exponent $\sigma = 1$, Newtonian $\sigma < 1$, shear-thinning</p> |
| <p><u>STARS Model</u></p> $k_{rg}^f = k_{rg} \times FM \quad (5-3)$ $FM = \frac{1}{1 + fmmob(F_1 \times F_2 \times F_3 \times F_4 \times F_5 \times F_6)} \quad (5-4)$ $F_2 = 0.5 + \frac{1}{\pi} \arctan(epdry(S_w - fmdry)) \quad (5-5)$ $F_5 = \begin{cases} \left(\frac{fmcap}{N_{ca}} \right)^{epcap} & ; N_{ca} > fmcap \\ 1 & ; N_{ca} \leq fmcap \end{cases} \quad (5-6)$ | <p>FM: mobility reduction factor $fmmob$: max. reduction factor F_2: dry-out function F_5: shear thinning function $epdry$: ref. dry-out slop in dimensionless dryout calculation $fmdry$: dry-out factor N_{ca}: capillary number $fmcap$: ref. capillary number $epcap$: exponent for capillary number contribution</p> |
| <p><u>Vassenden-Holt Model</u></p> $k_{rg}^f = k_{rg} \times F \quad (5-7)$ $F = \begin{cases} e^{(S_f - S_w)s_1} + \left(\frac{u_g}{u_{go}} \right)^a F_o e^{(S_f - S_w)s_2} & ; S_w > S_f \\ 1 & ; S_w \leq S_f \end{cases} \quad (5-8)$ | <p>u_g: gas Darcy velocity u_{go}: ref. gas Darcy velocity F: foam mobility multiplier F_o: foam mobility multiplier at ref. gas velocity S_f: lowest water saturation for foam effect s_1: slop of the gas relative permeability at high quality regime s_2: slop of the gas relative permeability at low quality regime a: shear thinning exponent (for original model $a = 1$)</p> |

5.2.2 Population-Balance Models

Foam mobility is influenced by its texture (Patzek, 1988; Falls *et al.*, 1988). Foam texture is quantified as the number of lamellae per unit volume of gas. Foam with fine texture has more lamellae in a given volume of gas and therefore induces more resistance to gas flow. Population-balance models incorporate foam texture explicitly to predict flow properties. A balance equation for lamellae allows the simulator to track foam texture dynamically, i.e. without the local-equilibrium assumption. The rates of accumulation, convection, generation, and coalescence of foam bubbles are incorporated into the bubble balance, and, if desired, rates of trapping and mobilization as well.

The transient population balance for the average flowing and trapped bubble sizes is written as (Chen *et al.*, 2010):

$$\frac{\partial}{\partial t} [\phi(S_f n_f + S_t n_t)] + \nabla \cdot (u_f n_f) = q_f + Q_b \quad (5-9)$$

where S_f and S_t are flowing and trapped gas saturations, and n_f and n_t are number density of flowing and trapped foam lamellae, respectively. Q_b is a source/sink term, and q_f is the net rate of generation of lamellae

$$q_f = r_g - r_c \quad (5-10)$$

where r_g and r_c represent generation and coalescence rates, respectively. The population balance model can be simplified by assuming local equilibrium if desired (Ettinger and Radke, 1992; Myers and Radke, 2000; Kam and Rossen, 2003; Chen *et al.*, 2010). In the LE version of the PB models, the rates of foam generation and coalescence are set equal to each other, which defines the LE value of foam texture n_f at each location. Equation (5-9) is eliminated from the set of governing equations.

In this section, the models of Chen *et al.* (2010), Kam *et al.* (2007), and Kam (2008) are described. The models are summarized in Table 5.2. The population-balance models examined here use the shear-thinning expression of Hirasaki and Lawson (1985) for the effective gas viscosity.

$$\mu_f = \mu_g + \frac{\alpha n_f}{|v_f|^{1/3}} \quad (5-11)$$

where μ_f and μ_g are the gas viscosity in the absence and presence of foam, n_f is the foam lamella density (number of lamella per unit volume), v_f is local gas velocity and α is a proportionality constant that depends on the surfactant formulation and permeability.

5.2.2.1 *Kovscek et al. (1994) Model, Modified by Chen et al. (2010).*

Kovscek *et al.* (1994) considered Roof snap-off as the mechanism of lamella creation. Their model employs a capillary-pressure-dependent kinetic expression for lamella coalescence (to reflect the limiting capillary pressure) and also a term to represent the trapped fraction of foam. The gas relative permeability is then reduced according to the fraction of flowing gas to reflect the effect of gas trapping (Equation (5-18)). Lamella-generation rate is taken as a power-law expression, proportional to the magnitude of the interstitial velocity of surfactant solution and 1/3 power of the interstitial gas velocity. Chen *et al.* (2010) introduced an upper limit for the concentration of lamellae that is related to pore size. The upper limit is achieved by reducing the lamella generation rate as this limit is approached; they contended that this accounts for pre-existing gas bubbles that occupy foam-generation sites. They showed that the LE form of this model can predict both low- and high-quality foam regimes.

5.2.2.2 *Kam et al. Model (2007)*

Kam *et al.* (2007) presented a foam model in which lamella creation depends on pressure gradient and also on water saturation or capillary pressure, which governs the presence of lenses or lamellae available to be mobilized (Rossen and Gauglitz, 1990; Gauglitz *et al.*, 2002). Specifically, lamella generation rate is proportional to water saturation and a power-law expression of pressure gradient. In this model, the lamella generation rate monotonically increases with the pressure gradient. The lamella coalescence rate is a power-law function of $(S_w - S_w^*)$, with the exponent an adjustable parameter. This model can represent multiple (coarse and strong) foam states at the same superficial velocity and jumps between those states, as well as the low- and high-quality regimes for strong foam.

5.2.2.3 *Kam (2008)*

In this extension of the model of Kam *et al.* (2007), for the lamella creation, the local pressure gradient must exceed the minimum pressure gradient required for lamellae mobilization and division. Kam (2008) proposed a new lamella-creation function, which reaches a plateau at higher pressure gradient (Equation (5-25)).

Table 5.2: A summary of PB models used in this study

| Model Description | Model Parameters |
|--|---|
| <u>Chen et al. (2010)</u> | |
| - generation rate $r_g = k_1 \left \vec{v}_w \right \left \vec{v}_f \right ^{1/3}$ (5-12) | v_f : local gas velocity v_w : local water velocity k_1 : generation coefficient |
| $k_1 = k_1^o \left[1 - (n_f/n^*)^o \right]$ (5-13) | k_1^o : model parameter (const.) n_f : flowing foam bubble density n^* : limiting (max) bubble density |
| - coalescence rate $r_c = k_{-1} \left \vec{v}_f \right n_f$ (5-14) | ω : constant exponent k_{-1} : coalescence coefficient |
| $k_{-1} = k_{-1}^o \left(\frac{P_c}{P_c^* - P_c} \right)^2$ (5-15) | k_{-1}^o : model parameter (const.) P_c : capillary pressure P_c^* : limiting capillary pressure |
| $P_c^* = P_{c,max}^* \tanh(C_s/C_s^o)$ (5-16) | $P_{c,max}^*$: limiting value of P_c^* C_s : surfactant concentration C_s^o : ref. surfactant concentration |
| - at local equilibrium $n_f^\omega + \frac{n^{*\omega} k_{-1} \left \vec{v}_f \right ^{2/3}}{k_1^o \left \vec{v}_w \right } n_f - n^{*\omega} = 0$ (5-17) | k_{rg}^o : gas endpoint relative permeability n_g : gas exponent relative permeability |
| - foam relative permeability $k_{rf} = k_{rg}^o \left((1 - X_t) S_{gD} \right)^{n_g}$ (5-18) | S_{gD} : dimensionless gas saturation X_t : trapping foam fraction |
| $X_t = X_{t,max} \left(\frac{\beta n_t}{1 + \beta n_t} \right)$ (5-19) | $X_{t,max}$: maximum trapping foam fraction n_t : trapping foam bubble density β : trapping parameter |
| - at local equilibrium $n_t = n_f$ | |
| <u>Kam et al. (2007)</u> | |
| generation rate $r_g = c_g S_w (\nabla p)^m$ (5-21) | n_f : foam bubble density c_g : generation rate coefficient |
| - coalescence rate $r_c = c_c n_f \left(\frac{1}{S_w - S_w^*} \right)^n$ (5-22) | c_c : coalescence rate coefficient S_w^* : limiting water saturation ∇P : pressure gradient n : coalescence exponent |
| - at local equilibrium $n_f = \frac{c_g}{c_c} S_w (S_w - S_w^*)^n (\nabla P)^m$ (5-23) | m : model parameter |
| <u>Kam (2008)</u> | |
| - generation rate $r_g = \frac{c_g}{2} \left(\operatorname{erf} \left(\frac{\nabla P - \nabla P_o}{\sqrt{2}} \right) - \operatorname{erf} \left(\frac{-\nabla P_o}{\sqrt{2}} \right) \right)$ (5-24) | n_f : foam bubble density c_g : generation rate coefficient c_c : coalescence rate coefficient |
| - coalescence rate $r_c = c_c n_f \left(\frac{S_w}{S_w - S_w^*} \right)^n$ (5-25) | S_w^* : limiting water saturation ∇P : pressure gradient ∇P_o : model parameters related to minimum pressure gradient |
| - at local equilibrium $n_f = \begin{cases} \frac{c_g}{2c_c} \left(\frac{S_w - S_w^*}{S_w} \right)^n \left(\operatorname{erf} \left(\frac{\nabla P - \nabla P_o}{\sqrt{2}} \right) - \operatorname{erf} \left(\frac{-\nabla P_o}{\sqrt{2}} \right) \right) & n_f < n_{max} \\ n_{max} & n_f \geq n_{max} \end{cases}$ (5-26) | n : coalescence exponent n_{max} : maximum (limiting) bubble density |

5.3 CORRESPONDING FOAM MODEL PARAMETERS

Parameters S_w^* , $fmdry$, and S_f represent the limiting water saturation in the IT models and the PB models of Kam, while Chen *et al.* use the corresponding capillary pressure P_c^* in their model. In the STARS model, foam weakens in the vicinity of $fmdry$ but does not collapse completely at any value of S_w . In the UT model, foam collapses in the vicinity of S_w^* , specifically in an interval of $(S_w^* \pm \varepsilon)$. In the other models foam collapses completely for $S_w < S_f$ or, $S_w < S_w^*$ or $P_c > P_c^*$. Parameters R_{ref} , $fmmob$, and $(1/F_o)$ represent a reference (or maximum) mobility reduction factor that could be achieved by foam when all the conditions are favorable and are directly set in the IT models. n^* and n_{max} are upper limits for the concentration of foam bubbles in the Chen *et al.*, Kam *et al.* and Kam models, respectively, and are related to pore size. More than one foam bubble per pore is not expected (Bertin *et al.* 1998; Kil *et al.*, 2011). Parameters ε , $epdry$, and s_1 control the sharpness of the transition from high-quality to low-quality regimes in the IT models. The extent of the saturation range in the transition from high-quality to low-quality regimes is set to 2ε in the UT model. In both STARS and the Vassenden-Holt models, for the large values of $epdry$ and s_1 the transition is sharp and foam collapses at very narrow range of water saturation. In the Kam *et al.* and Kam models, the coalescence exponent n controls the foam transition, with smaller n giving a sharper transition. The coalescence rate depends on nearness of capillary pressure to P_c^* with an exponent (-2) in the Chen *et al.* model (Equation (5-15)). Parameters σ , $epcap$, and a account for shear-thinning behavior in the low-quality regime in UT, STARS, and modified Vassenden-Holt models, respectively; this reflects both gas trapping and mobilization and the shear-thinning drag on individual moving bubbles. Population-balance models use the shear-thinning expression by Hirasaki and Lawson with an exponent of (-1/3) for the dependence of apparent gas viscosity on gas velocity.

5.4 FITTING FOAM MODELS TO EXPERIMENTAL DATA

In this section, different foam models are used to match the steady-state CO₂ foam experimental data reported by Moradi-Araghi *et al.* (1997) and the N₂ foam experimental data of Alvarez *et al.* (2001). The models are then compared and discussed.

5.4.1 Experimental Data

Moradi-Araghi *et al.* (1997): they conducted experiments with CO₂ at 98°F and 2000 psi in a 551.5-md-permeability reservoir core from the South Cowden Unit. The core plugs were 1 inch in diameter and 4.84 inches long. The core was positioned vertically in the cardholder with injection from the bottom. Foam was made with 2000 ppm Chaser CD-1050 surfactant in synthetic South Cowden formation brine. The overall pressure drop in the foam experiments was measured and divided by that for single-phase water flow and reported as the mobility reduction factor (*RF*). Therefore, to calculate the apparent viscosity of foam as a function of gas fraction or foam quality (f_g), the reported mobility reduction factor is multiplied by water viscosity at the experimental conditions.

$$\mu_{app}^f = \mu_w RF = 0.65RF \quad (5-27)$$

where μ_{app}^f is in cp. Note that *apparent viscosity of foam* (μ_{app}^f) is defined in Equation (5-27) in terms of the total mobility of foam treated as a single phase; *apparent viscosity of gas* (μ_f) is defined in the foam models above as the effective viscosity of the gas phase.

Moradi-Araghi *et al.* (1997) did not report the injection rate used in their experiments. Therefore, a total injection rate of 5 ft/day is assumed to model and match their experimental data. Farajzadeh *et al.* (2015) found that the choice of flow rate affects only the reference capillary number or reference gas superficial velocity in the UT and STARS models and therefore does not influence the generality of our conclusions.

Alvarez *et al.* (2001): they conducted experiments with N₂ at room temperature and 600 psi outlet pressure in 530 md Berea sandstone core. Hassler-type coreholder with four internal pressure taps was used, with a coreholder placed in vertical position and with injection from the top. The cores were 2 inches in diameter and 11 inches in length. Foam was generated with 1 wt% Bio-Terge AS-40 surfactant, a C₁₄₋₁₆ sodium a-olefin sulfonate (anionic surfactant). Brine composition was 3 wt% NaCl and 0.01 wt% CaCl₂ in deionized water. Gas and surfactant solution were injected simultaneously and flow rates were set to obtain a specific foam quality (f_g) at outlet conditions of 600 psi. To ensure a steady state, foam was injected at each flow rate for at least 24 hours. The pressure gradient at a fixed total superficial velocity of 2.5 ft/day was measured and apparent foam viscosity is reported here by multiplication by absolute permeability and dividing by total velocity:

$$\mu_{app}^f = \frac{-k\nabla P}{u_w + u_g} \quad (5-28)$$

Relative permeability data are not reported for the porous medium used in these experiments. Although the parameters depend somewhat on the choice of the relative permeability parameters (Ma *et al.*, 2014a), the generality of the results will not be affected (Farajzadeh *et al.*, 2015). A relative permeability function was estimated by fitting the data of Persoff *et al* (1991) in Boise sandstone. Two phase water-gas relative permeabilities are calculated from the following functions:

$$k_{rw} = k_{rw}^o (S_{wD})^{n_w} \quad (5-29)$$

$$k_{rg} = k_{rg}^o (1 - S_{wD})^{n_g} \quad (5-30)$$

where S_{wD} is dimensionless water saturation and is defined as

$$S_{wD} = \frac{S_w - S_{wr}}{1 - S_{wr} - S_{gr}} \quad (5-31)$$

The general form of gas-water capillary pressure represented by Li (2004) was used as

$$P_c = P_{c@S_{wc}} (1 - bS_{wD})^{-1/\lambda} \quad (5-32)$$

where $P_{c@S_{wc}}$ is the capillary pressure at the residual water saturation, (S_{wc}) when drainage capillary pressure is used. b and λ are constants and are defined as

$$n_w = 1 + \frac{2}{\lambda} \quad (5-33)$$

$$b = 1 - \left(\frac{P_{ce}}{P_{c@S_{wc}}} \right)^{-\lambda} \quad (5-34)$$

where P_{ce} is entry capillary pressure at the residual water saturation

$P_{c@S_{wc}} = 21.036$ psi and $P_{ce} = 0.042$ psi are picked for Nitrogen data of Alvarez *et al.* (N_2). Assuming a similar rock type, the capillary pressure for CO_2 flood of Moradi-Araghi *et al.* can be scaled based on interfacial tension (concept of J -Leverett) as

$$P_{c_{CO_2}} = P_{c_{N_2}} \frac{\sigma_{CO_2}}{\sigma_{N_2}} \quad (5-35)$$

where σ_{CO_2} and σ_{N_2} are CO_2 and N_2 interfacial tension with water.

Figure 5.1 shows the capillary pressure curves used to model CO_2 and N_2 experiments.

Table 5.3 summarizes all the rock and fluid properties used in this chapter.

5.4.2 Data Fitting Procedure

The objective function for the optimization of foam model parameters is defined as

$$\Phi(x) = \sum_{i=1}^{n_{data}} \left(\mu_{app_i}^f(x) - \mu_{app_i}^{f(\text{exp})} \right)^2 \quad (5-36)$$

where x is the vector of foam model parameters. For example in the STARS model, $x = [fmmob, epdary, fmdry, epcap]$. The reference capillary number, $fmcap$, is not an independent parameter and was set to a fixed value. $\mu_{app_i}^{f(\text{exp})}$ and μ_{app}^f are the experimental data and model values, respectively. A constrained least-square algorithm in the optimization toolbox of MATLAB (lsqnonlin function) was used to solve the non-linear data fitting problem. The constraints are set to physical limits for the foam parameters, e.g. $S_{wc} < S_w^*$, S_f or $fmdry$ ($P_{c@S_{wc}} > P_c^*$). The final set of fitted parameters sometimes depends on the initial guess. The issue of non-uniqueness in the various model fits is discussed below. In cases where the fit depends on the initial guess, the best fit (i.e., the fit with the smallest value of $\phi(x)$) is shown.

5.4.3 Steady-State Foam Simulation Results

Figure 5.2 through Figure 5.7 show the apparent gas viscosity as a function of foam quality. Symbols are the experimental data and the curves are the match using different foam models. The relevant model parameters are listed in Table 5.4 to Table 5.9.

The Vassenden and Holt model did not match the data in the low-quality regime until an exponent a for the velocity term (see Equation (5-8) and Figure 5.4) was added to the model. In effect, the original model assumed that the exponent a in Equation (5-8) is equal to one.

The results show that the two types of models match the experimental data equally well. Some individual models do better in matching some of the data and others at matching other data. For instance, for Alvarez *et al.* data, Kam, UT and Chen *et al.* models do slightly better in matching the high-quality data and UT and Kam *et al.* models in fitting the low-quality data. For the Moradi-Araghi *et al.* data UT, STARS and Kam *et al.* models do slightly better than the others.

For Chen *et al.* model, the experimental data was matched using three sets of foam parameters for both Moradi-Araghi *et al.* and Alvarez *et al.* (Table 5.7) data. In set #1 we assume a maximum gas trapping saturation of 50% and we scale the gas relative permeability along with the gas viscosity to match the experimental results; the resulting fit is shown in Figure 5.5. Since the value of trapped gas saturation is uncertain, in set #2 ignore gas trapping was ignored, but the same quality match by adjusting n^* and P_c^* was obtained. The fits are indistinguishable from each other, as shown in Figure 5.5. For at least these two experiments, the trapping parameter in the Chen *et al.* model does not play an essential part of the data-fitting procedure and could be ignored.

In all the models except that of Chen *et al.*, the limiting water saturation did not vary with the initial guess (although the other parameters did vary). In the Chen *et al.* model, however, the experimental data could be matched with different values of P_c^* by adjusting parameter k_{I^o} . In parameter set #1, $P_c^*=0.19$ psi ($S_w^*\sim 0.26$) and $P_c^*=0.55$ psi ($S_w^*\sim 0.31$) was used for Moradi-Araghi (CO₂) data and Alvarez (N₂) data, respectively. These parameters are compatible with those of other models. In set #2, P_c^* was slightly increased to account for trapped gas saturation. In set #3, essentially the same fit to the data using $P_c^*=0.8$ psi for both experiments ($S_w^*\sim 0.29$ for Moradi-Araghi and $S_w^*\sim 0.284$ for Alvarez) was obtained. In other words, one cannot derive even an approximate value

of P_c^* from these data using Chen's model without assuming a priori a value for the coalescence constant k_{-1}^o .

Dong (2001) examined this issue in the earlier model of Kovscek *et al.* (1995). Suppose, as posed in the introduction, that foam is initially at LE in the high-quality regime, and then gas superficial velocity increases by a factor X . In this model, lamella-generation rate increases by $X^{1/3}$ (see Equation (5-12)). Coalescence rate increases by the factor X (see Equation (5-14)) even with no change in capillary pressure. Thus equilibrium foam texture (n_f) changes by a factor of $X^{-2/3}$. Apparent gas viscosity is proportional to $(X^{-2/3}X^{-1/3})=X^{-1}$ because of the dependence on texture and the direct dependence on gas velocity (see Equation (5-11)). Through Darcy's law on the gas phase, pressure gradient is proportional to $(v_g \mu_{app}^f) \sim (XX^{-1})$, i.e. is constant, with no change in capillary pressure. In this model, pressure gradient is independent of gas superficial velocity in the high-quality regime because of the particular forms assumed for gas apparent viscosity and the lamella-generation and -coalescence rates, not the divergence of coalescence rate at the limiting capillary pressure.

In the model of Chen *et al.*, the dependence of lamella generation rate and gas mobility on gas superficial velocity is more complex. In the model match, the water saturation in the high-quality regime is the same for all three sets of parameters. Nevertheless, the fitted value of $S_w(P_c^*)$ varies among the parameter fits to the data from 0.265 to 0.263 to 0.219 for parameter sets #1, 2 and 3, respectively for Moradi-Araghi and 0.310 to 0.309 to 0.284 for Alvarez. In the model of Chen *et al.*, the high-quality regime need not reflect a capillary pressure close to P_c^* .

The water saturation in high-quality regime can be obtained from the slope of pressure gradient versus f_g in the experimental data, using Darcy's law for the water phase (Boeije and Rossen, 2013). The water saturation in the high-quality foam regime is

calculated to be 0.295 and 0.314 for the Moradi-Araghi and Alvarez data, respectively. Table 5.10 summarizes S_w^* values or its corresponding parameters in other models (f_{mdry} in STARS model and S_f in Vassenden-Holt) used to fit the experimental data using different models. While in UT, STARS, Kam *et al.*, and Kam models the value of S_w^* was close to the water saturation in the high-quality regime, in the Vassenden-Holt and Chen *et al.* models water saturation in the high-quality regime was not close to S_w^* (or $S_w(P_c^*)$).

5.5 COALESCENCE FUNCTION IN IMPLICIT-TEXTURE MODELS

In the IT models examined here foam experiences an abrupt change in its properties near the limiting water saturation. This abrupt change can be expressed by a lamella-destruction function similar to that in population balance models with a limiting capillary pressure.

The coalescence rate (r_c) in population-balance models (Equations (5-14), (5-22), and (5-25)) can be expressed as

$$r_c = c_c n_f f \equiv c_c n_f^* n_D f \quad (5-37)$$

$$f \equiv \frac{r_c}{c_c n_f^* n_D} \quad (5-38)$$

where c_c is constant, n_f is lamella density (foam texture), n_D is dimensionless foam texture, n_f^* is maximum foam texture in the low-quality regime (which we assume to be constant (Alvarez *et al.*, 2001)), and f is a destruction function. In other words, lamellae have a probability of breaking proportional to f , where f can be expressed in terms of water saturation or capillary pressure. Kavscek *et al.* (1993) suggested that $f \propto (P_c^* - P_c)^{-2}$; Bertin *et al.* (1998) proposed $f \propto (P_c^* - P_c)^{-1}$; Kam *et al.* (2007) and Kam

(2008) assumed $f \propto (S_w - S_w^*)^{-n}$ with n a fitted parameter. In all the models foam coalescence rate increases sharply at or near the limiting water saturation or the corresponding capillary pressure. Figure 5.8 and Figure 5.9 show the destruction function used in the PB models in terms of water saturation and capillary pressure. However, there is no theoretical reason nor direct experimental evidence for the choice of one mathematical form of the lamella-destruction function over the others, as long as it increases greatly as P_c approaches P_c^* . The mobility-reduction function (specifically the dry-out function) in IT models implies a lamella-destruction function that is similar to the corresponding function in PB models. In other words, the physics of foam collapse near P_c^* is essentially the same in the IT models as in the PB models.

In the UT foam model the gas mobility-reduction factor corresponds to a dimensionless foam lamella density defined by

$$n_D = \begin{cases} 0 & ; S_w < S_w^* - \varepsilon \\ (S_w - S_w^* + \varepsilon) / 2\varepsilon & ; S_w^* - \varepsilon \leq S_w \leq S_w^* + \varepsilon \\ 1 & ; S_w > S_w^* + \varepsilon \end{cases} \quad (5-39)$$

where for water saturations less than $(S_w^* - \varepsilon)$, foam does not exist ($n_D = 0$). In the high-quality regime, i.e. for $(S_w^* - \varepsilon \leq S_w \leq S_w^* + \varepsilon)$, n_D increases linearly with water saturation and reaches its maximum value at $(S_w^* + \varepsilon)$, where $n_D = 1$. Foam texture remains at its maximum value ($n_D = 1$) through the low-quality regime ($S_w > S_w^* + \varepsilon$).

Vassenden and Holt's model does not imply a fixed maximum foam texture in the low-quality regime. We interpret it in terms of foam texture as follows. The second term in Equation (5-8) corresponds to mobility in the low-quality regime. We interpret the $(u_g/u_{go})^a$ term reflecting non-Newtonian viscosity or gas trapping, but not changing foam

texture, in this regime. We use texture in the limit $S_w \rightarrow 1$ as the reference texture. Let F' be the function F defined in Equation (5-8) but without the (u_g/u_{go}) term. Then

$$F'(S_w) = \exp[(S_f - S_w)S_1] + F_o \exp[(S_f - S_w)S_2] \quad (5-40)$$

This function, related to the mobility-reduction factor F in Vassenden and Holt's model, is inversely proportional to foam texture. Thus

$$n_D = \left(\frac{1}{F'(S_w)} - 1 \right) \left(\frac{1}{F'(1)} - 1 \right)^{-1} \quad (5-41)$$

In the STARS gas mobility reduction is proportional to $1/FM$, with the maximum reduction when $FM = 1/(1+fmmob)$. This corresponds to a dimensionless foam texture defined by

$$n_D = \frac{\left(\frac{1}{FM} \right)}{(1 + fmmob)} \quad (5-42)$$

Different population balance models use different lamella-generation functions, and the best choice for this function remains controversial. Kam and Rossen (2003) show that different lamella-generation functions can give the same steady-state foam behavior. For simplicity, a constant bubble generation rate, r_g was assumed. Zitha (2006) assumed a constant generation rate in his model. More complicated generation functions could be used without changing the conclusions, which hinge on abrupt changes in foam behavior near P_c^* or S_w^* . Therefore, assuming local equilibrium, the destruction function is

$$f = \frac{r_g}{c_c n_D n_f^*} = \frac{r_{gD}}{n_D} \quad (5-43)$$

with

$$r_{gD} \equiv \frac{r_g}{c_c n_f^*} \quad (5-44)$$

Figure 5.10 through Figure 5.15 show the lamella-destruction functions implied by the UT, Vassenden-Holt, and STARS models, using the parameter values fit to the experimental data of Moradi-Araghi *et al.* and Alvarez *et al.* in Figure 5.2, Figure 5.3, and Figure 5.4b. The UT model implies a destruction function that remains constant in the low-quality regime and increases sharply in the interval $(S_w^* \pm \varepsilon)$, diverging to infinity at $(S_w^* - \varepsilon)$.

In Vassenden-Holt model, the destruction function increases sharply at high quality regime and it goes to infinity at S_f . In this model the destruction function increases with larger slope for the higher value of s_l .

The STARS model implies a destruction function that increases sharply in the vicinity of $fmdry$ but remains finite at all water saturations. In this model, destruction function is sharper for the larger value of $epdry$.

The lamella-destruction functions implied by these IT models are similar to those in the PB models. There is no theoretical reason or experimental justification to prefer any of the functions in Figure 5.9, Figure 5.11, Figure 5.13, or Figure 5.15 above the others. Thus, in terms of the most important mechanism in foam behavior without oil, i.e. foam collapse at the limiting capillary pressure, the IT models are as well-supported by theory and experiment as the population-balance models.

Figure 5.16 through Figure 5.19 show dimensional foam texture in implicit texture and population balance models, using the parameter values fit to Moradi-Araghi

et al. and Alvarez *et al.* experimental data. In population balance models, dimensional foam texture is defined as the foam bubble density (n_f) divided by the maximum foam bubble density in porous media n_{max} ($n_D = n_f/n_{max}$). In all the models, dimensionless foam texture increases sharply close to S_w^* . Explicit dimensionless foam textures implied in IT models are similar to those in Chen *et al.* and Kam population balance models.

5.6 NUMERICAL SIMULATION OF TRANSIENT FOAM EXPERIMENTS

In order to compare foam models during transient foam experiments, the LE version of Chen *et al.* population balance model was implemented in the numerical simulator UTCHEM and was verified with Chen *et al.* experimental data. Next, results using the Chen *et al.* PB model are compared with the UT foam model.

5.6.1 Chen *et al.* Experiment (2010)

The implementation of Chen *et al.* model in UTCHEM was verified with the experimental data presented in their paper. The experiment started with flushing the core with a large volume (> 20 PV) of 0.5 wt% brine to remove all the gas and surfactant from the core. Next, brine was replaced by surfactant solution to saturate the core. The aqueous surfactant (foamer) solution contains 1.0% active Stepan Bioterg AS40 (sodium C₁₄₋₁₆ olefin sulfonate) in 0.5 wt% NaCl (J.T Baker) brine. 15 to 20 PV of surfactant solution was injected into a Berea sandstone core to satisfy the surfactant adsorption to the rock. Then, nitrogen and aqueous surfactant solution were co-injected continuously into the pre-saturated core at liquid rate of 0.125 m/day, gas rate of 1.125 m/day, and 2.07 MPa backpressure. The pressure drop was measured during the experiment. An X-ray CT scanner provided in-situ measurements of aqueous phase saturation. Table 5.11 lists rock

and fluid properties for this experiment. The following form of the J -function approximate the capillary pressure relation for this experiment.

$$J(S_w) = \frac{P_c}{\sigma} \left(\frac{k}{\phi} \right)^{1/2} = \left(\frac{0.022}{S_w - 0.15} \right)^{0.2} \quad (5-45)$$

where σ is the surface tension of the surfactant solution and is about 33 mN/m in this experiment.

Chen *et al.*'s foam model parameters were used to history match the experimental data which are listed in Table 5.12 (field units were used in UTCHEM). Figure 5.20 and Figure 5.21 compare the experimental data of water saturation and pressure drop with population-balance simulation results. The simulation results fit the experimental data reasonably well. Figure 5.22 also shows the flowing foam texture profiles from the simulation. The results are very consistent with Chen *et al.* simulations.

Next, the UT foam model was used to simulate the same experiment. Table 5.13 lists UT foam model parameters used in the simulation. Figure 5.23 and Figure 5.24 compare the experimental data of water saturation and pressure drop with UT foam model simulation. The results show, the simpler UT foam model can also provide a good quality match with experimental data.

5.6.2 Effect of Foam Injection on Oil Recovery (Farajzadeh *et al.* 2010)

Farajzadeh *et al.* (2010) studied the effect of foam injection on oil recovery using N₂ and CO₂. In their experiment, the surfactant slug was followed by CO₂ or N₂ to a core containing water-flood residual oil. In this section, the experimental data of N₂-foam enhanced oil recovery is modeled.

The core was Bentheimer sandstone outcrop with 17 cm length and 4 cm diameter. The permeability to brine was 1010 mD and average porosity was $22 \pm 0.2\%$. The core was initially flushed with CO₂ for at least 30 min to replace the air in the system. Afterward, about 20 pore volumes of brine ($q_w = 2$ mL/min) were injected into the system to dissolve and remove all CO₂. After core was saturated with brine, it was flushed with oil ($q_o = 0.5$ ml/min) to displace the brine. Next, the brine ($q_w = 2$ mL/min) was injected from the bottom of the core until no more oil was produced and pressure drop along the core was constant. $47 \pm 2\%$ of oil was produced during the water injection with residual oil saturation of $32 \pm 2\%$.

After water flooding, 1-2 PV of surfactant solution (0.5 wt% AOS and 3 wt% of NaCl) was injected from the bottom of the core at rate of 2 mL/min at atmospheric pressure and room temperature. The injection of surfactant did not recover additional oil since the reduction in interfacial tension was not substantial. Finally, N₂ was injected into the core previously flushed with surfactant to generate foam in situ. Using N₂-foam leads to an additional recovery of $9.0 \pm 0.5\%$ of initial oil (total recovery = $56 \pm 2\%$).

Chen *et al.* population balance model was used to history match the oil recovery and pressure drop in Farajzadeh *et al.* (2010) experiment. Table 5.14 lists rock and fluid properties used in the simulations. The presence of the oil destabilizes the lamella and increases the rate of foam coalescence. Chen (2009) suggested the following expression to address the additional foam coalescence in presence of oil.

$$r_{co} = k_{-2}^0 \left(\frac{S_o - S_{or}}{S_{oi} - S_o} \right) |v_f| n_f \quad (5-46)$$

where k_{-2}^0 is the number of oil-gas contact sites per volume of gas. Therefore, the total foam coalescence rate is the summation of the coalescence rate due to water dry-out near

the limiting water saturation in Equation (5-14), and the coalescence rate due to the presence of oil in Equation (5-46).

Figure 5.25 and Figure 5.26 compare the experimental data of oil recovery and pressure drop with simulation results of Chen *et al.* foam model. The foam model parameters used in this simulation are listed in Table 5.15. The same form of the J -function in Equation (5-45) was used for this experiment. The model parameters of ω , n^* , $X_{t,max}$, and $P_{c,max}^*$ were picked from the Chen *et al.* (2010) experiment. k_{2^o} was picked from the data of Chen (2009). The values of k_1^o , k_{1^o} , and α were then updated to history match the coreflood experiment.

Next, the UT foam model was used to simulate this experiment. In UT foam model, foam completely collapses for the oil saturations above critical oil saturation (S_o^*). In this research, the following expression is suggested to reduce the foam resistance factor in presence of oil.

$$R = \begin{cases} R_{\max} & S_o \leq \text{SLOIL} \\ 1 + \left(\frac{S_o - \text{SMOIL}}{\text{SLOIL} - \text{SMOIL}} \right)^{\text{EXPOIL}} (R_{\max} - 1) & \text{SLOIL} < S_o < \text{SMOIL} \\ 1 & S_o \geq \text{SMOIL} \end{cases} \quad (5-47)$$

where SLOIL is the maximum oil saturation below that foam is not affected by oil ($R = R_{\max}$). SLOIL is equivalent to S_{or} in Equation (5-46). SMOIL is the minimum oil saturation above that foam completely collapses ($R = 1$). The foam resistance factor is scaled for the oil saturations between SLOIL and SMOIL, and EXPOIL is the model parameter.

Figure 5.27 and Figure 5.28 compare the experimental data of oil recovery and pressure drop with the simulation results of UT foam model. The foam model parameters

are listed in Table 5.16. Foam was assumed to be Newtonian in the simulation to reduce the number of foam model parameters (the shear thinning factor $\sigma = 1$, hence, the simulation results are not dependent to the value of $u_{g,ref}$). Figure 5.29 shows the effect of oil on the foam resistance factor in this simulation. SLOIL was set to the value of residual oil saturation and other parameters were determined to history match the experimental data.

5.7 SUMMARY AND CONCLUSIONS

Implicit-texture (IT) models are often perceived as not reflecting the essential physics of foam in porous media. Although only population balance models can represent the entrance region, dynamics at shock fronts, the process of foam generation, and regions in heterogeneous media -where abrupt heterogeneities mean that foam is not at local equilibrium-, in this study we focus on the range of steady state data. IT models all assume local equilibrium (LE). Therefore, we compare IT and LE version of population-balance (PB) models. The main conclusions are:

- The ultimate test of a model's usefulness is its ability to match the laboratory data. We showed both IT models and PB models at LE matched the steady state experimental data for CO₂ and N₂ foam presented here equally well. The corresponding parameters of the different foam models were also discussed.
- The original Vassenden-Holt model did not match the data in low-quality regime until an exponent a was introduced in the velocity term.
- The trapping parameter in the Chen *et al.* model does not play an essential part of the data-fitting procedure and can be ignored.

- Vassenden-Holt and Chen *et al.* models did not essentially predict the limiting water saturation (S_w^*) close to water saturation in high quality regime.
- Dimensionless foam bubble density was defined in IT models to derive explicitly the foam-coalescence-rate function implicit in these models. The results show the IT models that incorporate an abrupt change in foam properties can be recast as LE versions of population-balance models with a lamella-destruction function similar to those in current PB models. In other words, both types of models, at least in the LE approximation and without oil, equally honor the physics of foam behavior in porous media.
- Both Chen *et al.* model at LE and UT model successfully history matched the transient foam coreflood experiments.
- Population balance models often require more input parameters and is more difficult to tune the foam parameters compared to IT models.

NOMENCLATURE

| | |
|------------|--|
| a | = shear-thinning exponent in Vassenden-Holt model |
| b | = capillary pressure model parameters |
| c_c | = coalescence rate constant |
| c_g | = generation rate constant in Kam <i>et al.</i> and Kam model |
| C_s | = surfactant concentration |
| C_s^* | = threshold surfactant concentration in UT model |
| C_s^o | = reference surfactant concentration in Chen <i>et al.</i> model |
| $epcap$ | = exponent in factor (F_5) representing shear-thinning in STARS model |
| $epdry$ | = factor governing abruptness of dry-out calculation (F_2) in STARS model |
| F | = foam mobility multiplier in Vassenden- Holt model |
| f | = destruction function |
| F' | = function in Vassenden-Holt model reflecting foam texture but non-Newtonian effects |
| F_2 | = dry-out function in STARS model |
| F_5 | = shear-thinning function in STARS model |
| FM | = mobility reduction factor in STARS model |
| $fmcap$ | = reference capillary number in STARS model |
| $fmdry$ | = reference water saturation in dry-out calculation (F_2) in STARS model |
| $fmmob$ | = maximum resistance factor in STARS model |
| F_o | = foam mobility constant in Vassenden-Holt model |
| k | = Permeability |
| k_1 | = generation rate coefficient in Chen <i>et al.</i> model |
| $k_{.1}$ | = coalescence coefficient in Chen <i>et al.</i> model |
| k_1^o | = model parameter in Chen <i>et al.</i> model |
| $k_{.1}^o$ | = model parameter in Chen <i>et al.</i> model |
| k_{rg} | = gas relative permeability in absence of foam |
| k_{rg}^f | = gas relative permeability in presence of foam |
| k_{rg}^o | = gas endpoint relative permeability |
| m | = model parameter Kam <i>et al.</i> Model |
| n | = coalescence exponent in Kam <i>et al.</i> and Kam model |
| n^* | = limiting (maximum) lamella density in Chen <i>et al.</i> model |
| N_{ca} | = capillary number |

| | |
|--------------|---|
| n_D | = dimensionless lamella density |
| n_f | = number density of lamellae (lamellae/volume gas) |
| n_f^* | = reference lamella density used in definition of n_D |
| n_g | = gas exponent relative permeability |
| n_{max} | = Maximum foam lamella density in Kam model |
| n_t | = number density of trapped foam bubbles |
| n_w | = water exponent relative permeability |
| P_c | = capillary pressure |
| P_c^* | = limiting capillary pressure |
| P_{ce} | = entry capillary pressure |
| P_{cmax}^* | = limiting value of P_c^* in Chen <i>et al.</i> model |
| Q_b | = source/sink term for foam bubbles |
| q_f | = net rate of generation of foam bubbles |
| R | = foam resistance factor in UT model |
| r_c | = foam coalescence rate |
| RF | = mobility reduction factor |
| r_g | = foam generation rate |
| r_{gD} | = dimensionless foam generation rate |
| R_{ref} | = reference foam resistance factor at reference gas velocity in UT model |
| s_1 | = slope of the gas relative permeability at high quality regime in Vassenden-Holt model |
| s_2 | = slope of the gas relative permeability at low quality regime in Vassenden-Holt model |
| S_f | = flowing gas saturation or lowest water saturation for foam effect in Vassenden-Holt model |
| S_{fD} | = dimensionless gas saturation in the presence of foam |
| S_{gD} | = dimensionless gas saturation |
| S_t | = trapped gas saturation |
| S_w | = water saturation |
| S_w^* | = limiting water saturation |
| S_{wc} | = connate water saturation |
| S_{wD} | = dimensionless water saturation |
| u_f | = Darcy velocity of gas in foam |
| u_g | = gas Darcy velocity |

| | |
|----------------|--|
| u_{gref} | = reference gas Darcy velocity |
| u_w | = water Darcy velocity |
| v_f | = local gas velocity |
| v_w | = local water velocity |
| x | = vector of foam model parameters |
| X_t | = trapping foam fraction Chen <i>et al.</i> model |
| $X_{t,max}$ | = maximum trapping fraction in Chen <i>et al.</i> model |
| α | = proportionality constant |
| β | = trapping parameter Chen <i>et al.</i> model |
| ε | = width of high-quality regime in UT model (in terms of S_w) |
| λ | = capillary pressure model parameters |
| μ_f | = gas viscosity in the presence of foam |
| μ_f^{app} | = apparent viscosity of foam, treated as a single phase |
| μ_g | = gas viscosity in the absence of foam |
| σ | = power-law exponent in UT model |
| σ_{co2} | = CO ₂ -water surface tension |
| σ_{N2} | = N ₂ -water surface tension |
| Φ | = objective function for the optimization of foam model |
| ω | = constant exponent in Chen <i>et al.</i> Model |
| ∇P | = pressure gradient |
| ∇P_o | = model parameters related to minimum pressure gradient in Kam model |

Table 5.3: Rock and fluid properties for experimental data

| Parameters | Moradi-Araghi <i>et al.</i> | Alvarez <i>et al.</i> |
|-------------------------------|-----------------------------|-----------------------|
| <i>gas</i> | CO ₂ | N ₂ |
| <i>k</i> (md) | 551.5 | 530 |
| <i>u_t</i> (ft/day) | 5 | 2.5 |
| μ_w (cp) | 0.65 | 0.7 |
| μ_g (cp) | 0.05 | 0.02 |
| <i>S_{wr}</i> | 0.1 | 0.2 |
| <i>S_{gr}</i> | 0.05 | 0.2 |
| k_{rw}^o | 0.22 | 0.2 |
| k_{rg}^o | 1.0 | 0.94 |
| <i>n_w</i> | 4 | 4.2 |
| <i>n_g</i> | 1.83 | 1.3 |
| σ (dyne/cm) | 5 | 30 |

Table 5.4: UT model parameters to match experimental data

| Parameters | Moradi-Araghi <i>et al.</i> | Alvarez <i>et al.</i> |
|-------------------------------------|-----------------------------|-----------------------|
| <i>R_{ref}</i> | 8.4×10^3 | 5.6×10^4 |
| <i>S_w[*]</i> | 0.264 | 0.31 |
| ε | 0.015 | 0.002 |
| <i>u_{g,ref}</i> (ft / day) | 1.0 | 1.0 |
| σ | 0.8 | 0.6 |

Table 5.5: STARS model parameters to match experimental data

| Parameters | Moradi-Araghi <i>et al.</i> | Alvarez <i>et al.</i> |
|----------------|-----------------------------|-----------------------|
| <i>fmmob</i> | 1.58×10^4 | 1.6×10^5 |
| <i>fmdry</i> | 0.265 | 0.31 |
| <i>epdry</i> | 100 | 500 |
| <i>fmcap</i> * | 2.46×10^{-5} | 2.46×10^{-5} |
| <i>epcap</i> | 0.2 | 0.5 |

* *fmcap* is a reference capillary pressure below which shear-thinning is ignored. The choice of this reference also affects the value of *fmmob*

Table 5.6: Vassenden-Holt model parameters to match experimental data

| Parameters | <i>Moradi-Araghi et al.</i> | | <i>Alvarez et al.</i> | |
|------------|-----------------------------|----------------------|-----------------------------|----------------------|
| | Original Model ($a=1$) | Modified Model | Original Model ($a=1$) | Modified Model |
| F_o | 4.5×10^{-5} | 1.2×10^{-4} | 1.23×10^{-5} | 1.8×10^{-5} |
| S_f | 0.235 | 0.235 | 0.286 | 0.286 |
| s_1 | 280 | 280 | 500 | 500 |
| s_2 | 0.1 | 0.1 | 0.1 | 0.1 |
| u_{go} | 1.0 | 1.0 | 1.0 | 1.0 |
| a | 1.0 | 0.2 | 1.0 | 0.35 |

Table 5.7: Chen *et al.* (2010) Model Parameters to Fit Experimental Data

| Parameters | <i>Moradi-Araghi et al.</i> | | | <i>Alvarez et al.</i> | | |
|------------------------------------|-----------------------------|----------------------|----------------------|-----------------------|-----------------------|-----------------------|
| | set # 1 | set # 2 | set # 3 | set # 1 | set # 2 | set # 3 |
| $k_1^o (ft^{-13/3} day)$ | 8×10^{11} | 8×10^{11} | 8×10^{11} | 9×10^{11} | 9×10^{11} | 9×10^{11} |
| $k_{-1}^o (ft^{-1})$ | 3×10^{-3} | 3×10^{-3} | 1.5 | 2×10^{-6} | 2×10^{-6} | 3×10^{-3} |
| $n^* (ft^{-3})$ | 5.4×10^{11} | 1.9×10^{12} | 1.9×10^{12} | 5.4×10^{11} | 1.34×10^{12} | 1.34×10^{12} |
| $P_c^* (psi)$ | 0.19 | 0.20 | 0.8 | 0.55 | 0.555 | 0.8 |
| $X_{r,max}$ | 0.5 | 0 | 0 | 0.5 | 0 | 0 |
| β | 1×10^{-9} | - | - | 1×10^{-9} | - | - |
| $\alpha (ft^{10/3} day^{-1/3} cp)$ | 5×10^{-10} | 5×10^{-10} | 5×10^{-10} | 1.7×10^{-9} | 1.7×10^{-9} | 1.7×10^{-9} |

Table 5.8: Kam *et al.* (2007) parameters to fit experimental data

| Parameters | <i>Moradi-Araghi et al.</i> | <i>Alvarez et al.</i> |
|------------------------------------|-----------------------------|------------------------|
| c_g / c_c | 8×10^{16} | 8×10^{16} |
| S_w^* | 0.262 | 0.31 |
| n | 0.04 | 0.01 |
| m | 0.7 | 0.2 |
| $\alpha (ft^{10/3} day^{-1/3} cp)$ | 6×10^{-16} | 2.45×10^{-14} |

Table 5.9: Kam (2008) model parameters to fit experimental data

| Parameters | Moradi-Araghi <i>et al.</i> | Alvarez <i>et al.</i> |
|--|-----------------------------|-----------------------|
| $c_g/2c_c$ | 2.3×10^{15} | 2.3×10^{15} |
| S_w^* | 0.268 | 0.31 |
| n | 0.045 | 0.01 |
| ∇P_o (psi) | 0.01 | 0.01 |
| n_{\max} (ft^{-3}) | 5.4×10^{11} | 5.4×10^{11} |
| α ($ft^{10/3} day^{-1/3} cp$) | 4.57×10^{-13} | 4.2×10^{-9} |

Table 5.10: The Value of Limiting Water Saturation at Different Model

| Model | S_w^* (Moradi-Araghi) | S_w^* (Alvarez <i>et al.</i>) |
|--------------------|-------------------------|----------------------------------|
| UT | 0.264 | 0.310 |
| STARS | 0.265 | 0.310 |
| Vassenden-Holt | 0.235 | 0.286 |
| Chen <i>et al.</i> | 0.219-0.265 | 0.284-0.310 |
| Kam <i>et al.</i> | 0.262 | 0.310 |
| Kam | 0.268 | 0.310 |

Table 5.11: Rock and fluid properties in Chen *et al.* experiment

| Parameter | Value |
|-------------------|-------|
| core length (m) | 0.6 |
| core diameter (m) | 0.05 |
| k (md) | 304 |
| ϕ | 0.18 |
| S_{wc} | 0.38 |
| μ_w (cp) | 1.0 |
| μ_g (cp) | 0.018 |
| n_w | 3 |
| n_g | 3 |
| k_{rw}^o | 0.7 |
| k_{rg}^o | 1 |

Table 5.12: Population-balance foam model parameters for Chen *et al.* experiment

| Parameter | Value | SI Unit | Value | Field Unit |
|---------------|-----------------------|-----------------------|------------------------|---------------------------|
| k_l^o | 1.65×10^{15} | $S^{1/3} m^{-13/3}$ | 2.17×10^{11} | $day^{1/3} ft^{-13/3}$ |
| k_{-l}^o | 10 | m^{-1} | 3.05 | ft^{-1} |
| $P_{c,max}^*$ | 3×10^4 | Pa | 4.35 | psi |
| α | 7.4×10^{-18} | $Pa S^{2/3} m^{10/3}$ | 1.72×10^{-11} | $cp day^{-1/3} ft^{10/3}$ |
| $X_{t,max}$ | 0.78 | - | 0.78 | - |
| C_s^o | 0.083 | wt% | | |
| n^* | 1.0×10^{12} | m^{-3} | 2.83×10^{10} | ft^{-3} |
| ω | 3.0 | - | 3 | - |

Table 5.13: UT foam model parameters for Chen *et al.* experiment

| Parameters | Value |
|------------------------|-------|
| R_{ref} | 48 |
| C_s^* (volume frac.) | 0.001 |
| ε | 0.01 |
| $u_{g,ref}$ (ft/day) | 1.0 |
| σ | 1.0 |
| S_w^* | 0.39 |

Table 5.14: Rock and fluid properties in Farajzadeh *et al.* experiment

| Parameter | Value | Parameter | Value |
|--------------------|-------|------------|-------|
| core length (cm) | 17 | S_{org} | 0.3 |
| core diameter (cm) | 4 | S_{rg} | 0.15 |
| k (md) | 1010 | k_{rw}^o | 0.1 |
| ϕ | 0.22 | k_{ro}^o | 0.8 |
| μ_w (cp) | 1.09 | k_{rg}^o | 1.0 |
| μ_o (cp) | 1.35 | n_w | 2.5 |
| μ_g (cp) | 0.018 | n_o | 1.5 |
| S_{wr} | 0.28 | n_g | 1.3 |
| S_{orw} | 0.32 | | |

Table 5.15: Chen *et al.* foam model parameters to history match Farajzadeh *et al.* experiment

| Parameter | Value |
|---|---------|
| k_{l}^o (day ^{1/3} ft ^{-13/3}) | 1.5E+15 |
| k_{-1}^o (ft ⁻¹) | 1.0 |
| k_{-2}^o (ft ⁻¹) | 0.03 |
| $P_{c,max}^*$ (psi) | 4.35 |
| α (cp day ^{-1/3} ft ^{10/3}) | 2.0E-11 |
| $X_{t,max}$ | 0.78 |
| C_s^o (volume frac.) | 0.001 |
| n^* (ft ⁻³) | 1.0E+12 |
| ω | 3 |

Table 5.16: UT foam model parameters to history match Farajzadeh *et al.* experiment

| Parameters | Value |
|------------------------|-------|
| R_{ref} | 2500 |
| C_s^* (volume frac.) | 0.001 |
| ε | 0.01 |
| $u_{g,ref}$ (ft/day) | 1.0 |
| σ | 1.0 |
| S_w^* | 0.30 |
| SLOIL | 0.32 |
| SMOIL | 0.5 |
| EXPOIL | 1.8 |

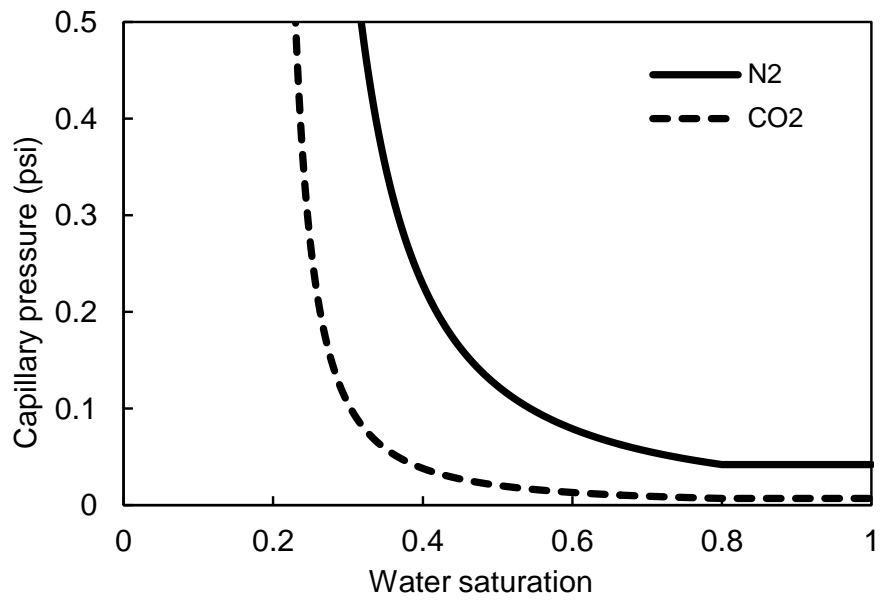


Figure 5.1: Capillary-pressure curves used to model CO₂ and N₂ foam experiments

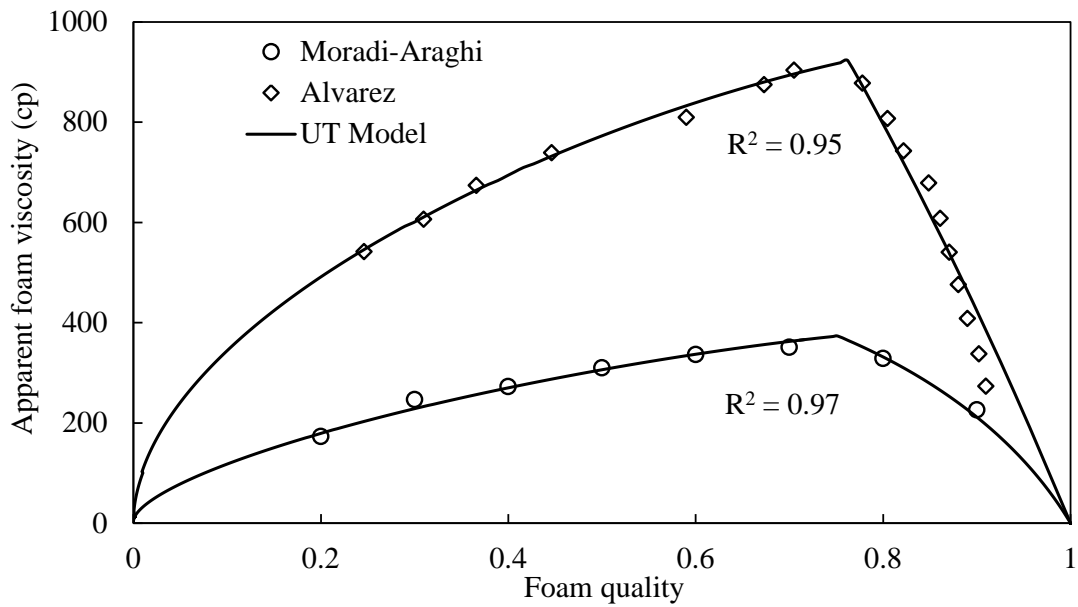


Figure 5.2: UT model fit to experimental data using the parameters in Table 5.4

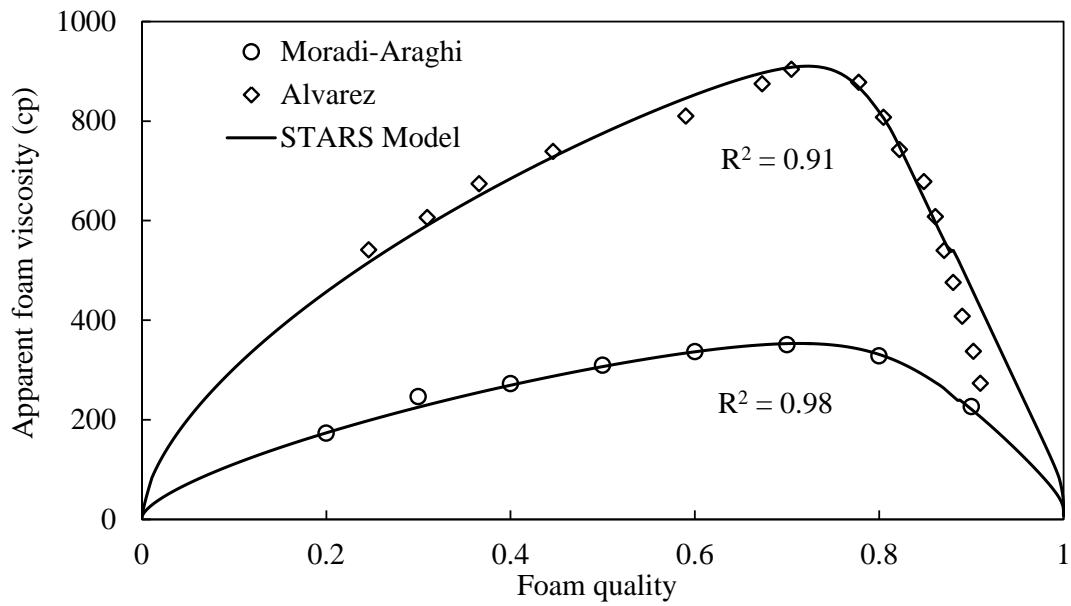


Figure 5.3: STARS model fit to experimental data using the parameters in Table 5.5

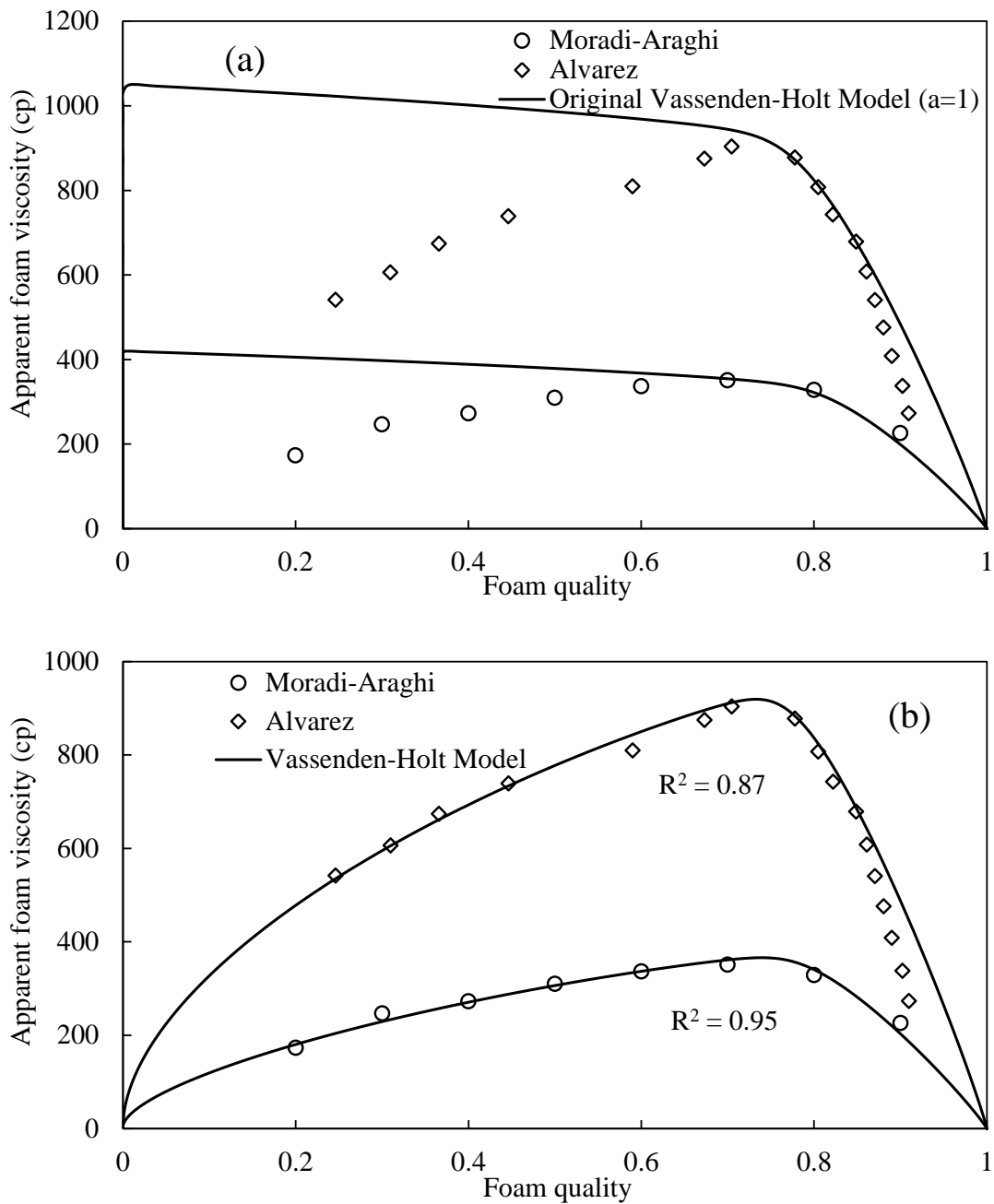


Figure 5.4: a) Vassenden-Holt model fit to experimental data using the parameters in Table 5.6, assuming $a = 1$ in Equation (5-8) b) Vassenden-Holt model fit to experimental data using the parameters in Table 5.6, including a .

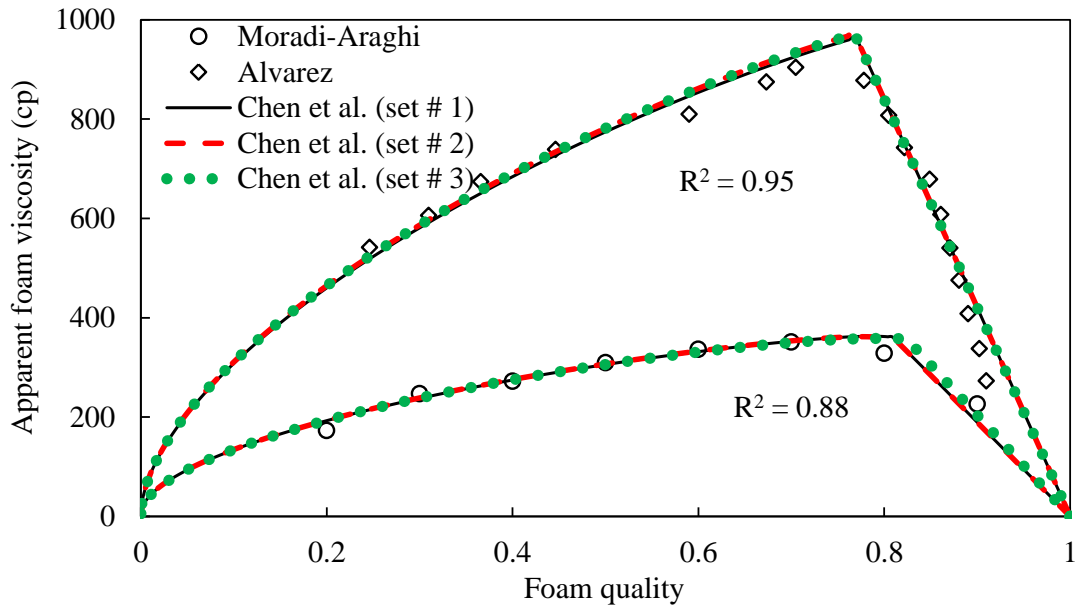


Figure 5.5: Chen *et al.* model fit to experimental data using the parameters in Table 5.7

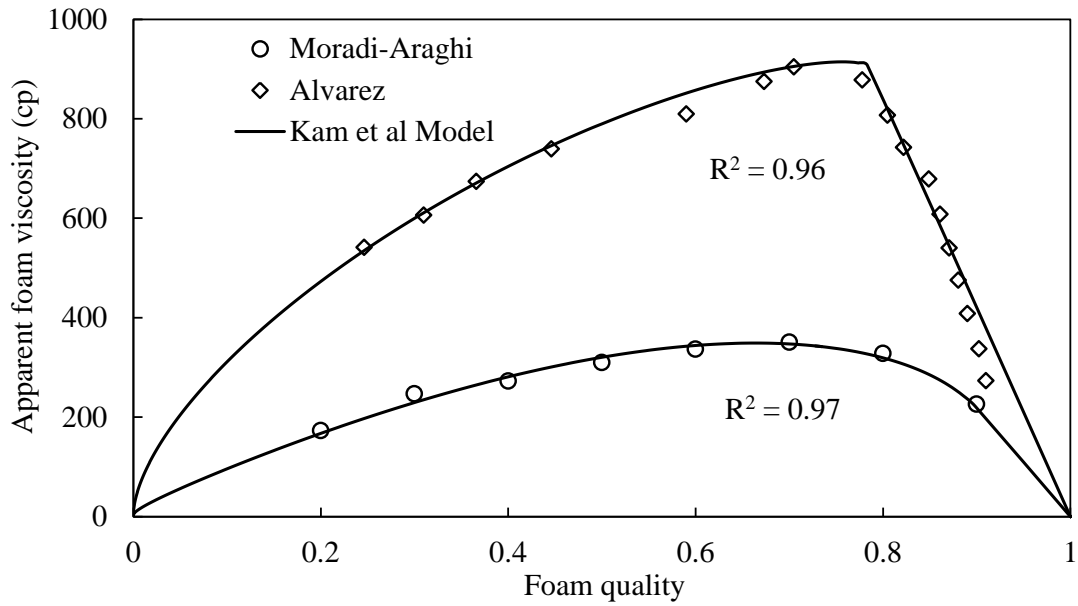


Figure 5.6: Kam *et al.* model fit to experimental data using the parameters in Table 5.8

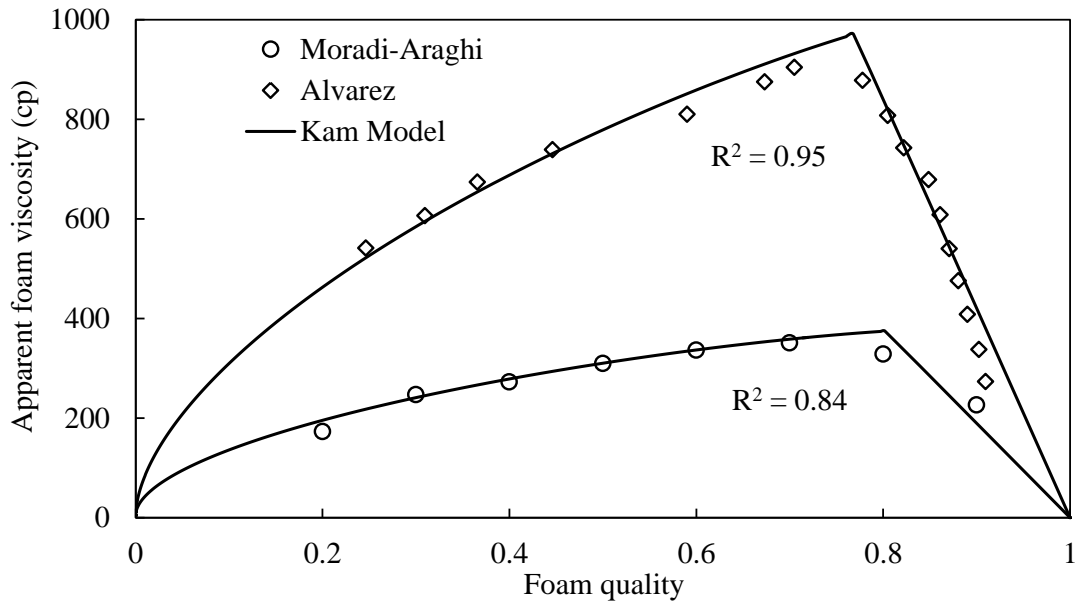


Figure 5.7: Kam model fit to experimental data using the parameters in Table 5.9

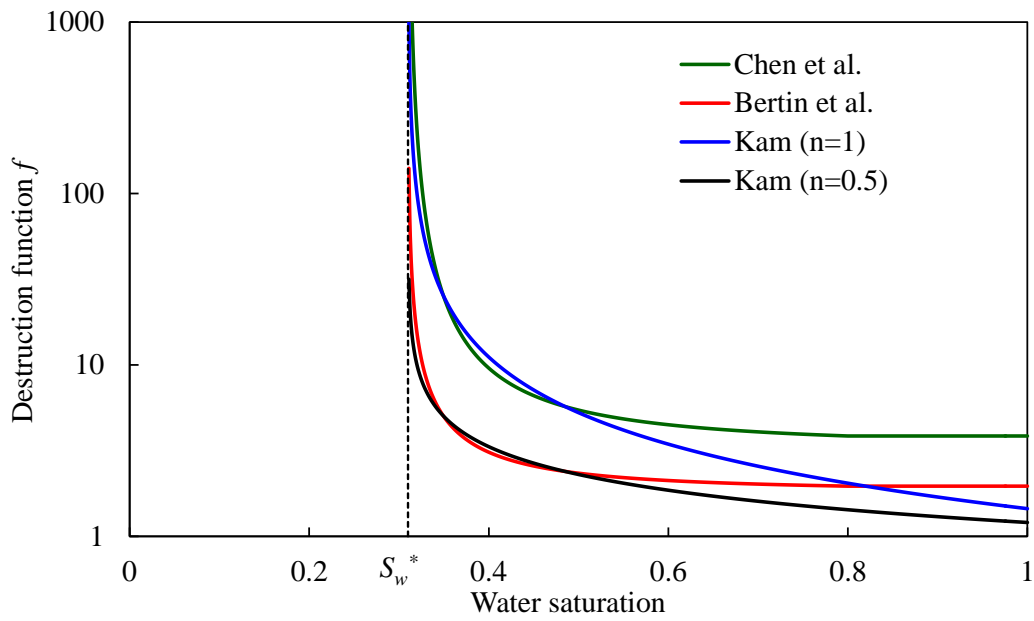


Figure 5.8: Lamella-destruction function f in different population balance models plotted as a function of water saturation. Vertical dotted line represents S_w^*

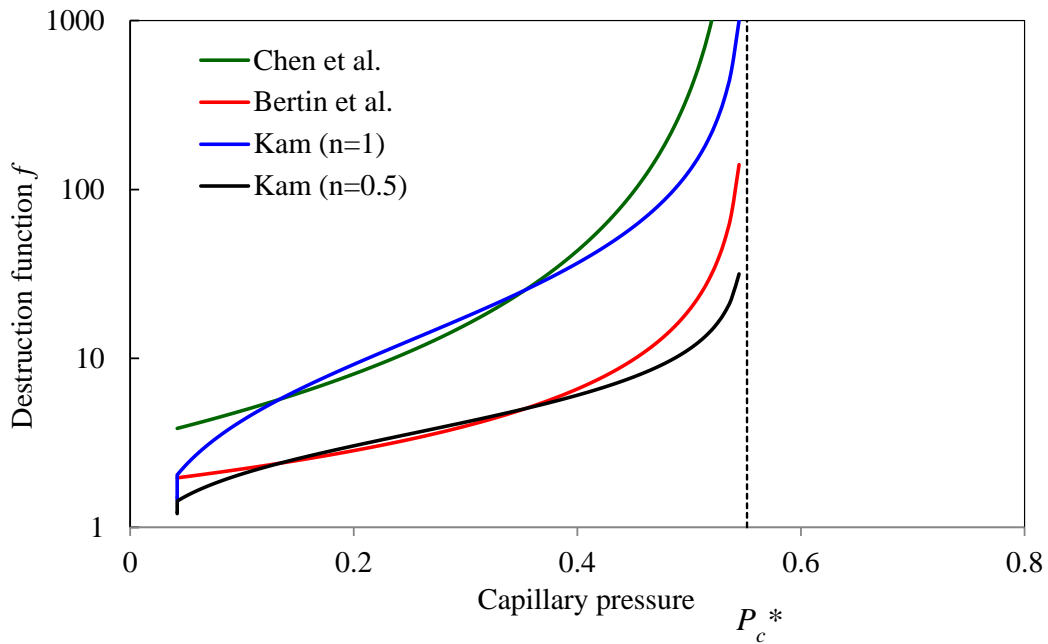


Figure 5.9: Lamella-destruction function f in different population-balance models plotted as a function of capillary pressure. Vertical dotted line represents P_c^*

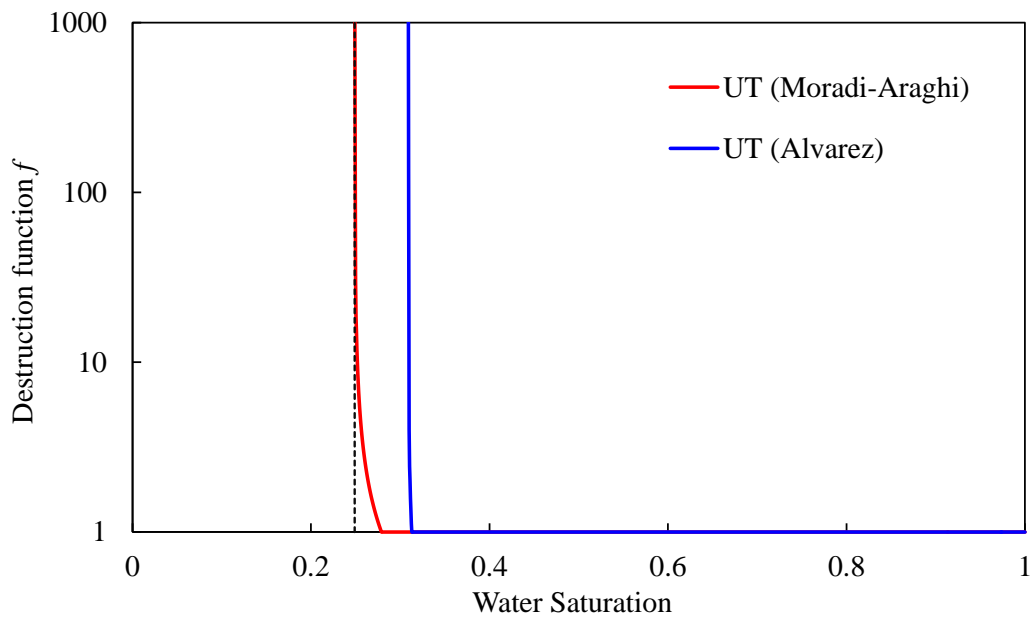


Figure 5.10: Lamella-destruction function f implied by the UT foam model plotted as a function of water saturation. Vertical dotted lines represent $S_w^* - \varepsilon$

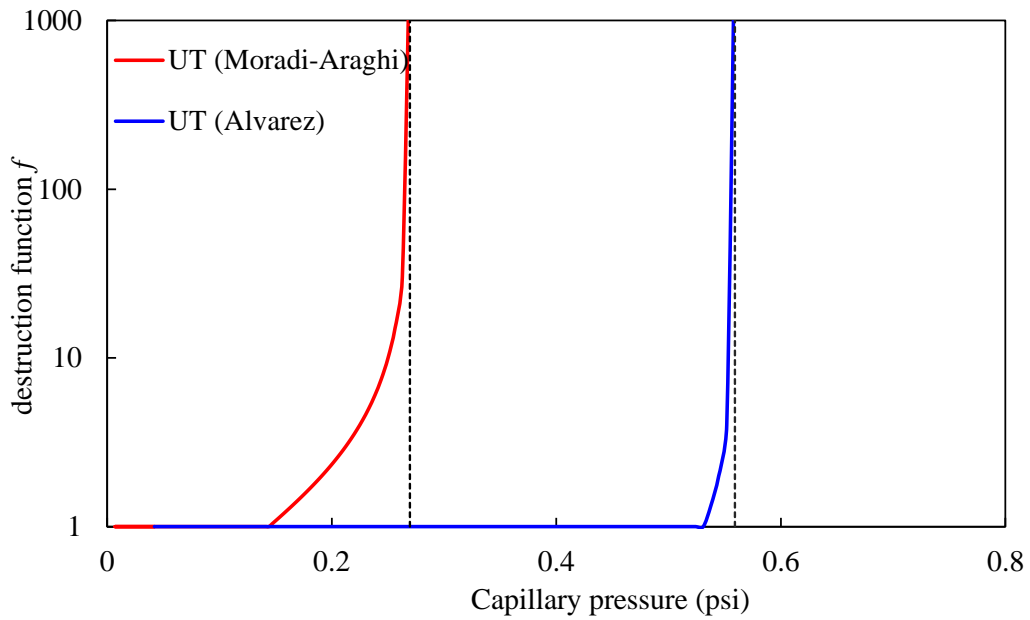


Figure 5.11: Lamella-destruction function f implied by the UT foam model plotted as a function of capillary pressure. Vertical dotted lines represent the capillary pressure at $S_w^* - \varepsilon$

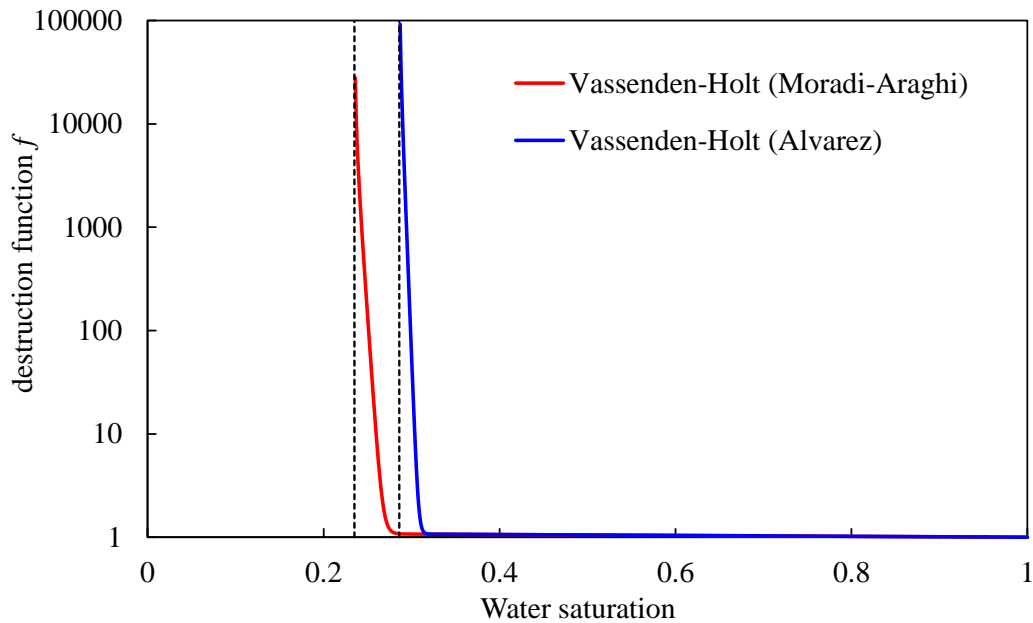


Figure 5.12: Lamella-destruction function f implied by the Vassenden-Holt foam model plotted as a function of water saturation. The vertical dotted lines is S_f

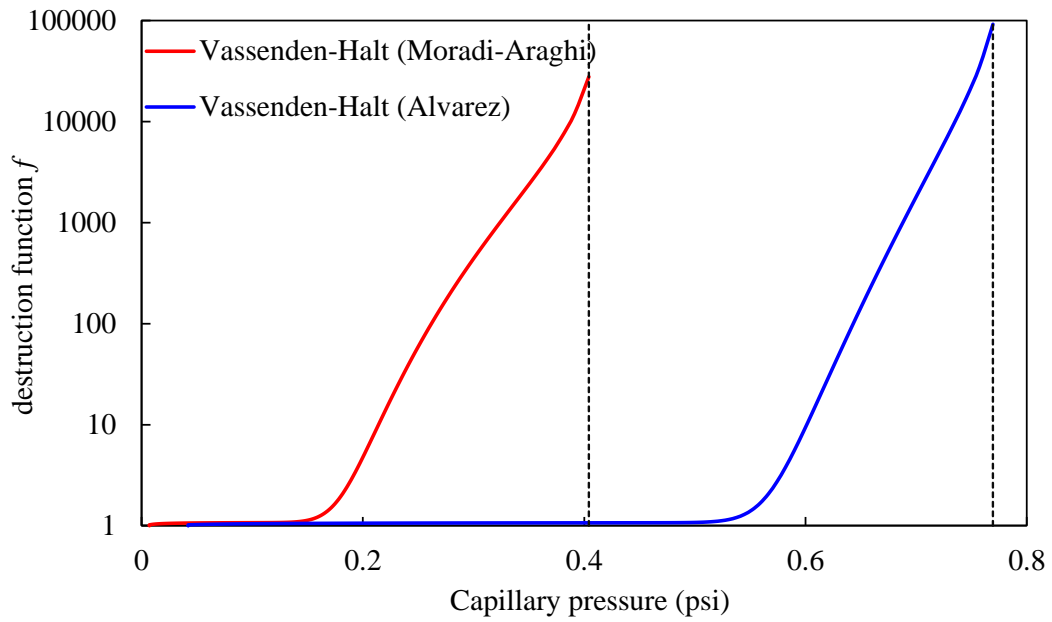


Figure 5.13: Lamella-destruction function f implied by the Vassenden-Holt foam model plotted as a function of capillary pressure. The vertical dotted lines represent the capillary pressure at S_f

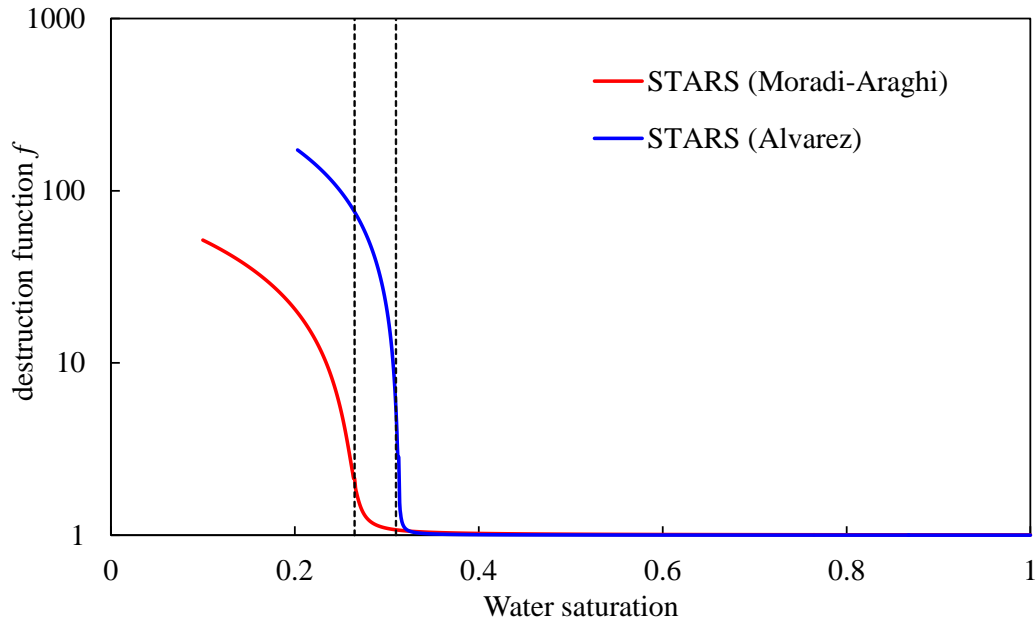


Figure 5.14: Lamella-destruction function f implied by the STARS foam model plotted as a function of water saturation. The vertical dotted lines represent f_{mdry} .

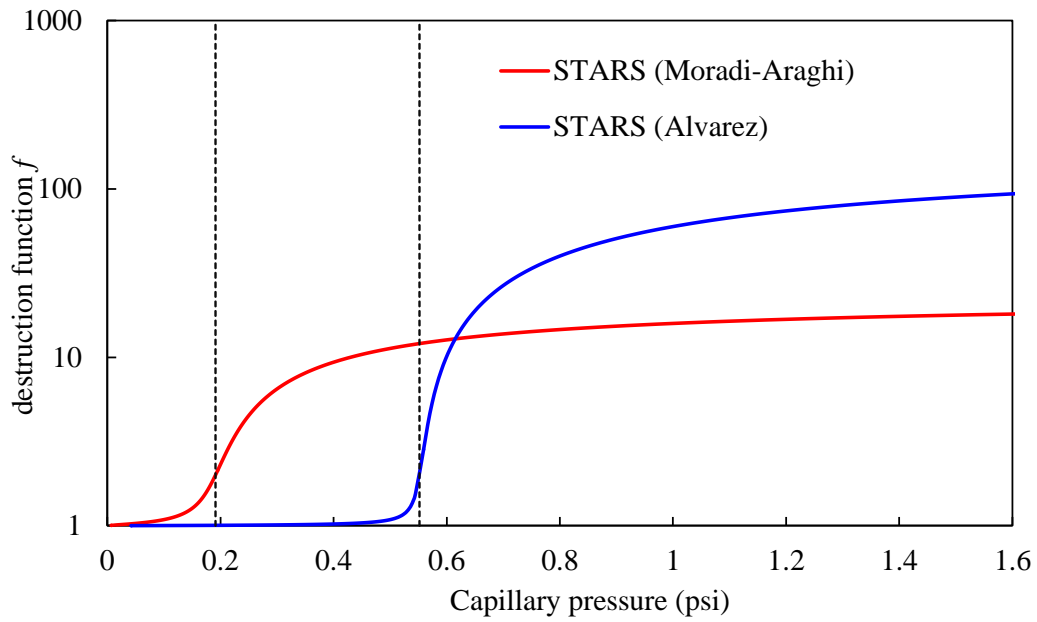


Figure 5.15: Lamella-destruction function f implied by the STARS foam model plotted as a function of capillary pressure. The vertical dotted lines represent capillary pressure at f_{mdry} .

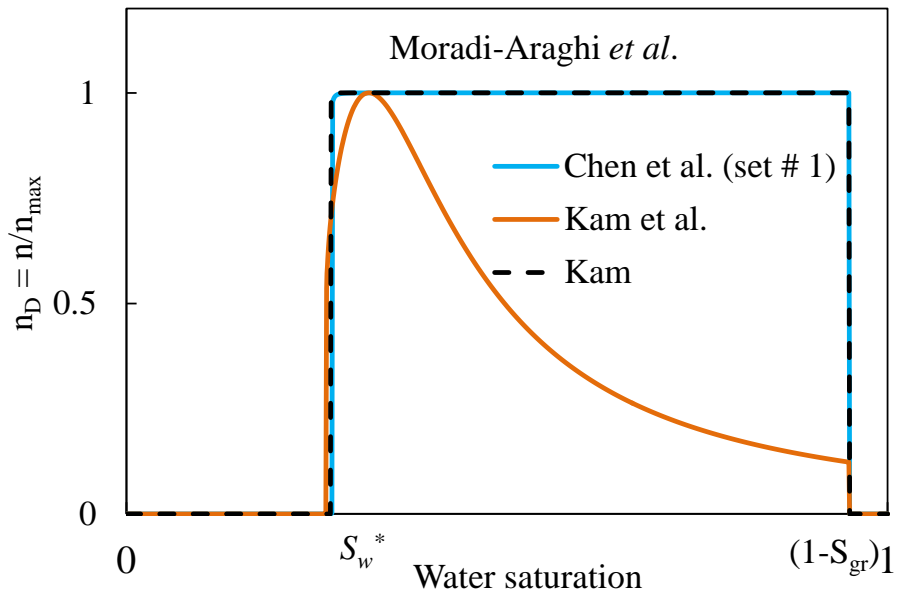


Figure 5.16: Dimensional foam texture obtained in population-balance models to fit Moradi-Araghi *et al.* experiment.

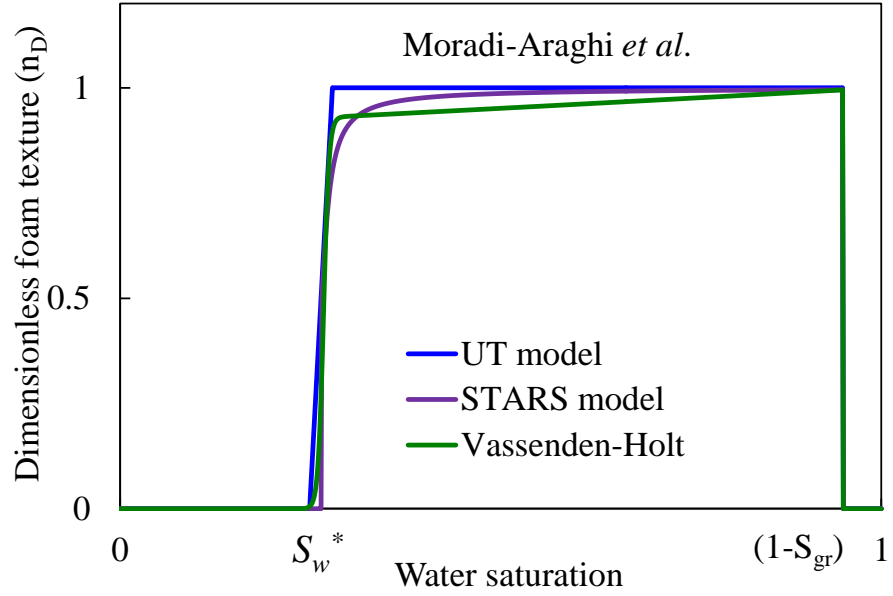


Figure 5.17: Explicit dimensionless foam texture defined in implicit texture models to fit Moradi-Araghi *et al.* experiment.

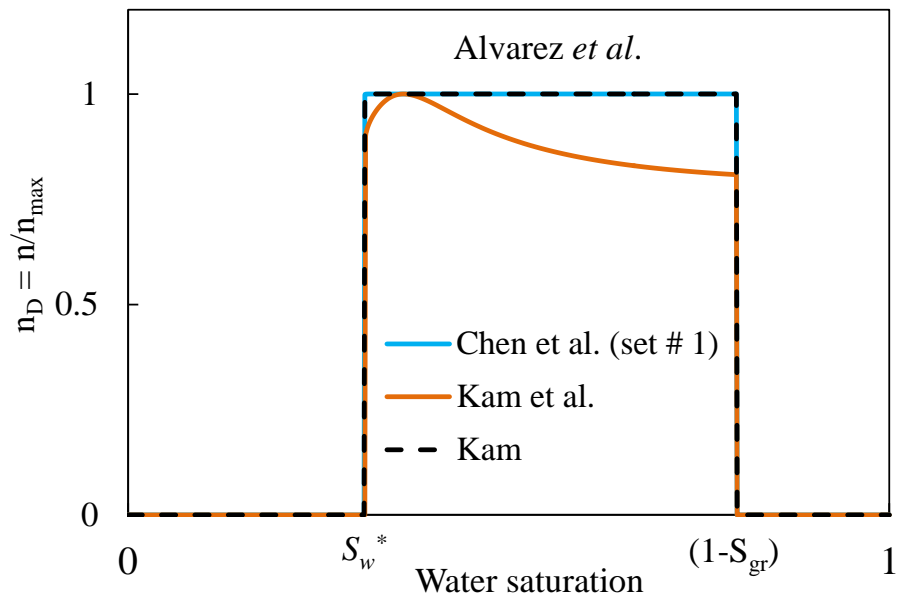


Figure 5.18: Dimensional foam texture obtained in population-balance models to fit Alvarez *et al.* experiment.

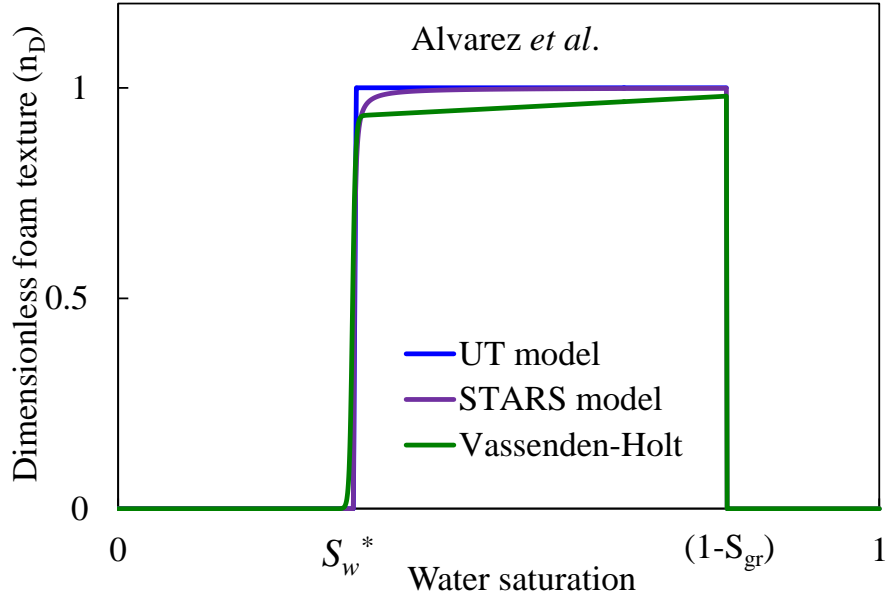


Figure 5.19: Explicit dimensionless foam texture defined in implicit texture models to fit Alvarez *et al.* experiment.

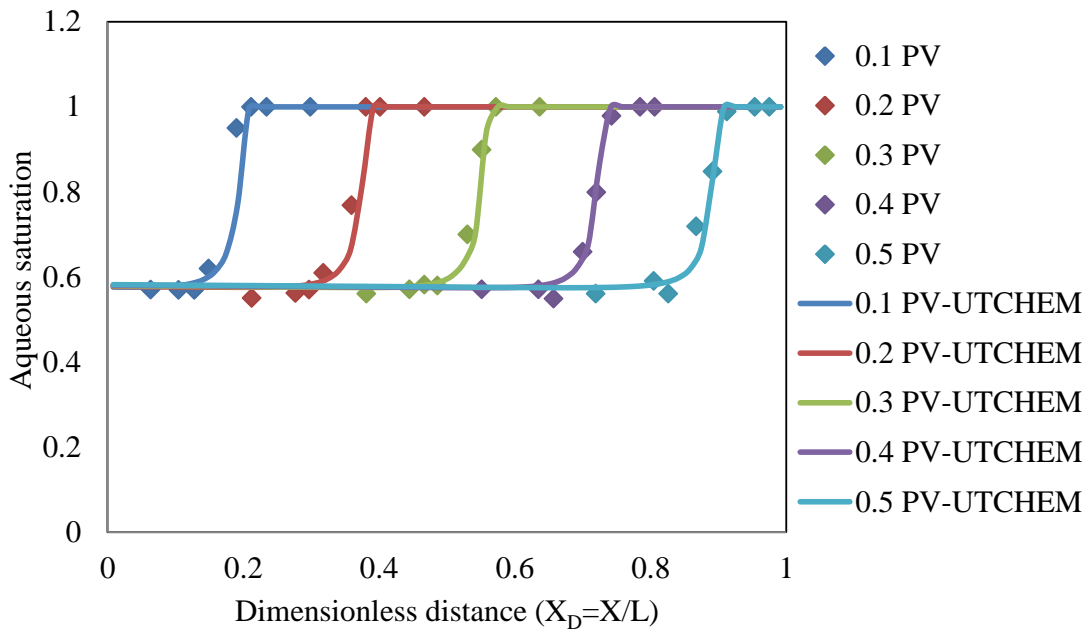


Figure 5.20: Transient aqueous phase saturation (experimental data from Chen *et al.* 2010 vs. simulation results using LE Chen *et al.* model in this work)

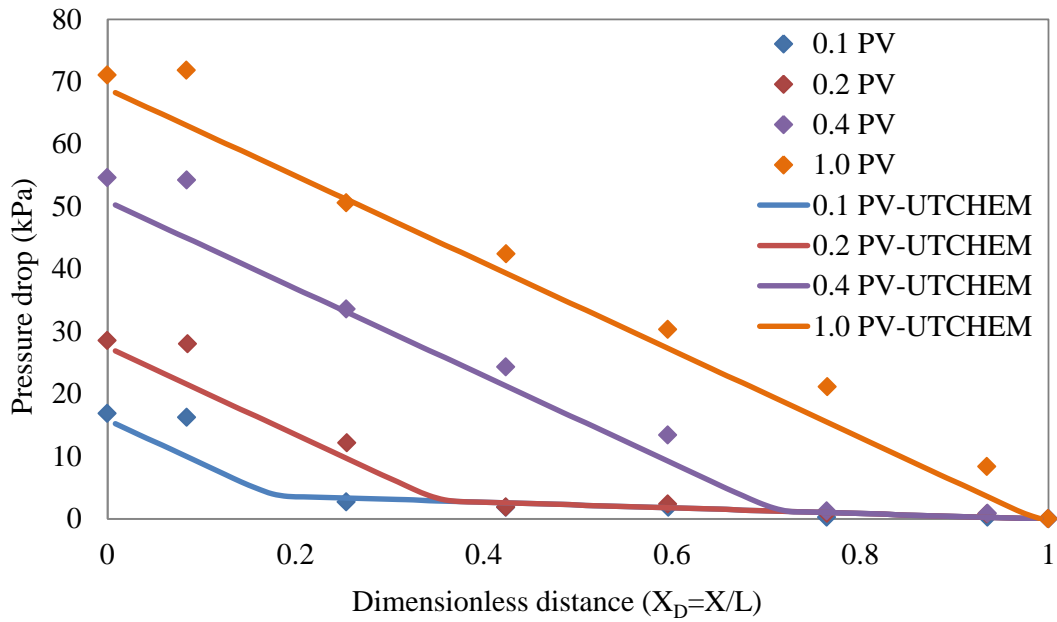


Figure 5.21: Transient pressure drop (experimental data from Chen *et al.* 2010 vs. simulation results using LE Chen *et al.* model in this work)

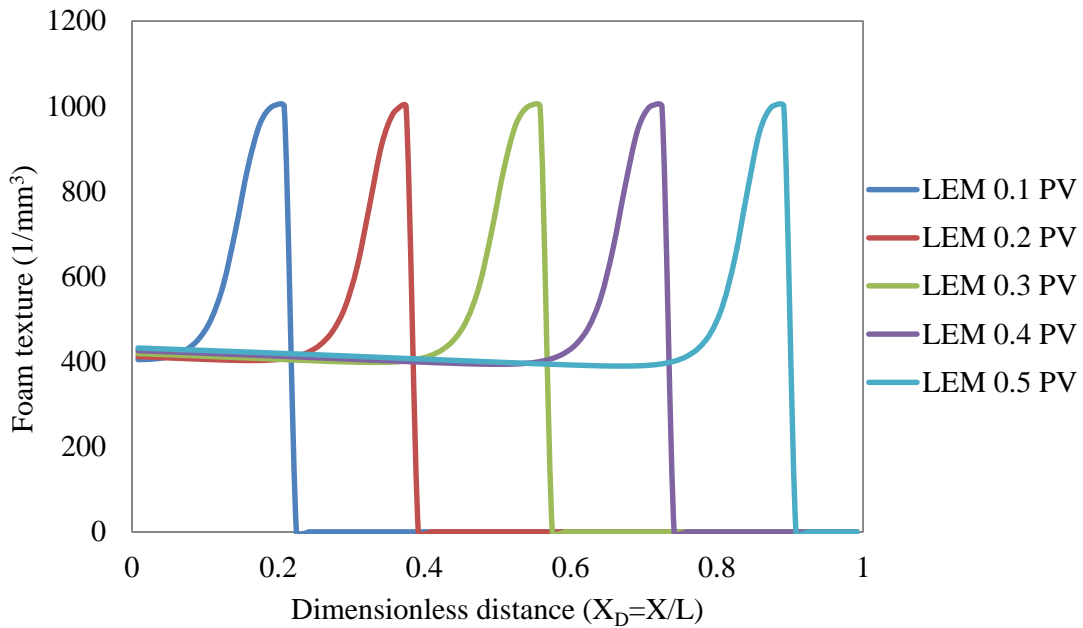


Figure 5.22: Simulation of transient flowing foam texture using LE Chen *et al.* model in this work

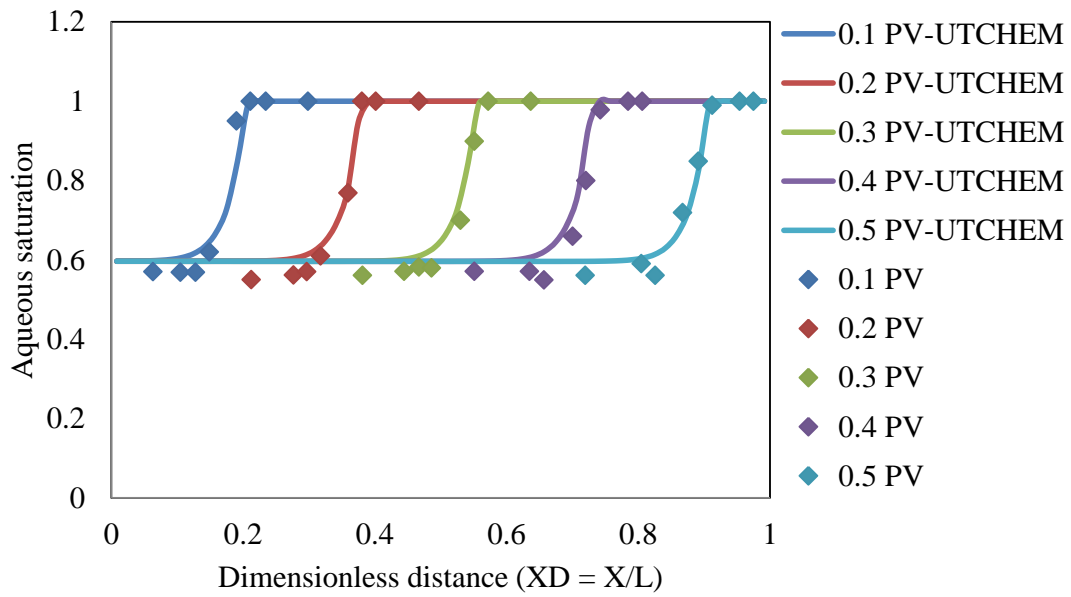


Figure 5.23: Transient aqueous phase saturation (experimental data from Chen *et al.* 2010 vs. simulation results using UT foam model in this work)

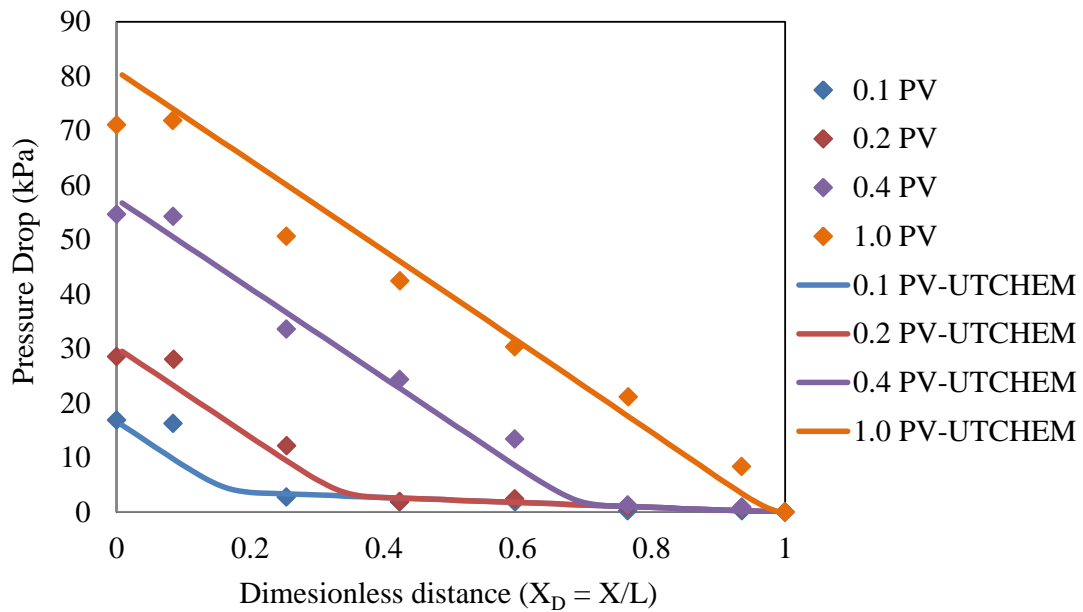


Figure 5.24: Transient pressure drop (experimental data from Chen *et al.* 2010 vs. simulation results using UT foam model in this work)

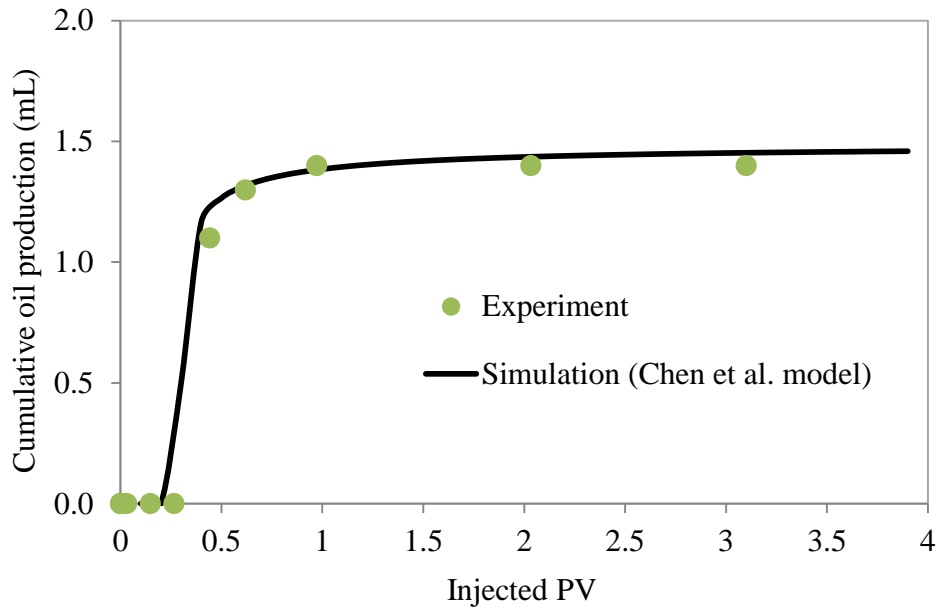


Figure 5.25: Cumulative oil production (experimental data from Farajzadeh *et al.* 2010 experiment vs. simulation results using Chen *et al.* model in this work)

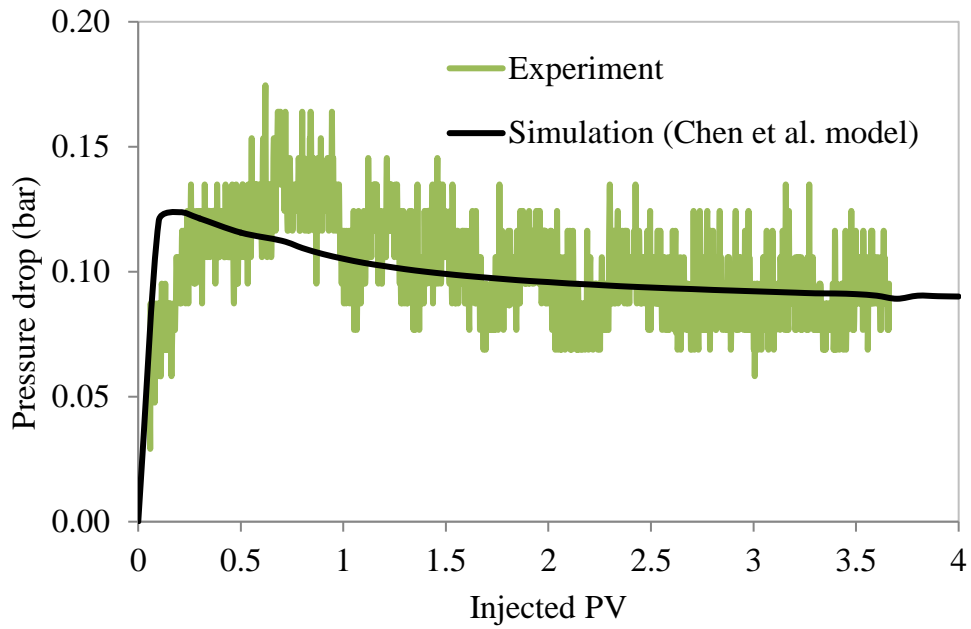


Figure 5.26: Pressure drop (experimental data from Farajzadeh *et al.* 2010 experiment vs. simulation results using Chen *et al.* model in this work)

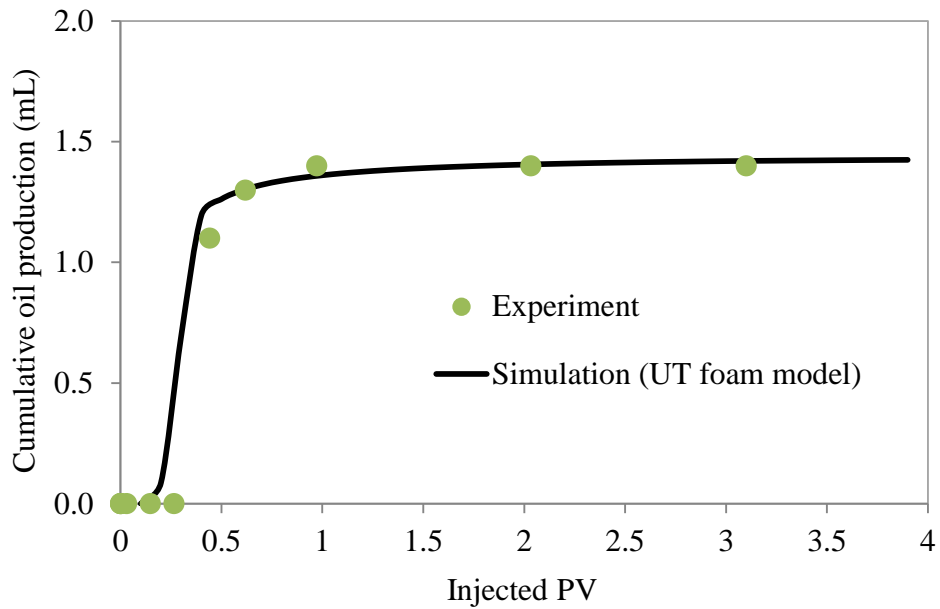


Figure 5.27: Cumulative oil production (experimental data from Farajzadeh *et al.* 2010 experiment vs. simulation results using UT foam model in this work)

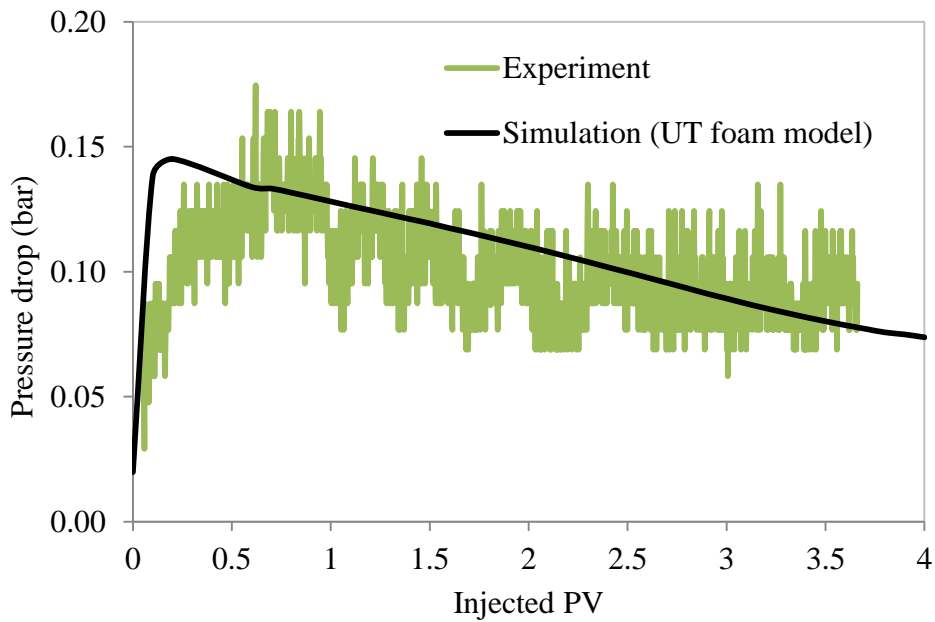


Figure 5.28: Pressure drop (experimental data from Farajzadeh *et al.* 2010 experiment vs. simulation results using UT foam model in this work)

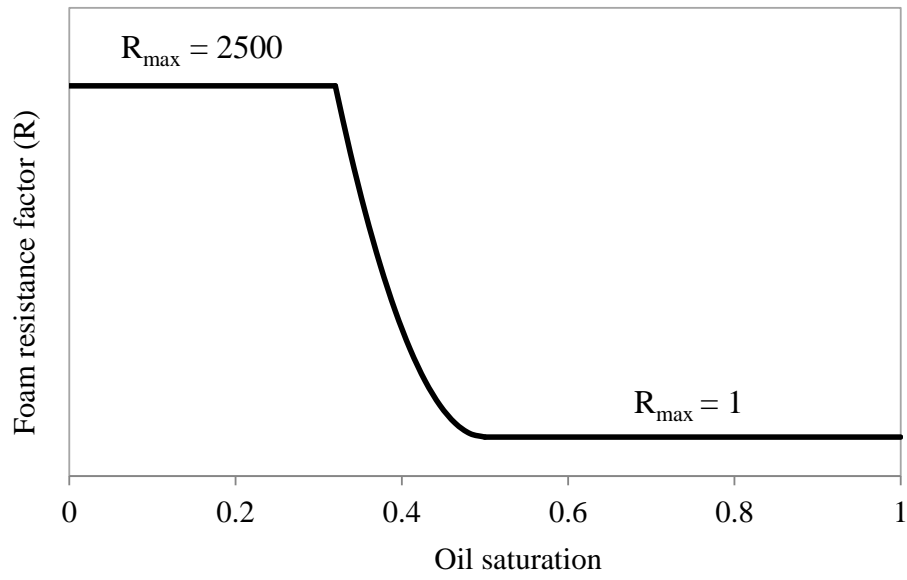


Figure 5.29: Effect of oil on foam resistance factor in UT foam model simulation

Chapter 6: Simulation Results

This chapter presents simulation results with four-phase flow oil reservoir simulator for gas and surfactant EOR processes and foam mobility control in alkali/surfactant flooding. Initially, the black-oil model was compared against a fully implicit black-oil commercial reservoir simulator, IMEX-CMG. New formulation was also compared against original UTCHEM in the absence of gas or gas is assumed to be slightly compressible without mass transfer with other phases (assumed in original UTCHEM).

A grid refinement study was also performed to check the dependence of the results on the gridblock size in both areal and vertical directions. Then, low-tension-gas (or foam) flooding with Surfactant Alternating Gas (SAG) and co-injection schemes were modeled. The combined effect of simultaneous injection of polymer and gas and the impact of Water Alternating Gas (WAG), Polymer Alternating Gas (PAG) and foam on gas mobility control were studied.

6.1 COMPARISON OF BLACK-OIL MODEL WITH IMEX-CMG

The black-oil formulation in UTCHEM was compared against a fully implicit black-oil commercial simulator IMEX (version 2011.10) developed by Computer Modeling Group of Calgary (CMG). A three dimensional model (10×10×2) was set up with one injector and one producer at two corners located at grid points (1, 1) and (10, 10) and completed in both layers. Figure 6.1 shows the reservoir grid and well locations. Pertinent data and constraints are given in Table 6.1. Oil and gas PVT properties (formation volume factor, viscosity, and solution gas) are plotted in Figure 6.2 to Figure

6.4, with data given in Table 6.2. The water/oil and oil/gas relative permeability curves are plotted in Figure 6.5 and Figure 6.6, with data given in Table 6.3 and Table 6.4.

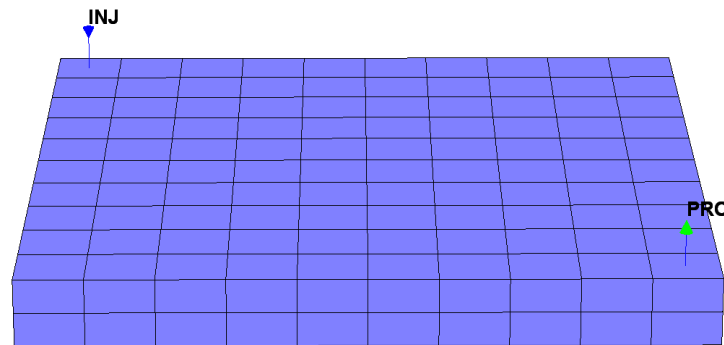


Figure 6.1: Reservoir model for UTCHEM and IMEX-CMG (Cases 1 to 3)

Table 6.1: Reservoir model and fluid properties (Cases 1 to 3)

| Parameters | Values |
|--|-------------------------|
| Number of grid blocks | $10 \times 10 \times 2$ |
| Grid block size (ft \times ft \times ft) | $10 \times 10 \times 5$ |
| Reservoir temperature ($^{\circ}$ F) | 150 |
| Initial pressure (top layer) (psi) | 2000 |
| Permeability (md) | 200 |
| Porosity | 0.3 |
| Rock compressibility (1/psi) | 1×10^{-6} |
| Wellbore radius (ft) | 0.25 |
| Well skin for both injector/producer | 0 |
| Capillary pressure (psi) | 0 |
| Water density at standard conditions (lbm/ft 3) | 63.02 |
| Oil density at standard conditions (lbm/ft 3) | 45 |
| Gas density at standard conditions (lbm/ft 3) | 0.0702 |
| Water viscosity at reference pressure (14.7 psi) (cp) | 0.96 |
| Water Formation volume factor at 14.7 psi (rb/scf) | 1.0 |
| Water compressibility (1/psi) | 3×10^{-6} |
| Pressure dependency of water viscosity (cp/psi) | 1.5×10^{-6} |
| Undersaturated oil compressibility (1/psi) | 2.18×10^{-5} |
| Pressure dependence of oil viscosity above bubble point (cp/psi) | 2.55×10^{-5} |

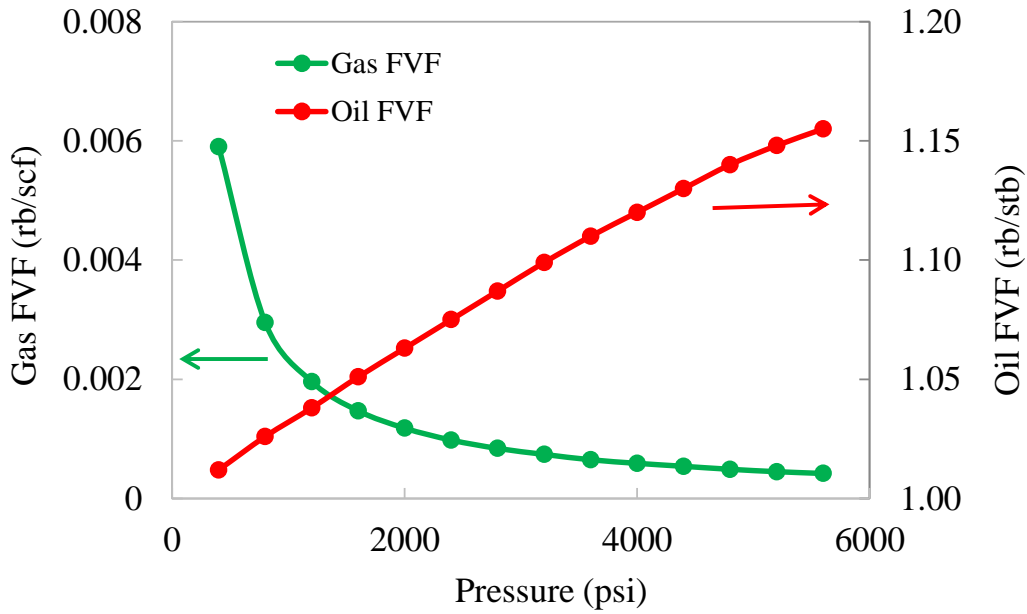


Figure 6.2: Oil and gas formation volume factor in UTCHEM and IMEX-CMG (Cases 1 to 3)

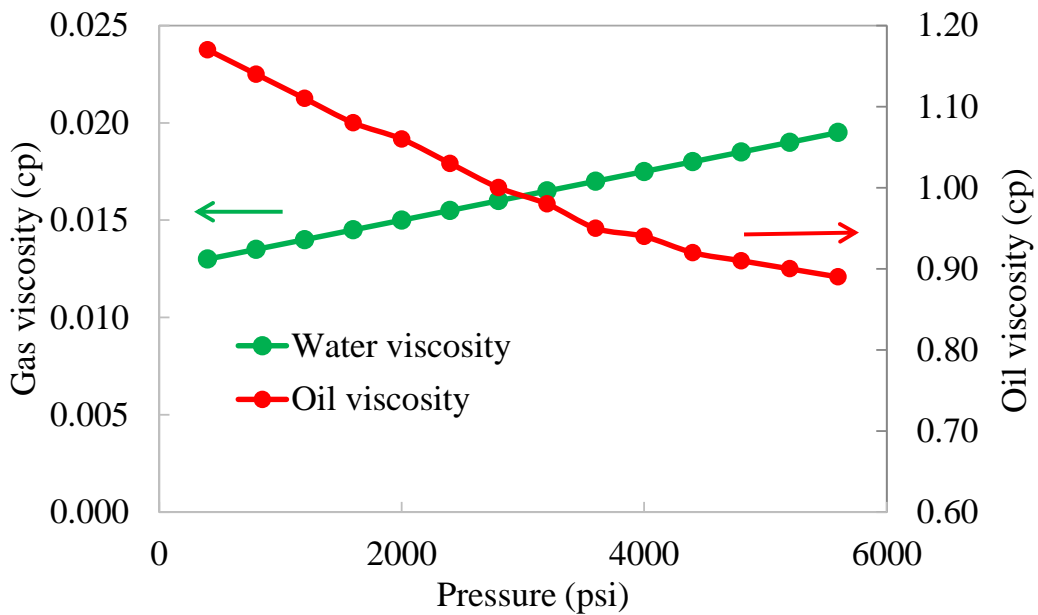


Figure 6.3: Oil and gas viscosity in UTCHEM and IMEX-CMG (Cases 1 to 3)

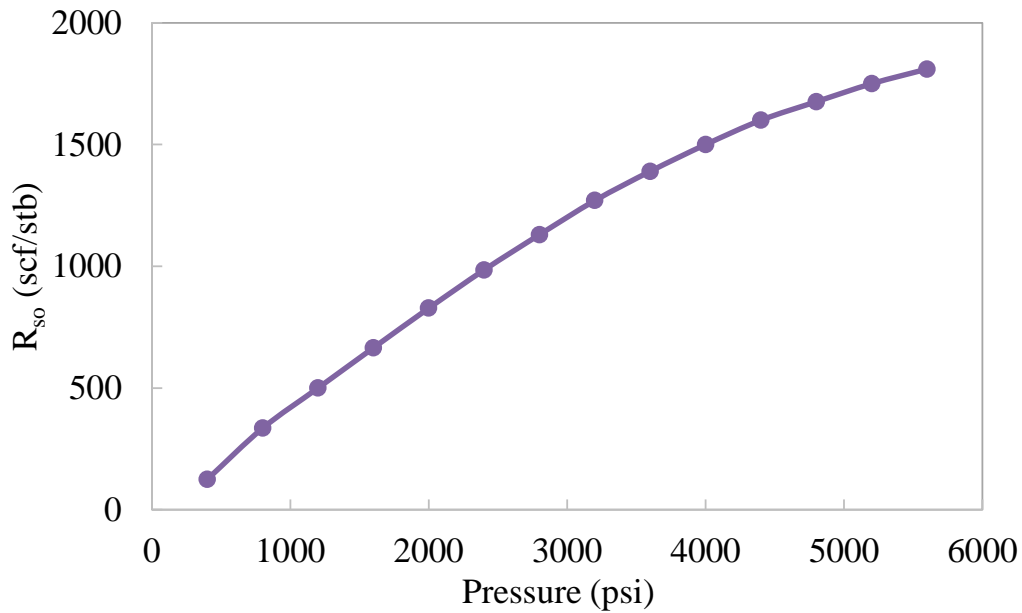


Figure 6.4: Solution gas/oil ratio in UTCHEM and IMEX-CMG (Cases 1 to 3)

Table 6.2: Saturated oil and gas PVT properties (Cases 1 to 3 and 6)

| Pressure (psi) | R_{so} (scf/stb) | B_o (rb/stb) | $E_g=1/B_g$ (scf/rb) | Oil viscosity (cp) | Gas viscosity (cp) |
|-------------------|-----------------------|-------------------|-------------------------|-----------------------|-----------------------|
| 400 | 125 | 1.012 | 169.49 | 1.17 | 0.0130 |
| 800 | 335 | 1.026 | 338.98 | 1.14 | 0.0135 |
| 1200 | 500 | 1.038 | 510.20 | 1.11 | 0.0140 |
| 1600 | 665 | 1.051 | 680.27 | 1.08 | 0.0145 |
| 2000 | 828 | 1.063 | 847.46 | 1.06 | 0.0150 |
| 2400 | 985 | 1.075 | 1020.40 | 1.03 | 0.0155 |
| 2800 | 1130 | 1.087 | 1190.50 | 1.00 | 0.0160 |
| 3200 | 1270 | 1.099 | 1351.40 | 0.98 | 0.0165 |
| 3600 | 1390 | 1.110 | 1538.50 | 0.95 | 0.0170 |
| 4000 | 1500 | 1.120 | 1694.90 | 0.94 | 0.0175 |
| 4400 | 1600 | 1.130 | 1851.90 | 0.92 | 0.0180 |
| 4800 | 1676 | 1.140 | 2040.80 | 0.91 | 0.0185 |
| 5200 | 1750 | 1.148 | 2222.20 | 0.90 | 0.0190 |
| 5600 | 1810 | 1.155 | 2381.00 | 0.89 | 0.0195 |

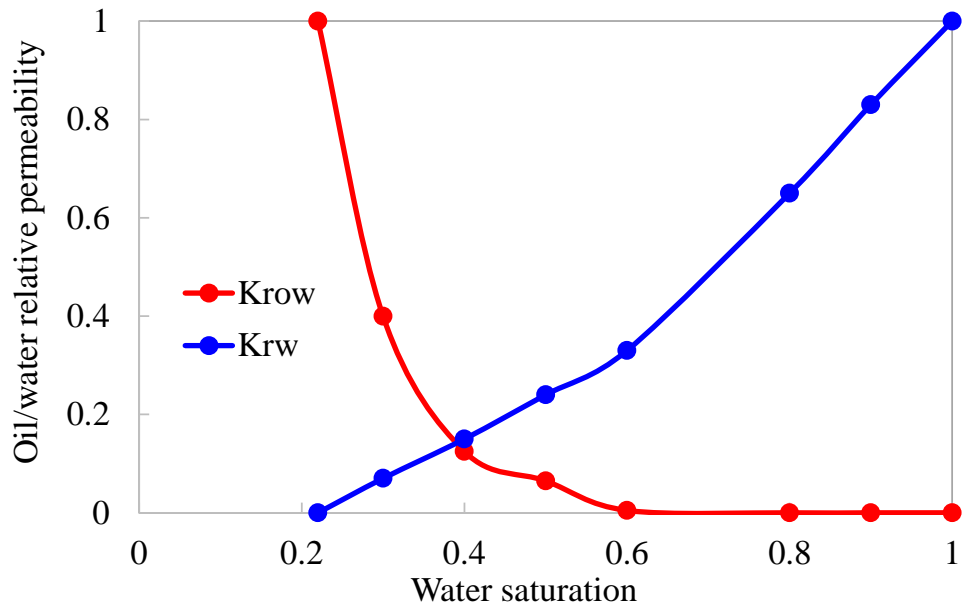


Figure 6.5: Oil/water relative permeability in UTCHEM and IMEX-CMG (Cases 1 to 3)

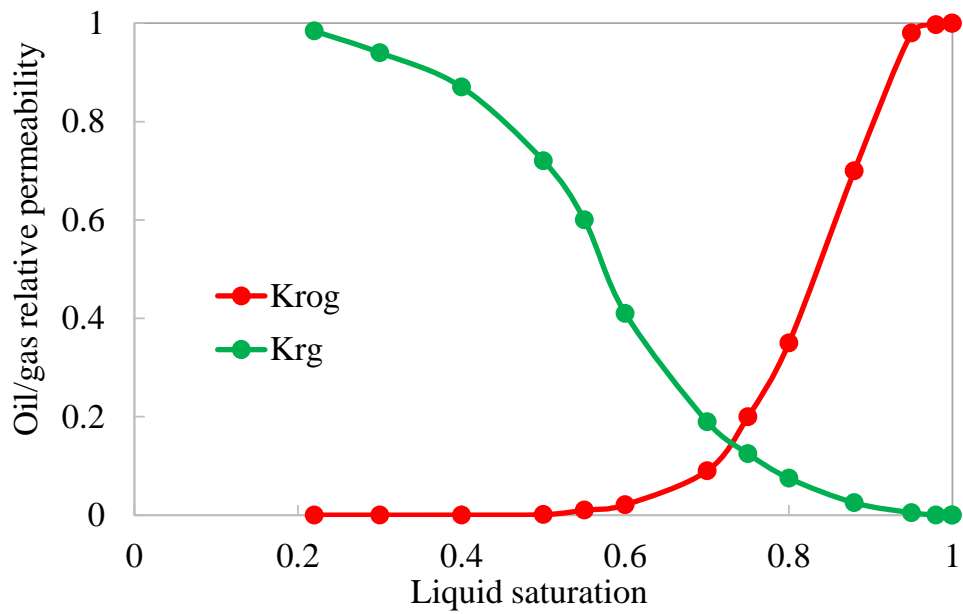


Figure 6.6: Oil/gas relative permeability in UTCHEM and IMEX-CMG (Cases 1 to 3)

Table 6.3: Water and oil relative permeability (Cases 1 to 3)

| S_w | k_{rw} | k_{row} |
|-------|----------|-----------|
| 0.22 | 0 | 1 |
| 0.3 | 0.07 | 0.4 |
| 0.4 | 0.15 | 0.125 |
| 0.5 | 0.24 | 0.0649 |
| 0.6 | 0.33 | 0.0048 |
| 0.8 | 0.65 | 0 |
| 0.9 | 0.83 | 0 |
| 1 | 1 | 0 |

Table 6.4: Oil and gas relative permeability (Cases 1 to 3)

| S_L | k_{rg} | k_{rog} |
|-------|----------|-----------|
| 0.22 | 0.984 | 0 |
| 0.3 | 0.94 | 0 |
| 0.4 | 0.87 | 0.0001 |
| 0.5 | 0.72 | 0.001 |
| 0.55 | 0.6 | 0.01 |
| 0.6 | 0.41 | 0.021 |
| 0.7 | 0.19 | 0.09 |
| 0.75 | 0.125 | 0.2 |
| 0.8 | 0.075 | 0.35 |
| 0.88 | 0.025 | 0.7 |
| 0.95 | 0.005 | 0.98 |
| 0.98 | 0 | 0.997 |
| 0.999 | 0 | 1 |
| 1 | 0 | 1 |

This section compares water flooding and gas flooding results between UTCHEM and IMEX-CMG.

6.1.1 Case 1 – Water Injection

The reservoir described above initially contains 30% water, 60% oil, and 10% initial gas. The water is injected at a constant rate of 100 STB/day and bottomhole pressure of the production well is 2000 psi. Figure 6.7 through Figure 6.13 compare the results between UTCHEM and IMEX-CMG.

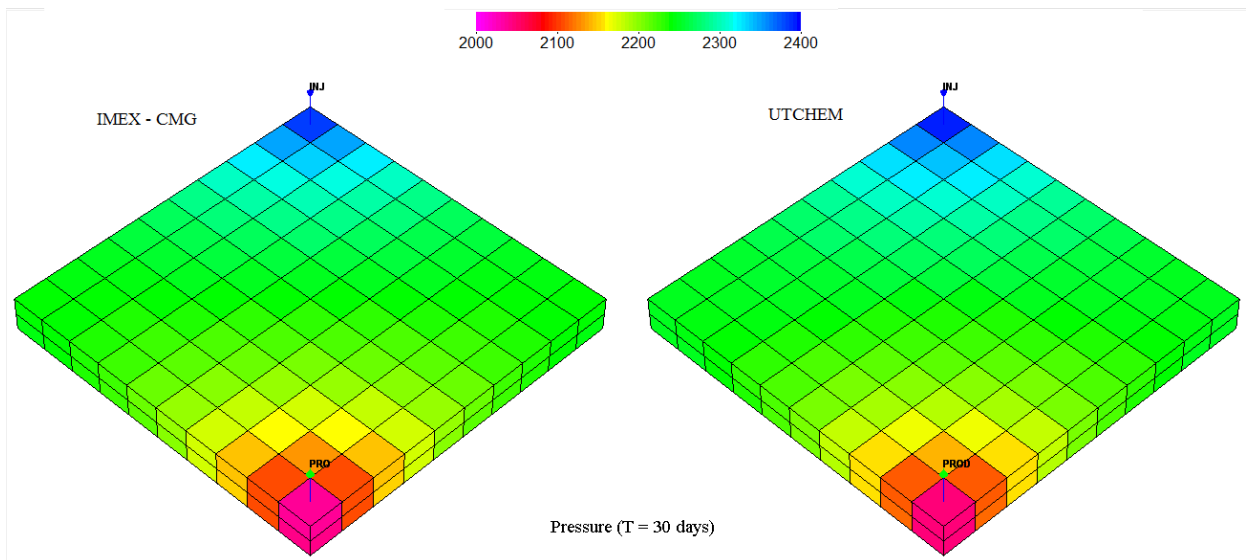


Figure 6.7: Case 1- Pressure map (psi) after 30 days (UTCHEM vs. IMEX-CMG)

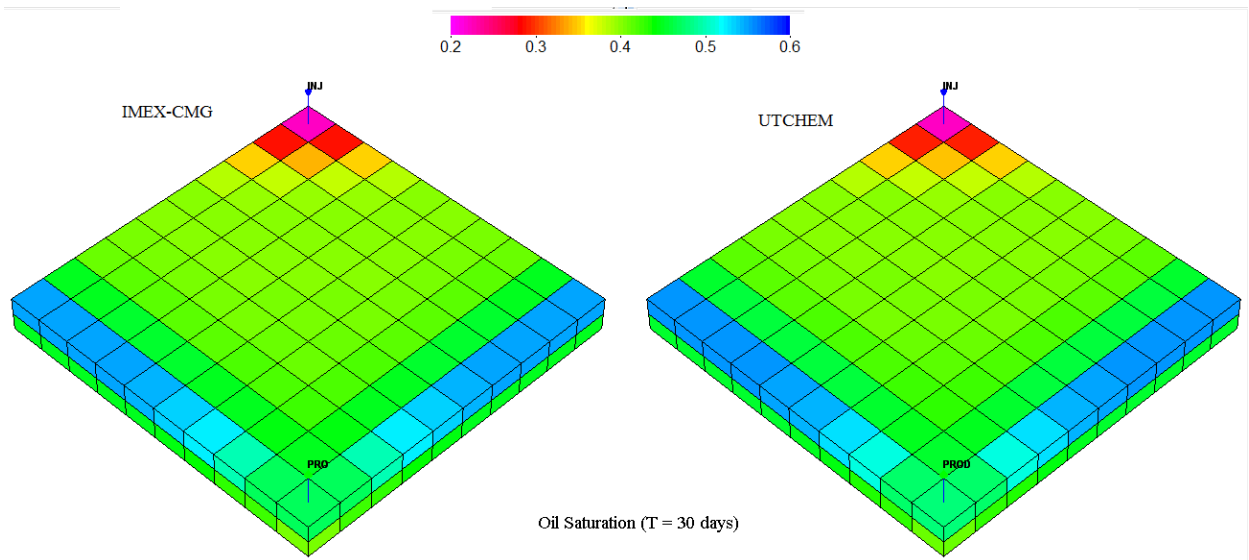


Figure 6.8: Case 1- Oil saturation map after 30 days (UTCHEM vs. IMEX-CMG)

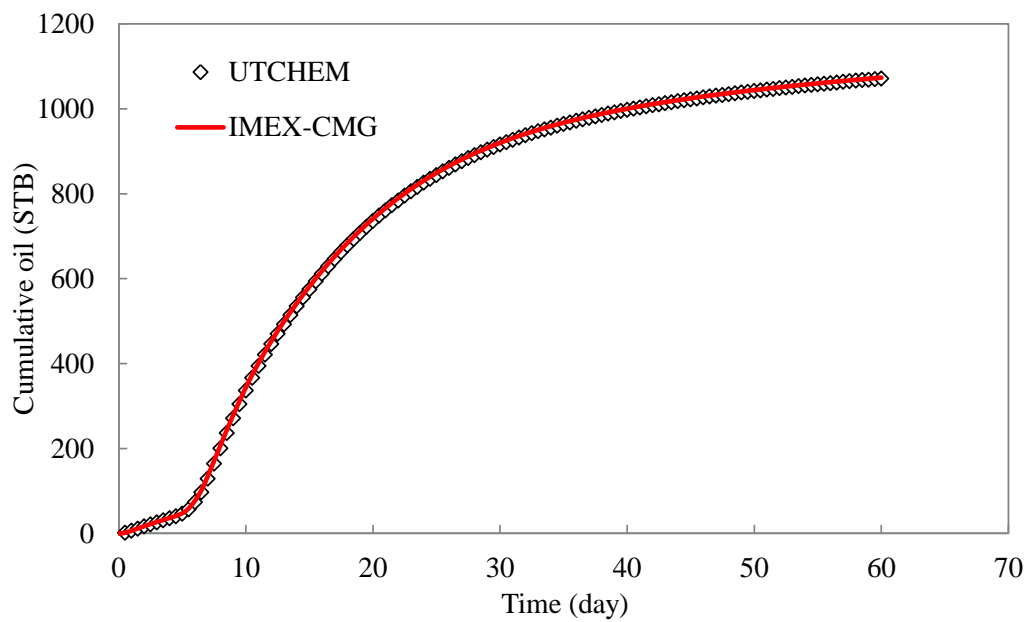


Figure 6.9: Case 1- Cumulative oil recovery (UTCHEM vs. IMEX-CMG)

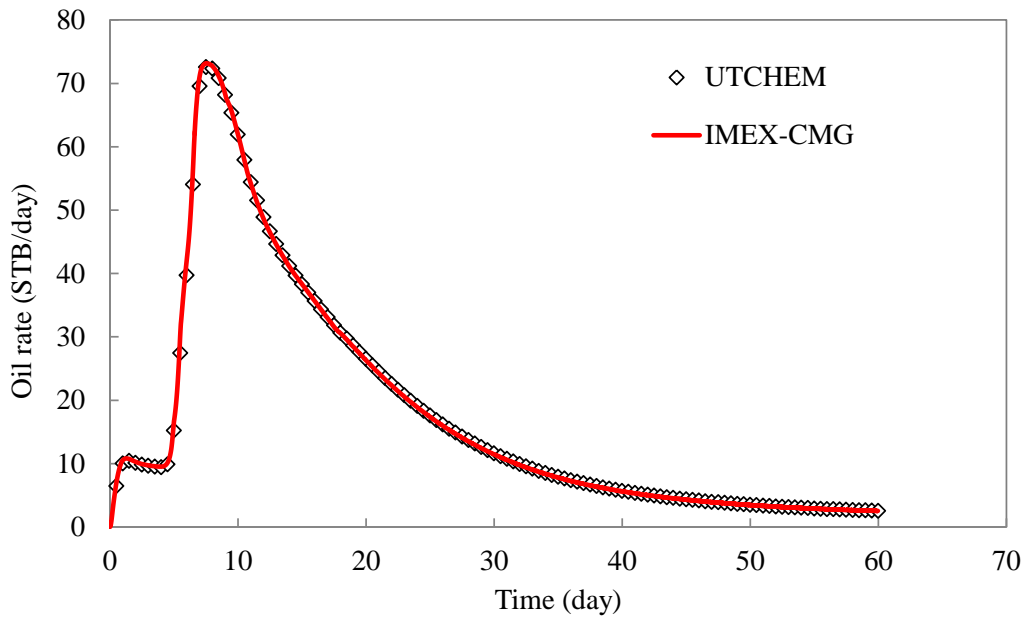


Figure 6.10: Case 1- Oil rate (UTCHEM vs. IMEX-CMG)

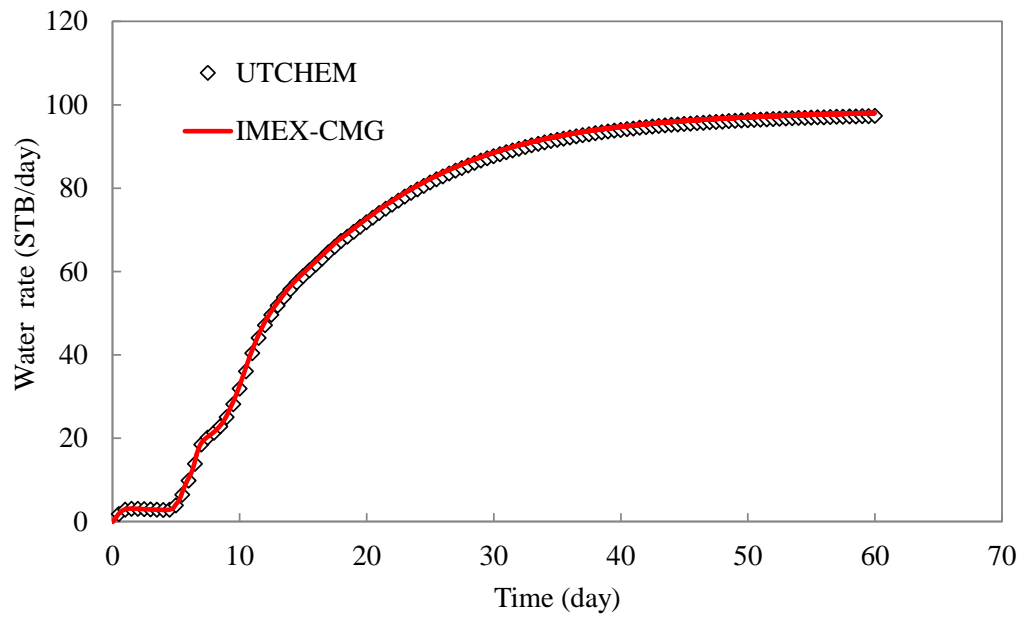


Figure 6.11: Case 1- Water rate (UTCHEM vs. IMEX-CMG)

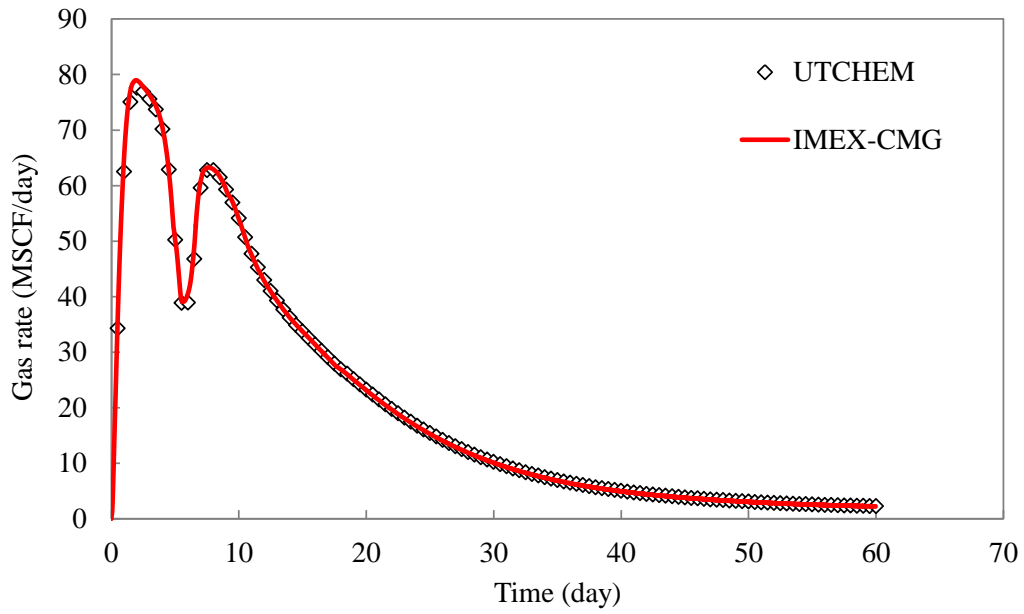


Figure 6.12: Case 1- Gas rate (UTCHEM vs. IMEX-CMG)

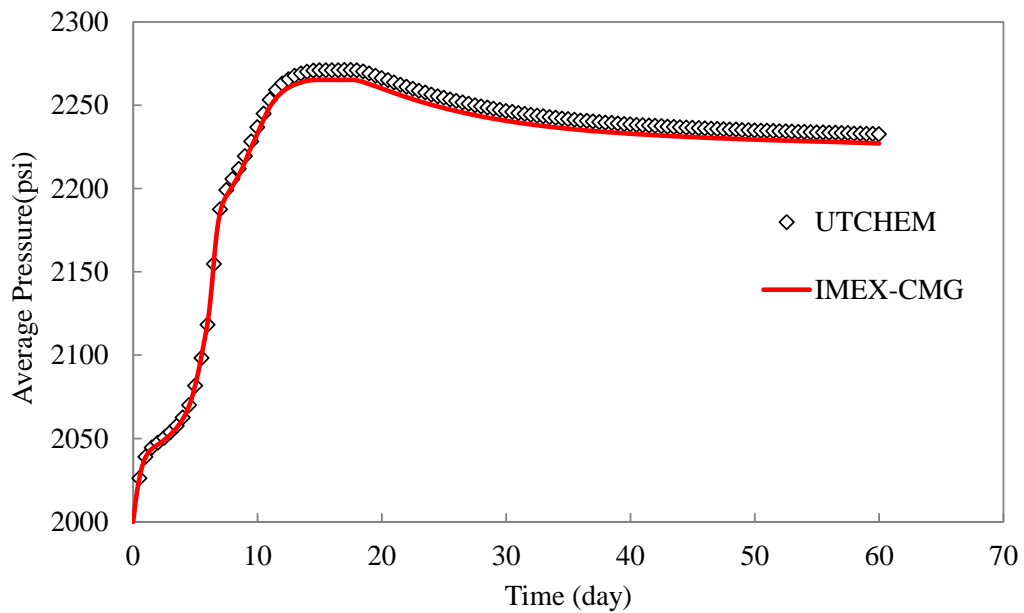


Figure 6.13: Case 1- Average pressure (UTCHEM vs. IMEX-CMG)

6.1.2 Case 2 – Gas Injection in Saturated Reservoir

The case description is similar to Case 1, but in this case gas is injected at a constant rate of 50 Mscf/day. Figure 6.14 through Figure 6.20 compare the simulation results between UTCHEM and IMEX-CMG.

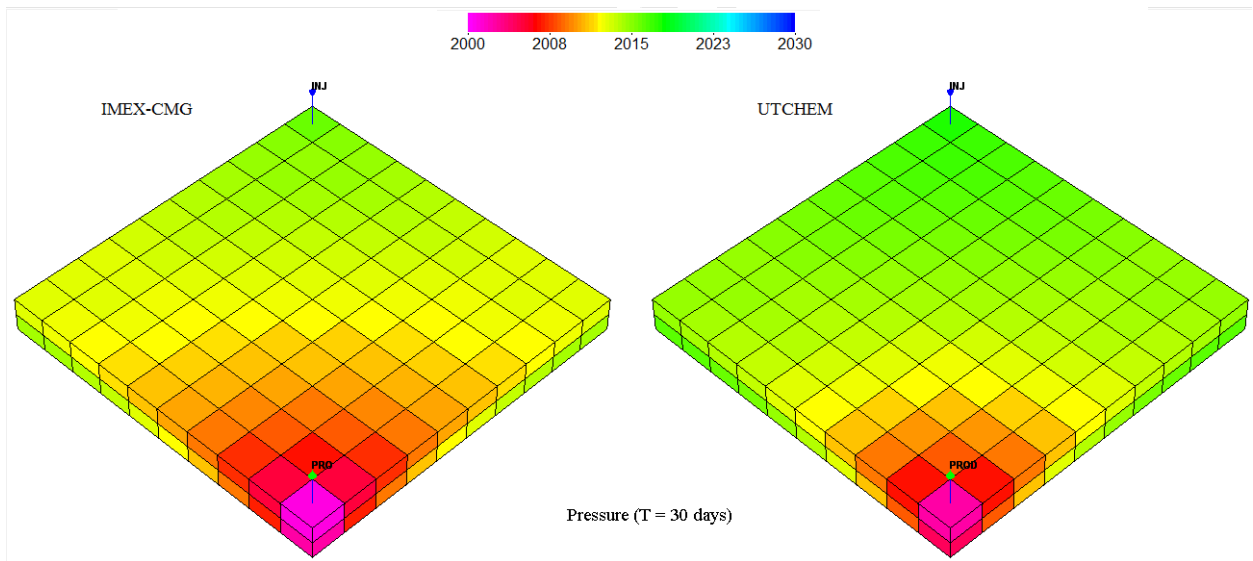


Figure 6.14: Case 2- Pressure map (psi) after 30 days (UTCHEM vs. IMEX-CMG)

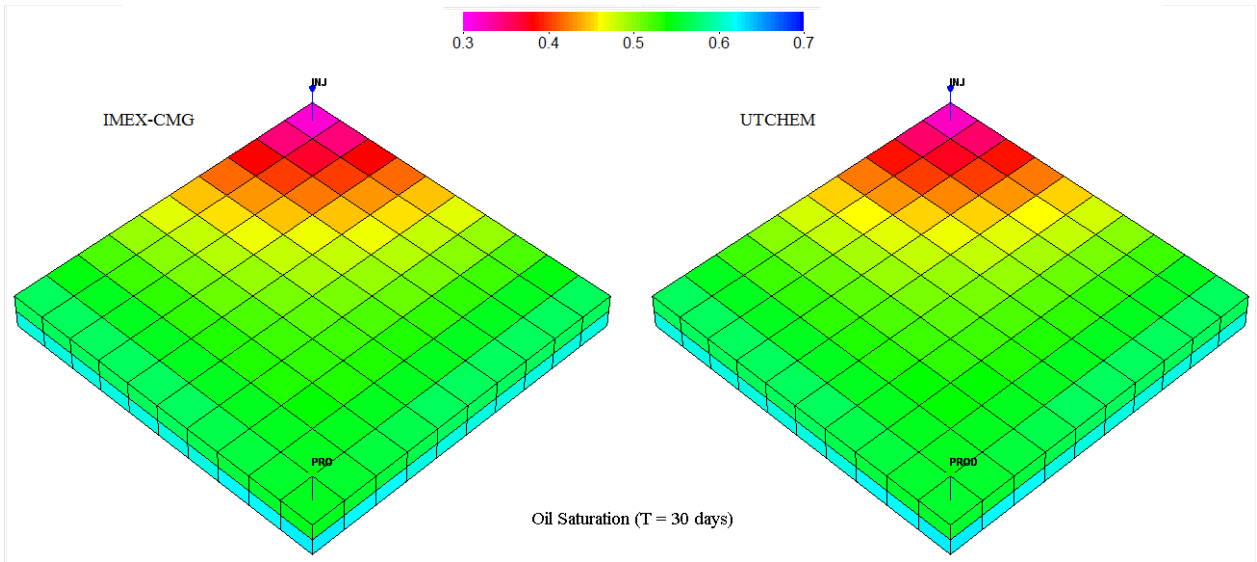


Figure 6.15: Case 2- Oil saturation map after 30 days (UTCHEM vs. IMEX-CMG)

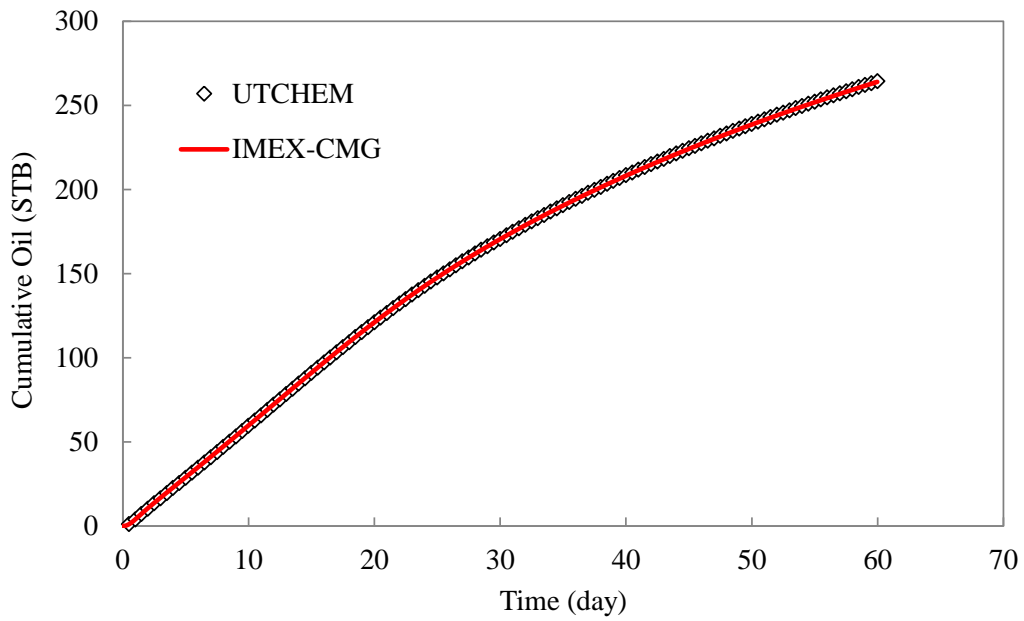


Figure 6.16: Case 2- Oil recovery (UTCHEM vs. IMEX-CMG)

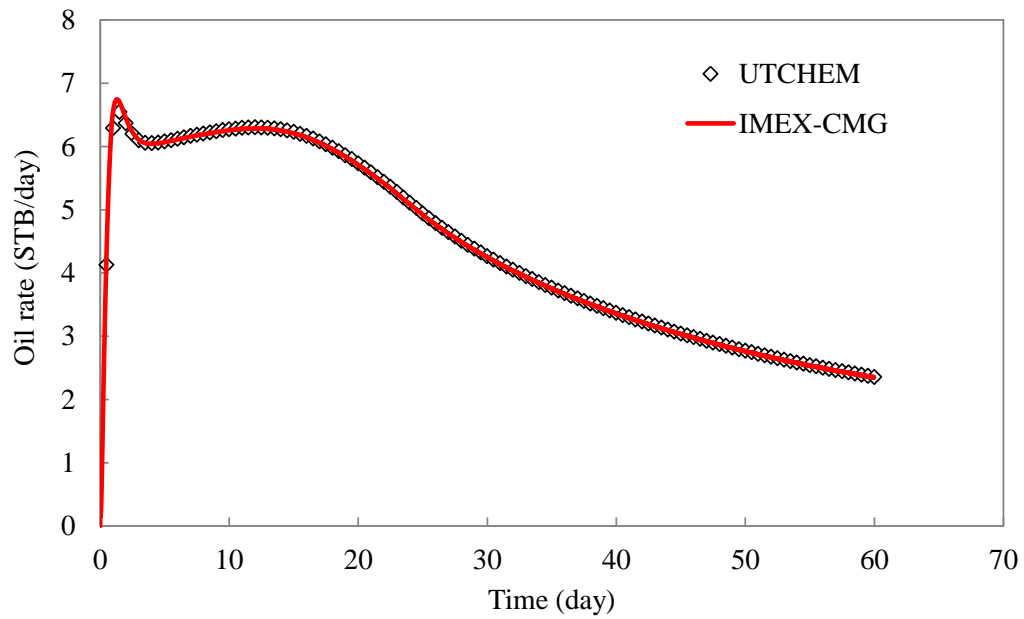


Figure 6.17: Case 2- Oil rate (UTCHEM vs. IMEX-CMG)

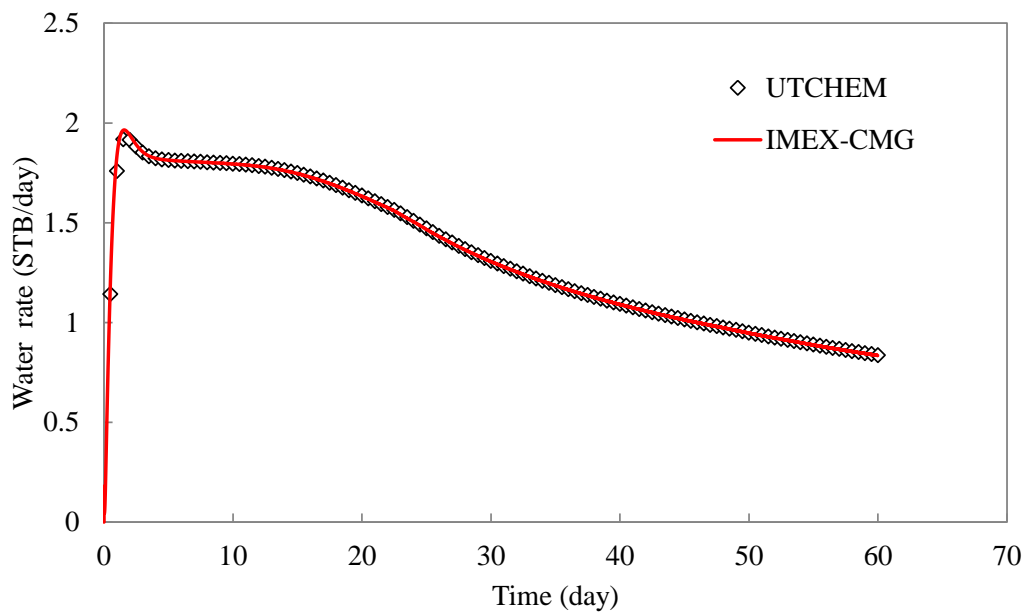


Figure 6.18: Case 2- Water rate (UTCHEM vs. IMEX-CMG)

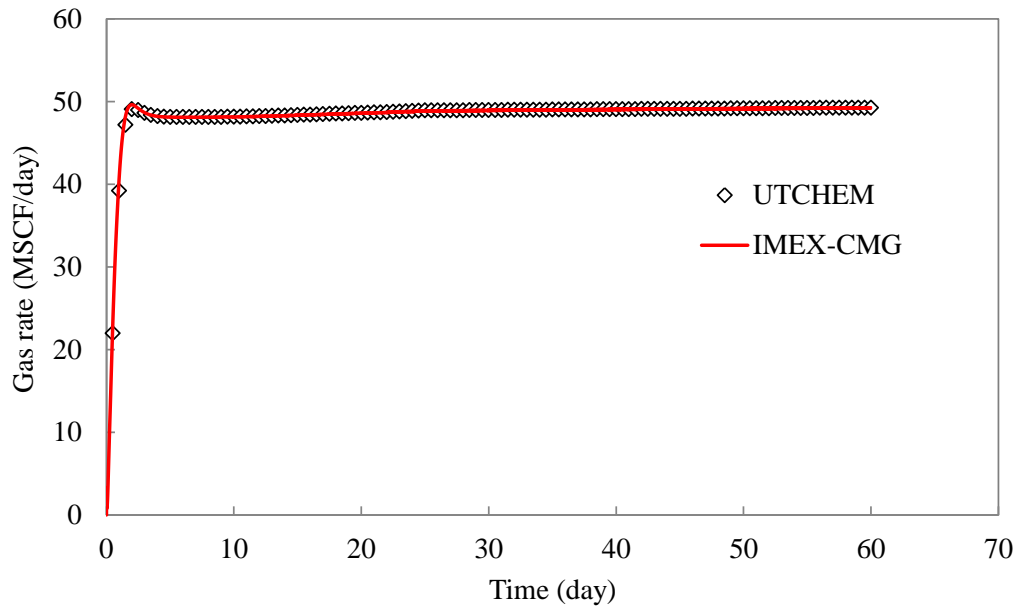


Figure 6.19: Case 2- Gas rate (UTCHEM vs. IMEX-CMG)

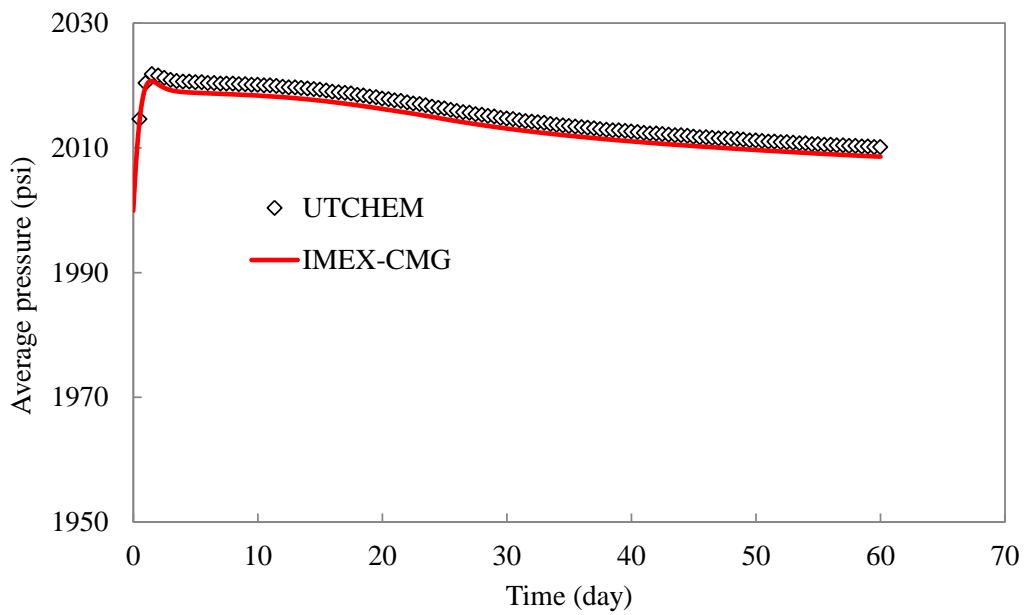


Figure 6.20: Case 2- Average pressure (UTCHEM vs. IMEX-CMG)

UTCHEM and IMEX-CMG input files for Case 2 are presented in Appendix B.1.

6.1.3 Case 3 – Gas Injection in Undersaturated Reservoir

The case description is similar to case 2, but the reservoir is initially above its bubble point pressure ($P_b = 1000$ psi) and there is no free gas in the reservoir. The initial water and oil saturations are 30% and 70%, respectively. The gas is injected at a constant rate of 50 Mscf/day and bottomhole pressure is set to 2000 psi for the production well. Figure 6.21 through Figure 6.27 compare the gas flooding results between UTCHEM and IMEX-CMG.

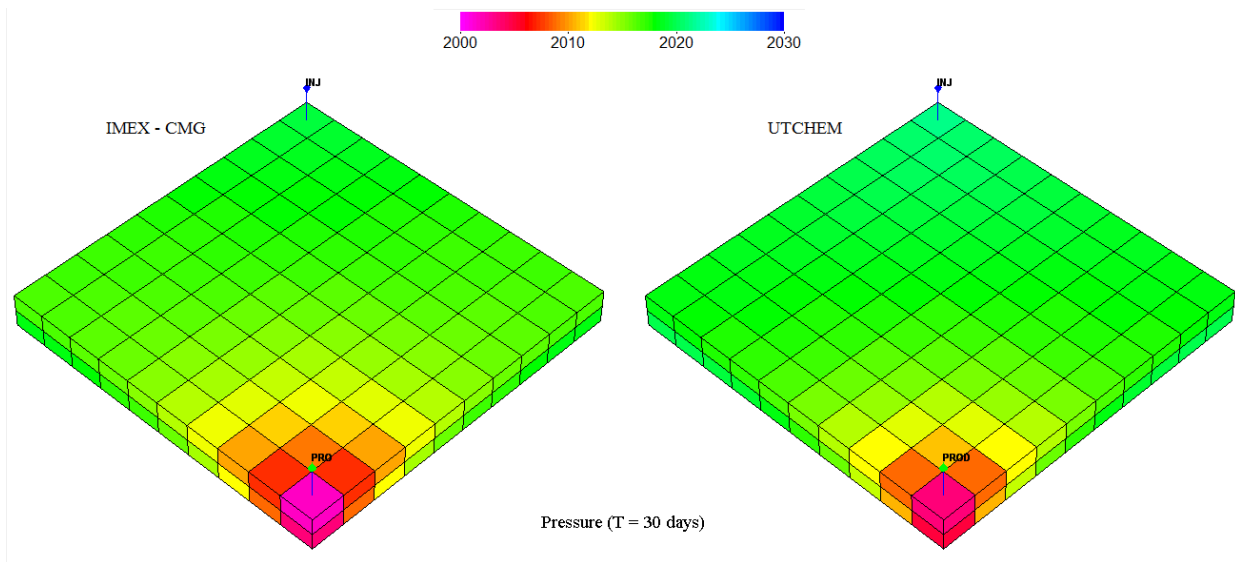


Figure 6.21: Case 3- Pressure map (psi) after 30 days (UTCHEM vs. IMEX-CMG)

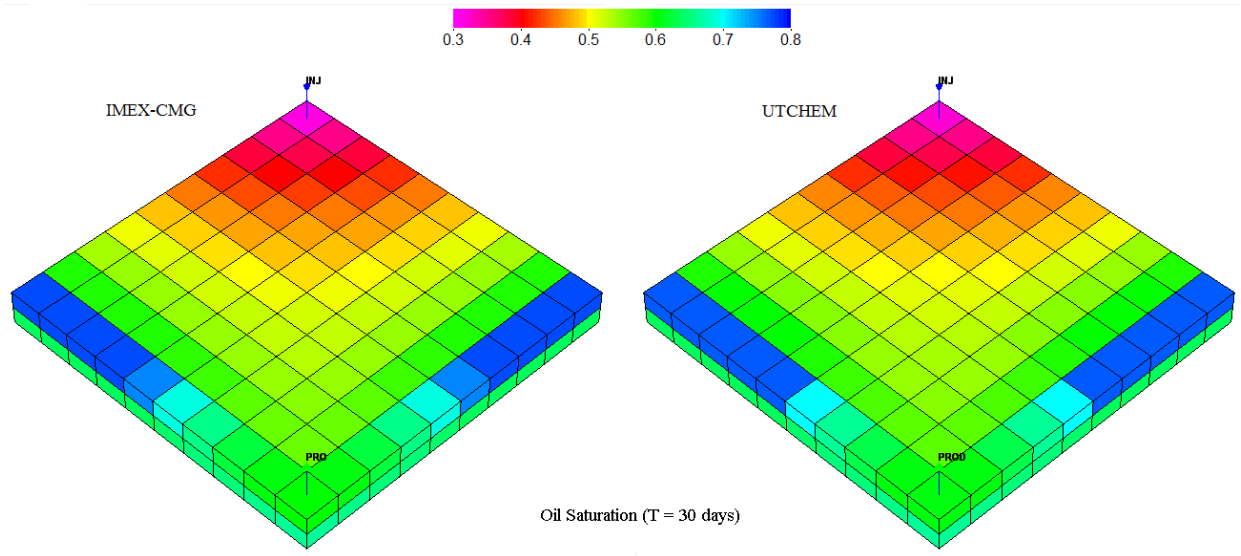


Figure 6.22: Case 3- Oil saturation after 30 days (UTCHEM vs. IMEX-CMG)

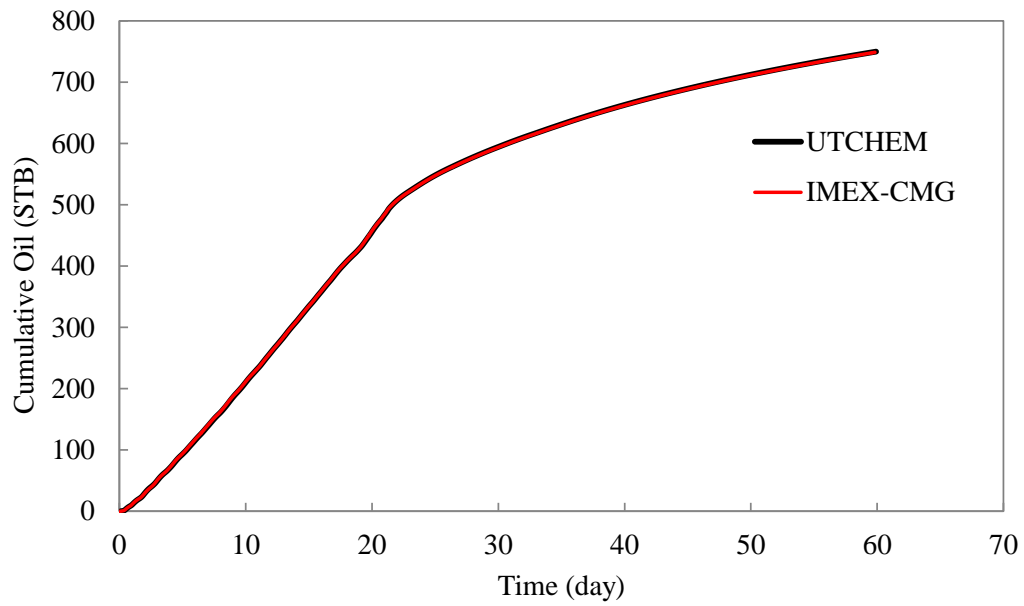


Figure 6.23: Case 3- Oil recovery (UTCHEM vs. IMEX-CMG) - two curves coincide

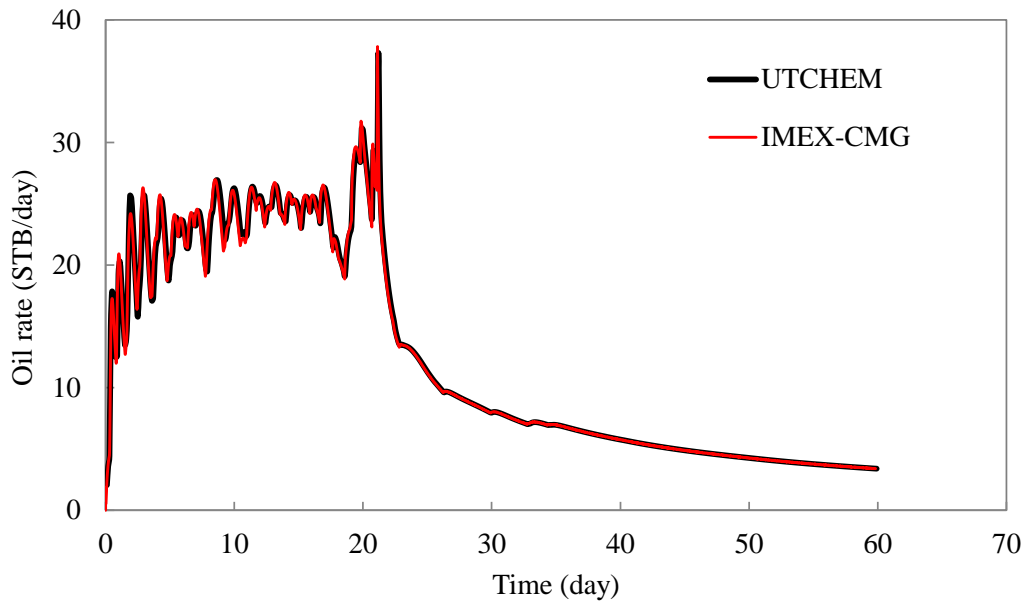


Figure 6.24: Case 3- Oil rate (UTCHEM vs. IMEX-CMG) - two curves coincide

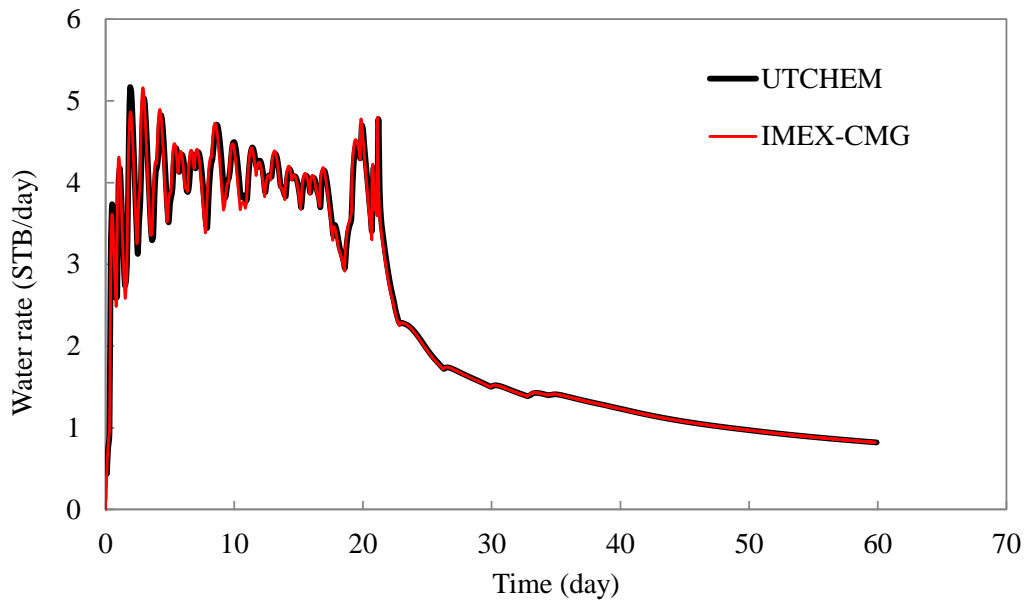


Figure 6.25: Case 3- Water rate (UTCHEM vs. CMG) - two curves coincide

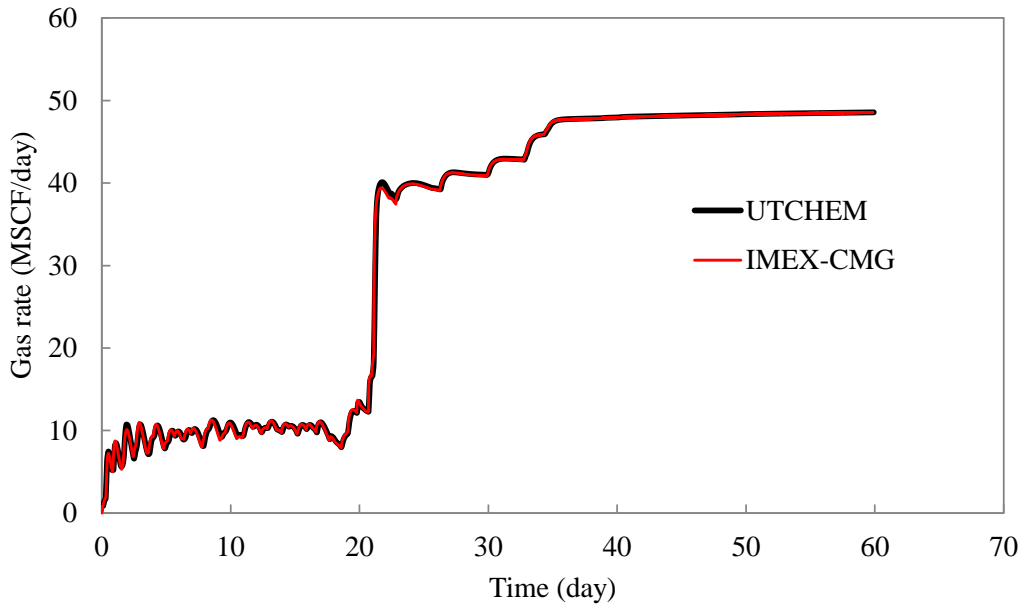


Figure 6.26: Case 3- Gas rate (UTCHEM vs. IMEX-CMG) - two curves coincide

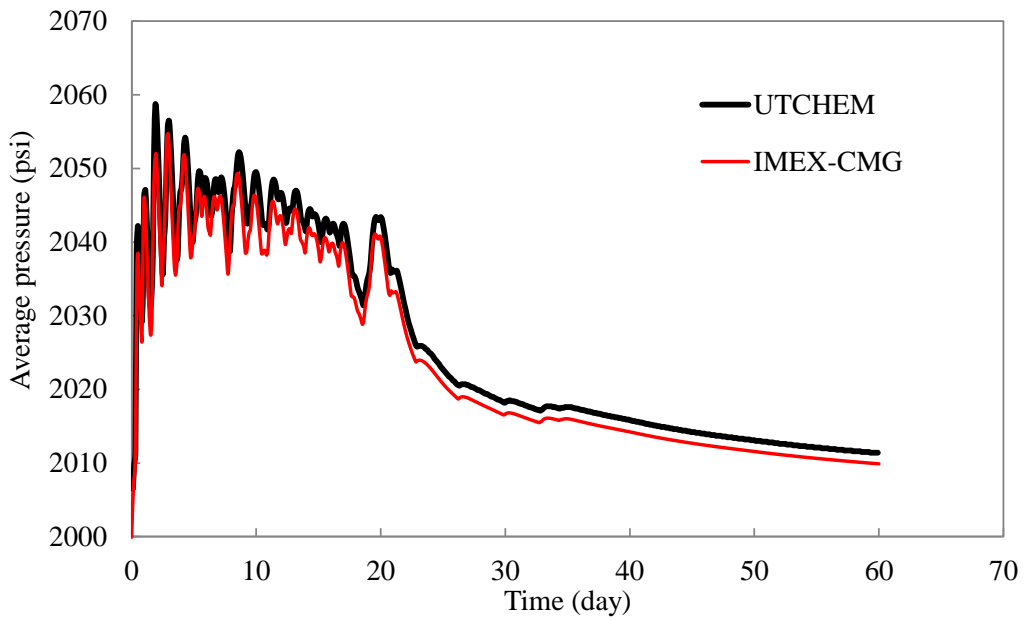


Figure 6.27: Case 3- Average pressure (UTCHEM vs. IMEX-CMG)

In all three cases presented here, UTCHEM results agree with those from IMEX-CMG.

6.2 VERIFICATION OF NEW UTCHEM FORMULATION AGAINST ORIGINAL UTCHEM

In previous versions of UTCHEM (labelled original here), the gas was modeled as a slightly compressible phase with no mass transfer with other phases (water, oil, or microemulsion phases). New formulation was also compared against original UTCHEM in the absence of gas or when gas was assumed to be slightly compressible with no communication with other phases.

The new formulation was compared with the original UTCHEM using a one-dimensional vertical model in Cases 4 and 5. The simulation case description is given in Table 6.5. Corey-type relative permeability data are listed in Table 6.6. Figure 6.28 depicts the oil/water solubilization ratio for surfactant formulation in this case. The surfactant adsorption is 0.22 (mg/g rock) and the maximum microemulsion viscosity is 9.2 cp. Surfactant phase behavior, surfactant adsorption and microemulsion viscosity parameters in UTCHEM are given in Table 6.7.

Table 6.5: Model description (Cases 4 and 5)

| Parameters | Values |
|-----------------------------------|--------------------|
| Number of grid blocks | 1×1×80 |
| Grid block size (ft×ft×ft) | 0.11×0.11×0.0093 |
| Initial pressure (top grid) (psi) | 14.7 |
| Horizontal Permeability (md) | 72 |
| Porosity | 0.219 |
| Rock compressibility (1/psi) | 1×10 ⁻⁶ |
| Capillary pressure (psi) | 0 |
| Water viscosity (cp) | 0.678 |
| Oil viscosity (cp) | 7.0 |
| Gas viscosity (cp) | 0.02 |
| Initial water saturation | 0.59 |
| Initial oil saturation | 0.31 |
| Initial gas saturation | 0.0 |
| Initial salinity (meq/ml) | 0.33 |

Table 6.6: Relative permeability parameters (Cases 4 and 5)

| Parameter | Value | Parameter | Value |
|-------------------------------------|------------|-------------------------------|----------|
| $S_{rw}^{low}, S_{rw}^{high}$ | 0.30, 0.0 | n_w^{low}, n_w^{high} | 2.0, 1.0 |
| $S_{row}^{low}, S_{row}^{high}$ | 0.33, 0.0 | n_o^{low}, n_o^{high} | 2.0, 1.0 |
| $S_{rog}^{low}, S_{rog}^{high}$ | 0.20, 0.0 | $n_{me}^{low}, n_{me}^{high}$ | 2.0, 1.0 |
| $S_{rme}^{low}, S_{rme}^{high}$ | 0.30, 0.0 | n_g^{low}, n_g^{high} | 1.5, 1.5 |
| $S_{rg}^{low}, S_{rg}^{high}$ | 0.10, 0.1 | T_{11} | 1865 |
| $k_{rw}^{o low}, k_{rw}^{o high}$ | 0.30, 1.0 | T_{22} | 59074 |
| $k_{ro}^{o low}, k_{ro}^{o high}$ | 0.60, 1.0 | T_{33} | 364.2 |
| $k_{rme}^{o low}, k_{rme}^{o high}$ | 0.30, 1.0 | T_{44} | 0 |
| $k_{rg}^{o low}, k_{rg}^{o high}$ | 0.94, 0.94 | | |

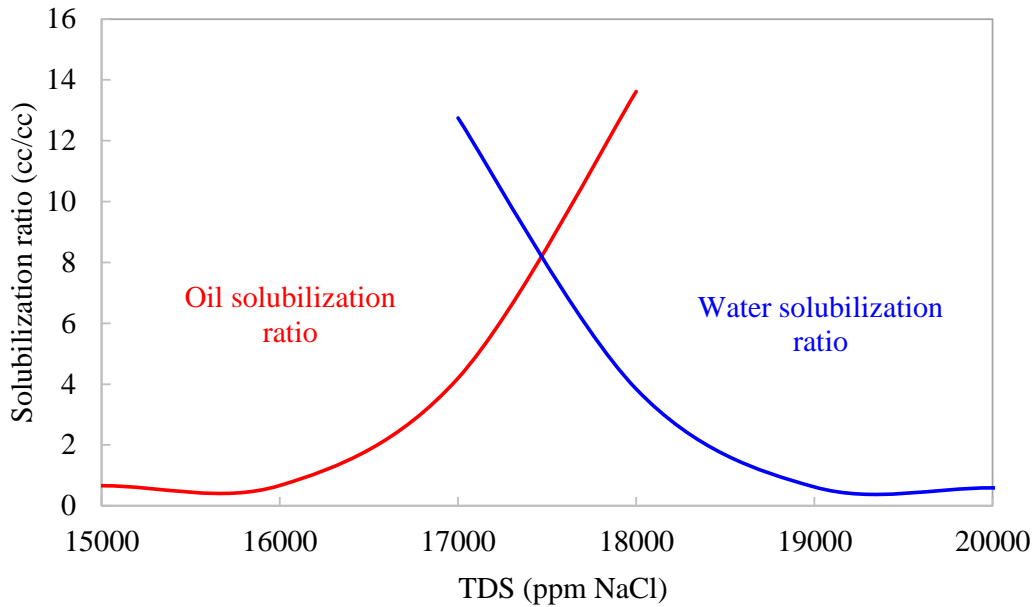


Figure 6.28: Oil/water solubilization ratio for surfactant formulation (Cases 4 and 5)

Table 6.7: Surfactant and microemulsion parameters (Cases 4 and 5)

| Surfactant Parameters | Values |
|---|-------------------------|
| <i>HBNC70, HBNC71, HBNC72</i> | 0.065, 0.060, 0.080 |
| $C_{SEL}, C_{SEOP}, C_{SEU}$ (meq/ml) | 0.282, 0.299, 0.316 |
| Surfactant adsorption parameters (AD31, AD32, B3D) | 2.0, 0.25, 1000 |
| Microemulsion viscosity: (<i>ALPHAV1, ..., ALPHAV5</i>) | 2.0, 2.0, 0.0, 0.9, 0.7 |

The polymer viscosity curve is given in Figure 6.29. The polymer adsorption is about 11 ($\mu\text{g/g}$ rock). The polymer viscosity and adsorption parameters in UTCHEM are listed in Table 6.8.

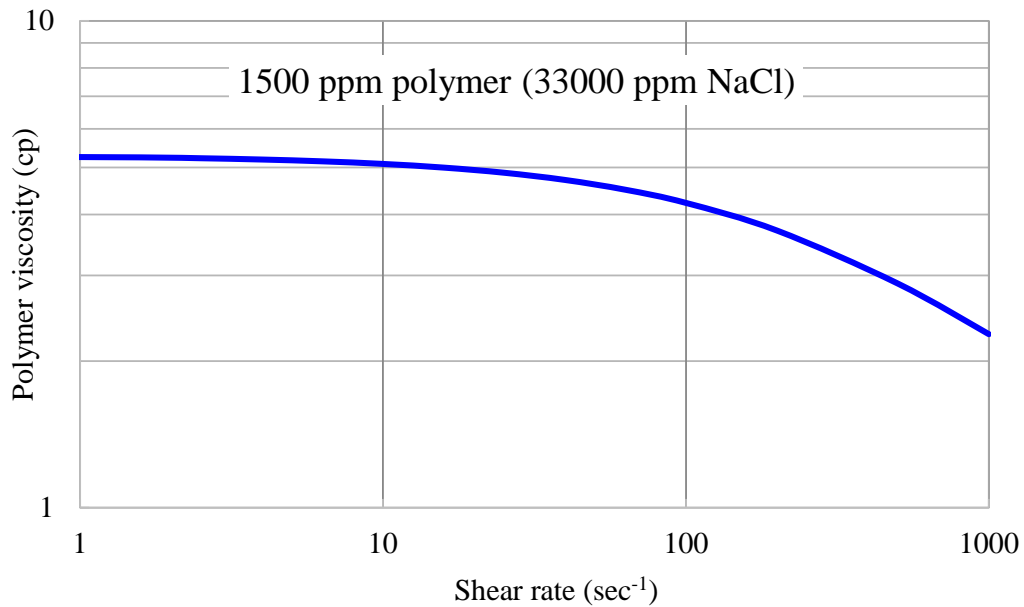


Figure 6.29: Polymer viscosity curve (Cases 4 and 5)

Table 6.8: Polymer properties (Cases 4 and 5)

| Polymer Parameters | Values |
|---|------------------|
| AP_1, AP_2, AP_3 | 12.54, 41, 715 |
| BETAP, SSLOPE | 1.0, -0.2398 |
| GAMMAC, GAMHF, POWN, GAMHF2 | 4.0, 450, 1.8, 0 |
| Polymer adsorption parameters (AD41, AD42, B4D) | 0.97, 0.5, 100 |

6.2.1 Case 4- Surfactant-Polymer Flood

In this case, an SP flood was simulated using both the new and original UTCHEM versions. The SP slug is injected upward and followed with a polymer drive and then a water drive. The injection time, rates, and concentrations are given in Table 6.9.

Table 6.9: Case 4- Injection scenario

| | |
|--------------|--|
| SP slug | 0.30 PV Injection rate : 0.0041 ft ³ /day Surfactant concentration: 1% Polymer concentration: 0.15 wt% Injection salinity: 0.30 meq/ml NaCl |
| Polymer slug | 1.0 PV Injection rate : 0.0041 ft ³ /day Polymer concentration: 0.15 wt% Injection salinity: 0.25 meq/ml NaCl |
| Water drive | 1.2 PV Injection rate : 0.0041 ft ³ /day Injection salinity: 0.25 meq/ml NaCl |

Figure 6.30 through Figure 6.34 compare the simulation results of Case 4 between new and original UTCHEM. Results indicate, in absence of gas the new formulation agrees with original UTCHEM.

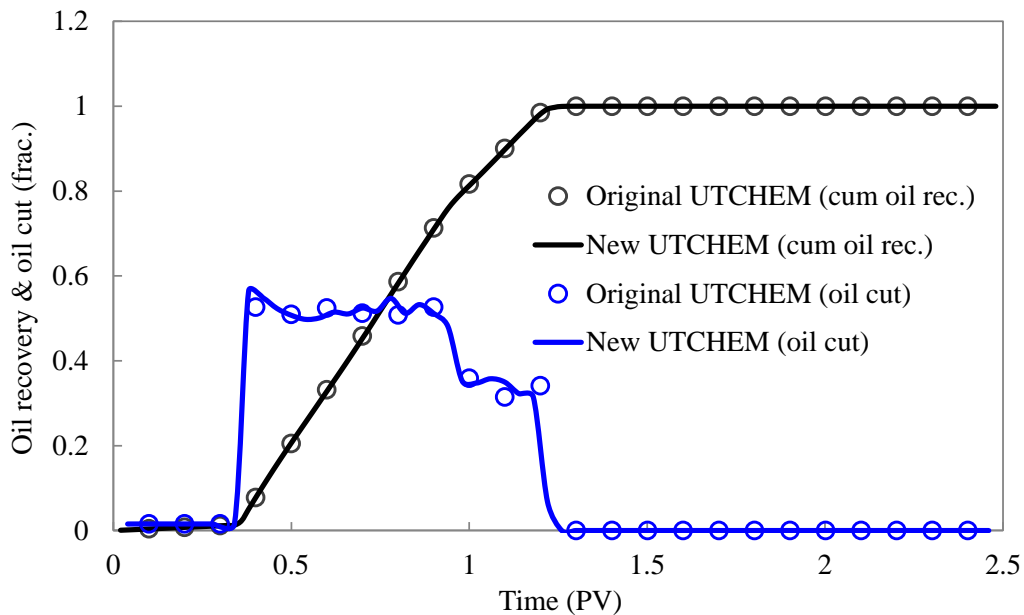


Figure 6.30: Case 4- Oil cut and cumulative oil recovery (New UTCHEM vs. Original UTCHEM)

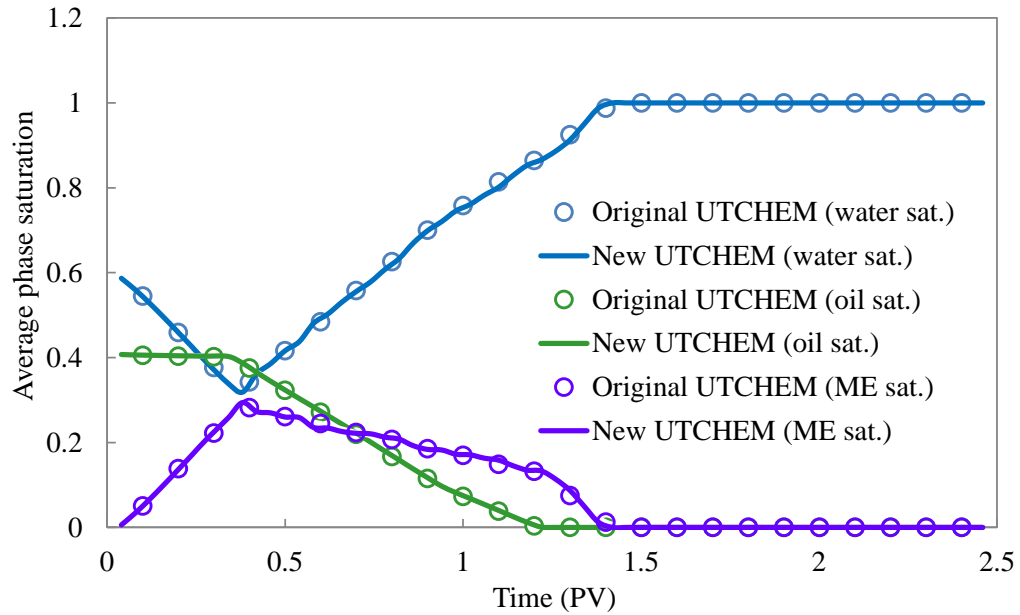


Figure 6.31: Case 4- Average phase saturations inside the core versus injected PV (New UTCHEM vs. Original UTCHEM)

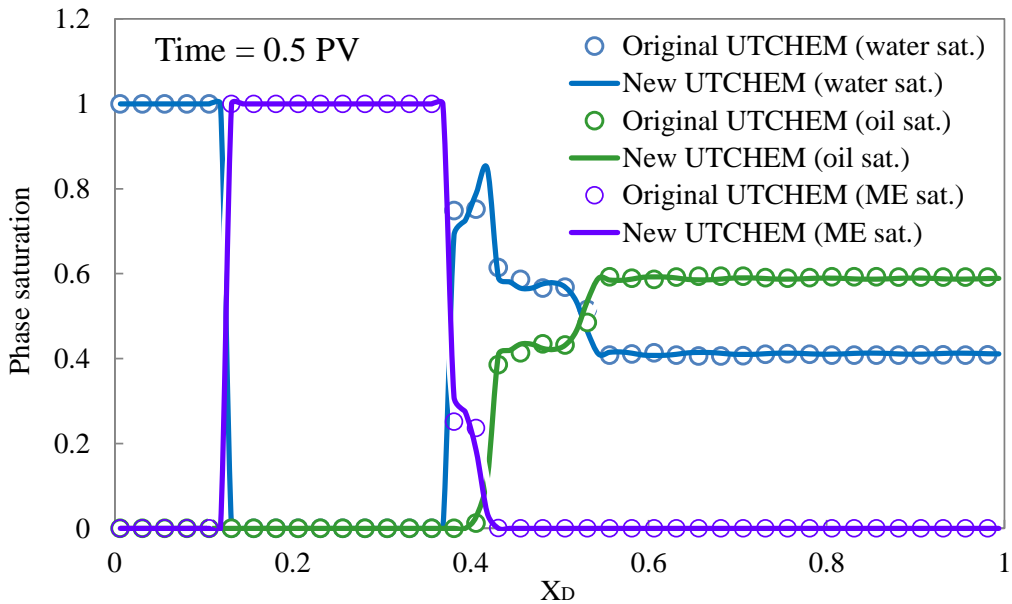


Figure 6.32: Case 4- Phase saturations versus dimensionless distance at 0.5 PV (New UTCHEM vs. Original UTCHEM)

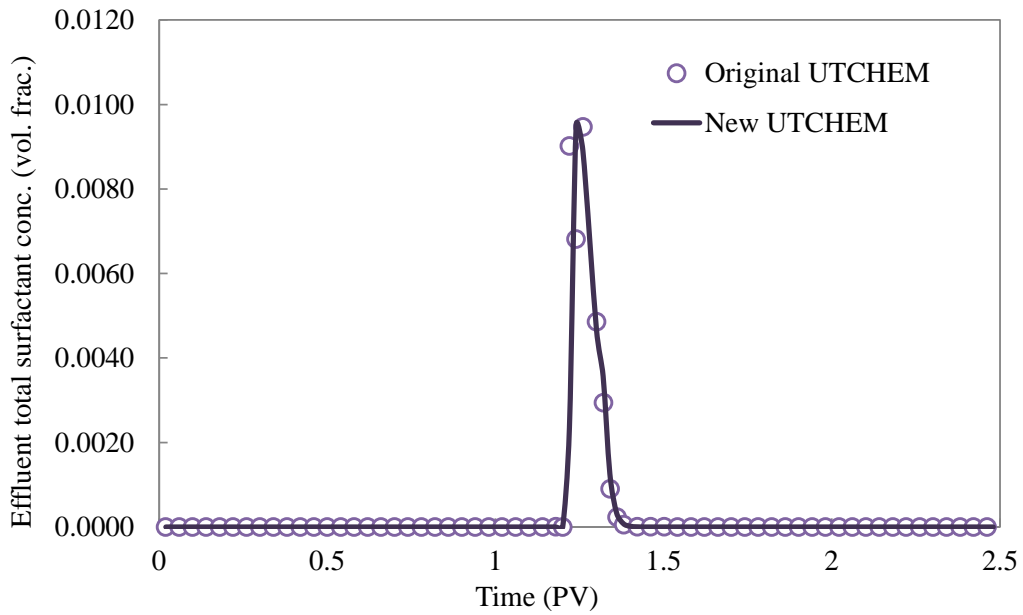


Figure 6.33: Case 4- Effluent total surfactant concentration (New UTCHEM vs. Original UTCHEM)

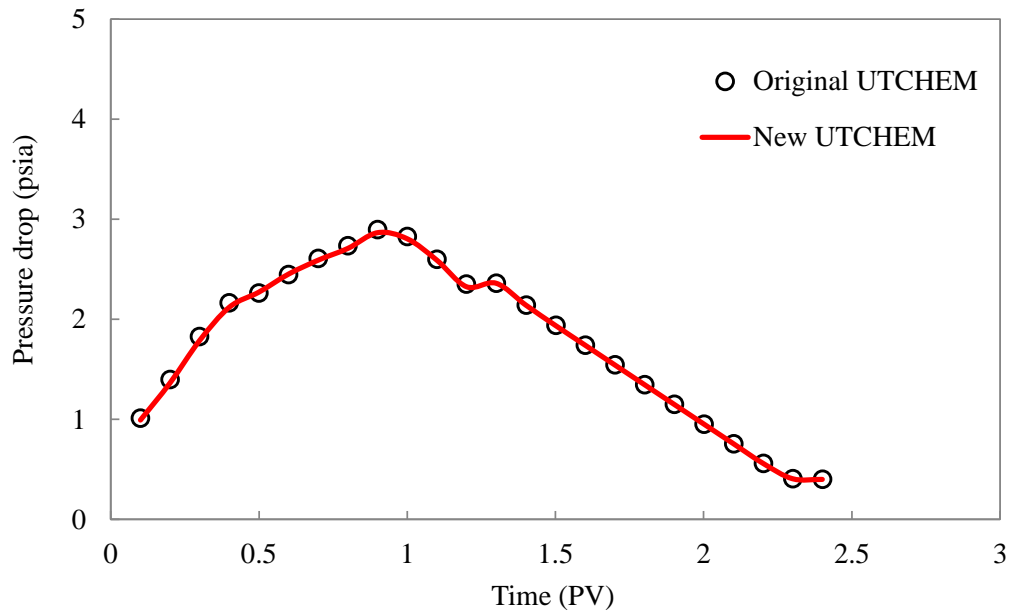


Figure 6.34: Case 4- Pressure drop across the core (New UTCHEM vs. Original UTCHEM)

6.2.2 Case 5- Surfactant Flood Assisted with Foam Drive

Original UTCHEM formulation models the gas phase as a slightly compressible component with no solubility in water and oil. Therefore, at the same conditions the new formulation has to agree with the original one ($R_{so} = 0$, $R_{sw} = 0$, and $B_g = \text{constant}$). Note, four-phase relative permeability calculations were improved in original UTCHEM formulation to be able to simulate surfactant and gas simultaneously.

The same one-dimensional vertical model (with injection from bottom of the core) in Case 4 was used to simulate the surfactant flood followed by co-injection of foaming surfactant and gas. Two surfactants were simulated. An ultralow IFT surfactant (labelled surf # 1 here, for example: long chain IOS surfactants) increases the capillary number and thus decreases the oil saturation. With less residual oil saturation, foam generates and remains more stable. A second surfactant (labelled surf # 2 here, for example: AOS 14-16) serves as a foaming agent to provide mobility control in the surfactant slug and foam drive.

All the surfactants affect both IFT and foaming to different degrees and are rarely independent. Antón *et al.* (2008) discuss mixing rules to estimate microemulsion phase behavior when more than one surfactant is present. The impact of mixing two surfactants also needs to be considered on foaming. At current time, due to lack of experimental measurements, Surf # 1 and Surf # 2 are assumed to be independent, where the first surfactant is only responsible for low IFT displacement (does not generate foam), and second surfactant only generates foam (does not reduce IFT).

The injection schedule is given in Table 6.10. Initially a surfactant/polymer slug is injected in optimum salinity and then is followed with co-injection of gas and foaming surfactant. The UT foam model is described in Section 2.9.1.1. The UT foam model parameters for this case are listed in Table 6.11.

Figure 6.35 through Figure 6.39 compare the simulation results of Case 5 between new and original UTCHEM. The simulation results of oil recovery, oil saturation, pressure, and effluent concentration agree with original UTCHEM. However, CPU time in new formulation increases with about 3 times in this case.

Table 6.10: Case 5- Injection scenario

| | |
|------------|---|
| SP slug | 0.30 PV Injection rate : 0.0041 ft ³ /day Surfactant concentration: 1% of Surf # 1 Polymer concentration: 0.15 wt% Injection salinity: 0.30 meq/ml NaCl |
| Foam drive | 2.20 PV Surfactant injection rate : 0.0021 ft ³ /day Gas injection rate : 0.0021 ft ³ /day Slug concentration : 0.2% of Surf # 2 Injection salinity: 0.25 meq/ml NaCl |

Table 6.11: UT foam model parameters (Case 5)

| Parameter | Value |
|---------------------------|--------|
| R_{ref} | 50 |
| S_w^* | 0.32 |
| S_o^* | 0.25 |
| C_s^* (volume fraction) | 0.0001 |
| ϵ | 0.01 |
| σ | 1.0 |
| $u_{g,ref}$ (ft / day) | 1.0 |

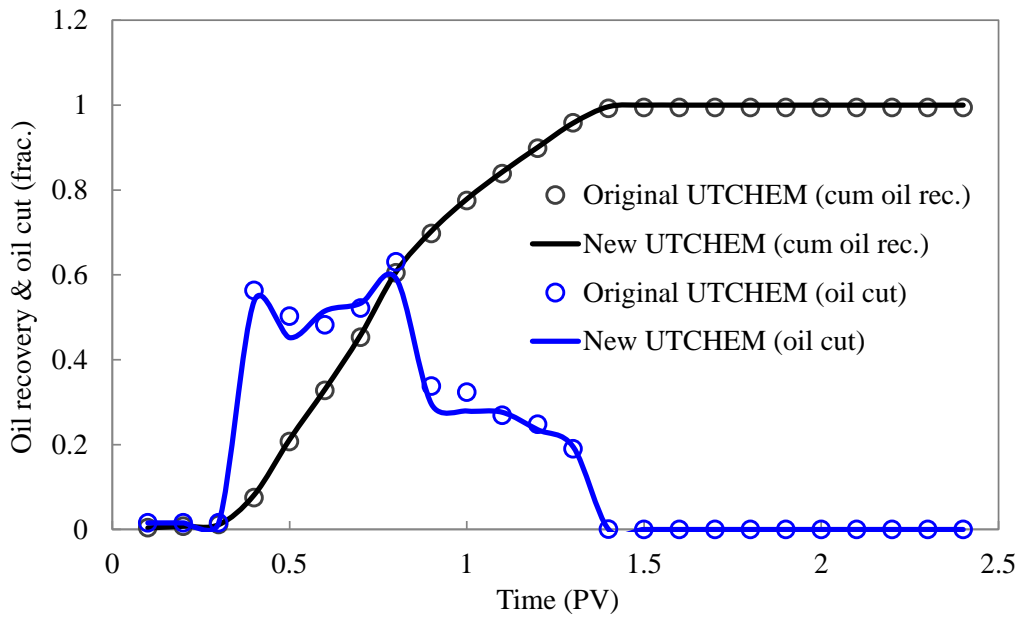


Figure 6.35: Case 5- Oil cut and cumulative oil recovery (New UTCHEM vs. Original UTCHEM)

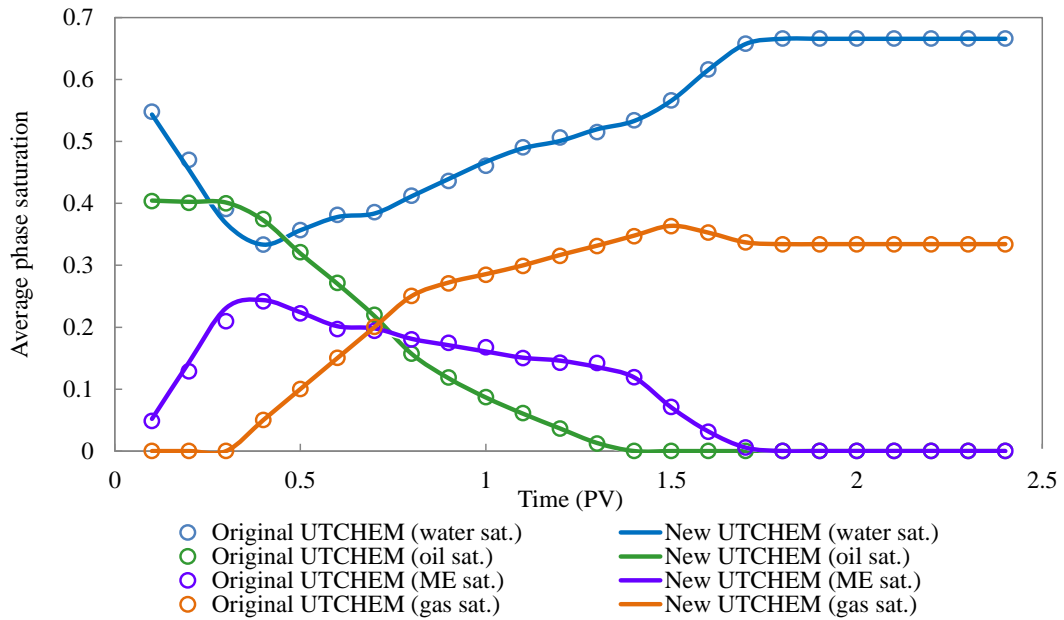


Figure 6.36: Case 5- Average phase saturations inside the core versus injected PV (New UTCHEM vs. Original UTCHEM)

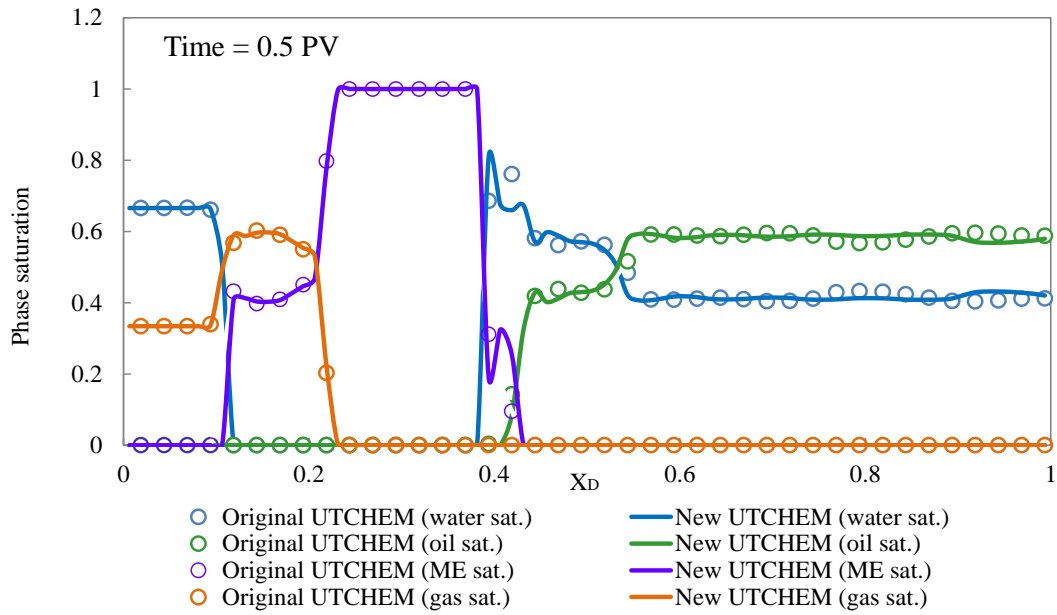


Figure 6.37: Case 5- Phase saturations versus dimensionless distance at 0.5 PV (New UTCHEM vs. Original UTCHEM)

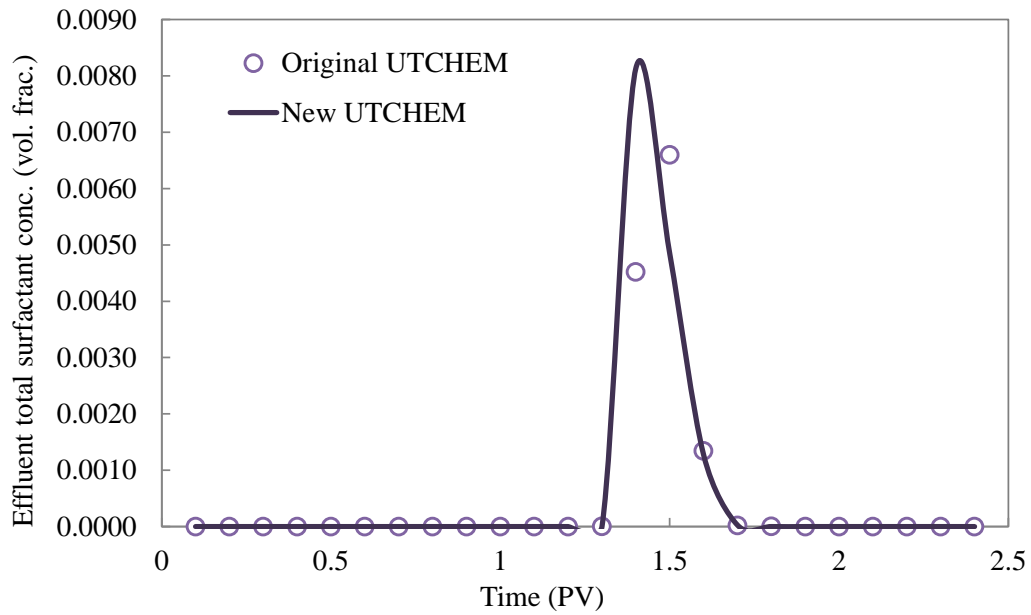


Figure 6.38: Case 5- Effluent total surfactant concentration (New UTCHEM vs. Original UTCHEM)

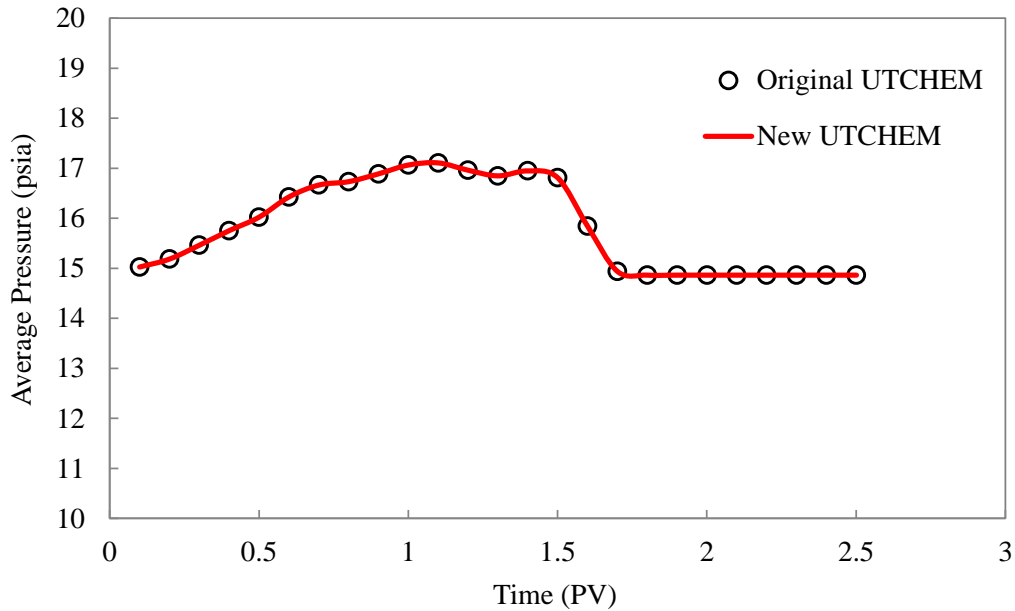


Figure 6.39: Case 5- Pressure drop across the core (New UTCHEM vs. Original UTCHEM)

6.3 GRID REFINEMENT STUDY

Next the effect of gridblock size and convergence was studied to determine the numerical accuracy of the results.

6.3.1 Case 6- Foam Injection as a Drive in the Surfactant-Polymer Process

The convergence of the new formulation was tested with a surfactant/polymer process in which the SP slug is followed by a co-injection of foaming surfactant and gas to generate foam and provide the essential mobility control for the SP slug instead of conventional polymer drive. The reservoir initially contains 10% initial gas. The injection pattern is five-spot with an injector at the center and four producers at the corners. Initially, a slug of ultra-low IFT surfactant/polymer is injected to reduce the residual saturation. Next, the low-tension slug is followed by co-injection of Surf # 2 and gas to

generate foam and provide the essential mobility control behind the slug. Reservoir model is given in Table 6.12. The oil and gas PVT data are the same as data in Table 6.2. Four-phase Corey-type relative permeability data are listed in Table 6.13. Figure 6.40 shows the oil/water solubilization ratio for surfactant formulation in this case. The surfactant adsorption is 0.18 (mg/g rock) and the maximum microemulsion viscosity is 2.2 cp. Surfactant phase behavior, surfactant adsorption and microemulsion viscosity parameters in UTCHEM are given in Table 6.14.

Table 6.12: Model description (Case 6)

| Parameters | Values |
|---|-----------------------|
| Size (ft×ft×ft) | 200×200×40 |
| Initial pressure in top layer (psi) | 2500 |
| Initial water saturation | 0.5 |
| Initial oil saturation | 0.4 |
| Initial gas saturation | 0.1 |
| Initial salinity (meq/ml NaCl) | 0.4 |
| Permeability (md) | 250 |
| Ratio of vertical permeability to horizontal permeability k_z/k_x | 0.1 |
| Porosity | 0.3 |
| Rock compressibility (1/psi) | 1×10^{-6} |
| Wellbore radius (ft) | 0.25 |
| Skin | 0 |
| Capillary pressure (psi) | 0 |
| Water density at standard conditions (lbm/ft ³) | 63.02 |
| Oil density at standard conditions (lbm/ft ³) | 45 |
| Gas density at standard conditions (lbm/ft ³) | 0.0702 |
| Water viscosity at reference pressure (14.7 psi) (cp) | 0.96 |
| Water Formation volume factor at 14.7 psi (rb/scf) | 1.0 |
| Water compressibility (1/psi) | 3×10^{-6} |
| Pressure dependency of water viscosity (cp/psi) | 1.5×10^{-6} |
| Undersaturated oil compressibility (1/psi) | 2.18×10^{-5} |
| Pressure dependence of oil viscosity above bubble point (cp/psi) | 2.55×10^{-5} |
| Producer bottom hole pressure (psi) | 2500 |

Table 6.13: Relative permeability data (Case 6)

| Parameter | Value | Parameter | Value |
|-------------------------------------|------------|-------------------------------|----------|
| $S_{rw}^{low}, S_{rw}^{high}$ | 0.25, 0.0 | n_w^{low}, n_w^{high} | 3.5, 1.0 |
| $S_{row}^{low}, S_{row}^{high}$ | 0.35, 0.0 | n_o^{low}, n_o^{high} | 2.5, 1.0 |
| $S_{rog}^{low}, S_{rog}^{high}$ | 0.20, 0.0 | $n_{me}^{low}, n_{me}^{high}$ | 3.5, 1.0 |
| $S_{rme}^{low}, S_{rme}^{high}$ | 0.25, 0.0 | n_g^{low}, n_g^{high} | 1.5, 1.5 |
| $S_{rg}^{low}, S_{rg}^{high}$ | 0.1, 0.1 | T_{11} | 1600 |
| $k_{rw}^{o low}, k_{rw}^{o high}$ | 0.2, 1.0 | T_{22} | 59000 |
| $k_{ro}^{o low}, k_{ro}^{o high}$ | 0.9, 1.0 | T_{33} | 364 |
| $k_{rme}^{o low}, k_{rme}^{o high}$ | 0.2, 1.0 | T_{44} | 0 |
| $k_{rg}^{o low}, k_{rg}^{o high}$ | 0.94, 0.94 | | |

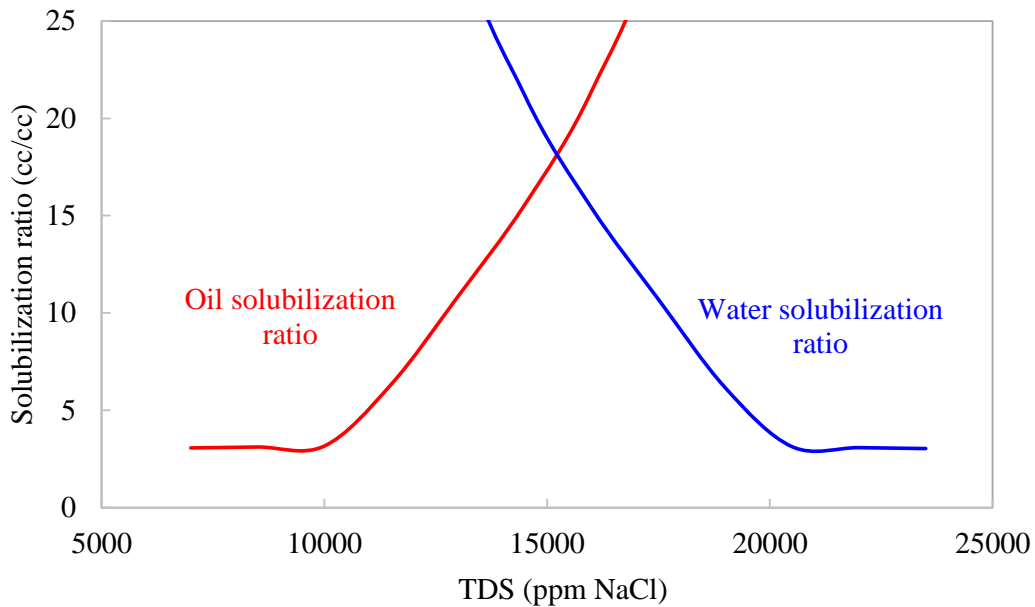


Figure 6.40: Oil/water solubilization ratio for surfactant formulation (Cases 6)

Table 6.14: Surfactant adsorption, microemulsion phase behavior and viscosity parameters (Case 6)

| Surfactant Parameters | Values |
|---|---------------------|
| <i>HBNC70, HBNC71, HBNC72</i> | 0.028, 0.026, 0.028 |
| $C_{SEL}, C_{SEOP}, C_{SEU}$ (meq / ml) | 0.177, 0.260, 0.344 |
| Surfactant adsorption parameters (AD31, AD32, B3D) | 1.0, 0.5, 1000 |
| Microemulsion viscosity: (<i>ALPHAV1, ..., ALPHAV5</i>) | 2, 2, 0, 0.9, 0.7 |

The polymer viscosity used in this simulation is shown in Figure 6.41. The polymer adsorption is about 13 ($\mu\text{g/g}$ rock). The polymer viscosity and adsorption parameters in UTCHEM are listed in Table 6.15.

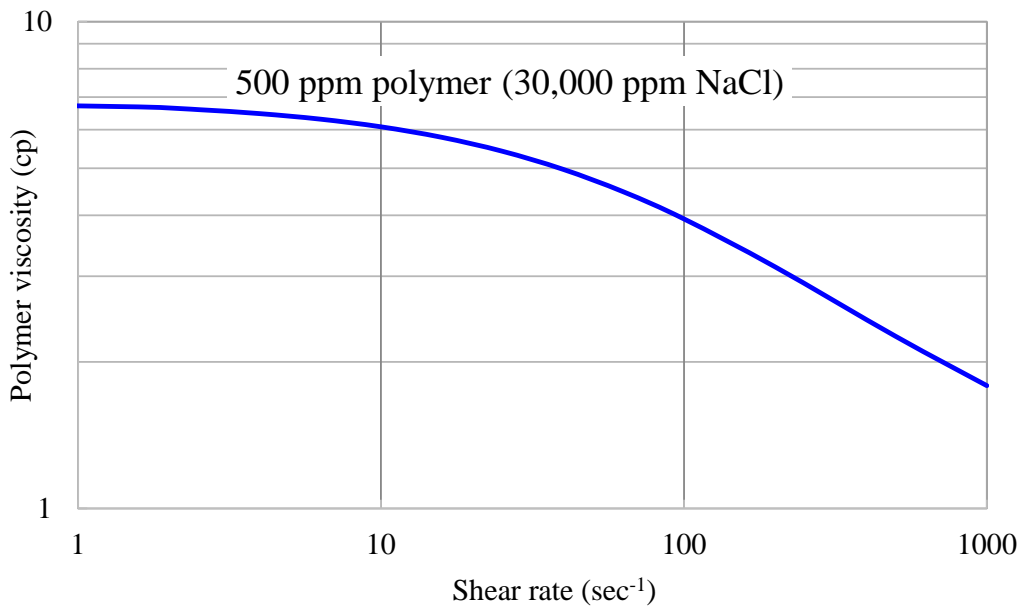


Figure 6.41: Polymer viscosity curve (Cases 6)

Table 6.15: Polymer properties (Cases 6)

| Polymer Parameters | Values |
|---|------------------|
| AP ₁ , AP ₂ , AP ₃ | 81, 220, 2500 |
| BETAP, SSLOPE | 1.0, -0.17 |
| GAMMAC, GAMHF, POWN, GAMHF2 | 4.0, 100, 1.8, 0 |
| Polymer adsorption parameters (AD41, AD42, B4D) | 0.7, 0.5, 100 |

Similar to Case 5, two surfactants were simulated (Surf # 1: low IFT surfactant, Surf # 2: foaming surfactant). Injection schedule, fluid rates, and injection species concentrations are presented in Table 6.16. UT foam model was used for these foam simulations. The UT foam model parameters are listed in Table 6.17.

Table 6.16: Case 6 – Injection schedule

| | |
|------------|---|
| SP slug | Time: 150 days ~ 0.25 PV Surfactant solution injection rate: 800 ft ³ /day Injection salinity: 0.3 meq/ml NaCl Slug concentration: 1% of surf # 1 and 500 ppm polymer (~ 6 cp) |
| Foam drive | Time: 1050 days Surfactant solution injection rate: 400 ft ³ /day Gas injection rate: 120 Mscf/day Injection salinity: 0.15 meq/ml NaCl Slug concentration: 0.2% of surf # 2 |

Table 6.17: UT foam model parameters (Case 6)

| Parameter | Value |
|---------------------------|--------|
| R_{ref} | 250 |
| S_w^* | 0.28 |
| S_o^* | 0.25 |
| C_s^* (volume fraction) | 0.0001 |
| ε | 0.01 |
| σ | 1.0 |
| $u_{g,ref}$ (ft / day) | 1.0 |

We performed a series of simulations with different gridblock sizes as listed in Table 6.18. The reservoir was refined in both horizontal and vertical directions to check the dependency of oil recovery on the size of the gridblocks in each direction. Figure 6.42 shows the reservoir model with different gridblock sizes. In runs 1 through 5, the reservoir model was refined in areal (x - y) direction with constant number of layers in z -direction ($N_z = 4$). In runs 6 through 9, the model was refined in z -direction with constant number of gridblocks in areal direction ($N_x = 15, N_y = 15$)

Table 6.18: Case 6- Number of gridblocks in different runs

| Run # 1 | Number of grids | Gridblock size (ft×ft×ft) |
|---------|-----------------|---------------------------|
| 1 | 11×11×4 | 18.18×18.18×10 |
| 2 | 15×15×4 | 13.33×13.33×10 |
| 3 | 21×21×4 | 9.52×9.52×10 |
| 4 | 41×41×4 | 4.88×4.88×10 |
| 5 | 101×101×4 | 1.98×1.98 |
| 6 | 15×15×2 | 13.33×13.33×20 |
| 7 | 15×15×6 | 13.33×13.33×6.67 |
| 8 | 15×15×10 | 13.33×13.33×4 |
| 9 | 15×15×20 | 13.33×13.33×2 |

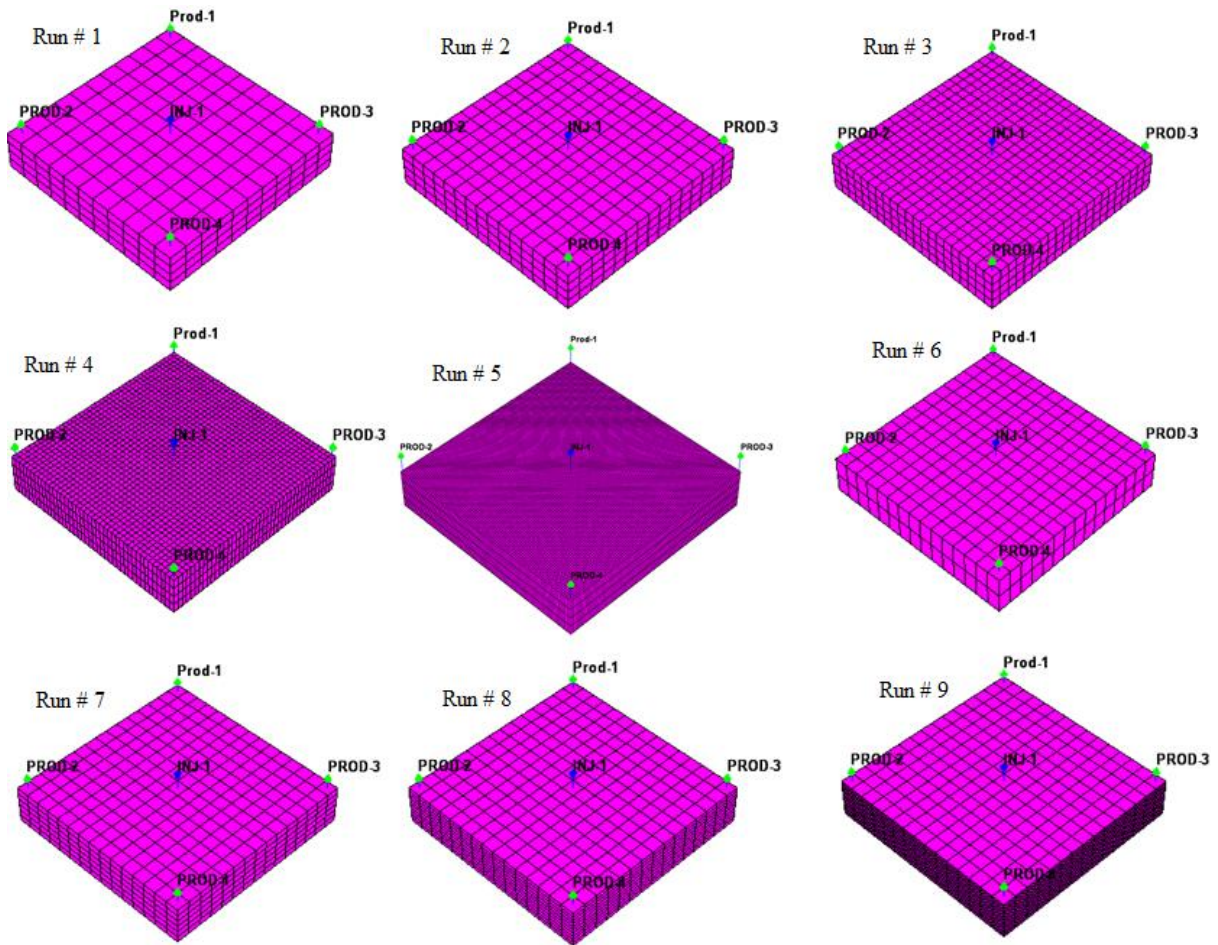


Figure 6.42: Case 6- Reservoir model and gridblock sizes for different simulations runs.

Figure 6.43 compares the cumulative oil recovery for all the runs. Figure 6.44 plots the final oil recovery against the dimensionless gridblock size in areal direction. Results show with using smaller gridblock sizes in areal direction the cumulative oil recovery increases and finally approaches to a constant value ($R = 0.67$). Cumulative oil recovery curves in Figure 6.43 coincide for Runs 4 and 5 with different gridblock size in x-y direction.

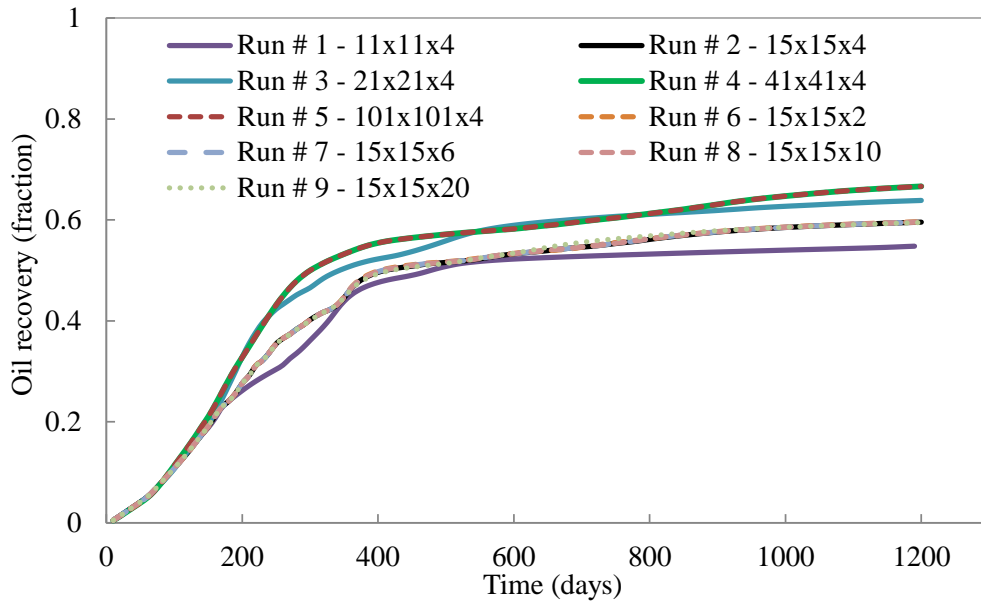


Figure 6.43: Case 6 - Cumulative Oil recovery (Runs 4, 5 and Runs 2, 6, 7, 8, 9 coincide)

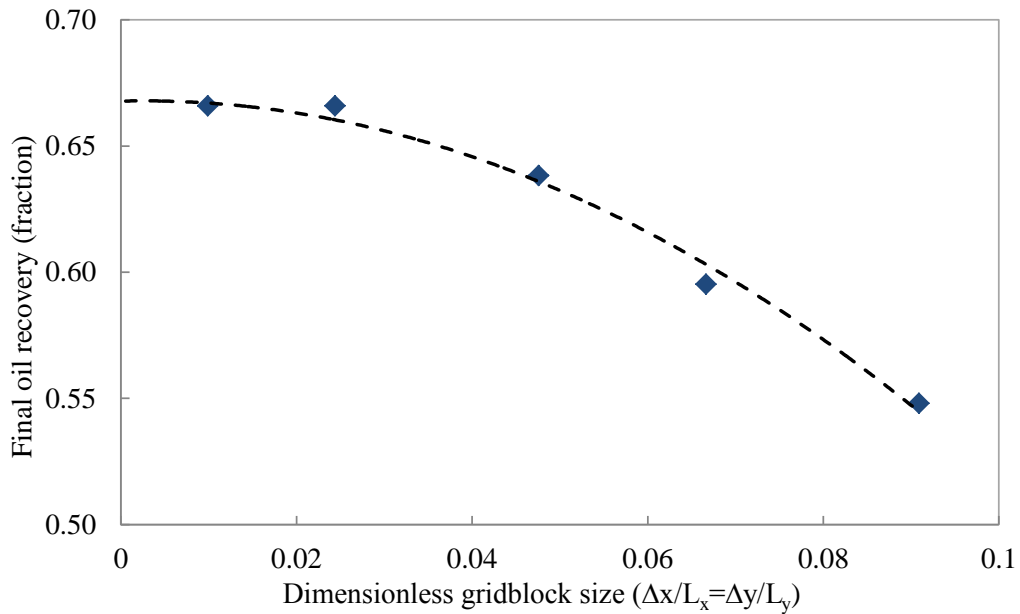


Figure 6.44: Case 6 – Final oil recovery versus dimensionless gridblock size in areal direction

Figure 6.45 plots the final oil recovery against the dimensionless gridblock size in vertical direction. Results show the oil recovery in this homogeneous case is independent of gridblock size in z -direction. Cumulative oil recovery curves in Figure 6.43 coincide in Runs 2, 6, 7, 8, and 9 with different gridblock size in z -direction. However, in a heterogeneous reservoir, the oil recovery depends on the gridblock size in vertical direction (Lim 1993)

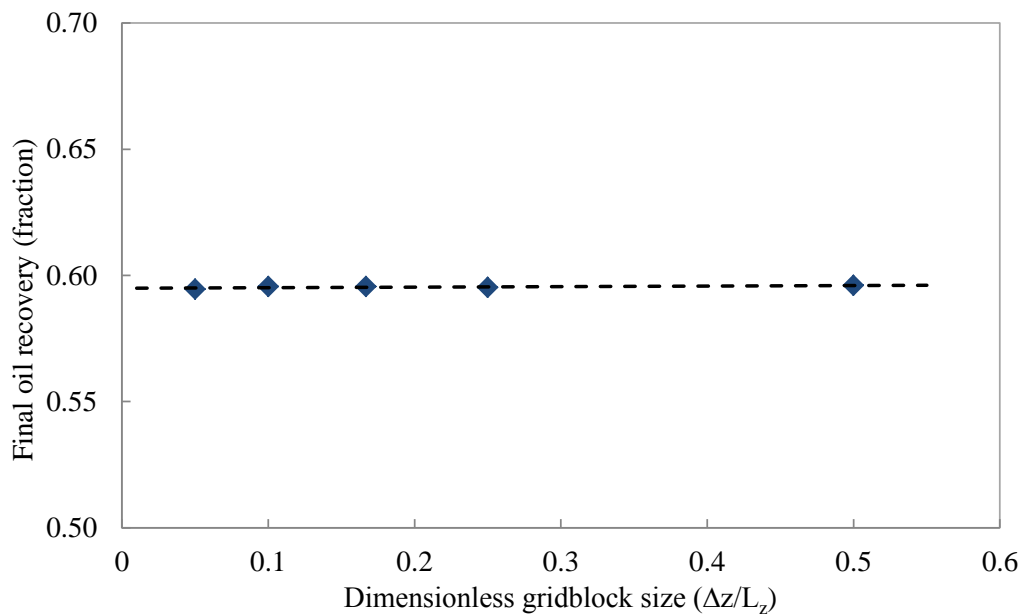


Figure 6.45: Case 6 – Final oil recovery versus dimensionless gridblock size in vertical direction

Figure 6.46 and Figure 6.47 show oil concentration and gas saturation at the end of the process (1200 days) for the full field and a quarter of the field. A very fine model ($51 \times 51 \times 16$) was used to capture fingers. The results show, foam improves the vertical sweep efficiency and provide a good mobility control behind the SP slug. The input file for this case is presented in Appendix B.2.

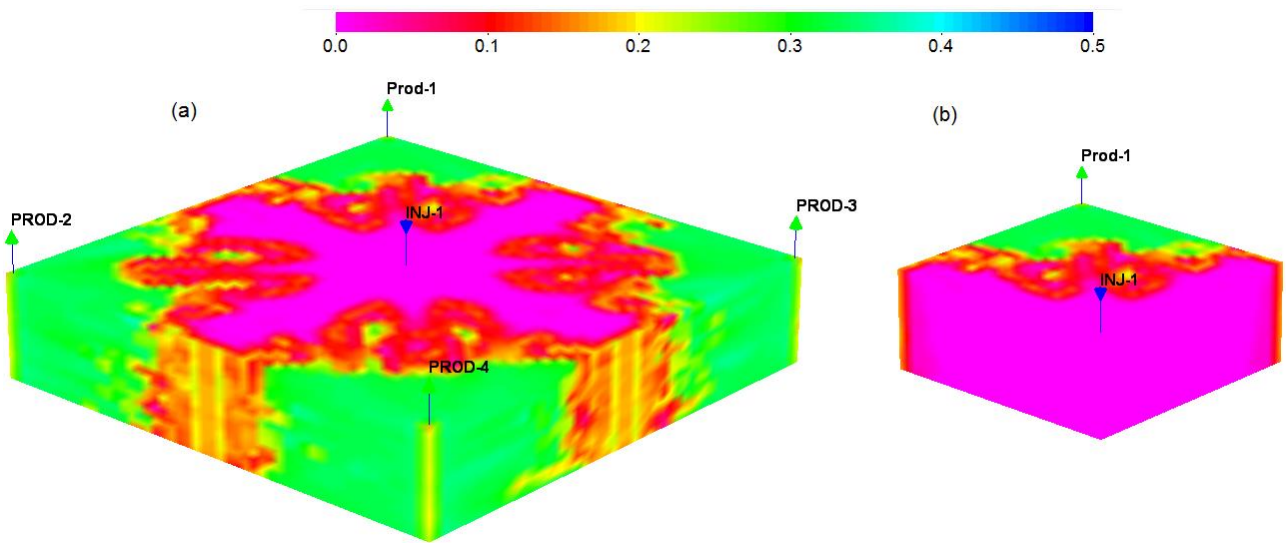


Figure 6.46: Case 6– Oil concentration after 1200 days a) full field and b) a quarter of the field

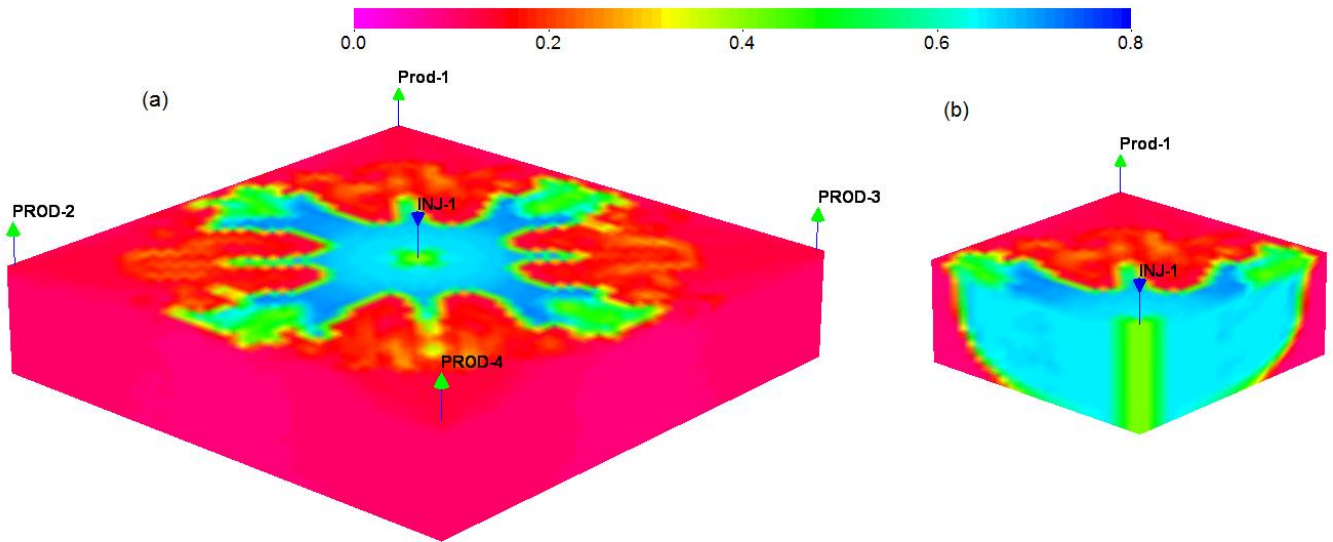


Figure 6.47: Case 6– Gas saturation after 1200 days a) full field and b) a quarter of the field

6.4 SIMULATION OF LOW-TENSION-GAS FLOODING

The main purpose for development of four-phase flow simulator is to model chemical flood processes involving gas (i.e. low-tension-gas or/and foam) and to account for the most important recovery mechanisms. A 2-D x - z model was set up to simulate low-tension-gas flooding with both the surfactant alternating gas (SAG) process and co-injection of gas and slug/drive surfactant solution. The reservoir permeability was generated using MDM software with average horizontal permeability of 127 md. Figure 6.48 shows the reservoir model, well locations, and permeability distribution. Wells are completed in all the vertical layers. The reservoir is initially undersaturated at residual oil saturation. Table 6.19 lists reservoir model and fluid properties in this case. Nitrogen serves as the gas with PVT properties listed in Table 6.20. Nitrogen solubility is assumed to be negligible in both water and oil (R_{so} and $R_{sw} \sim 0$). The four-phase Corey-type relative permeability parameters are in Table 6.21.

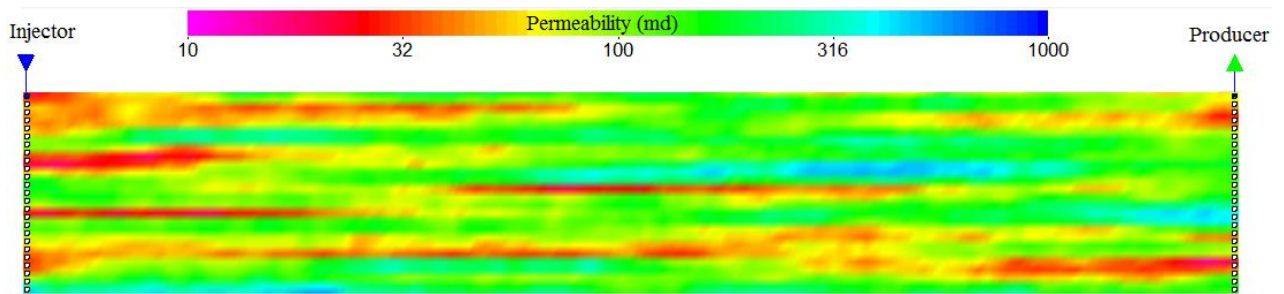


Figure 6.48: Reservoir model and permeability distribution (Cases 7 to 9)

Table 6.19: Reservoir and fluid properties for four-phase simulations (Cases 7 to 9)

| <u>Parameters</u> | <u>Values</u> |
|---|-----------------------|
| Number of gridblocks | 150×1×25 |
| Gridblock size (ft×ft×ft) | 2×10×2 |
| Initial pressure (top layer) (psi) | 2000 |
| Initial water saturation | 0.65 |
| Initial oil saturation | 0.35 |
| Initial salinity (meq/ml NaCl) | 0.26 |
| Average horizontal permeability (md) | 127 |
| Ratio of vertical permeability to horizontal permeability k_z/k_x | 0.1 |
| Dykstra-Parsons coefficient | 0.70 |
| Correlation length in x direction (ft) | 300 |
| Correlation length in z direction (ft) | 5 |
| Porosity | 0.3 |
| Rock compressibility (1/psi) | 1×10^{-6} |
| Wellbore radius (ft) | 0.25 |
| Skin | 0 |
| Capillary pressure (psi) | 0 |
| Water density at standard conditions (lbm/ft ³) | 63.02 |
| Oil density at standard conditions (lbm/ft ³) | 57 |
| Gas density at standard conditions (lbm/ft ³) | 0.0702 |
| Water viscosity (cp) | 1.0 |
| Water formation volume factor (rb/scf) | 1.0 |
| Water compressibility (1/psi) | 3×10^{-6} |
| Oil viscosity (cp) | 1.17 |
| Oil formation volume factor (rb/scf) | 1.05 |
| Oil compressibility (1/psi) | 2.18×10^{-5} |
| R_{so} and R_{sw} (scf/stb) | ~ 0 |
| Producer bottom hole pressure (psi) | 2000 |

Table 6.20: Gas phase properties (Cases 7 to 9)

| Pressure (psi) | E_g (scf/rb) | Gas viscosity (cp) |
|----------------|----------------|--------------------|
| 400 | 169.49 | 0.0130 |
| 800 | 338.98 | 0.0135 |
| 1200 | 510.20 | 0.0140 |
| 1600 | 680.27 | 0.0145 |
| 2000 | 847.46 | 0.0150 |
| 2400 | 1020.40 | 0.0155 |
| 2800 | 1190.50 | 0.0160 |
| 3200 | 1351.40 | 0.0165 |
| 3600 | 1538.50 | 0.0170 |
| 4000 | 1694.90 | 0.0175 |
| 4400 | 1851.90 | 0.0180 |
| 4800 | 2040.80 | 0.0185 |
| 5200 | 2222.20 | 0.0190 |
| 5600 | 2381.00 | 0.0195 |

Table 6.21: Relative permeability for four-phase simulations (Cases 7 to 9)

| <u>Parameter</u> | <u>Value</u> | <u>Parameter</u> | <u>Value</u> |
|------------------------------------|--------------|---|--------------|
| $S_{rw}^{low} / S_{rw}^{high}$ | 0.25 / 0.0 | n_w^{low} / n_w^{high} | 3.5 / 1.0 |
| $S_{row}^{low} / S_{row}^{high}$ | 0.35 / 0.0 | n_o^{low} / n_o^{high} | 2.5 / 1.0 |
| $S_{rog}^{low} / S_{rog}^{high}$ | 0.20 / 0.0 | $n_{me}^{low} / n_{me}^{high}$ | 3.5 / 1.0 |
| $S_{rme}^{low} / S_{rme}^{high}$ | 0.25 / 0.0 | n_g^{low} / n_g^{high} | 1.5 / 1.5 |
| $S_{rg}^{low} / S_{rg}^{high}$ | 0.1 / 0.1 | $T_{DC_w} (T_{11} \text{ in } UTCHEM)$ | 1600 |
| $k_{rw}^{o,low} / k_{rw}^{o,high}$ | 0.2 / 1.0 | $T_{DC_o} (T_{22} \text{ in } UTCHEM)$ | 59000 |
| $k_{ro}^{o,low} / k_{ro}^{o,high}$ | 0.9 / 1.0 | $T_{DC_{me}} (T_{33} \text{ in } UTCHEM)$ | 364 |
| $k_{me}^{o,low} / k_{me}^{o,high}$ | 0.2 / 1.0 | $T_{DC_g} (T_{44} \text{ in } UTCHEM)$ | 0 |
| $k_{rg}^{o,low} / k_{rg}^{o,high}$ | 0.94 / 0.94 | | |

The model used one surfactant to reduce IFT (surf # 1) and a second surfactant for foam generation (surf # 2) with no impact on microemulsion phase behavior. Figure 6.49

shows the oil/water solubilization ratio for surfactant formulation in this case. The surfactant adsorption is about 0.18 (mg/g rock) and the maximum microemulsion viscosity is 2.5 cp. Surfactant phase behavior, surfactant adsorption and microemulsion viscosity parameters in UTCHEM are given in Table 6.22.

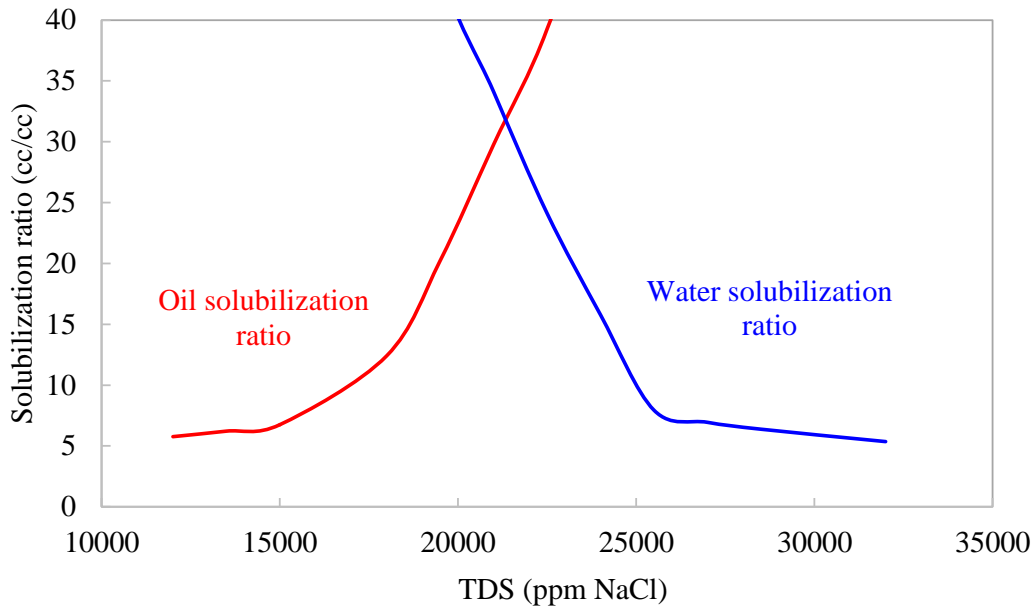


Figure 6.49: Oil/water solubilization ratio for surfactant formulation (Cases 7 to 9)

Table 6.22: Surfactant adsorption, microemulsion phase behavior and viscosity parameters (Cases 7 to 9)

| Surfactant Parameters | Values |
|---|---------------------|
| <i>HBNC70, HBNC71, HBNC72</i> | 0.025, 0.015, 0.025 |
| $C_{SEL}, C_{SEOP}, C_{SEU}$ (meq / ml) | 0.28, 0.365, 0.45 |
| Surfactant adsorption parameters (AD31, AD32, B3D) | 1.0, 0.5, 1000 |
| Microemulsion viscosity: (<i>ALPHAV1, ..., ALPHAV5</i>) | 2, 2, 0, 0.9, 0.7 |

A series of simulations were done to study the impact of foam mobility control on oil recovery during surfactant flooding. The UT foam model was used in the simulations with the maximum gas reduction factor of 100. UT foam model parameters are listed in Table 6.23.

Table 6.23: UT foam model parameters (Cases 8 and 9)

| Foam Parameters | Value |
|------------------------------------|-------|
| R_{ref} | 100 |
| S_w^* | 0.28 |
| S_o^* | 0.25 |
| C_s^* (<i>volume fraction</i>) | 0.001 |
| \mathcal{E} | 0.01 |
| σ | 1.0 |
| $u_{g,ref}$ (<i>ft / day</i>) | 1.0 |

6.4.1 Case 7 – Base Case (Surfactant Flooding without Mobility Control)

In this case, 1% of low-tension surfactant slug (surf # 1) is injected for 0.2 PV (35 days) and then followed by a water drive. Injection schedule, fluid rates and concentrations are presented in Table 6.24. Daily oil production rate and cumulative oil recovery are plotted in Figure 6.50. In the absence of mobility control agents, a large portion of the reservoir is not swept by the surfactant and only 43% of the initial oil is recovered with an average remaining oil saturation of 0.20.

Table 6.24: Case 7 – Injection Schedule

| | |
|-----------------|--|
| Surfactant slug | Time: 35 days ~ 0.2 PV Injection rate : 250 ft ³ /day Injection salinity: 0.65 meq/ml NaCl Surfactant concentration: 1% surf # 1 |
| Water drive | Time: 325 days ~ 1.85 PV Injection rate: 250 ft ³ /day Injection salinity: 0.22 meq/ml NaCl |

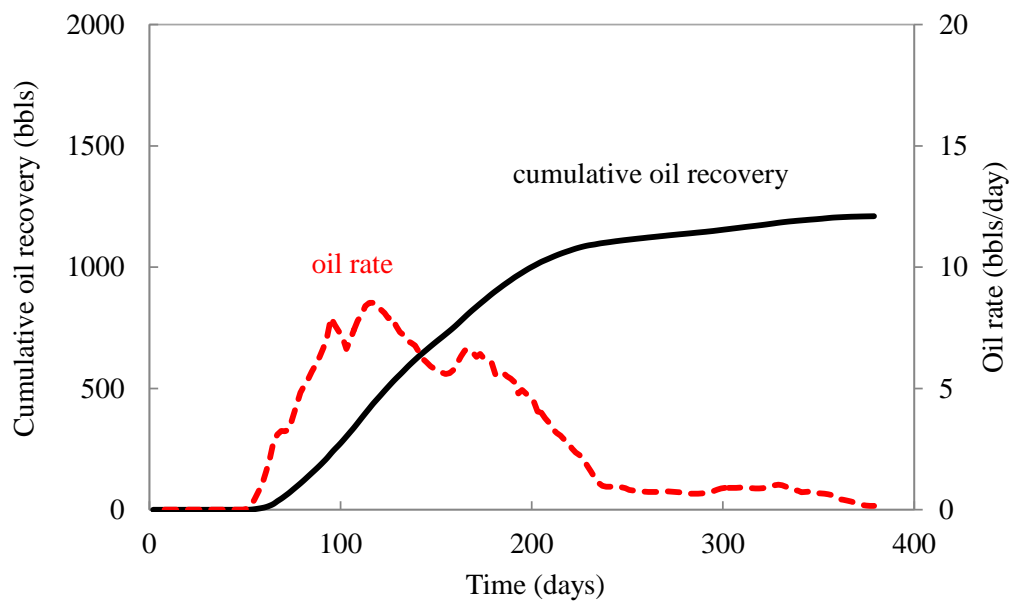


Figure 6.50: Case 7 - Cumulative oil recovery and oil rate

In next two cases, foam serves as a mobility control agent for low-tension surfactant flooding.

6.4.2 Case 8 – Surfactant Alternating Gas (SAG) with Foam

The process is performed in two cycles. In the first cycle, a blend of 5:1 of low-tension surfactant and foaming surfactant (1% surf # 1 and 0.2% surf # 2) is injected and followed by a slug of nitrogen. In the second cycle, the surfactant slug only contains surfactant # 2 and followed by nitrogen to generate foam and provide the essential mobility control for the low-tension surfactant flooding in the first cycle. Injection schedule, fluid rates and concentrations are presented in Table 6.25. Daily oil production rate and cumulative oil recovery are plotted in Figure 6.51. In this case, 58% of initial oil is recovered with an average remaining oil saturation of 0.147.

Table 6.25: Case 8 – Injection Schedule

| | |
|---------------------|--|
| Surfactant slug #1 | Time: 35 days ~ 0.2 PV Injection rate: 250 ft ³ /day Injection salinity: 0.65 meq/ml NaCl Surfactant concentration: blend of 1% of surf # 1 and 0.2% of surf # 2 |
| Gas slug | Time: 35 days Injection rate : 50 Mscf/day |
| Surfactant slug # 2 | Time: 145 days ~ 0.82 PV Injection rate: 250 ft ³ /day Injection salinity: 0.22 meq/ml NaCl Surfactant concentration: 0.2% of surf # 2 |
| Gas drive | Time: 145 days Injection rate: 50 Mscf/day |

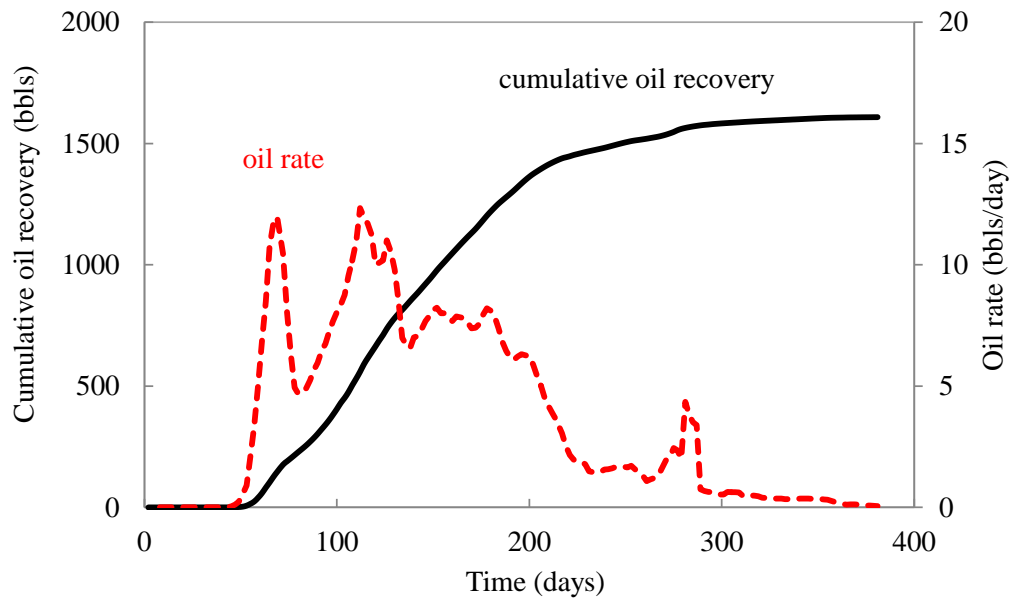


Figure 6.51: Case 8 - Cumulative oil recovery and oil rate

6.4.3 Case 9 – Co-injection of Surfactant and Gas

In this case the blend of 5:1 of surfactants (1% surf # 1 and 0.2% surf # 2) is co-injected with nitrogen ($f_g = 57\%$ at 2000 psi). Next, low-tension gas slug is followed by drive injection of 0.2% surf # 2 co-injected with nitrogen at the same rate and gas quality. For a fair comparison with SAG process, the same amount of fluids and surfactants are injected in both cases. Injection schedule, fluid rates and concentrations are presented in Table 6.26. Daily oil production rate and cumulative oil recovery are plotted in Figure 6.52. In this case, 71% of the initial oil is recovered with an average remaining oil saturation of 0.10.

Table 6.26: Case 9 – Injection Schedule

| | |
|---------------------|--|
| Surfactant/gas slug | Time: 70 days Surfactant solution injection rate: 125 ft ³ /day Gas injection rate: 25 Mscf/day Injection salinity: 0.65 meq/ml NaCl Surfactant concentration: blend of 1% of surf # 1 and 0.2% of surf # 2 |
| Foam drive | Time: 290 days Surfactant solution injection rate: 125 ft ³ /day Gas injection rate: 25 Mscf/day Injection salinity: 0.22 meq/ml NaCl Surfactant concentration: 0.2% of surf # 2 |

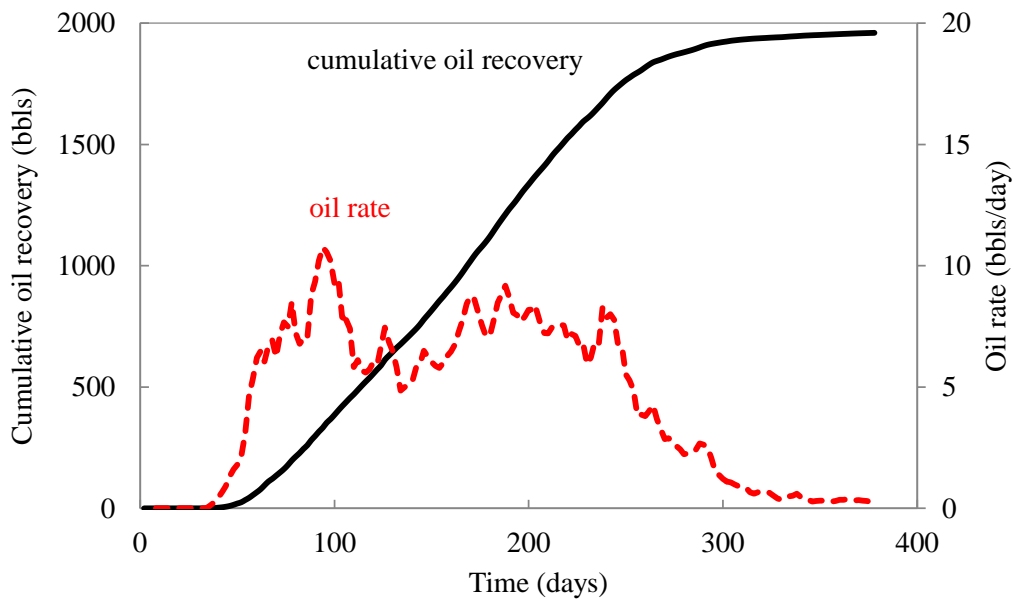


Figure 6.52: Case 9 - Cumulative oil recovery and oil rate

6.4.4 Results and Discussions

Figure 6.53 compares the recovery factor for all the cases. With using foam in Case 8 and Case 9, the oil recovery increases by 15% and 28% respectively compared to

Case 7 due to better mobility control. Figure 6.54 shows the remaining oil saturation at the end of each process (360 days). In the absence of mobility control agents (polymer or foam) in Case 7, the injected surfactant was produced quickly through the high permeability layers and a large portion of the reservoir is not swept by surfactant. Using foam in Cases 8 and 9 blocks the high permeability layers and diverts the flow to low permeability zones. Figure 6.55 plots effluent salinity at the producer for all three cases. The surfactant slug was designed to pass the optimum salinity to achieve ultra-low IFT for the best performance. Comparison of the oil recovery in Cases 8 and 9 indicates the co-injection scheme has a higher recovery factor compared to SAG process. However, the co-injection of surfactant solution and gas may cause some operational difficulty due to injectivity loss. Figure 6.56 plots injection pressure for all three cases. Co-injection scheme has a higher bottomhole pressure compared to SAG process.

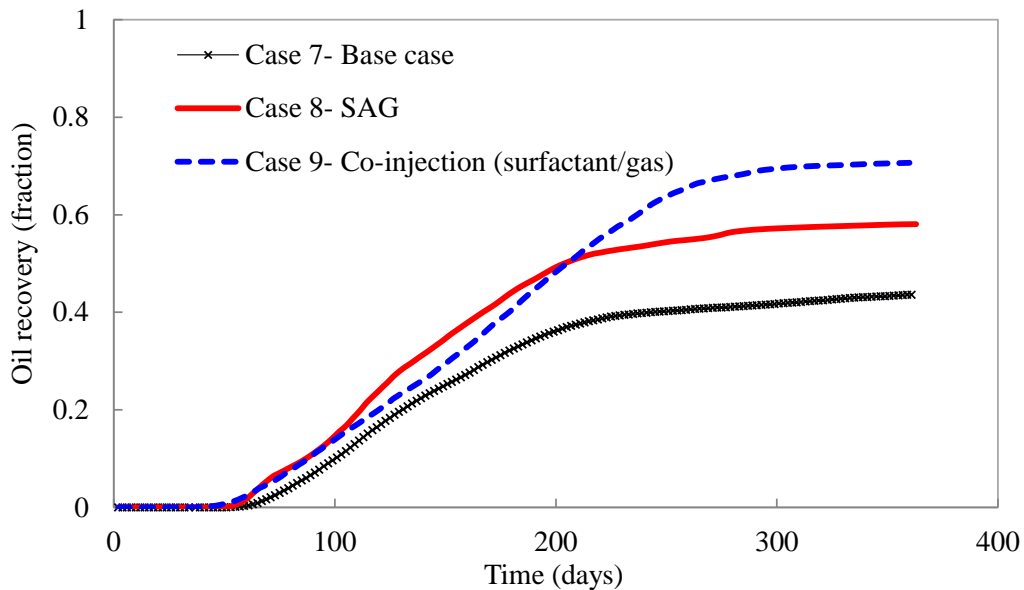


Figure 6.53: Comparison of recovery factor between Cases 7 to 9

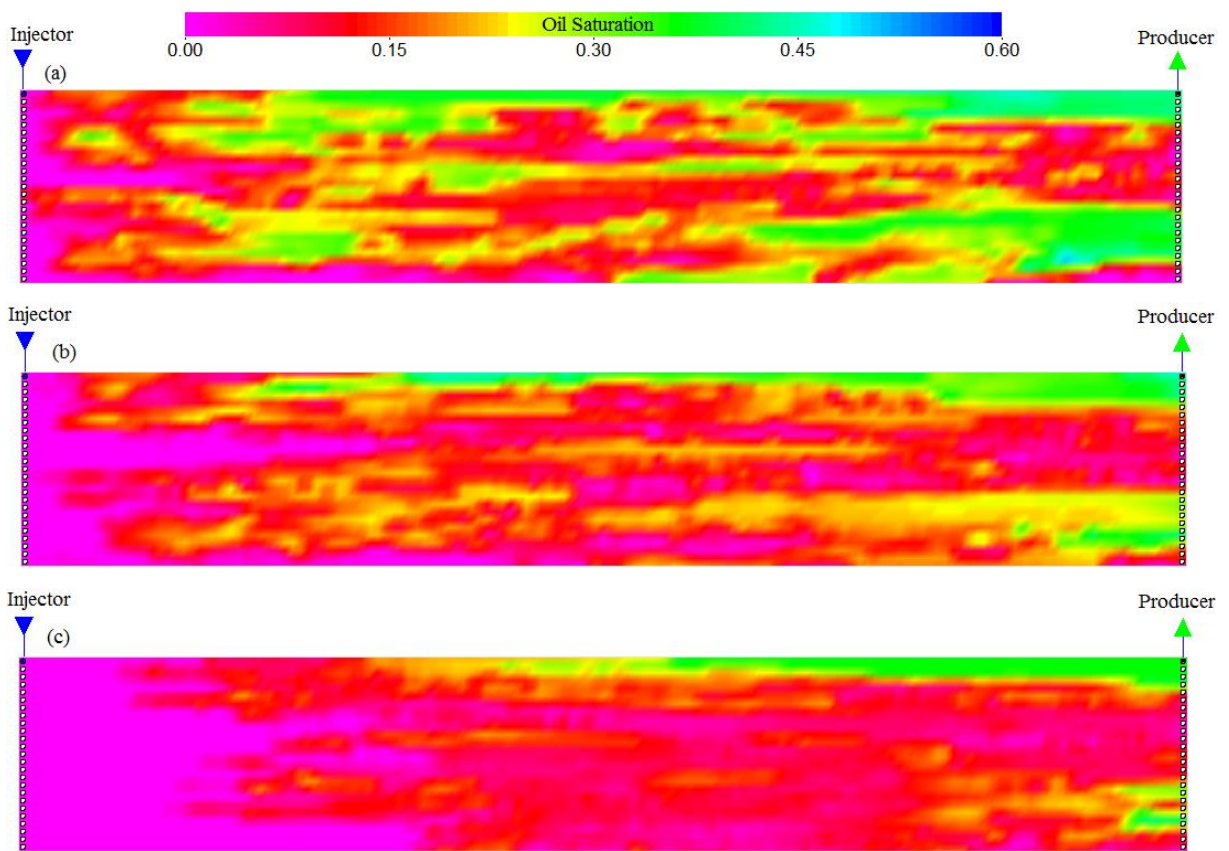


Figure 6.54: Remaining oil saturation (after 360 days) a) Case 7- Base case b) Case 8- SAG c) Case 9- Co-injection (surfactant/gas)

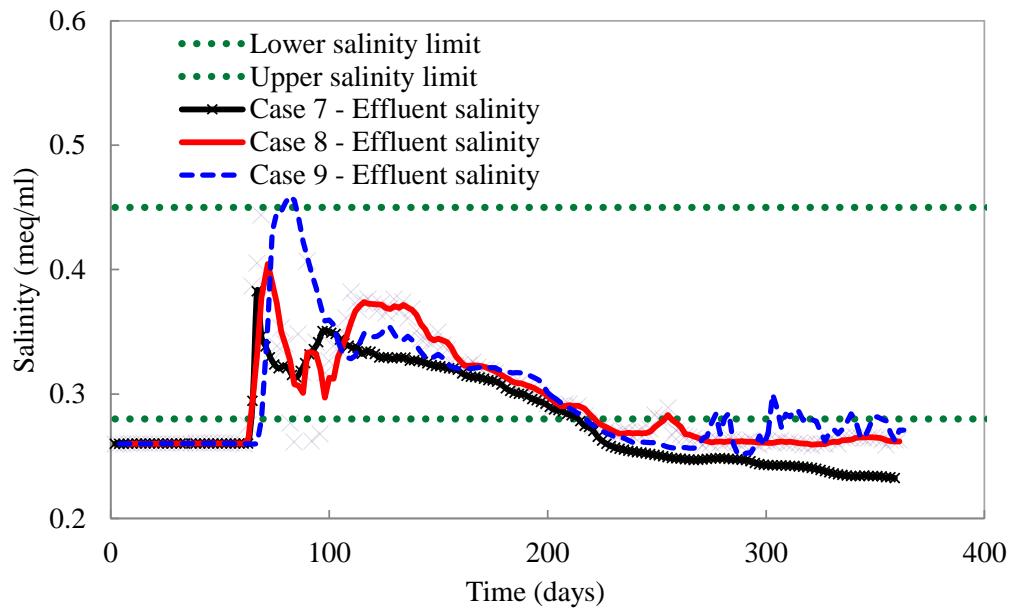


Figure 6.55: Salinity limits and effluent salinity for Cases 7 to 9

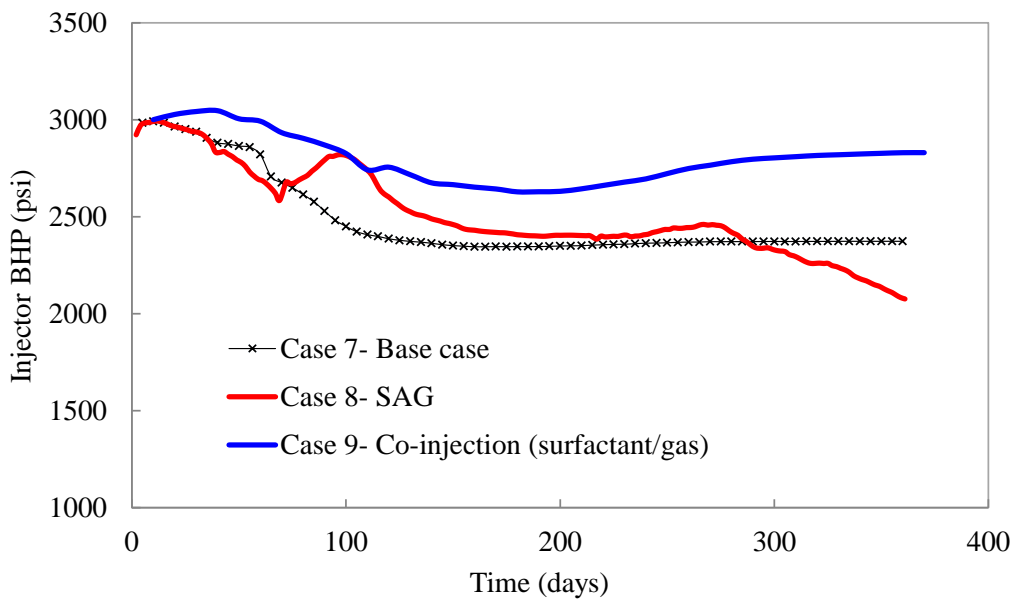


Figure 6.56: Injector bottomhole pressure for Cases 7 to 9

6.5 MOBILITY CONTROL FOR GAS FLOODING

The application of gas injection for enhanced oil recovery has been shown to be a technically successful process. Many parameters control the performance of gas flooding in field scale. The oil recovery is particularly sensitive to reservoir heterogeneity, vertical to horizontal permeability, well trajectory (horizontal or vertical well), well location, the choice of relative permeability, and etc. (Lim 1993). However, oil recoveries are often compromised by poor sweep efficiencies because of low gas viscosities and densities.

The Water Alternating Gas (WAG) process was known to provide better sweep efficiency and reduce gas channeling from injector to producer. However, gravity segregation of the water and gas often reduces the effectiveness of WAG. Two approaches have been studied to minimize this problem. Polymer can be added to the water to increase its viscosity and surfactant can be added to the water to generate a foam.

In this section, the impact of WAG, Polymer Alternating Gas (PAG), and foam on gas mobility was simulated in a heterogeneous reservoir. The average reservoir permeability is 82 md and permeability map was generated using MDM software with parameters provided in Table 6.27. Figure 6.57 shows the reservoir model and permeability distribution. Injection and production wells are horizontal and are located at the bottom of the reservoir to minimize the gas segregation and give the best performance for the gas flooding (Lim, 1993). However, the benefits of using horizontal wells are very sensitive to both the reservoir description and the layer in which the horizontal wells are located. The impact of hysteresis on gas relative permeability was not modeled in the simulations. The more accurate simulations need to include hysteresis to model the effect of cycle dependency during alternative injection of gas and chemical (i.e. SAG, PAG,

and etc). Beygi *et al.* (2015) proposed a three-phase hysteresis model to add the cycle-dependent relative permeability in multicycle processes.

The reservoir is initially undersaturated with 75% initial oil saturation. Reservoir model and fluid properties are listed in Table 6.27.

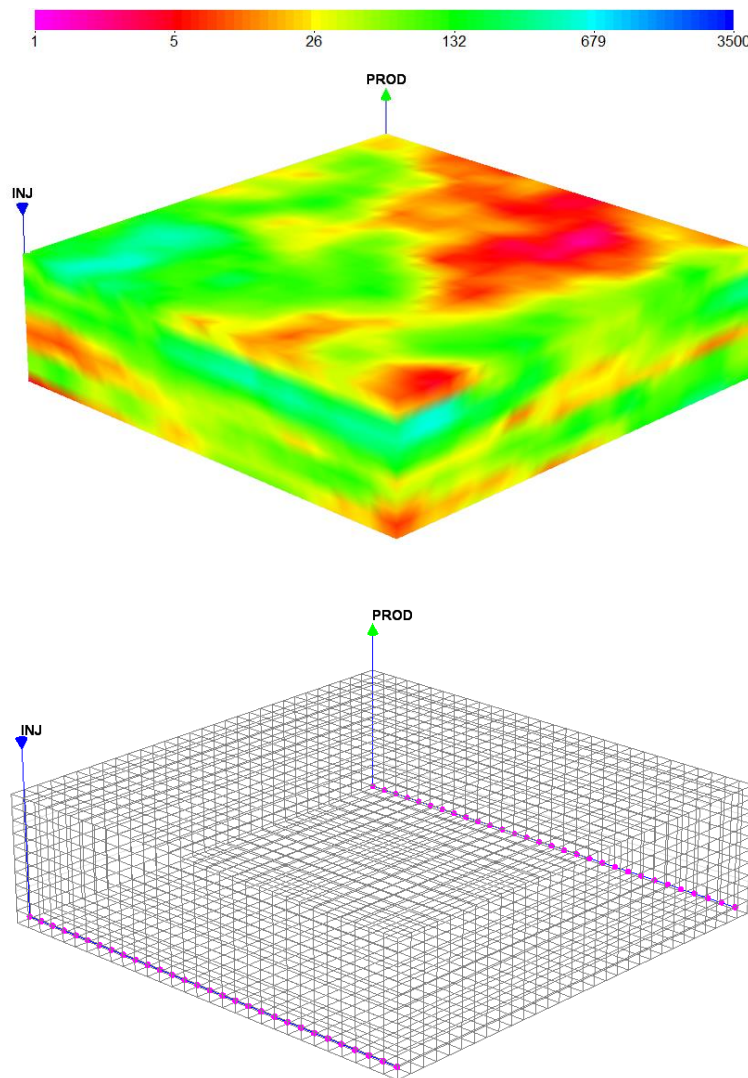


Figure 6.57: Reservoir model, well locations and permeability distribution ($L_x = L_y = 150$ ft, $L_z = 40$ ft)

Table 6.27: Reservoir and fluid properties (Cases 10 to 13)

| Parameters | Values |
|---|-----------------------|
| Number of gridblocks | 30×30×10 |
| Gridblock size (ft×ft×ft) | 5×5×4 |
| Initial pressure (top layer) (psi) | 3100 |
| Initial water saturation | 0.25 |
| Initial oil saturation | 0.75 |
| Initial salinity (meq/ml NaCl) | 0.20 |
| Average areal permeability (md) | 82 |
| Ratio of vertical permeability to horizontal permeability k_z/k_x | 0.2 |
| Dykstra-Parsons coefficient | 0.75 |
| Correlation length in x and y direction (ft) | 150 |
| Correlation length in z direction (ft) | 5 |
| Porosity | 0.27 |
| Rock compressibility (1/psi) | 1×10^{-6} |
| Wellbore radius (ft) | 0.25 |
| Skin | 0 |
| Capillary pressure (psi) | 0 |
| Water density at standard conditions (lbm/ft ³) | 62.24 |
| Oil density at standard conditions (lbm/ft ³) | 46.24 |
| Gas density at standard conditions (lbm/ft ³) | 0.0647 |
| Water viscosity (cp) | 0.47 |
| Water compressibility (1/psi) | 2.98×10^{-6} |
| Compressibility of undersaturated oil (1/psi) | 1.37×10^{-5} |
| Pressure dependence of oil viscosity above bubble point pressure (cp/psi) | 4.6×10^{-5} |
| Gas/oil mobility ratio | ~ 13 |

Methane is the injection gas. Oil/gas PVT properties (formation volume factor, viscosity, and solution gas/oil ratio) are plotted in Figure 6.58 to Figure 6.60, with data listed in Table 6.28.

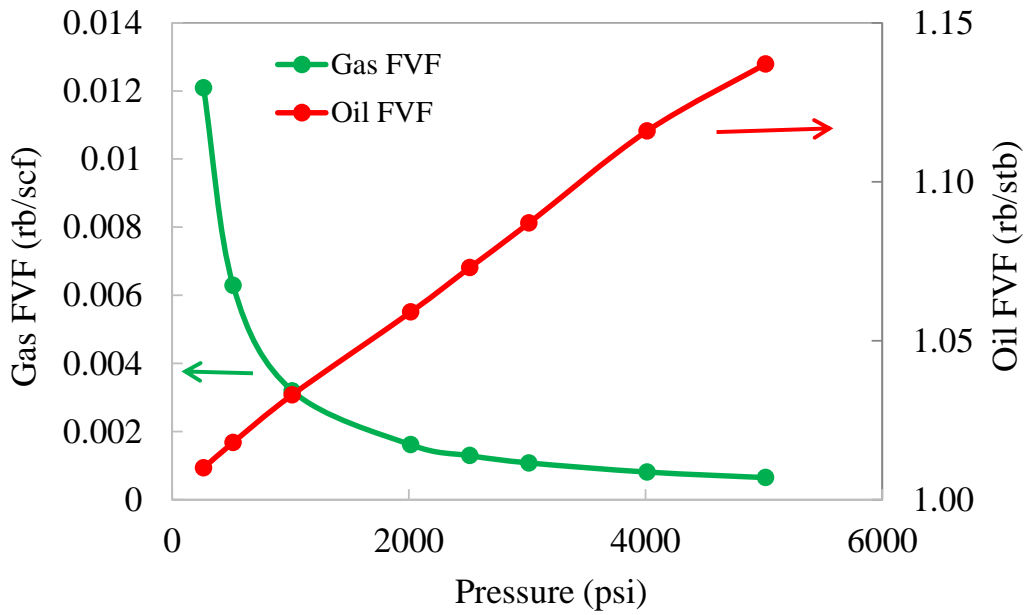


Figure 6.58: Oil and gas formation volume factor (Cases 10 to 13)

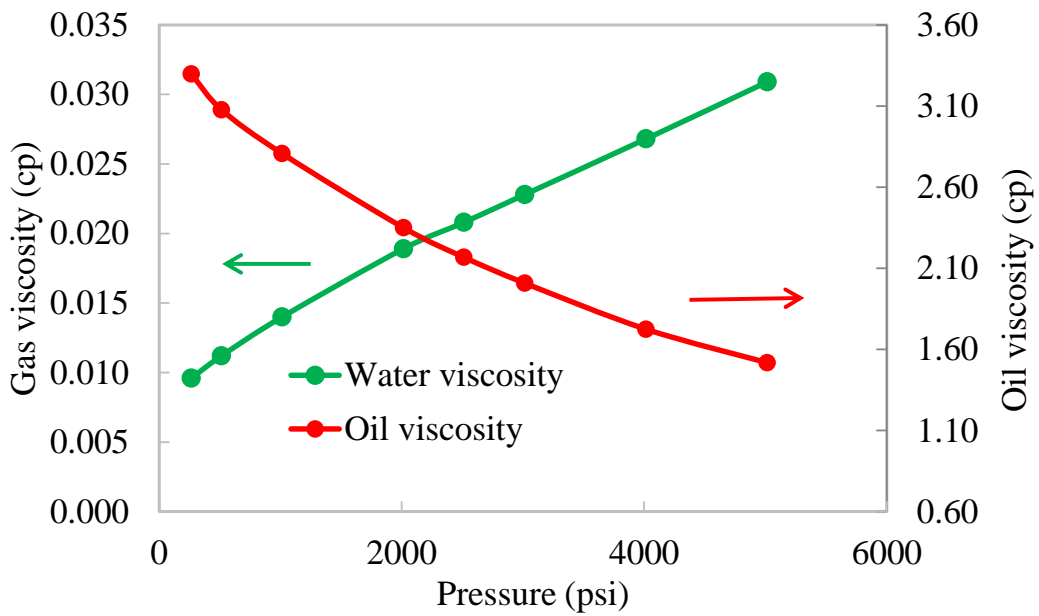


Figure 6.59: Oil and gas viscosity (Cases 10 to 13)

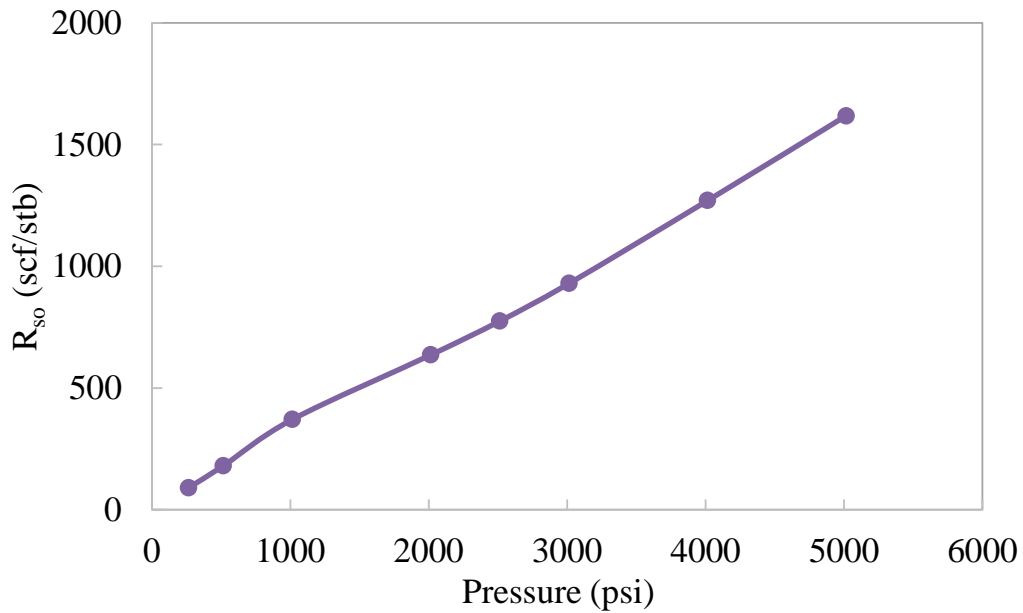


Figure 6.60: Solution gas/oil ratio (Cases 10 to 13)

Table 6.28: Oil-Gas PVT properties (Cases 10 to 13)

| P (psi) | R _{so} (scf/stb) | B _o (rb/stb) | E _g =1/B _g (scf/rb) | Oil viscosity (cp) | gas viscosity (cp) |
|---------|---------------------------|-------------------------|---|--------------------|--------------------|
| 264.7 | 90.5 | 1.01 | 82.7 | 3.2967626 | 0.0096 |
| 514.7 | 180 | 1.018 | 159 | 3.0769784 | 0.0112 |
| 1014.7 | 371 | 1.033 | 313 | 2.8064748 | 0.014 |
| 2014.7 | 636 | 1.059 | 620 | 2.35 | 0.0189 |
| 2514 | 775 | 1.073 | 773 | 2.1674101 | 0.0208 |
| 3014.7 | 930 | 1.087 | 926 | 2.0084892 | 0.0228 |
| 4014.7 | 1270 | 1.116 | 1233 | 1.7244604 | 0.0268 |
| 5014.7 | 1618 | 1.137 | 1541 | 1.5182014 | 0.0309 |

The relative permeability data was picked from the work by Lim (1993) and are listed in 6.28.

Table 6.29: Corey-relative permeability parameters (Lim 1993) (Cases 10 to 13)

| Parameter | Value | Parameters | Value |
|------------|-------|------------|-------|
| S_{rw} | 0.25 | k_{ro}^o | 0.71 |
| S_{row} | 0.27 | k_{rg}^o | 1.0 |
| S_{rog} | 0.18 | n_w | 1.5 |
| S_{rg} | 0.05 | n_o | 2.5 |
| k_{rw}^o | 0.21 | n_g | 2.5 |

6.5.1 Case 10 – Gas Injection

This case serves as a base case. Methane is injected to the reservoir for 700 days with the injection rate of 200 Mscf/day. Producer operates at constant bottomhole pressure 3100 psi. Injected gas tends to segregate to upper layers due to low gas density and override in thin stringers by viscous fingering of gas caused by high flow velocities and adverse mobility ratio. Therefore, a large portion of the reservoir is not swept by gas. Figure 6.61 shows daily oil production rate and cumulative oil recovery for case 11. In this case, 40.3% of original oil was produced with the remaining oil saturation of 0.44.

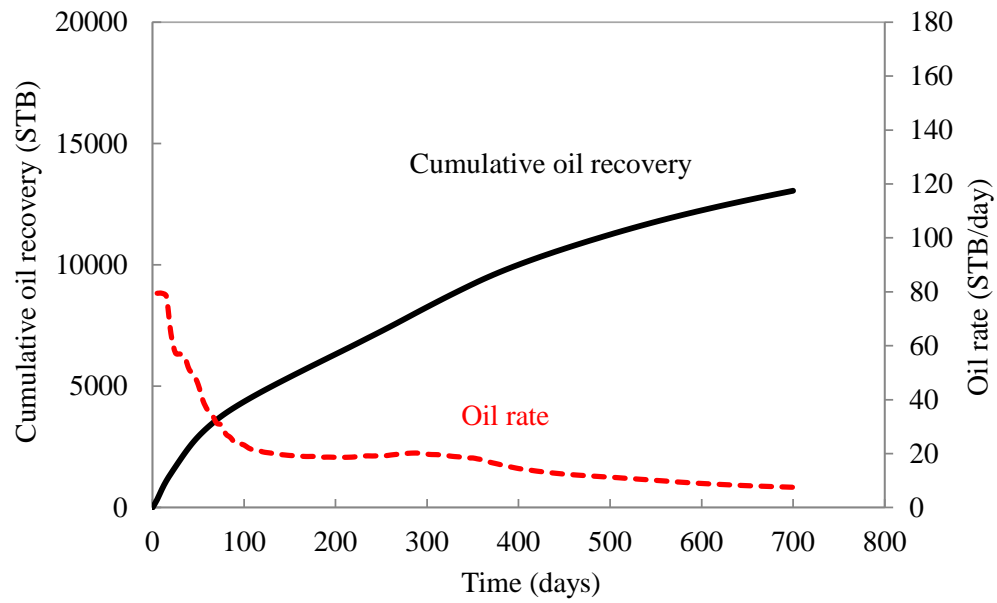


Figure 6.61: Case 10 - Cumulative oil recovery and oil rate

Figure 6.62 shows the oil saturation at the end of gas flooding (700 days). The saturation map shows most of the oil production is close to injector and top layers.

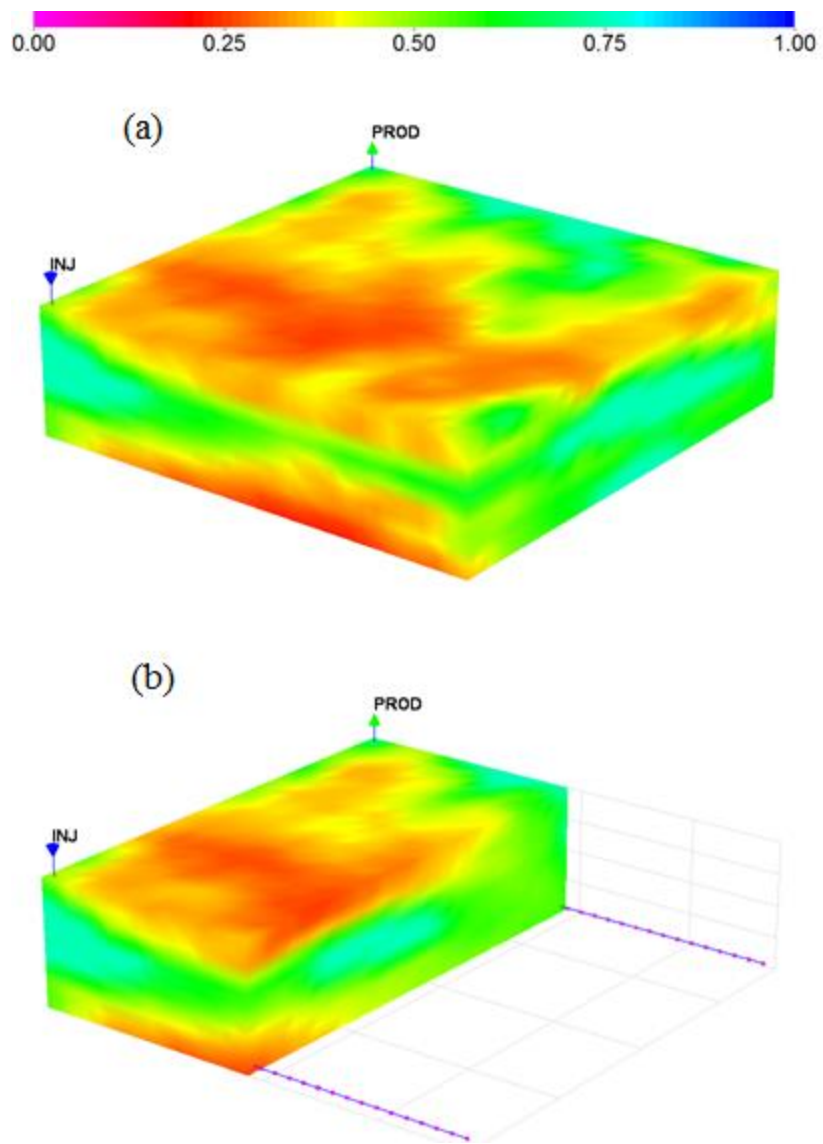


Figure 6.62: Case 10 - Remaining oil saturation at the end of the gas flood (700 days) a) full field and b) cross-section between injector and producer

6.5.2 Case 11 – Water Alternating Gas

The main design parameters for WAG injection techniques are fluid properties, rock-fluid interaction, availability and composition of injection gas, heterogeneous permeability, injection pattern, cycling time, WAG ratio, injection/production pressure and rate, three-phase relative permeability effects and flow dispersion and finally time to initiate the WAG (Christensen *et al.*, 2001; Heeremans *et al.*, 2006; Zahoor, 2011; Nangacovie, 2012; Pudugramam, 2014).

WAG ratio plays an important role to obtain the optimum value of the recovery factor. The optimal WAG ratio depends on permeability distribution, as well as other factors such as fluid densities, viscosities, and reservoir flow rates that determine the impact of gravity segregation. High WAG ratios may not provide sufficient gas-oil contact for oil production. Low WAG ratios may not be efficient to reduce gas mobility. Therefore, find the optimal WAG ratio is necessary to perform sensitivity analysis.

In terms of reservoir simulation, the rock fluid properties like adhesion, spreading and wettability are reflected as relative permeability. Thus relative permeability is very important when predictions are realized in reservoir simulation (Roger 2000).

Water Alternating Gas (WAG) was simulated with the 1:2 WAG ratio according to study by Ramachandran *et al.* (2010). A slug of gas is injected for 70 days and followed by a slug of water for 30 days (~0.1 PV). This cycle is repeated seven times for the total 700 days. The gas injection rate is 200 Mscf/day and water injection rate is 1500 ft³/day. The oil recovery by WAG was 48.4% of the initial oil with the remaining oil saturation of 0.39. Figure 6.63 shows daily oil production rate and cumulative oil recovery for Case 11.

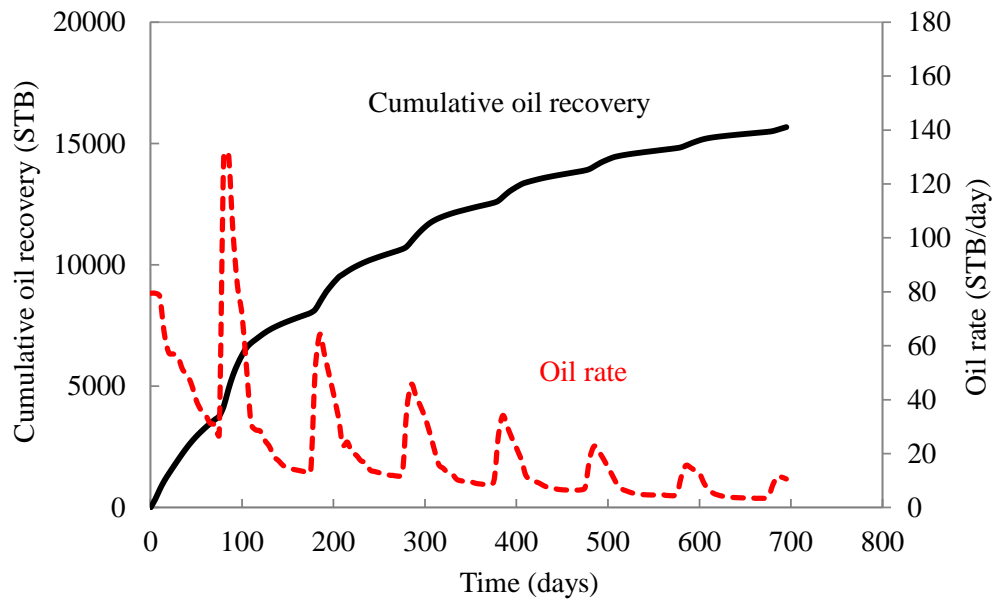


Figure 6.63: Case 11 - Cumulative oil recovery and oil rate

Figure 6.64 shows the oil saturation after seven cycles of WAG. Alternate injection of water and gas decreases the gas mobility and improves the vertical gas sweep efficiency. However, very low permeability layers are still unwept by gas.

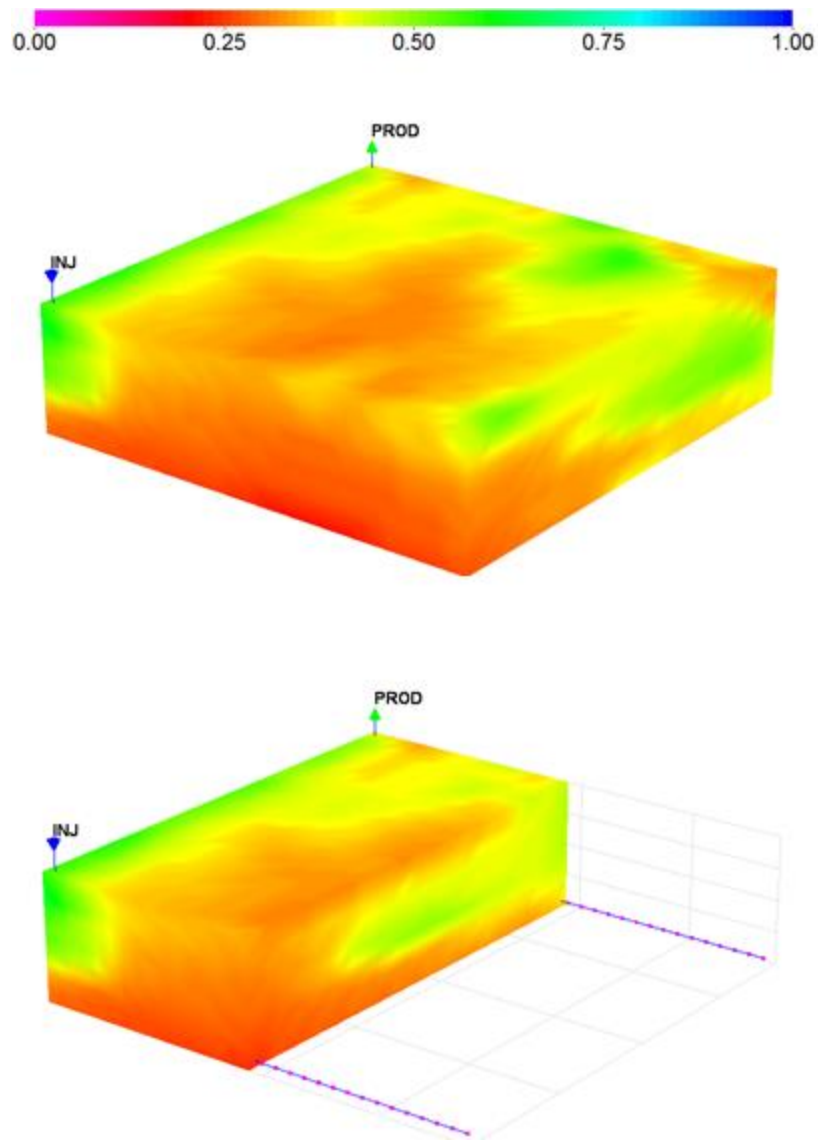


Figure 6.64: Case 11 - Remaining oil saturation after seven cycle of WAG a) full field and b) across-section between injector and producer

6.5.3 Case 12 – Polymer Alternating Gas (PAG)

If water-oil mobility ratio is large, the water slug may not be very efficient during WAG process due to adverse mobility ratio. Therefore, polymer needs to be added to water to decrease water mobility and subsequently improve the water sweep efficiency.

For the stable polymer flood, the total mobility of polymer solution needs to be less than the total mobility of oil bank.

$$\lambda_{i_{oil\ bank}} < \lambda_{i_{polymer\ slug}} \quad (6-1)$$

where total mobility is defined as

$$\lambda_t = \frac{k_{rw}(S_w)}{\mu_w} + \frac{k_{ro}(S_w)}{\mu_o} \quad (6-2)$$

The polymer solution viscosity needed for a stable displacement is 5.1 cp. This case is the same as Case 11 (WAG process), but 500 ppm of polymer is added to the water. The polymer properties are the same as data given in Figure 6.41. The oil recovery in this case increased to 56.4% of the initial oil with the remaining oil saturation of 0.33. Figure 6.65 shows daily oil production rate and cumulative oil recovery for Case 12.

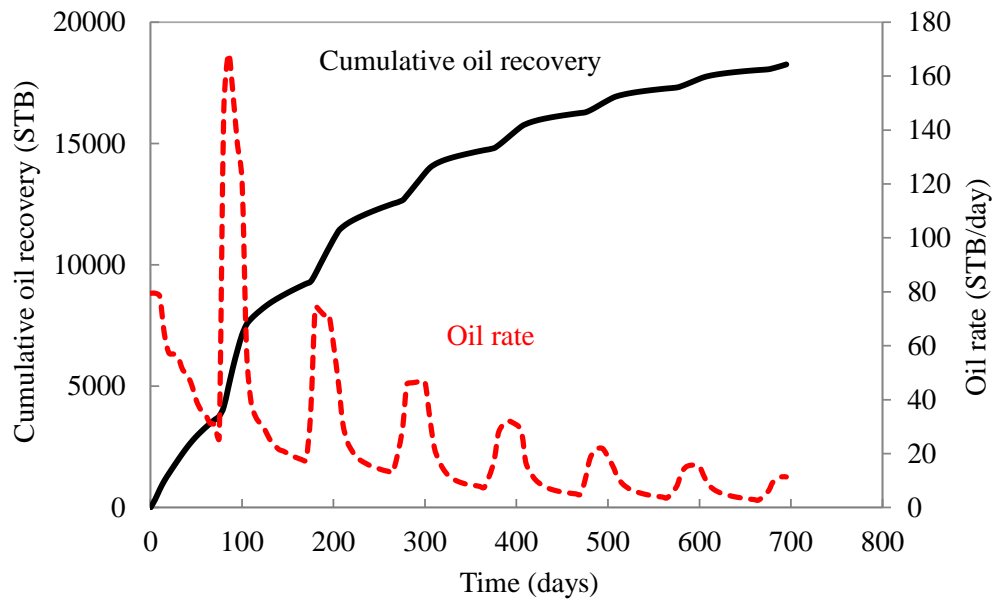


Figure 6.65: Case 12 - Cumulative oil recovery and oil rate

Figure 6.66 shows the oil saturation after seven cycles of PAG. Alternative injection of polymer with gas improves the gas sweep in low permeability zones. The high viscous polymer solution blocks high permeability layers and diverts the gas flow to lower permeability zones in the middle of the reservoir.

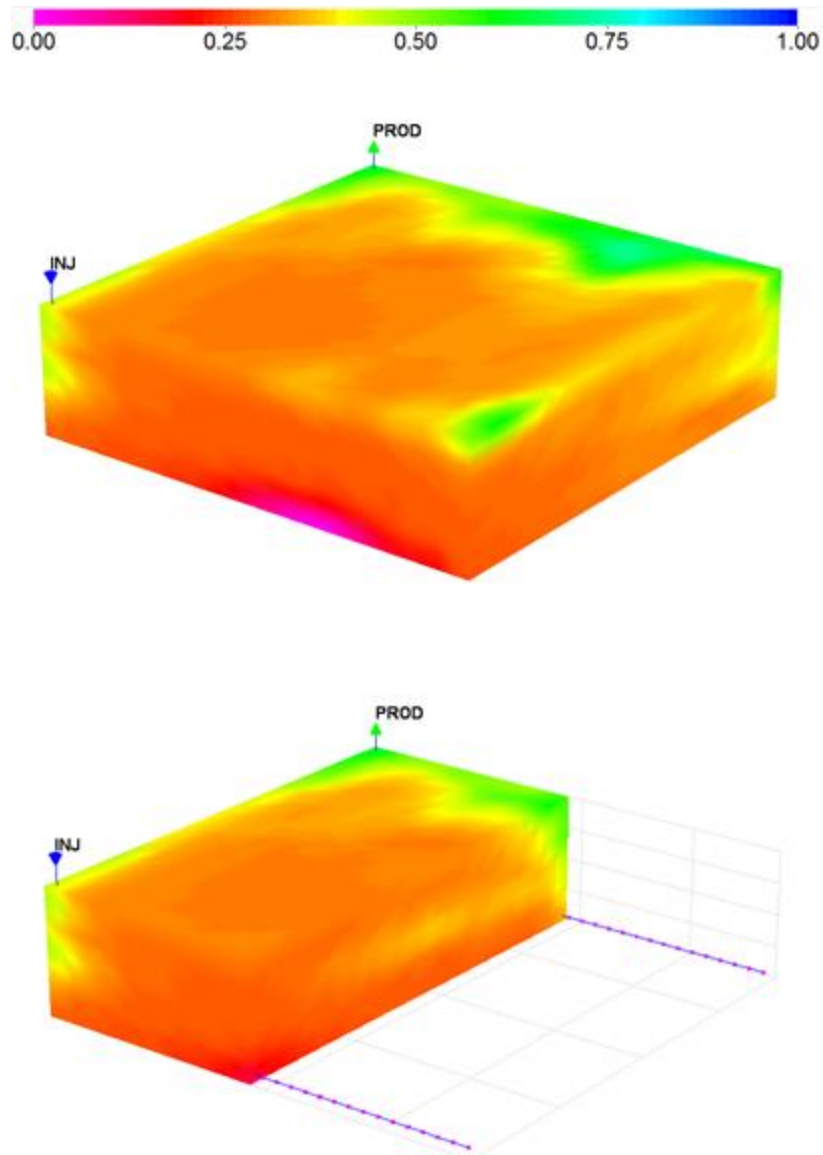


Figure 6.66: Case 12 - Remaining oil saturation after seven cycle of PAG a) full field and b) across-section between injector and producer

6.5.4 Case 13 – Surfactant Alternating GAS (SAG)

Foam directly addresses the problem of high gas mobility in porous media. Foam has the potential to improve gas volumetric sweep efficiency during gas injection processes. In this case, the gas is alternatively injected with surfactant solution to generate foam in-situ and reduce gas mobility. Injected surfactant is assumed to serve as a foaming agent in these simulations without a noticeable interfacial tension reduction between water and oil. The injection cycles and rates are the same as Case 11, but water slugs are replaced with 0.2% of surfactant solution. The foam properties are given in Table 6.30. In this case, 58% of the initial oil is recovered with the remaining oil saturation of 0.315. Figure 6.67 shows daily oil production rate and cumulative oil recovery for Case 13.

Table 6.30: UT Foam model parameters (Case 13)

| Parameter | Value |
|---------------------------|--------|
| R_{ref} | 300 |
| S_w^* | 0.29 |
| S_o^* | 0.40 |
| C_s^* (volume fraction) | 0.0001 |
| ϵ | 0.01 |
| σ | 1.0 |
| $u_{g,ref}$ (ft / day) | 1.0 |

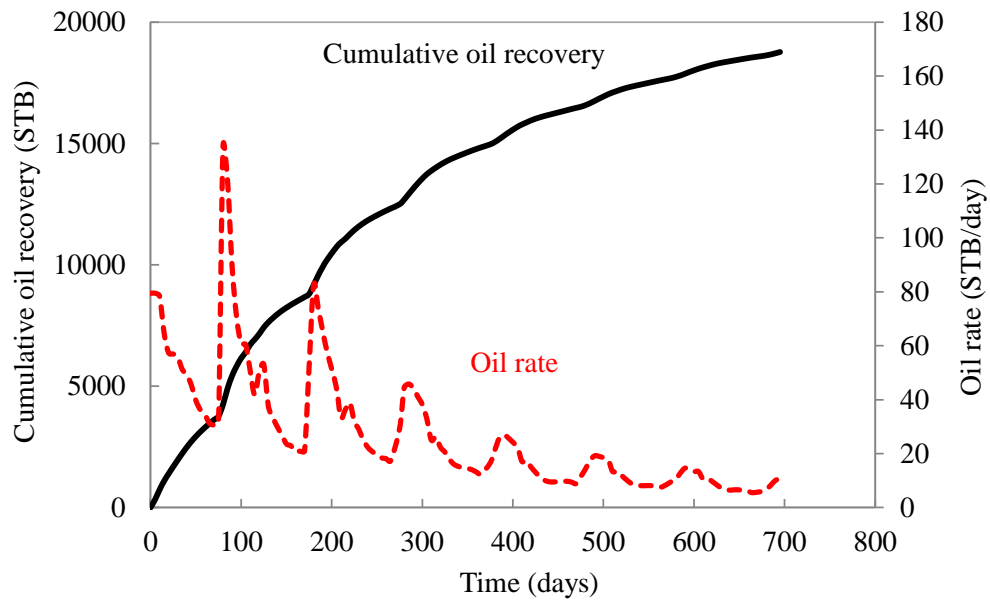


Figure 6.67: Case 13 - Cumulative oil recovery and oil rate

Figure 6.68 shows the remaining oil saturation after seven cycles of surfactant solution and gas. The gas initially displaces the oil in high permeable regions and upper layers. With less oil, foam forms and remains more stable in regions which have been already swept by gas. Foam partially plugs the high permeability regions and diverts the flow into the low permeability layers. Therefore, foam front moves through the low permeability regions faster than in the high permeability regions.

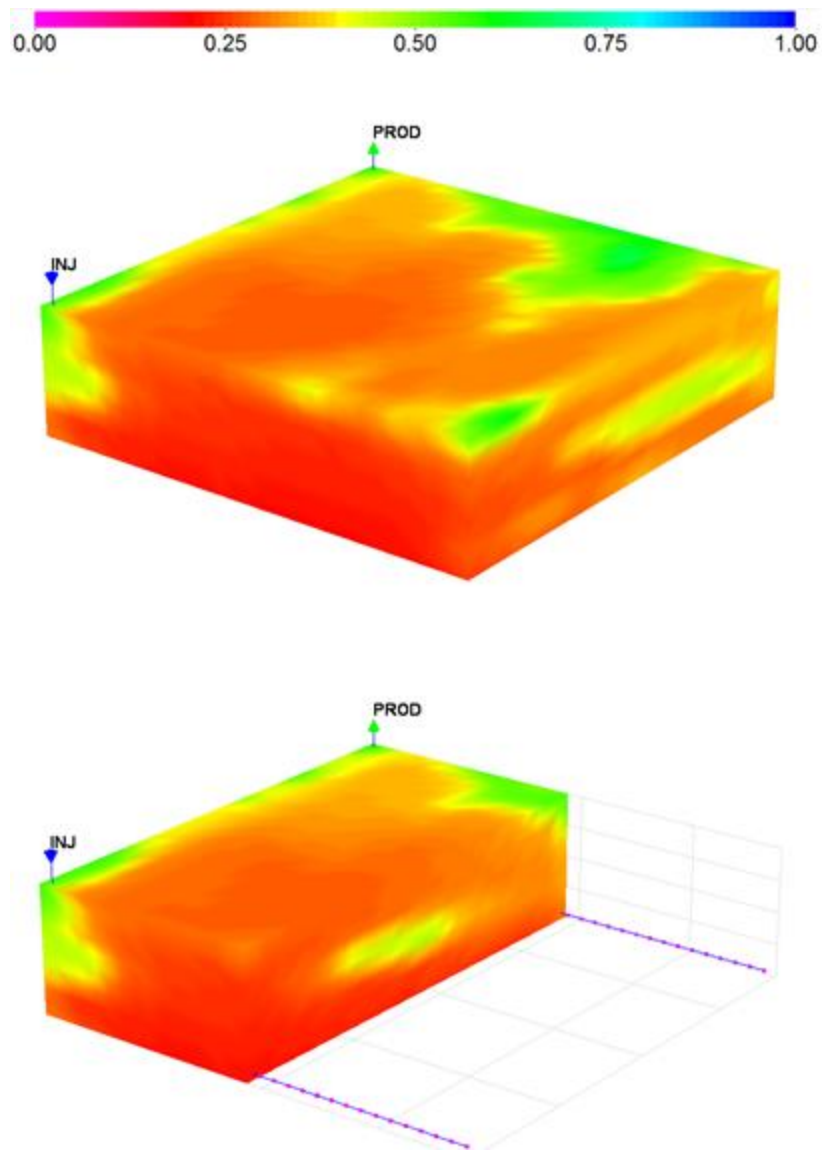


Figure 6.68: Case 13 - Remaining oil saturation after gas injection with foam a) full field and b) across-section between injector and producer

6.5.5 Results and Discussions

Figure 6.69 and Figure 6.70 compare the oil recovery factor and oil rates for Cases 10 through 13. Continuous gas injection (Case 10) is an unstable displacement since low density and viscosity of gas causes poor vertical sweep efficiency due to gravity override and poor areal sweep efficiency in high permeability channels with high conductivity. Therefore, a large amount of oil is bypassed and is not produced. Using WAG (Case 11) instead of continuous gas injection improves the gas sweep efficiency and increases the oil recovery by a factor of 8% compared to continuous gas injection. Adding polymer to injection water (Case 12) decreases the water mobility and makes a stable front behind the oil bank. In this case, oil recovery increases by 16% compared to continuous gas injection. Using foam in Case 13 reduces the gas mobility and the oil recovery increases by 17.7% compared to continuous gas injection. Figure 6.71 plots the average oil concentration during each process.

Figure 6.72 and Figure 6.73 compares bottomhole injection pressure and average reservoir pressure for simulation Cases 10 to 13. Polymer alternating gas has a higher bottomhole pressure compared to other cases due to high polymer solution viscosity. However, as far as the injection pressure is below the parting pressure, polymer has a good potential to increase the oil recovery. In Case 13, by reducing the oil saturation, foam becomes stronger gradually and injection pressure increases with time. Figure 6.74 shows the gas saturation maps after 370 days (after gas slug in 4th cycle in Cases 11 to 13). In Case 12 (PAG), most of the injected gas is dissolved in the oil at high reservoir pressure.

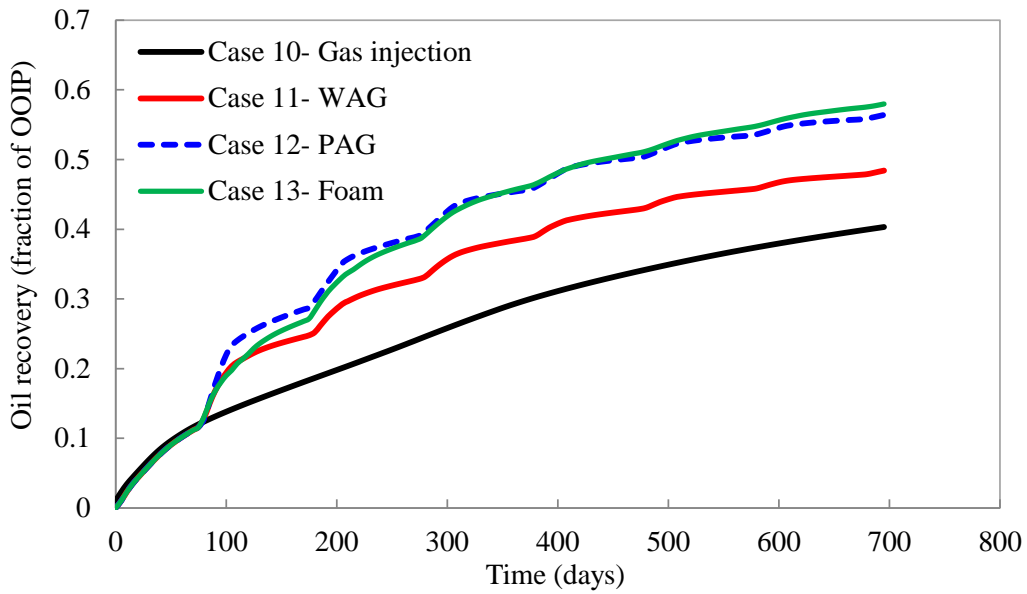


Figure 6.69: Oil recovery factor for Cases 10 through 13

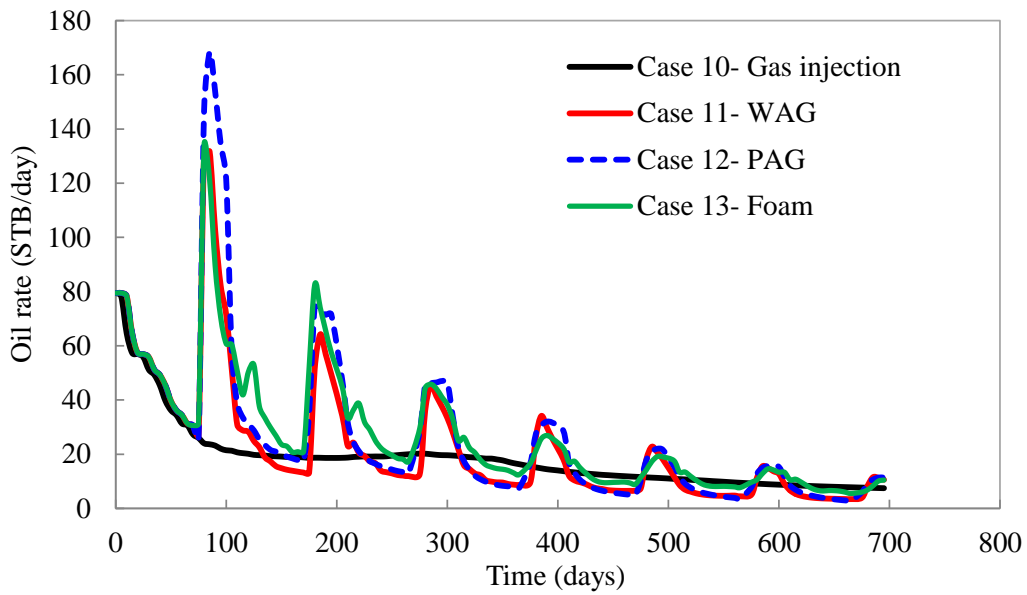


Figure 6.70: Oil rate for Cases 10 through 13

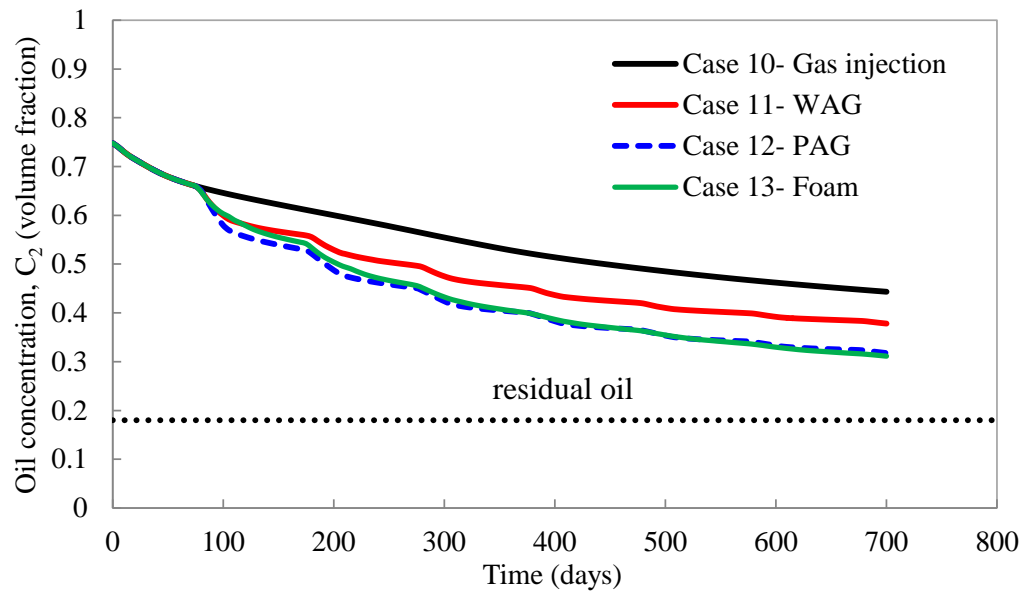


Figure 6.71: Oil concentration for Cases 10 through 13

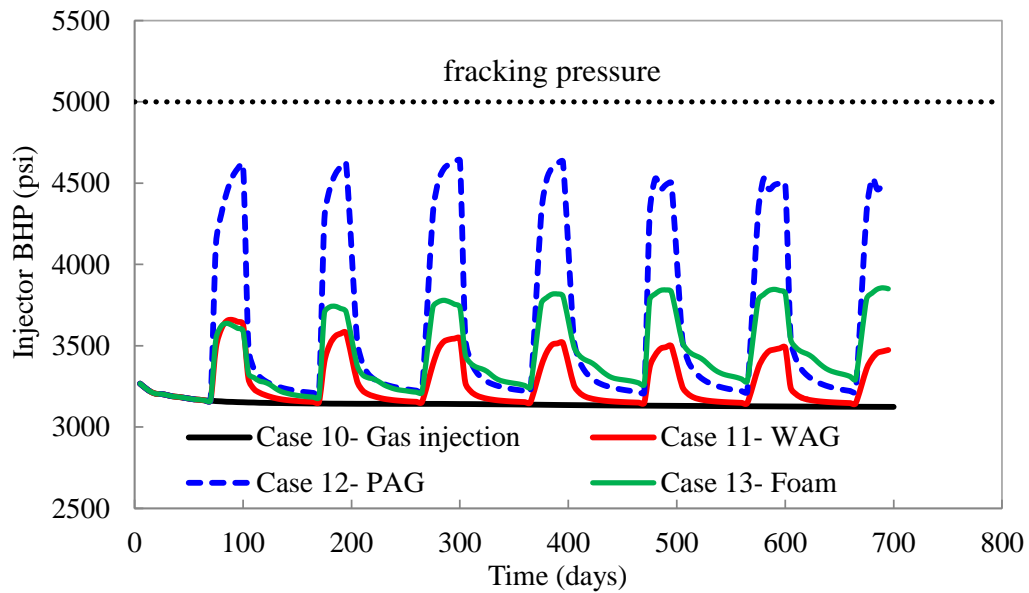


Figure 6.72: Injector bottomhole-pressure for Cases 10 through 13

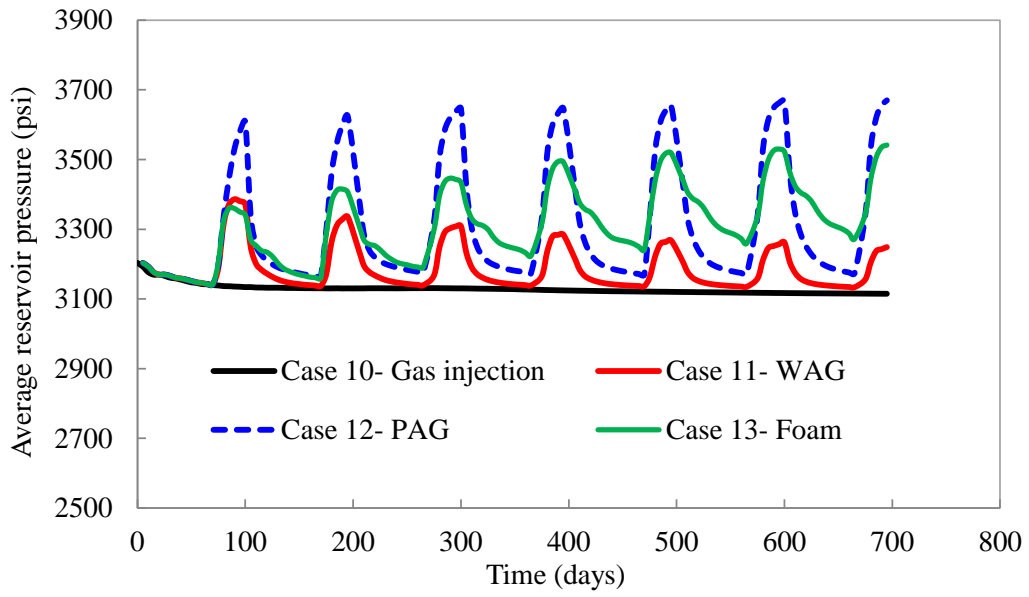


Figure 6.73: Average reservoir pressure for Cases 10 through 13

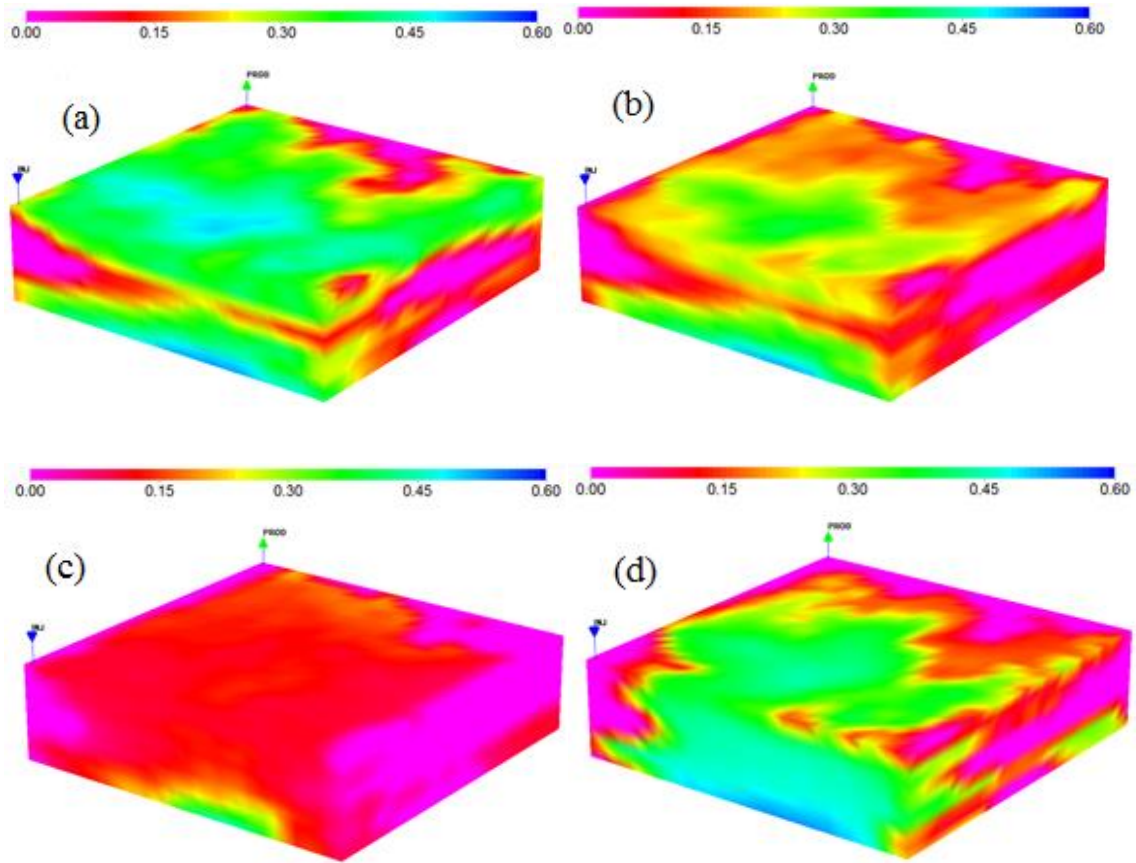


Figure 6.74: Gas saturation (after 370 days) a) Case 10- Gas injection b) Case 11- WAG
 c) Case 12- PAG d) Case 13- Foam

6.6 COREFLOOD SIMULATION OF LOW-TENSION-GAS FLOODING IN TIGHT FORMATIONS (CASE 14)

Szlendak *et al.* (2013) studied the low-tension-gas (LTG) as a method for sub-miscible tertiary recovery in tight rocks. They used surfactant and gas to mobilize and then displace residual crude after waterflood at ultra-low oil/water interfacial tension. In this section, we model LTG coreflood experiment, labelled LTG_Tert_#1, from the work by Szlendak *et al.* (2013).

In this experiment, the core was Texas Cream limestone with 10.8 md permeability to brine and average porosity of 21.2%. Core dimensions were 1.5×12 in. The crude oil had a viscosity of 1.9 cp and a gravity of 45 °API. Crude oil was not reactive. Phase-behavior tests indicated that mixing of the crude with Na₂CO₃ did not result in production of microemulsion and soap.

Two surfactants were used in this experiment. An alcohol propoxy sulfate (with C₁₆₋₁₇ branched alcohol hydrophobe and seven propylene oxide groups) and an internal olefin sulfonate (IOS) (with C₁₅₋₁₈ twin-tailed hydrophobe). IOS showed good foaming behavior at low concentration. The co-solvent triethylene glycol monobutyl ether (TEGBE) was added to improve equilibrium time. Figure 6.75 depicts the oil/water solubilization ratio for selected surfactant formulation (1.25% surfactant at 1:3 alcohol propoxy sulfate (APS) to internal olefin sulfonate (IOS) with 1.0% TEGBE) as a function of total dissolved solids (TDS). TDS was the sum of consistence 1.0% Na₂CO₃ and a variable NaCl concentration. Optimum salinity was observed at approximately 35000 ppm TDS. The symbols are experimental measurements and lines are model fit in Figure 6.75. The model fit parameters for the oil/water solubilization ratio are given in Table 6.31.

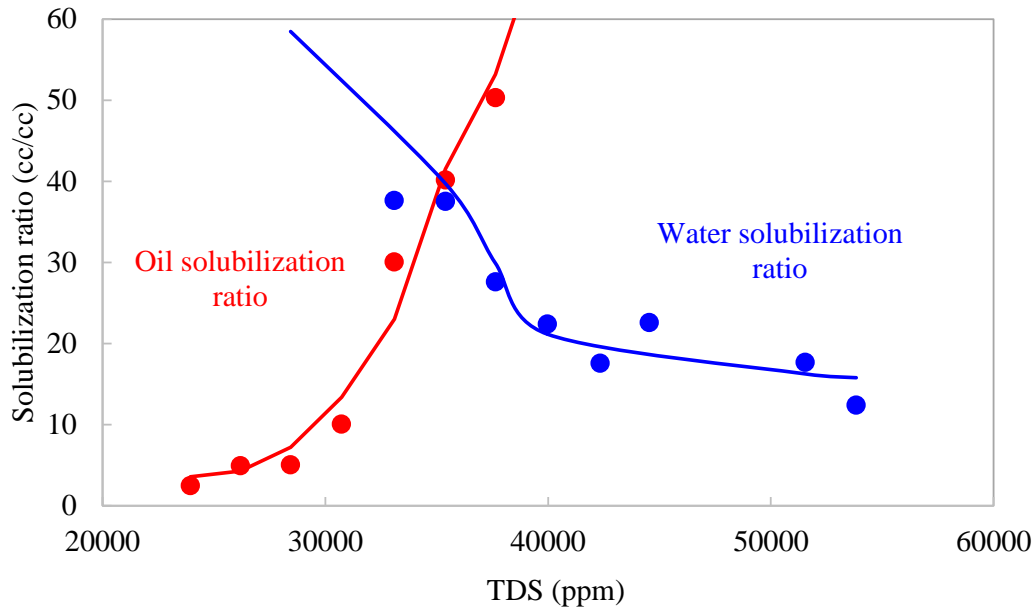


Figure 6.75: Case 14- Oil and water solubilization ratio for selected surfactant formulation (symbols are experimental data and lines are model fit)

Table 6.31: Model fit parameters for microemulsion phase behavior in Figure 6.75 (Case 14)

| Parameters | Value |
|------------|-------|
| HBNC70 | 0.045 |
| HBNC71 | 0.012 |
| HBNC72 | 0.015 |
| CSEL (ppm) | 26400 |
| CSEU (ppm) | 44000 |

The following procedure describes the LTG experiment. The core initially vacuumed and then saturated at low rate to 100% brine. 10 PV brine with high concentration of Na_2CO_3 (1.0%) was displaced through the core to establish a low-adsorption environment for later chemical flood. Next, oil injection was performed at 10

cm³/hr (~ 6 ft/day) for 2 PV, at which point $f_w \sim 0$. Oil was then displaced by injecting brine at 2 ft/day. The remaining oil saturation at the end of brine injection was 29%. After waterflood, 0.3 PV of chemical slug (1.25% APS:IOS=3:1, 1% TEGBE) was co-injected with nitrogen at 50% gas fraction (total PV = 0.6) at liquid rate of 1 ft/day (total rate = 2 ft/day). The back-up pressure was set to 580 psi as a compromise to minimize gas expansion and the desire to minimize nitrogen miscibility ($R_{so} \approx 0$). Chemical slug was then followed with drive injection at identical rate and gas quality. Table 6.32 lists the injection strategy and species concentration in this flood.

Table 6.32: Case 14 – Injection strategy and species concentration (LTG_Tert_#1)

| | |
|-----------------|--|
| Brine injection | Injected volume: 2 PV Injection rate : 2 ft/day Injection salinity: 1.00 wt% Na ₂ CO ₃ and 3.46 wt% NaCl |
| LTG slug | Injected volume: 0.6 total PV Surfactant injection rate : 1 ft/day Gas injection rate: 1 ft/day Injection salinity: 1.00% Na ₂ CO ₃ and 1.73% NaCl Surfactant concentration: 1.25% APS:IOS=3:1, 1% TEGBE |
| Foam drive | Injected volume: 3.4 total PV Surfactant injection rate : 1 ft/day Gas injection rate: 1 ft/day Injection salinity: 1.00% Na ₂ CO ₃ and 0.0% NaCl Surfactant concentration: 0.1% IOS |

The four-phase flow simulator was used to history match LTG_Tert_#1 coreflood experiment (after brine injection). Corey-type relative permeability parameters to history match this experiment are given in Table 6.33. UT foam model represents the foam behavior in this experiment. The foam model parameters are listed in Table 6.34. The

maximum value of gas reduction factor by foam (R_{ref}) was determined to be 150 from the pressure drop data at steady state.

Table 6.33: Corey relative permeability parameters (Cases 14)

| Parameter | Value | Parameter | Value |
|---------------------------------------|------------|-------------------------------|----------|
| $S_{rw}^{low}, S_{rw}^{high}$ | 0.44, 0.0 | n_w^{low}, n_w^{high} | 3.4, 1.0 |
| $S_{row}^{low}, S_{row}^{high}$ | 0.25, 0.0 | n_o^{low}, n_o^{high} | 2.7, 1.0 |
| $S_{rog}^{low}, S_{rog}^{high}$ | 0.18, 0.0 | $n_{me}^{low}, n_{me}^{high}$ | 3.4, 1.0 |
| $S_{rme}^{low}, S_{rme}^{high}$ | 0.44, 0.0 | n_g^{low}, n_g^{high} | 2.4, 2.4 |
| $S_{rg}^{low}, S_{rg}^{high}$ | 0.05, 0.05 | T_{11} | 1865 |
| $k_{rw}^{o\ low}, k_{rw}^{o\ high}$ | 0.12, 1.0 | T_{22} | 59074 |
| $k_{ro}^{o\ low}, k_{ro}^{o\ high}$ | 0.35, 1.0 | T_{33} | 364.2 |
| $k_{rme}^{o\ low}, k_{rme}^{o\ high}$ | 0.12, 1.0 | T_{44} | 0 |
| $k_{rg}^{o\ low}, k_{rg}^{o\ high}$ | 0.80, 0.80 | | |

Table 6.34: UT foam model parameters (Case 14)

| Parameter | Value |
|---------------------------|-------|
| R_{ref} | 150 |
| S_w^* | 0.46 |
| S_o^* | 0.30 |
| C_s^* (volume fraction) | 0.001 |
| ε | 0.01 |
| σ | 1.0 |
| $u_{g,ref}$ (ft / day) | 1.0 |

Figure 6.76 and Figure 6.77 compare the experimental data of oil recovery and pressure drop with simulation results. The oil cut in this experiment is summation of pure oil cut and dissolved oil in microemulsion phase. Simulation results predict faster oil recovery compared to experimental data. Simulator was not able to capture the gradual oil production behind the oil bank.

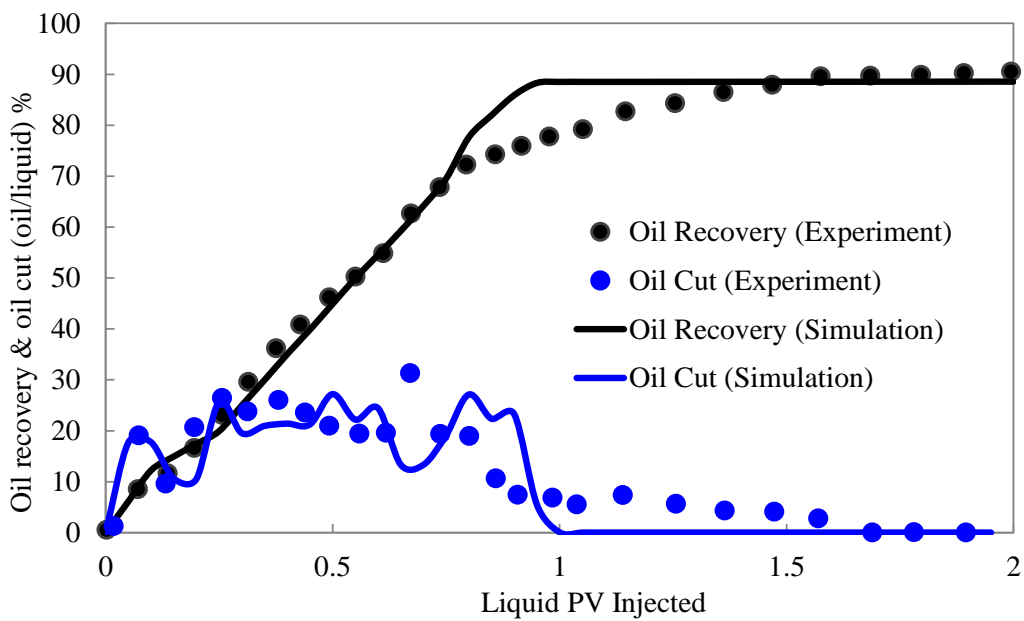


Figure 6.76: Case 14 - Oil cut and cumulative oil recovery (experimental data from the work by Szlendak *et al.* 2013 vs. simulation results in this work)

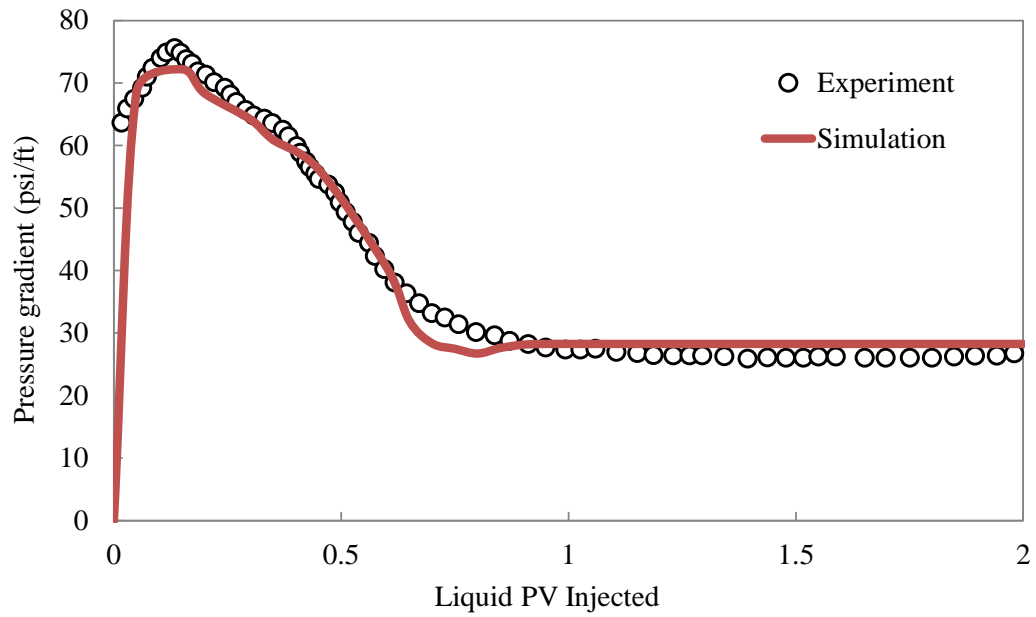


Figure 6.77: Case 14 - Pressure drop over the entire core (experimental data from the work by Szlendak *et al.* 2013 vs. simulation results in this work)

Chapter 7: Summary, Conclusions, and Recommendations

This chapter provides the key findings and recommendations of this dissertation research.

7.1 SUMMARY AND CONCLUSIONS

In this research, a four-phase reservoir simulator for water, oil, microemulsion, and gas phases was developed to simulate and interpret chemical EOR processes including free and/or solution gas. These EOR processes are either hybrid gas/chemical injection such as foam, low-tension-gas, and polymer alternating gas or surfactant (alkali/surfactant) flooding in reservoirs with live crude oils.

For this purpose, the black-oil PVT model consistent with original UTCHEM framework was implemented to model water/oil/gas phase behavior. In this model, water and oil phases were assumed to be immiscible with no mass transfer between them, However gas could dissolve in both water and oil phases. The water/oil/gas PVT properties including formation volume factor, solution gas ratio, and viscosity were read from the input PVT tables consistent with the format in commercial reservoir simulators. The black oil formulation was verified against the commercial black-oil simulator IMEX-CMG.

Next, the implemented black-oil model was coupled with the microemulsion/oil/water phase behavior to simulate four-phase flow of water, oil, microemulsion, and gas in porous media. The mass equation was solved for the total volumetric concentration of each species at standard conditions (in original UTCHEM equations are solved at reservoir conditions). New pressure equation was obtained by summing the mass balance equations over volume occupying components (water, oil, surfactant, and gas). The pressure equation was solved separately for saturated ($P < P_b$) and

undersaturated ($P > P_b$) PVT conditions. The bubble-point was tracked to determine gridblock PVT conditions at each time.

The microemulsion phase properties such as viscosity, formation volume factor, solution gas ratio, density, and compressibility were defined based on pure component properties and its constituent composition. An important and valid assumption was that the solubilized oil and water components in the microemulsion phase had the same properties as the excess oil and water phases.

The Corey-type relative permeability model was extended for the four-phase flow. In this case, the relative permeability for each phase was assumed to be only function of its respective saturation. The residual saturations, endpoints, and exponents were functions of trapping number. The Brooks-Corey model was also extended to calculate the capillary pressure. The capillary pressure was scaled for interfacial tension, permeability, and porosity according to J-Leverett function. The direction of descending wettability was assumed to be water, microemulsion, oil, and gas in this model.

The microemulsion phase behavior (Hand's rule) was modified in the presence of gas. The original Hand's rule is based on the three main components of water, oil, and surfactant. Therefore, the free gas volume was excluded from the phase behavior calculations and the overall volume concentrations of water, oil, and surfactant were normalized for the volume of free gas. Effect of solution gas on microemulsion phase behavior was discussed. Then, the phase saturations were computed from the phase overall composition, and saturation constraints. At the end, saturations were re-normalized for the volume of the free gas.

Transport equations were discretized and solved in an IMPEC scheme, which is implicit in pressure and explicit in concentration.

To model the foam behavior in porous media, a comprehensive research was performed on existing foam models to evaluate the capabilities and limitations of each model. Foam models for enhanced oil recovery are mainly divided to two groups. The first group is population-balance (PB) models which attempt to represent all the dynamic processes of lamella creation and destruction as well as the effect of bubble size on gas mobility. These models can be set to assume local equilibrium (LE) between the processes of lamella creation and destruction. The second group treats the effect of foam texture implicitly through a gas mobility reduction factor that depends on saturations, superficial velocities and other factors. The latter group of models implicitly assumes local equilibrium (LE) between the processes of foam creation and destruction. In this research, they are referred to implicit-texture (IT) models. In this research, we studied models of Kovscek *et al.* (1994) (modified later by Chen *et al.* 2010), Kam *et al.* (2007), and Kam (2008) from the population-balance group, and UT, STARS, and Vassenden-Holt (1998) models from IT models.

Dimensionless foam bubble density was defined in IT models to derive explicitly the foam-coalescence-rate function implicit in these models. Results showed that each of the IT models examined was equivalent to the LE formulation of a population-balance model with a lamella-destruction function that increased abruptly in the vicinity of the limiting capillary pressure, as in current population-balance models. In other words, the physics of foam collapse near P_c^* was essentially the same in the IT models as in the PB models.

Since the ultimate test of a model was its ability to represent and explain a variety of data, foam models were compared based on their ability to represent a set of N₂ and CO₂ steady-state foam experiments. Among all the models, Vassenden-Holt model was not able to history match the experimental data in low-quality regime until we introduced

an exponent a for the velocity term. More importantly, while in UT, STARS, Kam *et al.* (2007), and Kam (2008) models the value of S_w^* was close to the water saturation in the high-quality regime, Chen *et al.* (2010) and Vassenden-Holt (1998) models did not essentially predict a S_w^* (or P_c^*) close to the water saturation (or capillary pressure) in high quality regime. It was also found that in Chen *et al.* model, pressure gradient was independent of gas superficial velocity in the high-quality regime because of the particular forms assumed for gas apparent viscosity and the lamella-generation and -coalescence rates, not the divergence of coalescence rate at the limiting capillary pressure.

UT foam model and Chen *et al.* foam model at LE were implemented in UTCHEM to history match the transient foam experiments. UT foam model was also modified in presence of microemulsion phase. Foam does not form or collapses in Winsor Type II with high oil concentration in microemulsion phase.

Typically, a mixture of surfactants is used during the low-tension-gas experiments. A low interfacial tension surfactant to increase the capillary number by reducing the IFT to ultra-low values and thereby reducing residual oil saturation, and a good foaming surfactant to provide the essential mobility control during the flood. Therefore, a secondary surfactant was implemented in UTCHEM to model EOR processes with using the mixture of surfactants.

The developed simulator was used to history match published low-tension-gas flooding and foam experiments. The simulation was also extended to field scale with different injection scenarios (surfactant alternating gas (SAG), co-injection of gas and surfactant). Simulation results indicated a well-designed low-tension-gas flooding has the potential to recover the trapped oil. Foam can serve for mobility control during surfactant and surfactant-alkaline flooding in the reservoirs with very low permeability.

The impact of water alternating gas (WAG), polymer alternating gas (PAG), and foam on gas mobility were studied during the gas injection in a heterogeneous reservoir. Simulation results showed both foam and alternate injection of polymer with gas reduced the gas mobility and consequently increased the oil recovery significantly. However, foam had a better injectivity compared to PAG process.

7.2 RECOMMENDATIONS FOR FUTURE WORK

The following recommendations are suggested for future study:

- Low-tension-gas flooding often uses a mixture of low tension and foaming surfactants. In this work, due to the lack of experimental data, two surfactants are assumed to be independent. The primary surfactant was only responsible for low IFT displacement (does not generate foam), and secondary surfactant only generated foam (does not reduce the water/oil IFT to ultralow values). In reality, all the surfactants have both IFT and foaming to different degrees and are rarely independent. We need more experiments to fully understand the synergy between the two surfactants and the impact on foaming behavior.
- The effect of pressure and solution gas on microemulsion phase behavior can be modeled once a trend in optimum salinity and solubilization ratio is understood and correlations are developed.
- Corey relative permeability model assumes the same input endpoint and exponent for the microemulsion phase for different phase environments. Of course, the microemulsion relative permeability is calculated as a function of trapping number in each gridblock. Microemulsion relative permeability depends on its composition where microemulsion behaves similar to the water phase in Winsor Type I and

similar to oil properties in Winsor Type II. The effect of microemulsion composition on relative permeability is recommended for future studies.

- The effect of hysteresis on gas relative permeability, including the effects of cycle dependency during alternative injection of gas and chemical (i.e. SAG, PAG, and etc.) needs to be considered to make more accurate predictions of these methods.
- Currently, there is no verified correlation to model the effect of crude oil and its composition on foam coalescence. A further research is recommended to investigate the effect of oil on foam coalescence in porous media.

Appendix A: Gas/surfactant simulation in UTCHEM-2011-9

A synthetic one-dimensional case was set up to show the limitations of modeling surfactant and gas in UTCHEM-2011-9. In this case, the oil saturation was initially 45% and the initial salinity was 0.4 meq/ml (Type II). Then, surfactant solution was co-injected with gas at total Darcy velocity of 2.8 ft/day and gas volume fraction of 90%. The injection salinity was 0.27 meq/ml (Type I). The relative permeability and surfactant properties are the same as data in Table 6.6 and Table 6.7, respectively. The model parameters are listed in Table A.1.

Table A.1: Model parameters for synthetic one-dimensional case

| Parameters | Values |
|----------------------------------|--------------|
| Number of gridblocks | 100×1×1 |
| Gridblock size (ft×ft×ft) | 0.01×0.1×0.1 |
| Initial oil saturation | 0.45 |
| Initial gas saturation | 0.0 |
| Initial salinity (meq/lit NaCl) | 0.4 |
| Permeability (md) | 200 |
| Porosity | 0.22 |
| Water viscosity (cp) | 0.43 |
| Oil viscosity (cp) | 1.35 |
| Total Injection rate (ft/day) | 3.0 |
| Injection salinity (meq/ml NaCl) | 0.27 |
| Gas volume fraction (%) | 80 |

UTCHEM-2011-9 failed after 0.751 PV of total injection of surfactant and gas with negative values for the gas saturation in some gridblocks. The oil recovery and oil cut are plotted in Figure A.1 until it fails at 0.751 PV. Figure A.2 shows the gas saturation at 0.751 PV with negative value for gas saturation in second gridblock close to the injector.

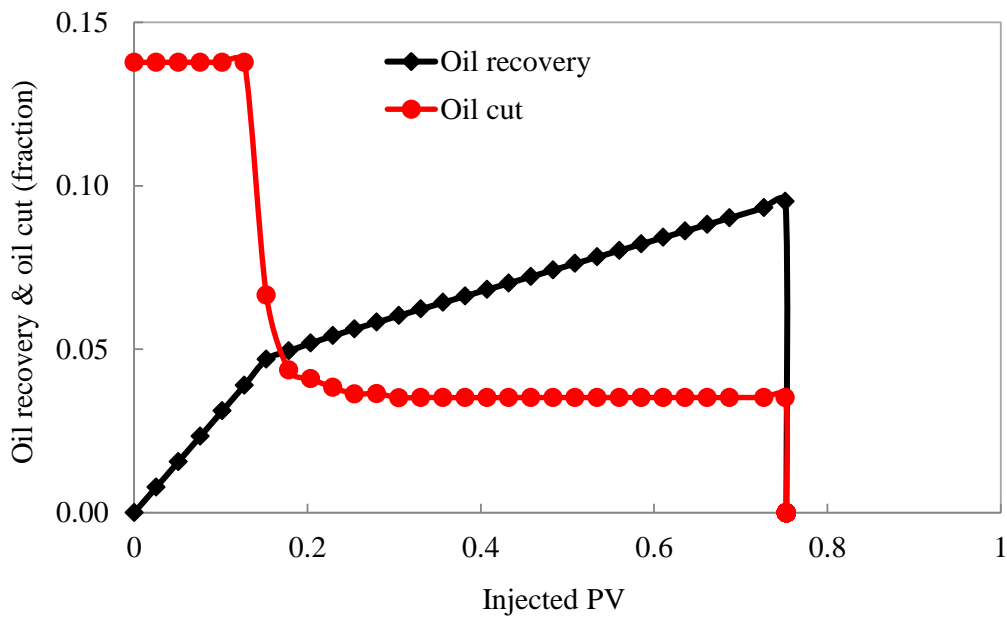


Figure A.1: Oil recovery and oil cut for the co-injection of surfactant and gas using UTCHEM-2011-9. Simulation failed after 0.751 PV.

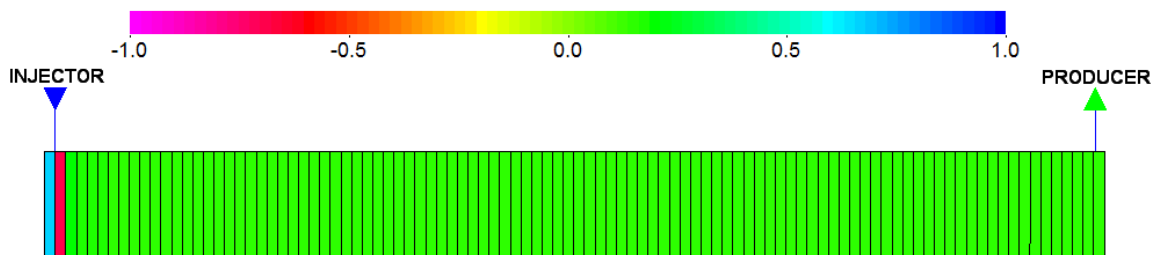


Figure A.2: Gas saturation at 0.751 PV. Gas saturation in second gridblock close to the injector is -0.681 (UTCHEM-2011-9)

Next, the same case was run using improved UTCHEM in this research. No numerical problem or convergence issue was observed during the simulation. The oil recovery and oil cut for up to 3 PV are plotted in Figure A.3. Figure A.4 shows the gas saturation at 0.751 PV with no negative values.

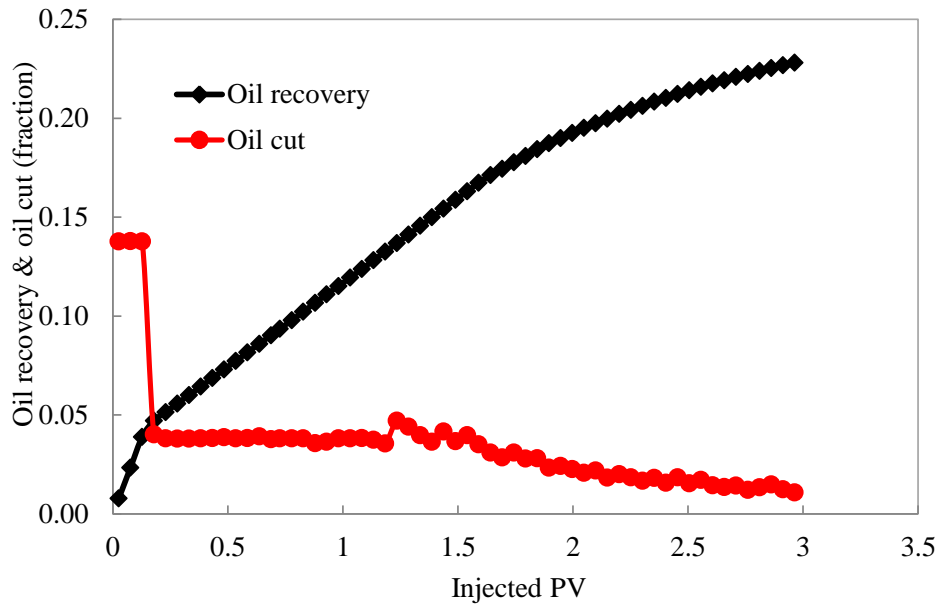


Figure A.3: Oil recovery and oil cut for the co-injection of surfactant and gas using new improved UTCHEM code.

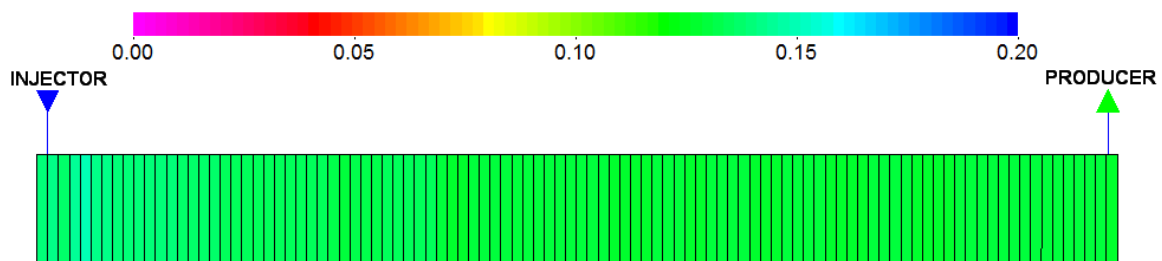


Figure A.4: Gas saturation at 0.751 PV using new improved UTCHEM code.

The simulation results of oil recovery and oil cut using UTCHEM-2011-9 and new improved UTCHEM code are compared in Figure A.5 and Figure A.6.

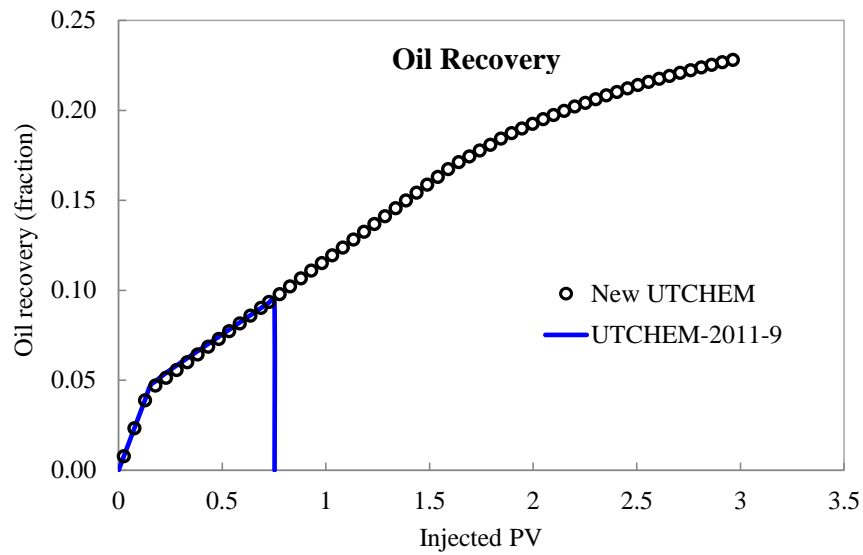


Figure A.5: Comparison of oil recovery between UTCHEM-2011-9 and new improved UTCHEM code.

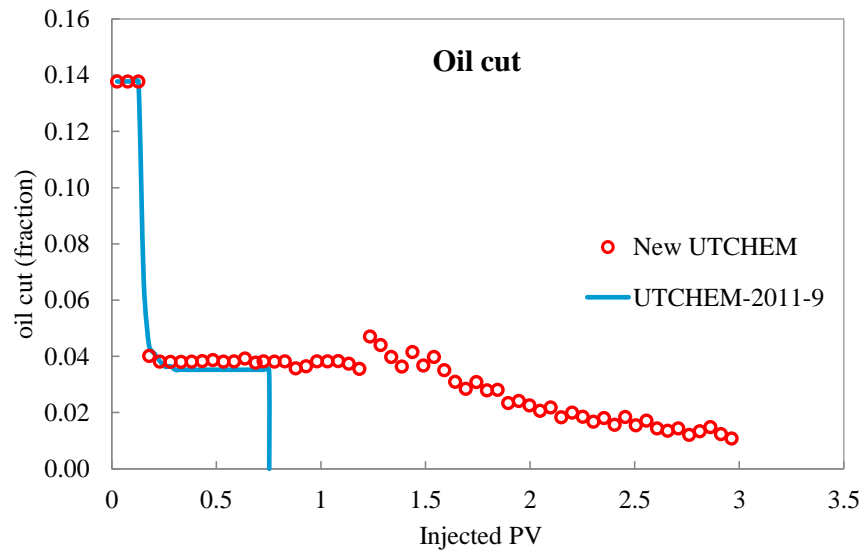


Figure A.6: Comparison of oil cut between UTCHEM-2011-9 and new improved UTCHEM code.

Appendix B: Sample Input Files

B.1: Input file for Case 2 – Gas Injection in Saturated Reservoir (UTCHEM and IMEX-CMG)

```

CC*****
CC                                                                 *
CC  BRIEF DESCRIPTION OF DATA SET: UTCHEM INPUT                    *
CC                                                                 *
CC*****
CC                                                                 *
CC                                                                 *
CC                                                                 *
CC  LENGTH (FT):          PROCESS:                                  *
CC  THICKNESS (FT):      INJ. RATE (FT3/DAY):                       *
CC  WIDTH (FT):         COORDINATES: CARTESIAN                       *
CC  POROSITY:                                                    *
CC  GRID BLOCKS:                                                *
CC  DATE:                                                         *
CC                                                                 *
CC*****
CC
CC*****
CC                                                                 *
CC  RESERVOIR DESCRIPTION                                          *
CC                                                                 *
CC*****
CC
CC RUN NUMBER
*---- RUNNO
Case-2
CC
CC TITLE AND RUN DESCRIPTION
*---- TITLE
Black-Oil Model
Gas Injection
Verification of UTCHEM with IMEX-CMG
CC
CC SIMULATION FLAGS
*---- IMODE IMES IDISPC ICWM ICAP IREACT IBIO ICOORD ITREAC ITC IGAS IENG IBLACK
      1    4    0    0    0    0    0    1    0    0    1    0    1
CC
CC NO. OF GRIDBLOCKS, FLAG SPECIFIES CONSTANT OR VARIABLE GRID SIZE, UNIT
*---- NX  NY  NZ  IDXYZ  IUNIT
      10  10  2   0    0
CC
CC CONSTANT GRID BLOCK SIZE IN X, Y, AND Z
*---- DX  DY  DZ
      10  10  5
CC
CC TOTAL NO. OF COMPONENTS, NO. OF TRACERS, AND NO. OF GEL COMPONENTS
*----N  NO  NTW  NTA  NGC  NG  NOTH
      8  0  0   0   0  0  0
CC
CC NAME OF THE COMPONENTS
*----SPNAME (I) FOR I=1 TO N
Water
Oil

```

```

Surfactant (no)
Polymer (no)
Anion (no)
Cation (no)
Alcohol (no)
Gas
CC
CC FLAG INDICATING IF THE COMPONENT IS INCLUDED IN CALCULATIONS OR NOT
*----ICF (KC) FOR KC=1, N
  1  1  0  0  0  0  0  0  1

CC
CC*****
CC                                          *
CC  OUTPUT OPTIONS                          *
CC                                          *
CC*****
CC
CC
CC FLAG TO WRITE TO UNIT 3, FLAG FOR PV OR DAYS TO PRINT OR TO STOP THE RUN
*---- ICUMTM  ISTOP  IOUTGMS  IS3G
      0      0      2      1

CC
CC FLAG INDICATING IF THE PROFILE OF KCTH COMPONENT SHOULD BE WRITTEN
*---- IPRFLG (KC), KC=1, N
  1  1  0  0  0  0  0  0  1

CC
CC FLAG FOR PRES., SAT., TOTAL CONC., TRACER CONC., CAP., GEL, ALKALINE PROFILES
*---- IPPRES  IPSAT  IPCTOT  IPBIO  IPCAP  IPGEL  IPALK  IPTEMP  IPOBS
      1      1      1      0      0      0      0      0      0

CC
CC FLAG FOR WRITING SEVERAL PROPERTIES TO UNIT 4 (Prof)
*---- ICKL  IVIS  IPER  ICNM  ICSE  IHYSTP  IFOAMP  INONEQ
      1      1      1      1      0      0      1      0

CC
CC FLAG FOR VARIABLES TO PROF OUTPUT FILE
*---- IADS  IVEL  IRKF  IPHSE
      0      1      0      0

CC
CC*****
CC                                          *
CC  RESERVOIR PROPERTIES                      *
CC                                          *
CC*****
CC
CC
CC MAX. SIMULATION TIME (DAYS)
*---- TMAX
      60

CC
CC ROCK COMPRESSIBILITY (1/PSI), STAND. PRESSURE (PSIA)
*---- COMPR  PSTAND
      1E-6    3600

CC
CC FLAGS INDICATING CONSTANT OR VARIABLE POROSITY, X, Y, AND Z PERMEABILITY
*---- IPOR1  IPERMX  IPERMY  IPERMZ  IMOD  ITRNZ  INTG
      0      0      3      3      0      0      0

CC
CC
*-----POR
      0.3

CC
CC

```

```

*-----PRMX
    200
CC
CC CONSTANT Y-PERMEABILITY (MILIDARCY) FOR LAYER K = 1, NZ
*---- PERMY
    1
CC
CC CONSTANT Z-PERMEABILITY FOR WHOLE EESERVOIR
*---- PERM Z
    1
CC
CC FLAG FOR DEPTH, PRESSURE, WATER SATURATION, INITIAL AQUEOUS PHASE COMPOSITIONS
*----IDEPTH IPRESS ISWI ICWI
    0      0      0      -1
CC
CC
*---- DEPTH
    0
CC
CC
*---- PRESSURE
    2000
CC
CC
*----- SWI
    0.3
CC
CC
*----- ISGI
    0
CC
CC
*----- SGI
    0.1
CC
CC BRINE SALINITY AND DIVALENT CATION CONCENTRATION (MEQ/ML)
*---- C50  C60
    0.2    0
CC
CC*****
CC*****
CC      PHYSICAL PROPERTY DATA
CC*****
CC*****
CC
CC
CC OIL CONC. AT PLAIT POINT FOR TYPE II (+) AND TYPE II (-), CMC
*---- C2PLC C2PRC EPSME IHAND
    0      1      0.0001  0
CC
CC FLAG INDICATING TYPE OF PHASE BEHAVIOR PARAMETERS
*---- IFGHBN
    0
CC
CC SLOPE AND INTERCEPT OF BINODAL CURVE AT ZERO, OPT., AND 2XOPT SALINITY
*---- HBNS70 HBNC70 HBNS71 HBNC71 HBNS72 HBNC72
    0      0.025  0      0.016  0      0.025
CC
CC SLOPE AND INTERCEPT OF BINODAL CURVE AT ZERO, OPT., AND 2XOPT SALINITY FOR ALCOHOL 2
*---- HBNS80 HBNC80 HBNS81 HBNC81 HBNS82 HBNC82
    0      0      0      0      0      0
CC
CC LOWER AND UPPER EFFECTIVE SALINITY
*---- CSEL7 CSEU7 CSEL8 CSEU8
    0.5    1.5    0      0

```

```

CC
CC THE CSE SLOPE PARAMETER FOR CALCIUM AND ALCOHOL 1 AND ALCOHOL 2
*---- BETA6  BETA7  BETA8
      0      0      0
CC
CC FLAG FOR ALCOHOL PART. MODEL AND PARTITION COEFFICIENTS
*---- IALC  OPSK7O  OPSK7S  OPSK8O  OPSK8S
      0      0      0      0      0
CC
CC NO. OF ITERATIONS, AND TOLERANCE
*---- NALMAX  EPSALC
      20      0.0001
CC
CC ALCOHOL 1 PARTITIONING PARAMETERS IF IALC=1
*---- AKWC7  AKWS7  AKM7  AK7  PT7
      0      0      0      0      0
CC
CC ALCOHOL 2 PARTITIONING PARAMETERS IF IALC=1
*---- AKWC8  AKWS8  AKM8  AK8  PT8
      0      0      0      0      0
CC
CC IFT MODEL FLAG
*---- IFT
      1
CC
CC INTERFACIAL TENSION PARAMETERS
*---- CHUH  AHUH
      0.3    13
CC
CC LOG10 OF OIL/WATER INTERFACIAL TENSION
*---- XIFTW
      1.65
CC
CC ORGANIC MASS TRANSFER FLAG
*---- IMASS  ICOR
      0      0
CC
CC
*--- IWALT  IWALF
      0      0
CC
CC CAPILLARY DESATURATION PARAMETERS FOR PHASE 1, 2, AND 3
*---- ITRAP  T11  T22  T33
      0      1600  59000  364
CC
CC FLAG FOR RELATIVE PERMEABILITY AND CAPILLARY PRESSURE MODEL
*---- IPERM  IRTYPE
      4      0
CC
CC LOG OF IFT BTW GAS/OIL AND GAS/WATER
---- XIFTG  XIFTGW
      1.477  1.477
CC
CC COMPOSITIONAL PHASE VISCOSITY PARAMETERS
*---- ALPHAV1  ALPHAV2  ALPHAV3  ALPHAV4  ALPHAV5
      0.1      0.1      0.1      0.9      0.7
CC
CC PARAMETERS TO CALCULATE POLYMER VISCOSITY AT ZERO SHEAR RATE
*---- AP1  AP2  AP3
      81  2700  2500
CC
CC PARAMETER TO COMPUTE CSEP, MIN. CSEP, AND SLOPE OF LOG VIS. VS. LOG CSEP
*---- BETAP  CSE1  SSLOPE
      10  0.01  0.17
CC

```

```

CC PARAMETER FOR SHEAR RATE DEPENDENCE OF POLYMER VISCOSITY
*---- GAMMAC  GAMHF  POWN  IPMODE  ISHEAR  RWEFF  GAMHF2  IGAMC
      20      10      1.8      0      0      0      0.25      0
CC
CC FLAG FOR POLYMER PARTITIONING, PERM. REDUCTION PARAMETERS
*---- IPOLYM  EPHI3  EPHI4  BRK  CRK  RKCUT
      1      1      0.8  1000  0.0186  10
CC
CC SPECIFIC WEIGHT FOR COMPONENTS 1, 2,3,7,8, COEFFICIENT OF OIL AND GRAVITY FLAG
*---- DEN1  DEN2  DEN23  DEN3  DEN7  DEN8  IDEN
      0.428  0.3806  0.571  0.428  0.3637  0.000512  2
CC
CC FLAG FOR CHOICE OF UNITS (0: BOTTOMHOLE CONDITION, 1: STOCK TANK)
*----- ISTB
      0
CC
CC COMPRESSIBILITY FOR VOL. OCCUPYING COMPONENTS 1, 2, 3, 7, AND 8
*---- COMPC (1)  COMPC (2)  COMPC (3)  COMPC (7)  COMPC (8)
      0      0      0      0      0
CC
CC MOLECULAR DIFFUSIVITY OF KCTH COMPONENT IN PHASE 1 (D (KC), KC=1, N)
*---- D (1)  D (2)  D (3)  D (4)  D (5)  D (6)  D (7)  D (8)
      0.      0.      0.      0.      0.      0.      0.      0
CC
CC MOLECULAR DIFFUSIVITY OF KCTH COMPONENT IN PHASE 2 (D (KC), KC=1, N)
*---- D (1)  D (2)  D (3)  D (4)  D (5)  D (6)  D (7)  D (8)
      0.      0.      0.      0.      0.      0.      0.      0
CC
CC MOLECULAR DIFFUSIVITY OF KCTH COMPONENT IN PHASE 3 (D (KC), KC=1, N)
*---- D (1)  D (2)  D (3)  D (4)  D (5)  D (6)  D (7)  D (8)
      0.      0.      0.      0.      0.      0.      0.      0
CC
CC MOLECULAR DIFFUSIVITY OF KCTH COMPONENT IN PHASE 4 (D (KC), KC=1, N)
*---- D (1)  D (2)  D (3)  D (4)  D (5)  D (6)  D (7)  D (8)
      0.      0.      0.      0.      0.      0.      0.      0
CC
CC LONGITUDINAL AND TRANSVERSE DISPERSIVITY OF PHASE 1 (feet)
*----ALPHAL (1)  ALPHAT (1)
      0.      0.
CC
CC LONGITUDINAL AND TRANSVERSE DISPERSIVITY OF PHASE 2
*----ALPHAL (2)  ALPHAT (2)
      0.      0.
CC
CC LONGITUDINAL AND TRANSVERSE DISPERSIVITY OF PHASE 3
*----ALPHAL (3)  ALPHAT (3)
      0.      0.
CC
CC LONGITUDINAL AND TRANSVERSE DISPERSIVITY OF PHASE 4
*----ALPHAL (4)  ALPHAT (4)
      0.      0.
CC
CC FLAG TO SPECIFY ORGANIC ADSORPTION CALCULATION
*----IADSO
      0
CC
CC SURFACTANT AND POLYMER ADSORPTION PARAMETERS
*----AD31  AD32  B3D  AD41  AD42  B4D  IADK  IADS1  FADS  REFK
      1.0  0.5  1000  0.7  0  100  0  0  0  0
CC
CC PARAMETERS FOR CATION EXCHANGE OF CLAY AND SURFACTANT
*----QV  XKC  XKS  EQW
      0  0  0  419

```

```

CC
CC*****
CC
CC BLACK OIL PVT
CC
CC*****
CC
CC
CC
*--- NROCK NPVT IBP
      1    1    1
CC
CC
*---- NDATA1
      8
CC
CC

```

```

*--- SWTAB RPWT RPOT PCOWT
      0.22  0.0  1.0  0.0
      0.30  0.07  0.4  0.0
      0.40  0.15  0.125  0.0
      0.50  0.24  0.0649  0.0
      0.60  0.33  0.0048  0.0
      0.80  0.65  0.0  0.0
      0.90  0.83  0.0  0.0
      1.00  1.00  0.0  0.0

```

```

CC
CC
*--- NDATA2
      14

```

```

CC
CC
*--- SLTAB RPGT RPOGT PCGOT
      0.22  0.984  0.0  0.0
      0.30  0.94  0.0  0.0
      0.40  0.87  0.0001  0.0
      0.50  0.72  0.001  0.0
      0.55  0.6  0.01  0.0
      0.6  0.41  0.021  0.0
      0.7  0.19  0.09  0.0
      0.75  0.125  0.2  0.0
      0.8  0.075  0.35  0.0
      0.88  0.025  0.7  0.0
      0.95  0.005  0.98  0.0
      0.98  0.0  0.997  0.0
      0.999  0.0  1.0  0.0
      1.0  0.0  1.0  0.0

```

```

CC
CC
*--- PBO PBDPTH PBGRD
      1000  0  0.1

```

```

CC
CC
*--- NDATA3
      14

```

```

CC
CC
*---- POT RSOT FVFOT EGT VISOT VISGT
      400.0  125.0  1.012  169.49  1.17  0.0130
      800.0  335.0  1.0255  338.98  1.14  0.0135
      1200.0  500.0  1.038  510.2  1.11  0.0140
      1600.0  665.0  1.051  680.27  1.08  0.0145

```

| | | | | | |
|--------|--------|--------|--------|------|--------|
| 2000.0 | 828.0 | 1.063 | 847.46 | 1.06 | 0.0150 |
| 2400.0 | 985.0 | 1.075 | 1020.4 | 1.03 | 0.0155 |
| 2800.0 | 1130.0 | 1.087 | 1190.5 | 1.00 | 0.0160 |
| 3200.0 | 1270.0 | 1.0985 | 1351.4 | 0.98 | 0.0165 |
| 3600.0 | 1390.0 | 1.11 | 1538.5 | 0.95 | 0.0170 |
| 4000.0 | 1500.0 | 1.12 | 1694.9 | 0.94 | 0.0175 |
| 4400.0 | 1600.0 | 1.13 | 1851.9 | 0.92 | 0.0180 |
| 4800.0 | 1676.0 | 1.14 | 2040.8 | 0.91 | 0.0185 |
| 5200.0 | 1750.0 | 1.148 | 2222.2 | 0.90 | 0.0190 |
| 5600.0 | 1810.0 | 1.155 | 2381.0 | 0.89 | 0.0195 |

CC
CC
*---- IPVTW
0

CC
CC
*---- REFPW VISWC FVFWC COMPWC CVW
14.7 0.96 1 3E-6 1.5E-6

CC
CC
*---- DENWS DENOS DENG
63.02 45.0 0.0702

CC
CC
*---- CBO CVISO
2.18E-5 2.55E-5

CC
CC*****
CC *
CC WELL DATA *
CC *
CC*****

CC
CC
CC FLAG FOR SPECIFIED BOUNDARY AND ZONE IS MODELED
*---- IBOUND IZONE
0 0

CC
CC TOTAL NUMBER OF WELLS, WELL RADIUS FLAG, FLAG FOR TIME OR COURANT NO.
*---- NWEEL IRO ITSTEP NWREL
2 2 0 2

CC
CC WELL ID, LOCATIONS, AND FLAG FOR SPECIFYING WELL TYPE, WELL RADIUS, SKIN
*---- IDW IW JW IFLAG RW SWELL IDIR IFIRST ILAST IPRF
1 1 1 1 0.25 0 3 1 2 0

CC
CC WELL NAME
*---- WELNAM
INJ

CC
CC ICHEK, MAX. AND MIN. ALLOWABLE BOTTOMHOLE PRESSURE AND RATE
*---- ICHEK PWFMIN PWFMAX QTMIN QTMAX
0 0 5000 0 50000

CC
CC WELL ID, LOCATIONS, AND FLAG FOR SPECIFYING WELL TYPE, WELL RADIUS, SKIN
*---- IDW IW JW IFLAG RW SWELL IDIR IFIRST ILAST IPRF
2 10 10 2 0.25 0 3 1 2 0

CC
CC WELL NAME
*---- WELNAM
PROD

CC
CC ICHEK, MAX. AND MIN. ALLOWABLE BOTTOMHOLE PRESSURE AND RATE
*---- ICHEK PWFMIN PWFMAX QTMIN QTMAX
0 0 5000 0 50000

CC

CC RATES NEED TO BE IN STANDARD CONDITIONS (@ Standard Conditions)

| *---- ID | QI (M, L) | C (M, KC, L) | | | | | | | | |
|----------|-----------|--------------|---|---|---|-------|---|---|---|---|
| 1 | 0 | 1 | 0 | 0 | 0 | 0.293 | 0 | 0 | 0 | 0 |
| 1 | 0. | 0 | 0 | 0 | 0 | 0 | 0 | 0 | 0 | 0 |
| 1 | 0. | 0 | 0 | 0 | 0 | 0 | 0 | 0 | 0 | 0 |
| 1 | 50000 | 0 | 0 | 0 | 0 | 0 | 0 | 0 | 0 | 1 |

CC

CC ID, BOTTOM HOLE PRESSURE FOR PRESSURE CONSTRAINT WELL (IFLAG=2 OR 3)

| *---- ID | PWF |
|----------|------|
| 2 | 2000 |

CC

CC CUM. INJ. TIME, AND INTERVALS (PV OR DAY) FOR WRITING TO OUTPUT FILES

| *---- TINJ | CUMPR1 | CUMH11 | WRHPV | WRPRF | RSTC |
|------------|--------|--------|-------|-------|------|
| 60 | 1 | 1 | 1 | 1 | 30 |

CC

CC FOR IMES=4, THE INI. TIME STEP, CONC. TOLERANCE, MAX., MIN. COURANT NUMBERS

| *---- DT | DCLIM | CNMAX | CNMIN |
|----------|----------|-------|-------|
| 0.0001 | 8*0.0001 | .05 | 0.01 |

```

*****
** Case 2
*****
**
** FILE: MXSMO001.DAT
**
** MODEL: 10x10x2
** FIELD UNIT
**
*****
** CASE-2: Comparison of IMEX-CMG and UTCHEM
**
*****
** CONTACT: CMG, (403)531-1300; 282-6495 (fax);support@cmgl.ca (Internet)
*****

```

RESULTS SIMULATOR IMEX

```

*****
** I/O Control section
*****

```

```

*TITLE1
'CASE-2'
*TITLE2
'GAS INJECTION IN SATURATED RESERVOIR'

```

*INUNIT *FIELD

```

*WPRN *WELL 10
*WPRN *GRID 10
*WPRN *ITER *ALL
*OUTPRN *WELL *ALL
*OUTPRN *GRID *ALL **SO *SW *SG *PRES *BPP *KRO *KRW *KRG
*WSRF *GRID 10
*OUTSRF *GRID *ALL **SO *SW *SG *PRES *BPP *KRO *KRW *KRG
*GRID *CART 10 10 2

```

```

*****
** Reservoir Description section

```

*DI *CON 10
*DJ *CON 10
*DK *CON 5

*POR *CON 0.3 ** Porosity is constant throughout.
*PRPOR 3600.0 ** Rock compressibility and
*CPOR 1E-6 ** Reference pressure

*PERMI *CON 200
*PERMJ *EQUALSI
*PERMK *EQUALSI

*MODEL *BLACKOIL ** Three phase problem

** Component Properties Section

*PVT

| ** p | rs | bo | eg | viso | visg |
|--------|--------|--------|--------|------|--------|
| 400.0 | 125.0 | 1.012 | 169.49 | 1.17 | 0.0130 |
| 800.0 | 335.0 | 1.0255 | 338.98 | 1.14 | 0.0135 |
| 1200.0 | 500.0 | 1.038 | 510.2 | 1.11 | 0.0140 |
| 1600.0 | 665.0 | 1.051 | 680.27 | 1.08 | 0.0145 |
| 2000.0 | 828.0 | 1.063 | 847.46 | 1.06 | 0.0150 |
| 2400.0 | 985.0 | 1.075 | 1020.4 | 1.03 | 0.0155 |
| 2800.0 | 1130.0 | 1.087 | 1190.5 | 1.00 | 0.0160 |
| 3200.0 | 1270.0 | 1.0985 | 1351.4 | 0.98 | 0.0165 |
| 3600.0 | 1390.0 | 1.11 | 1538.5 | 0.95 | 0.0170 |
| 4000.0 | 1500.0 | 1.12 | 1694.9 | 0.94 | 0.0175 |
| 4400.0 | 1600.0 | 1.13 | 1851.9 | 0.92 | 0.0180 |
| 4800.0 | 1676.0 | 1.14 | 2040.8 | 0.91 | 0.0185 |
| 5200.0 | 1750.0 | 1.148 | 2222.2 | 0.90 | 0.0190 |
| 5600.0 | 1810.0 | 1.155 | 2381.0 | 0.89 | 0.0195 |

*DENSITY *OIL 45.0
*DENSITY *GAS 0.0702
*DENSITY *WATER 63.02

*CO 2.18E-5 ** Oil compressibility
*CVO 2.55E-5 ** Pressure dependence on oil compressibility
*BWI 1 ** Water formation volume factor
*CW 3E-6 ** Water compressibility 3.0E-6
*REFPW 14.7 ** Reference pressure
*VWI 0.96 ** Water viscosity at reference pressure
*CVW 1.5E-6 ** Pressure dependence on water compressibility

*ROCKFLUID

**Rock-fluid Property Section

*RPT

*KROIL *STONE2

*SWT *SMOOTHEND *OFF

| ** sw | krw | krow | pcow |
|-------|------|--------|------|
| 0.22 | 0.0 | 1.0 | 0.0 |
| 0.30 | 0.07 | 0.4 | 0.0 |
| 0.40 | 0.15 | 0.125 | 0.0 |
| 0.50 | 0.24 | 0.0649 | 0.0 |
| 0.60 | 0.33 | 0.0048 | 0.0 |
| 0.80 | 0.65 | 0.0 | 0.0 |
| 0.90 | 0.83 | 0.0 | 0.0 |

| 1.00 | 1.00 | 0.0 | 0.0 |
|-------|------------|--------|------|
| *SLT | *SMOOTHEND | *OFF | |
| ** sl | krq | krog | pcow |
| 0.22 | 0.984 | 0.0 | 0.0 |
| 0.30 | 0.94 | 0.0 | 0.0 |
| 0.40 | 0.87 | 0.0001 | 0.0 |
| 0.50 | 0.72 | 0.001 | 0.0 |
| 0.55 | 0.6 | 0.01 | 0.0 |
| 0.6 | 0.41 | 0.021 | 0.0 |
| 0.7 | 0.19 | 0.09 | 0.0 |
| 0.75 | 0.125 | 0.2 | 0.0 |
| 0.8 | 0.075 | 0.35 | 0.0 |
| 0.88 | 0.025 | 0.7 | 0.0 |
| 0.95 | 0.005 | 0.98 | 0.0 |
| 0.98 | 0.0 | 0.997 | 0.0 |
| 0.999 | 0.0 | 1.0 | 0.0 |
| 1.0 | 0.0 | 1.0 | 0.0 |

*INITIAL

 ** Initial Conditions Section

*USER_INPUT
 *PRES *CON 2000
 *PB *CON 1000. ** Initial bubble point pressure is constant.

*SW *CON .3
 *SO *CON .6

*NUMERICAL

 ** Numerical Control Section

*MAXSTEPS 9999
 *NORM *PRESS 25
 *DTMAX .01
 *DTMIN .000001
 *RUN

** Well Data Section

 DATE 2008 1 1
 DTWELL 0.0001

WELL 1 'INJ'
 *INJECTOR MOBWEIGHT 1
 *INCOMP GAS
 OPERATE MAX STG 50000
 GEOMETRY K 0.25 0.249 1. 0.
 PERF GEO 1
 **\$ UBA ff Status Connection
 1 10 1:2 1. OPEN FLOW-TO 'SURFACE'
 **\$

WELL 2 'PRO'
 PRODUCER 2
 OPERATE BHP 2000
 GEOMETRY K 0.25 0.28 1. 0.
 PERF GEO 2
 **\$ UBA ff Status Connection
 10 1 1:2 1. OPEN FLOW-TO 'SURFACE'

DATE 2008 1 1.5
 DATE 2008 1 2

DATE 2008 1 3
DATE 2008 1 6
DATE 2008 1 10
DATE 2008 1 20
DATE 2008 1 30
DATE 2008 2 10
DATE 2008 2 20
DATE 2008 2 30

STOP

B.2: Input file for Case 6 – Foam Injection as a Drive in the Surfactant-Polymer Process

```

CC*****
CC
CC BRIEF DESCRIPTION OF DATA SET: UTCHEM INPUT
CC
CC*****
CC
CC
CC
CC LENGTH (FT):          PROCESS:
CC THICKNESS (FT):      INJ. RATE (FT3/DAY):
CC WIDTH (FT):          COORDINATES: CARTESIAN
CC POROSITY:
CC GRID BLOCKS:
CC DATE:
CC
CC*****
CC
CC*****
CC
CC RESERVOIR DESCRIPTION
CC
CC*****
CC
CC Run number
*---- RUNNO
Case-6
CC
CC TITLE AND RUN DESCRIPTION
*---- TITLE
Simulation of Foam Drive in Surfactant-Polymer Flood
IBLACK =1
Pc* foam model (tracer serves as a foaming agent)
CC
CC SIMULATION FLAGS
*---- IMODE IMES IDISPC ICWM ICAP IREACT IBIO ICOORD ITREAC ITC IGAS IENG IBLACK
          1   2   3     0    0    0    0    1    0    0    2    0    1
CC
CC NO. OF GRIDBLOCKS, FLAG SPECIFIES CONSTANT OR VARIABLE GRID SIZE, UNIT
*---- NX  NY  NZ  IDXYZ  IUNIT
          51  51  16    0    0
CC
CC CONSTANT GRID BLOCK SIZE IN X, Y, AND Z
*---- DX    DY    DZ
          3.92157  3.92157  2.5
CC
CC TOTAL NO. OF COMPONENTS, NO. OF TRACERS, AND NO. OF GEL COMPONENTS
*----N  NO  NTW  NTA  NGC  NG  NOTH
          9  0  1  0  0  0  0
CC
CC NAME OF THE COMPONENTS
*----SPNAME (I) FOR I=1 TO N
Water
Oil
Surfactant
Polymer
Anion
Cation
Alcohol
Gas
Surfactant # 2 (foaming surfactant)

```

```

CC
CC FLAG INDICATING IF THE COMPONENT IS INCLUDED IN CALCULATIONS OR NOT
*----ICF (KC) FOR KC=1, N
  1  1  1  1  1  1  0  1  1

CC
CC*****
CC
CC  OUTPUT OPTIONS
CC
CC*****
CC
CC
CC FLAG TO WRITE TO UNIT 3, FLAG FOR PV OR DAYS TO PRINT OR TO STOP THE RUN
*---- ICUMTM  ISTOP  IOUTGMS  IS3G
      0      0      2      1

CC
CC FLAG INDICATING IF THE PROFILE OF KCTH COMPONENT SHOULD BE WRITTEN
*---- IPRFLG (KC), KC=1, N
      1  1  1  1  1  1  0  1  1

CC
CC FLAG FOR PRES., SAT., TOTAL CONC., TRACER CONC., CAP., GEL, ALKALINE PROFILES
*---- IPPRES  IPSAT  IPTOT  IPBIO  IPCAP  IPGEL  IPALK  IPTEMP  IPOBS
      1      1      1      0      0      0      0      0      0

CC
CC FLAG FOR WRITING SEVERAL PROPERTIES TO UNIT 4 (Prof)
*---- ICKL  IVIS  IPER  ICNM  ICSE  IHYSTP  IFOAMP  INONEQ
      1      1      1      1      0      0      1      0

CC
CC FLAG FOR VARIABLES TO PROF OUTPUT FILE
*---- IADS  IVEL  IRKF  IPHSE
      0      1      0      0

CC
CC*****
CC
CC  RESERVOIR PROPERTIES
CC
CC*****
CC
CC
CC MAX. SIMULATION TIME (DAYS)
*---- TMAX
      1200

CC
CC ROCK COMPRESSIBILITY (1/PSI), STAND. PRESSURE (PSIA)
*---- COMPR  PSTAND
      1E-6    2500

CC
CC FLAGS INDICATING CONSTANT OR VARIABLE POROSITY, X, Y, AND Z PERMEABILITY
*---- IPOR1  IPERMX  IPERMY  IPERMZ  IMOD  ITRNZ  INTG
      0      0      3      3      0      0      0

CC
CC
*-----POR
      0.3

CC
CC
*-----PRMX
      250

CC
CC CONSTANT Y-PERMEABILITY (MILIDARCY) FOR LAYER K = 1, NZ
*---- PERMY
      1

CC

```

```

CC CONSTANT Z-PERMEABILITY FOR WHOLE EESERVOIR
*---- PERM Z
      0.05
CC
CC FLAG FOR DEPTH, PRESSURE, WATER SATURATION, INITIAL AQUEOUS PHASE COMPOSITIONS
*----DEPTH  IPRESS  ISWI  ICWI
      0      0      0     -1
CC
CC
*---- DEPTH
      0
CC
CC
*---- PRESSURE
      2500
CC
CC
*----- SWI
      0.5
CC
CC
*---- ISGI
      0
CC
CC
*---- SGI
      0.1
CC
CC BRINE SALINITY AND DIVALENT CATION CONCENTRATION (MEQ/ML)
*---- C50   C60
      0.4   0
CC
CC*****
CC
CC PHYSICAL PROPERTY DATA
CC
CC*****
CC
CC
CC OIL CONC. AT PLAIT POINT FOR TYPE II (+) AND TYPE II (-), CMC
*---- C2PLC C2PRC  EPSME  IHAND
      0      1      0.0001  0
CC
CC FLAG INDICATING TYPE OF PHASE BEHAVIOR PARAMETERS
*---- IFGHBN
      0
CC
CC SLOPE AND INTERCEPT OF BINODAL CURVE AT ZERO, OPT., AND 2XOPT SALINITY
*---- HBNS70 HBNC70 HBNS71 HBNC71 HBNS72 HBNC72
      0      0.028  0      0.026  0      0.028
CC
CC SLOPE AND INTERCEPT OF BINODAL CURVE AT ZERO, OPT., AND 2XOPT SALINITY FOR ALCOHOL 2
*---- HBNS80 HBNC80 HBNS81 HBNC81 HBNS82 HBNC82
      0      0      0      0      0      0
CC
CC LOWER AND UPPER EFFECTIVE SALINITY
*---- CSEL7 CSEU7 CSEL8 CSEU8
      0.177  0.344  0      0
CC
CC THE CSE SLOPE PARAMETER FOR CALCIUM AND ALCOHOL 1 AND ALCOHOL 2
*---- BETA6  BETA7  BETA8
      0      0      0
CC
CC FLAG FOR ALCOHOL PART. MODEL AND PARTITION COEFFICIENTS
*---- IALC  OPSK7O  OPSK7S  OPSK8O  OPSK8S

```

```

0      0      0      0      0
CC
CC NO. OF ITERATIONS, AND TOLERANCE
*---- NALMAX  EPSALC
      20      0.0001
CC
CC ALCOHOL 1 PARTITIONING PARAMETERS IF IALC=1
*---- AKWC7  AKWS7  AKM7  AK7  PT7
      0      0      0      0      0
CC
CC ALCOHOL 2 PARTITIONING PARAMETERS IF IALC=1
*---- AKWC8  AKWS8  AKM8  AK8  PT8
      0      0      0      0      0
CC
CC IFT MODEL FLAG
*---- IFT
      1
CC
CC INTERFACIAL TENSION PARAMETERS
*---- CHUH  AHUH
      0.3    13
CC
CC LOG10 OF OIL/WATER INTERFACIAL TENSION
*---- XIFTW
      1.65
CC
CC ORGANIC MASS TRANSFER FLAG
*---- IMASS  ICOR
      0      0
CC
CC
*--- IWALT  IWALF
      0      0
CC
CC CAPILLARY DESATURATION PARAMETERS FOR PHASE 1, 2, AND 3
*---- ITRAP  T11    T22    T33
      2    1600  59000  364
CC
CC FLAG FOR RELATIVE PERMEABILITY AND CAPILLARY PRESSURE MODEL
*---- IPERM  IRTYPE
      0      0
CC
CC FLAG FOR CONSTANT OR VARIABLE REL. PERM. PARAMETERS
*----ISRW  IPRW  IEW
      0      0      0
CC
CC CONSTANT RES. SATURATION OF PHASES 1, 2, AND 3 AT LOW CAPILLARY NO.
*----S1RWC  S2RWC  S3RWC
      0.25  0.35  0.25
CC
CC CONSTANT ENDPOINT REL. PERM. OF PHASES 1,2,AND 3 AT LOW CAPILLARY NO.
*----P1RW  P2RW  P3RW
      0.2  0.9  0.2
CC
CC CONSTANT REL. PERM. EXPONENT OF PHASES 1,2,AND 3 AT LOW CAPILLARY NO.
*----E1W  E2W  E3W
      3.5  2.5  3.5
CC
CC CONSTANT RES. SATURATION OF PHASES 1,2,AND 3 AT high CAPILLARY NO.
*----S1RWC  S2RWC  S3RWC
      0.0  0.0  0.0
CC
CC CONSTANT ENDPOINT REL. PERM. OF PHASES 1,2,AND 3 AT high CAPILLARY NO.
*----P1RW  P2RW  P3RW
      1.0  1.0  1.0

```

CC
 CC CONSTANT REL. PERM. EXPONENT OF PHASES 1,2,AND 3 AT high CAPILLARY NO.
 *---E1W E2W E3W
 1.0 1.0 1.0
 CC
 CC WATER AND OIL VISCOSITY, RESERVOIR TEMPERATURE (VISCOSITY IS READ FROM PVT TABLE)
 *---VIS1 VIS2 TEMPV
 0.6 1.0 0.
 CC
 CC GAS VISCOSITY AT REF. TEMPERATURE AND PRESSURE,SLOPE OF GAS VISCOSITY
 *--- VIS4 VSLOPG (GAS VISCOSITY IS READ FROM PVT TABLE)
 0.02 0
 CC
 CC CONSTANT RESIDUAL OIL/GAS SATURATION FOR ENTIRE RESERVOIR
 *--- S2RWC4 S4RWC
 0.20 0.1
 CC
 CC CONSTANT GAS ENDPOINT RELATIVE PERMEABILITY FOR ENTIRE RESERVOIR
 *--- P4RWC
 0.94
 CC
 CC CONSTANT GAS RELATIVE PERMEABILITY EXPONENT FOR ENTIRE RESERVOIR
 *--- E4WC
 1.5
 CC
 CC GAS PROPERTIES AT HIGH CAPILLARY
 *--- S4RC P4RC E4C T44 S2RC4
 0.099 0.94 1.5 0 0
 CC
 CC LOG OF IFT BTW GAS/OIL AND GAS/WATER
 --- XIFTG XIFTGW
 1.477 1.477
 CC
 CC COMPOSITIONAL PHASE VISCOSITY PARAMETERS
 *--- ALPHAV1 ALPHAV2 ALPHAV3 ALPHAV4 ALPHAV5
 0.1 0.1 0.1 0.9 0.7
 CC
 CC PARAMETERS TO CALCULATE POLYMER VISCOSITY AT ZERO SHEAR RATE
 *--- AP1 AP2 AP3
 81 2700 2500
 CC
 CC PARAMETER TO COMPUTE CSEP, MIN. CSEP, AND SLOPE OF LOG VIS. VS. LOG CSEP
 *--- BETAP CSE1 SSLOPE
 10 0.01 0.17
 CC
 CC PARAMETER FOR SHEAR RATE DEPENDENCE OF POLYMER VISCOSITY
 *--- GAMMAC GAMHF POWN IPMODE ISHEAR RWEFF GAMHF2 IGAMC
 20 10 1.8 0 0 0 0.25 0
 CC
 CC FLAG FOR POLYMER PARTITIONING, PERM. REDUCTION PARAMETERS
 *--- IPOLYM EPHI3 EPHI4 BRK CRK RKCUT
 1 1 0.8 1000 0.0186 10
 CC
 CC SPECIFIC WEIGHT FOR COMPONENTS 1, 2,3,7,8, COEFFICIENT OF OIL AND GRAVITY FLAG
 *--- DEN1 DEN2 DEN23 DEN3 DEN7 DEN8 IDEN (WATER/OIL/GAS DENSITY COMES FROM PVT TABLE)
 0.428 0.3806 0.571 0.428 0.3637 0.000512 2
 CC
 CC FLAG FOR CHOICE OF UNITS (0: BOTTOMHOLE CONDITION, 1: STOCK TANK)
 *----- ISTB
 0
 CC
 CC COMPRESSIBILITY FOR VOL. OCCUPYING COMPONENTS 1, 2, 3, 7, AND 8
 *--- COMPC (1) COMPC (2) COMPC (3) COMPC (7) COMPC (8)
 0 0 0 0 0
 CC

CC CONSTANT OR VARIABLE PC PARAM., WATER-WET OR OIL-WET PC CURVE FLAG

*---- ICPC IEPC IOW
0 0 1

CC

CC

*---- CPC
0

CC

CC

*---- EPC
0

CC

CC MOLECULAR DIFFUSIVITY OF KCTH COMPONENT IN PHASE 1 (D (KC), KC=1, N)

*---- D (1) D (2) D (3) D (4) D (5) D (6) D (7) D (8)
0. 0. 0. 0. 0. 0. 0. 0

CC

CC MOLECULAR DIFFUSIVITY OF KCTH COMPONENT IN PHASE 2 (D (KC), KC=1, N)

*---- D (1) D (2) D (3) D (4) D (5) D (6) D (7) D (8)
0. 0. 0. 0. 0. 0. 0. 0

CC

CC MOLECULAR DIFFUSIVITY OF KCTH COMPONENT IN PHASE 3 (D (KC), KC=1, N)

*---- D (1) D (2) D (3) D (4) D (5) D (6) D (7) D (8)
0. 0. 0. 0. 0. 0. 0. 0

CC

CC MOLECULAR DIFFUSIVITY OF KCTH COMPONENT IN PHASE 4 (D (KC), KC=1, N)

*---- D (1) D (2) D (3) D (4) D (5) D (6) D (7) D (8)
0. 0. 0. 0. 0. 0. 0. 0

CC

CC LONGITUDINAL AND TRANSVERSE DISPERSIVITY OF PHASE 1 (feet)

*----ALPHAL (1) ALPHAT (1)
0. 0.

CC

CC LONGITUDINAL AND TRANSVERSE DISPERSIVITY OF PHASE 2

*----ALPHAL (2) ALPHAT (2)
0. 0.

CC

CC LONGITUDINAL AND TRANSVERSE DISPERSIVITY OF PHASE 3

*----ALPHAL (3) ALPHAT (3)
0. 0.

CC

CC LONGITUDINAL AND TRANSVERSE DISPERSIVITY OF PHASE 4

*----ALPHAL (4) ALPHAT (4)
0. 0.

CC

CC FLAG TO SPECIFY ORGANIC ADSORPTION CALCULATION

*----IADSO
0

CC

CC SURFACTANT AND POLYMER ADSORPTION PARAMETERS

*----AD31 AD32 B3D AD41 AD42 B4D IADK IADS1 FADS REFK
1.0 0.5 1000 0.7 0 100 0 0 0 0

CC

CC PARAMETERS FOR CATION EXCHANGE OF CLAY AND SURFACTANT

*----QV XKC XKS EQW
0 0 0 419

CC

CC TRACER DATA (TRACER IS USED AS A FOAM GENERATOR)

*----
0

CC

CC

*----
0 0

CC

CC

```

*---
0
CC
CC
*---
0
CC
CC
CC UT FOAM MODEL (IFOAM=1) – LOW TENSION FOAM (IFOAMTYPE=2)
*--- IFOAM IFOAMTYPE IFOAMOIL
      1      2      0
CC
CC
*--- RFMAX  SOSTAR  CSTAR  EPXLO  SHRT  VELGR
      250    0.25   0.0001  0.01   1.0   1.0
CC
CC
*--- SWSTAR
      41616*0.28
CC
CC*****
CC
CC BLACK OIL PVT
CC
CC*****
CC
CC
CC
*--- NROCK NPVT IBP
      1      1      1
CC
CC
*--- PBO PBDPTH PBGRD
      1000   0      0.1
CC
CC
*--- NDATA3
      14
CC
CC
*--- POT  RSOT  FVFOT  EGT  VISOT  VISGT
      400.0  125.0  1.012  169.49  1.17  0.0130
      800.0  335.0  1.0255  338.98  1.14  0.0135
      1200.0  500.0  1.038  510.2  1.11  0.0140
      1600.0  665.0  1.051  680.27  1.08  0.0145
      2000.0  828.0  1.063  847.46  1.06  0.0150
      2400.0  985.0  1.075  1020.4  1.03  0.0155
      2800.0  1130.0  1.087  1190.5  1.00  0.0160
      3200.0  1270.0  1.0985  1351.4  0.98  0.0165
      3600.0  1390.0  1.11  1538.5  0.95  0.0170
      4000.0  1500.0  1.12  1694.9  0.94  0.0175
      4400.0  1600.0  1.13  1851.9  0.92  0.0180
      4800.0  1676.0  1.14  2040.8  0.91  0.0185
      5200.0  1750.0  1.148  2222.2  0.90  0.0190
      5600.0  1810.0  1.155  2381.0  0.89  0.0195
CC
CC
*--- IPVTW
      0
CC
CC
*--- REFPW VISWC FVFWC COMPWC CVW
      14.7   0.96   1      3E-6  1.5E-6
CC
CC
*--- DENWS DENOS DENGs

```

```

63.02  45.0  0.0702
CC
CC
*---- CBO  CVISO
      2.18E-5  2.55E-5
CC
CC*****
CC
CC WELL DATA
CC
CC*****
CC
CC
CC FLAG FOR SPECIFIED BOUNDARY AND ZONE IS MODELED
*---- IBOUND  IZONE
      0      0
CC
CC TOTAL NUMBER OF WELLS, WELL RADIUS FLAG, FLAG FOR TIME OR COURANT NO.
*---- NWELL  IRO  ITSTEP  NWREL
      5      2      0      5
CC
CC WELL ID, LOCATIONS, AND FLAG FOR SPECIFYING WELL TYPE, WELL RADIUS, SKIN
*---- IDW  IW  JW  IFLAG  RW  SWELL  IDIR  IFIRST  ILAST  IPRF
      1  26  26  1  0.25  0      3      1      16      0
CC
CC WELL NAME
*---- WELNAM
INJ-1
CC
CC ICHEK, MAX. AND MIN. ALLOWABLE BOTTOMHOLE PRESSURE AND RATE
*---- ICHEK  PWFMIN  PWFMAX  QTMIN  QTMAX
      0      0      5000      0      50000
CC
CC WELL ID, LOCATIONS, AND FLAG FOR SPECIFYING WELL TYPE, WELL RADIUS, SKIN
*---- IDW  IW  JW  IFLAG  RW  SWELL  IDIR  IFIRST  ILAST  IPRF
      2  1  1  2  0.25  0      3      1      16      0
CC
CC WELL NAME
*---- WELNAM
PROD-1
CC
CC ICHEK, MAX. AND MIN. ALLOWABLE BOTTOMHOLE PRESSURE AND RATE
*---- ICHEK  PWFMIN  PWFMAX  QTMIN  QTMAX
      0      0      5000      0      50000
CC
CC WELL ID, LOCATIONS, AND FLAG FOR SPECIFYING WELL TYPE, WELL RADIUS, SKIN
*---- IDW  IW  JW  IFLAG  RW  SWELL  IDIR  IFIRST  ILAST  IPRF
      3  1  51  2  0.25  0      3      1      16      0
CC
CC WELL NAME
*---- WELNAM
PROD-2
CC
CC ICHEK, MAX. AND MIN. ALLOWABLE BOTTOMHOLE PRESSURE AND RATE
*---- ICHEK  PWFMIN  PWFMAX  QTMIN  QTMAX
      0      0      5000      0      50000
CC
CC WELL ID, LOCATIONS, AND FLAG FOR SPECIFYING WELL TYPE, WELL RADIUS, SKIN
*---- IDW  IW  JW  IFLAG  RW  SWELL  IDIR  IFIRST  ILAST  IPRF
      4  51  1  2  0.25  0      3      1      16      0
CC
CC WELL NAME
*---- WELNAM
PROD-3
CC

```

CC ICHEK, MAX. AND MIN. ALLOWABLE BOTTOMHOLE PRESSURE AND RATE

*---- ICHEK PWFMIN PWFMAX QTMIN QTMAX
0 0 5000 0 50000

CC

CC WELL ID, LOCATIONS, AND FLAG FOR SPECIFYING WELL TYPE, WELL RADIUS, SKIN

*---- IDW IW JW IFLAG RW SWELL IDIR IFIRST ILAST IPRF
5 51 51 2 0.25 0 3 1 16 0

CC

CC WELL NAME

*---- WELNAM

PROD-4

CC

CC ICHEK, MAX. AND MIN. ALLOWABLE BOTTOMHOLE PRESSURE AND RATE

*---- ICHEK PWFMIN PWFMAX QTMIN QTMAX
0 0 5000 0 50000

CC low tension SP slug

CC RATES NEED TO BE IN STANDARD CONDITIONS (@ Standard Conditions)

*---- ID QI (M, L) C (M, KC, L)
1 800 0.99 0 0.01 0.05 0.3 0 0 0 0.002
1 0 0 0 0 0 0 0 0 0 0
1 0 0 0 0 0 0 0 0 0 0
1 0 0 0 0 0 0 0 0 1 0

CC

CC ID, BOTTOM HOLE PRESSURE FOR PRESSURE CONSTRAINT WELL (IFLAG=2 OR 3)

*---- ID PWF
2 2500

CC

CC ID, BOTTOM HOLE PRESSURE FOR PRESSURE CONSTRAINT WELL (IFLAG=2 OR 3)

*---- ID PWF
3 2500

CC

CC ID, BOTTOM HOLE PRESSURE FOR PRESSURE CONSTRAINT WELL (IFLAG=2 OR 3)

*---- ID PWF
4 2500

CC

CC ID, BOTTOM HOLE PRESSURE FOR PRESSURE CONSTRAINT WELL (IFLAG=2 OR 3)

*---- ID PWF
5 2500

CC

CC CUM. INJ. TIME AND INTERVALS (PV OR DAY) FOR WRITING TO OUTPUT FILES

*---- TINJ CUMPR1 CUMH11 WRHPV WRPRF RSTC
150 10 10 10 10 50

CC

CC FOR IMES=2, THE INI. TIME STEP, CONC. TOLERANCE, MAX., MIN. COURANT NUMBERS

*---- DT DCLIM CNMAX CNMIN
0.00001 0.01 0.05 0.01

CC

CC

*---- IBMOD
0

CC

CC

*---- IRO ITIME IFLAG
5 0 1 2 2 2 2

CC

CC NUMBER OF WELLS CHANGES IN LOCATION OR SKIN OR PWF

*----NWEL1
0

CC

CC NUMBER OF WELLS WITH RATE CHANGES, ID

*----NWEL2 ID
1 1

CC foam drive

CC RATES NEED TO BE IN STANDARD CONDITIONS (@ Standard Conditions)

*---- ID QI (M, L) C (M, KC, L)

| | | | | | | | | | | |
|---|--------|-----|---|---|---|-----|---|---|---|-------|
| 1 | 400 | 1.0 | 0 | 0 | 0 | 0.3 | 0 | 0 | 0 | 0.002 |
| 1 | 0 | 0 | 0 | 0 | 0 | 0 | 0 | 0 | 0 | 0 |
| 1 | 0 | 0 | 0 | 0 | 0 | 0 | 0 | 0 | 0 | 0 |
| 1 | 120000 | 0 | 0 | 0 | 0 | 0 | 0 | 0 | 1 | 0 |

CC

CC CUM. INJ. TIME AND INTERVALS (PV OR DAY) FOR WRITING TO OUTPUT FILES

*---- TINJ CUMPR1 CUMHI1 WRHPV WRPRF RSTC

| | | | | | |
|------|----|----|----|----|----|
| 1200 | 10 | 10 | 10 | 10 | 50 |
|------|----|----|----|----|----|

CC

CC FOR IMES=2, THE INI. TIME STEP, CONC. TOLERANCE, MAX., MIN. COURANT NUMBERS

*---- DT DCLIM CNMAX CNMIN

| | | | |
|---------|------|-------|-------|
| 0.00001 | 0.01 | 0.025 | 0.005 |
|---------|------|-------|-------|

Bibliography

- Agarwal, B. and Blunt, M.J. 2001. Full-physics, streamline-based method for history matching performance data of a north sea field. Paper SPE 66388 presented at the SPE Reservoir Simulation Symposium, Houston, TX. 11-14 February.
- Alvarez, J., Rivas, H. and Rossen, W. R. 2001. Unified Model for Steady-State Foam Behavior at High and Low Foam Qualities. *SPEJ* **6** (03): 325–333. SPE-74141-PA.
- Andrianov, A., Farajzadeh, R., Mahamoodi Nick, M., Talanana, M. Zitha, P. L. J. 2012. Immiscible Foam for Enhancing Oil Recovery: Bulk and Porous Media Experiments. *Ind. Eng. Chem. Res.* **51** (5): 2214–2226
- Antón, R. E., Andérez, J. M., Bracho, C., Vejar, F., and Salager, J. L. 2008. Practical Surfactant Mixing Rules Based on the Attainment of Microemulsion–Oil–Water Three-Phase Behavior Systems. *Adv Polym Sci.* **218**: 83-113.
- Aronson, A.S., Bergeron, V., Fagan, M.E., Radke, C.J. 1994. The influence of disjoining pressure on foam stability and flow in porous media, *Colloids and Surface A. Phys. And Eng. Aspects.* **83** (2): 109-120.
- Austad, T., and Strand, S. 1996. Chemical Flooding of Oil Reservoirs 4. Effects of Temperature and Pressure on the Middle Phase Solubilization Parameters Close to Optimum Flood Conditions. *Colloids and Surfaces A: Physicochemical and Engineering Aspects*, **108** (2-3): 243-252.
- Austad, T., Hodne, H., and Staurland, G. 1990. Effects of Pressure, Temperature and Salinity on the Multiphase Behavior of the Surfactant/Methane and n-Decane/NaCl Brine System. *Progr. Colloid Polym. Sci.* **82**:296-310.
- Austad, T., Hodne, H., Strand, S., and Veggeland, K. 1996. Chemical Flooding of Oil Reservoirs 5. The Multiphase Behavior of Oil/Brine/Surfactant Systems in Relation to Changes in Pressure, Temperature, and Oil Composition. *Colloids and Surfaces A: Physicochemical and Engineering Aspects* **108** (2-3): 253-262.
- Aziz, K. and Settari, A. 1979. Petroleum Reservoir Simulation. Elsevier Applied Science Publishers, London.
- Bear, J. 1979. Hydraulics of Ground Water, McGraw Hill, New York.

- Behie, G.A., Forsyth, P.A. and Sammon, P.H. 1987. Adaptive implicit methods applied to thermal simulation. *SPE Reservoir Engineering*, 2 (04): 596-598. SPE-14043-PA.
- Bernard, G. G., and Holm, L. W. 1964. Effect of Foam on Permeability of Porous Media to Gas. *SPEJ* 4 (03): 267-274. SPE-983-PA.
- Bernard, G. G., Holm, L. W., and Jacobs, W. L. 1965. Effect of Foam on Trapped Gas Saturation and on Permeability of Porous Media to Water. *SPEJ* 5 (04): 195-300. SPE-1204-PA.
- Bertin, H. J., Quintard, M. Y. and Castanier, L. M. 1998, Modeling Transient Foam Flow in Porous Media Using a Bubble Population Correlation. *SPEJ* 3 (04): 356–362. SPE-49020 PA.
- Beygi, M. R., Delshad, M., Pudugramam, V. S., Pope, G. A., and Wheeler, M. F. 2015. Novel Three-Phase Compositional Relative Permeability and Three-Phase Hysteresis Models. *SPEJ* 20 (01) 21-34. SPE-165324-PA.
- Bhuyan, D. 1989. Development of an Alkaline/Surfactant/Polymer Flood Compositional Reservoir Simulator,” Ph.D. dissertation. The University of Texas at Austin.
- Bhuyan, D., Pope, G.A., and Lake, L.W. 1990. Mathematical Modeling of High-pH Chemical Flooding. *SPE Reservoir Engineering*. 5 (02) 213-220. SPE-17398-PA.
- Bhuyan, D., Pope, G.A., and Lake, L.W. 1991. Simulation of High-pH Coreflood Experiments Using a Compositional Chemical Flood Simulator. Paper SPE 21029 presented at the SPE International Symposium on Oilfield Chemistry, Anaheim, CA. 20-22 February.
- Blake, T., Celius, H. K., Lie, T., Martinsen, H. A., Rasmussen, L., and Vassenden, F. 1999. Foam for Gas Mobility Control in the Snorre Field: The FAWAG Project. Paper SPE 56478 presented at the SPE Annual Technical Conference and Exhibition held in Houston, TX. 3-6 October.
- Boeije, C. S., and Rossen, W. R. 2013 Fitting Foam Simulation Model Parameters to Data. Presented at the 17th European Symposium on Improved Oil Recovery, St. Petersburg, Russia, 16-18 April.
- Breit, V.S., Bishop, K.A., Green, D.W. and Trompeter, E.E. 1973. A technique for assessing and improving the quality of reservoir parameter estimates used in numerical simulators. Paper SPE 4546 presented at the 48th Annual Fall Meeting of the Society of Petroleum Engineers of AIME, LV, NV. 30 September-3 October.

- Brooks, R.H. and Corey, A.T. Properties of Porous Media Affecting Fluid Flow. 1966. *J. of the Irrigation and Drainage Division*. **92** (2), 61-90.
- Buchwalter, J.L., and Miller, C.A. 1993. A new simplified compositional simulator. Paper SPE 25858 presented at SPE Rocky Mountain Regional/Low Permeability reservoir symposium, Denver, CO. 26-28 April
- Camilleri, D., Fil, A., Pope, G.A., and Sepehrnoori, K. 1987b. Improvements in Physical-Property Models Used in Micellar/Polymer Flooding. *SPE Res. Eng.* **2** (04): 433-440. SPE-12723-PA.
- Camilleri, D., Fil, A., Pope, G.A., Rouse, B.A., and Sepehrnoori, K. 1987a. Comparison of an Improved Compositional Micellar/Polymer Simulator With Laboratory Core Floods. *SPE Res. Eng.* **2** (04): 441-451. SPE 12083-PA.
- Camilleri, D., Lin E., Ohno, T., Engelsen, S., Pope, G.A., and Sepehrnoori, K. 1987c. Description of an Improved Compositional Micellar/Polymer Simulator. *SPE Res. Eng.* **2** (04): 427-432. SPE 13967-PA.
- Chen, Q. 2009. Assessing and Improving Steam-Assisted Gravity Drainage: Reservoir Heterogeneities, Hydraulic Fracture, and Mobility Control Foams. PhD dissertation. Stanford University.
- Chen, Q., Gerritsen, M. G., Kovscek, A. R. 2010. Modeling Foam Displacement With the Local-Equilibrium Approximation: Theory and Experimental Verification. *SPEJ* **15** (01) 171-183. SPE-116735-PA.
- Chen, Z., Qin, G. and Ewing, R.E. 2000. Analysis of a compositional model for fluid flow in porous media. *SIAM J. Appl. Math.*, **60** (3): 747-777.
- Cheng, L., Reme, A. B., Shan, D., Coombe, D.A., and Rossen, W. R. 2000. Simulating Foam Processes at High and Low Foam Qualities. Paper SPE 59278 presented at the SPE/DOE Improved Oil Recovery Symposium, Tulsa, OK, 3-5 April.
- Christensen, J. R., Stenby, E. H., Skauge, A. 2001. Review of WAG field experience. *SPE Reservoir Evaluation & Engineering*. **4** (02): 97-106. SPE-71203-PA.
- Coats, K.H. 1982. Reservoir simulation: State of art. *JPT*, 1633-1642.
- Coats, K.H. 1999. A note on IMPES and some IMPES-based simulation models. 1999. Paper SPE 49774 presented at the 15th symposium on reservoir simulation, Houston, TX. 14-17 February.
- Coats, K.H., Thomas, L.K. and Pierson, R.G. 1998. Compositional and black oil reservoir simulation. *SPEJ* **1** (04): 372-379. SPE-50990-PA.

- Collins, D.A., Nghiem, L.X., Li, Y.K. and Grabenstetter, J.E. 1992. An efficient approach to adaptive implicit compositional simulation with an equation of state. *SPE Reservoir Engineering* **7** (02): 259-264. SPE-15133-PA.
- Computer Modeling Group Ltd. 2011. IMEX, Advanced Oil/Gas Reservoir Simulator. Calgary, Canada.
- Computer Modeling Group. 2012. STARS. Thermal & Advanced Processes Reservoir Simulator. Calgary, Canada.
- Cook, R.E., Jacoby, R.H. and Ramesh, A.B. 1974. A beta-type reservoir simulator for approximating compositional effects during gas injection. *SPEJ* **14** (05): 471-481. SPE-4272-PA.
- Datta Gupta, A., Pope, G.A., Sepehrnoori, K., and Thrasher, R.L. 1986. A Symmetric, Positive Definite Formulation of a Three-Dimensional Micellar/Polymer Simulator, *SPE Reservoir Eng.*, **1**(06): 622-632. SPE-13504-PA.
- de Vries, A. S. and Wit, K. 1990. Rheology of Gas/Water Foam in the Quality Range Relevant to Steam Foam. *SPE Reservoir Engineering* **5** (02): 185-192. SPE-18075-PA.
- Delshad, M. and Pope, G.A. 1989. Comparison of the Three-Phase Oil Relative Permeability Models, *J.Transport in Porous Media*, **4** (1): 59-83.
- Delshad, M., Delshad, M., Bhuyan, D., Pope, G.A., and Lake, L.W. 1986. Effect of Capillary Number on the Residual Saturation of a Three-Phase Micellar Solution. Paper SPE 14911 presented at the SPE Enhanced Oil Recovery Symposium, Tulsa, Oklahoma, April 20-23.
- Delshad, M., Kim, D. H., Magbagbeola, O. A., Huh, C. Pope, G. A., Tarahhom, F. 2008. Mechanistic Interpretation and Utilization of Viscoelastic Behavior of Polymer Solutions for Improved Polymer-Flood Efficiency. Paper SPE 113620, presented at the SPE Symposium on Improved Oil Recovery, Tulsa, Oklahoma. 20-23 April.
- Delshad, M., Wheeler, M.F., Sepehrnoori, K., UTDOE-CO₂ CO₂ Flooding Reservoir Simulator. 2013. U.S. Department of Energy (DOE) under Contract Number DE-FE0005952.
- Delshad, The University of Texas Chemical Flooding Simulator, UTCHEM. The University of Texas at Austin. 2013.

- Dimitrie, B. -C., Bia, P.R. and Sabathier, J. -C. 1982. The “Checker Model”, An improvement in modeling naturally fractured reservoir with a tridimensional, triphasic, black oil numerical model. *SPEJ* 25 (05) 743-756. SPE-10977-PA.
- Dong, Y. 2001. Experimental Study of CO₂ Foam Flow in Porous Media and Application of Fractional-Flow Method to Foam Flow. Ms. Thesis. The University of Texas at Austin
- Douglas, J. and Peaceman, D.W. 1955. Numerical solution of two dimensional heat flow problems. *A.I. Ch. E. Jour.*, **1** (4): 505-512.
- Ertekin, T, Abou-Kassem, J. H., and King, G. R. 2001. Basic Applied Reservoir Simulation. Henry L. Doherty Memorial Fund of AIME. Society of Petroleum Engineering. Richardson, TX
- Ettinger, R. A., and Radke, C. J., 1992. Influence of Texture on Steady Foam Flow in Berea Sandstone. *SPE Reservoir Engineering* **7** (01) 83-90. SPE-19688-PA.
- Exerowa, D.; Kruglyakov, P.M. 1998. Foam and Foam Films, Elsevier Science.
- Falls, A. H., Hirasaki, G. J., Patzek, T. W., Gauglitz, D. A., Miller, D. D., and Ratulowski, J., 1988. Development of a Mechanistic Foam Simulator: The Population Balance and Generation by Snap-Off. *SPE Reservoir Engineering* **3** (03) 884-892. SPE-14961-PA.
- Falls, A.H., Musters, J.J., Ratulowski, J. 1989. The apparent viscosity of foams in homogeneous bead packs. *SPE Reservoir Engineering* **4** (2): 155–164. SPE-16048-PA.
- Fanchi, J. R., Harpole, K. J., and Bujnowski, S. W. 1982. BOAST: A Three-dimensional, Three-phase Black Oil Applied Simulation Tool (Version 1.1) Vol I: Technical Description and Fortran Code. Keplinger and Associate, Inc., Tulsa, Oklahoma and The BDM Corporation, Bartlesville, Oklahoma.
- Fanchi, J.R. 1987. Phase transitions in black oil reservoir simulation. Paper SPE 17003-MS.
- Farajzadeh, R., Ameri, A., Faber, M. J., van Batenburg, D. W., Boersma, D. M., and Bruining, J. 2013. Effect of Continuous, Trapped, and Flowing Gas on Performance of Alkaline Surfactant Polymer (ASP) Flooding. *Ind. Eng. Chem. Res.* **52** (38): 13839–13848.
- Farajzadeh, R., Andrianov, A., and Zitha, P. L. J. 2010. Investigation of Immiscible and Miscible Foam for Enhancing Oil Recovery. *Ind. Eng. Res.* **49** (4): 1910-1919

- Farajzadeh, R., Andrianov, A., Krastev, R., Hirasaki, G., and Rossen W. R. 2012. Foam–oil interaction in porous media: Implications for foam-assisted enhanced oil recovery. *Advances in Colloid and Interface Science*. **183–184**: 1-13.
- Farajzadeh, R., Krastev, R., Zitha, P.L.J. 2008. Foam films stabilized with alpha olefin sulfonate (AOS). *Colloids and Surfaces A: Physicochemical and Engineering Aspects*, **324** (1-3) 35-40.
- Farajzadeh, R., Lotfollahi, M., Eftekhari, A. A., Rossen, W. R., and Hirasaki, G. J. H. 2015. Effect of Permeability on Implicit-Texture Foam Model parameters and the Limiting Capillary Pressure. *Energy & Fuels*.
- Farajzadeh, R., Muruganathan, R.M., Rossen, W.R., Krastev, R., 2011. Effect of Gas Type on Foam Film Permeability and its Implications for Foam Flow in Porous Media. *Advances in Colloid and Interface Science* **168** (1–2): 71–78.
- Fayers, F.J. and Matthews, J.P. 1982. Evaluation of Normalized Stone's Methods for Estimating Three-Phase Relative Permeabilities. *SPEJ*. **24** (02): 224-232. SPE-11277-PA.
- Fevang, Q., Singh, K. and Whitson, C. 2000. Guidelines for choosing compositional and black oil models for volatile oil and gas condensate reservoir. SPE 63087 presented at the SPE Annual Technical Conference and Exhibition, Dallas, TX. 1-4 October.
- Forsythe Jr., P., and Sammon, P.H. 1984. Gas phase appearance and disappearance in fully implicit black oil simulation. *SPEJ* **24** (05) 505 – 507. SPE-11757-PA.
- Friedmann, F., Chen, W. H., and Gauglitz, P.A. 1991. Experimental and Simulation Study of High-Temperature Foam Displacement in Porous Media. *SPE Reservoir Engineering* **6**, 37-45.
- Ganzer, L.J. and Heinemann, Z.E. 1997. Reservoir simulation using mixed models. Paper SPE 37981 presented at the 14th SPE Symposium on Reservoir Simulation, Dallas, TX. 8-11 June.
- Garver, F.J., Sharma, M.M., and Pope, G.A. 1989. The Competition for Chromium Between Xanthan Biopolymer and Resident Clays in Sandstone. Paper SPE 19632 presented at the 64th Annual Conference, San Antonio, TX. 8-11 October.
- Gauglitz, P. A., Friedmann, F., Kam, S. I., and Rossen, W. R. 2002. Foam Generation in Homogeneous Porous Media. *Chemical Engineering Science* **57** (19): 4037–4052.
- Gjerde, O., Jarosch, H.S. and Kaarstad, T. 1988. Improvements to the black-oil simulator. SPE 18612.

- Hand, D.B. 1939. Dimeric Distribution: I. The Distribution of a Consolute Liquid Between Two Immiscible Liquids. *J. of Physics and Chem.* **34**, 1961-2000.
- Heeremans, J. C., Esmail, T. E, Van Kruijsdijk, C. P. J. W.2006. Feasibility Study of WAG Injection in Naturally Fractured Reservoirs. Paper SPE 100034 presented at SPE/DOE Symposium on Improved Oil Recovery, Tulsa, OK, 22-16 April.
- Hirasaki, G. J. and Lawson, J. B. 1985, Mechanisms of Foam Flow in Porous Media: Apparent Viscosity in Smooth Capillaries. *SPEJ* **25** (02): 176–190. SPE-12129-PA.
- Hirasaki, G.J. and Pope, G.A. 1974. Analysis of Factors Influencing Mobility and Adsorption in the Flow of Polymer Solution Through Porous Media. *SPEJ* **14** (04) 337 – 346. SPE-4026-PA.
- Huan G. 1986. The black oil model for a heavy oil reservoir. 1986. Paper SPE 14853 presented at International Meeting on Petroleum Engineering, Beijing, China. 17-20 March.
- Huan, G.R. 1985. A flash black oil model. SPE 13521 presented at SPE Reservoir Simulation Symposium, Dallas, TX. 10-13 February.
- Jang, S. H., Liyanage, P. J., Lu, J., Kim, D. H., Arachchilage, G. W. P. P., Britton, C., Weerasooriya, U., and Pope, G. A. Microemulsion Phase Behavior Measurements Using Live Oils at High Temperature and Pressure. Paper SPE 169169 presented at the SPE Improved Oil Recovery Symposium, Tulsa, OK, 12-16 April.
- Jin, M. 1995. A Study of Nonaqueous Phase Liquid Characterization and Surfactant Remediation. Ph.D. dissertation, The University of Texas at Austin.
- Kam, S. I. and Rossen, W. R. 2003. A Model for Foam Generation in Homogeneous Porous Media. *SPEJ* **8** (4): 417–425. SPE-77698-PA.
- Kam, S. I., 2008. Improved Mechanistic Foam Simulation with Foam Catastrophe Theory. *Colloids and Surfaces A: Physicochemical and Engineering Aspects.* **318** (1-3): 62-77.
- Kam, S. I., Nguyen, Q. P., Li, Q. and Rossen, W. R. 2007, Dynamic Simulations With an Improved Model for Foam Generation. *SPEJ* **12** (1): 35–48. SPE-90938-PA.
- Kamal, M., and Mardsen Jr., S. S. 1973. Displacement of a Micellar Slug Foam in Unconsolidated Porous Media. Paper SPE 4584 presented at the Fall Meeting of the Society of Petroleum Engineers of AIME. Las Vegas, Nevada. 30 September-3 October.

- Kazemi, H., Vestal, C.R., and Shank, G.D. 1978. An efficient multicomponent numerical simulator. *SPEJ*, 18 (05) 355-68. SPE-6890-PA.
- Kendall, R.P., Morrell, G.O., Peaceman, D.W., Silliman, W.J., and Watts, J.W. 1983. Development of a multiple application reservoir simulator for use on a vector computer. Paper SPE 11483 presented at the SPE Middle East oil Technical Conference, Manama, Bahrain, 14-17 March.
- Khatib, Z. I, Hirasaki, G. J., and Falls, A. H. 1988. Effects of Capillary Pressure on Coalescence and Phase Mobilities in Foams Flowing Through Porous Media. *SPE Reservoir Engineering* **3** (03) 919-926. SPE 15442-PA.
- Kibodeaux, K.R. 1997. Experimental and theoretical studies of foam mechanisms in enhanced oil recovery and matrix acidization applications, Ph.D. Dissertation, The University of Texas at Austin.
- Kil, R. A., Nguyen, Q. P., and Rossen, W. R. 2011. Determining Trapped Gas in Foam From CT Images. *SPEJ* **16** (01): 24-34. SPE-124157-PA.
- Kim, H. 1995. A Simulation Study of Gel Conformance Treatments. Ph.D. dissertation. The University of Texas, Austin.
- Kim, M. W., Bock, J., and Huang, J. S. 1985. Pressure-Induced Critical Phenomena of a Microemulsion System. *Phy. Rev. Lett.* **54** (1): 46-48.
- Kim, M. W., Gallagher, W., and Bock, J. 1988. Pressure Dependence on Multiphase Microemulsions. *J. Phys. Chem.* **92** (5): 1226-1230.
- Kovscek, A. R. and Radke, C. J. 1994, Fundamentals of Foam Transport in Porous Media, in L. Schramm (ed.), *Foams: Fundamentals and Applications in the Petroleum Industry*, ACS Symposium Series No. 242, American Chemical Society, Washington D.C., pp. 115–163.
- Kovscek, A. R., Patzek, T. W. and Radke, C. J. 1995, A Mechanistic Population Balance Model for Transient and Steady-State Foam Flow in Boise Sandstone. *Chem. Eng. Science* **50** (23), 3783–3799.
- Kovscek, A. R., Patzek, T. W. and Radke, C. J. 1997, Mechanistic Foam Flow Simulation in Heterogeneous and Multidimensional Porous Media. *SPEJ* **2** (4): 511–526. SPE-39102 PA.
- Lake, L. W., Johns, R. T., Pope, G. A., and Rossen, W. R. 2014. *Fundamentals of Enhanced Oil Recovery*, Society of Petroleum Engineers, Richardson, TX, 2014.

- Lashgari, H. R., Lotfollahi, M., Delshad, M., Sepehrnoori, K., and DeRouffignac, E. 2014. Steam Foam Modeling in Heavy Oil Reservoirs. Paper SPE 170178 presented at SPE Heavy Oil Conference, Calgary, Alberta, Canada, June 10-12.
- Lawson, J. B. and Reisberg, J. 1980. Alternate Slugs of Gas and Dilute Surfactant For Mobility Control During Chemical Flooding. Paper SPE 8839 presented at SPE/DOE Enhanced Oil Recovery Symposium. Tulsa, Oklahoma. 20-23 April.
- Li, K., 2004. Generalized Capillary Pressure and Relative Permeability Model Inferred From Fractal Characterization of Porous Media. Paper SPE 89874 presented at SPE Annual Technical Conference and Exhibition, Houston, TX, 26-29 September.
- Li, R. F., Yan, W., Liu, S., Hirasaki, G. J., and Miller, C. A. 2010. Foam Mobility Control for Surfactant Enhanced Oil Recovery. *SPE J.* **15** (04): 928-942. SPE 113910-PA.
- Lim, M. T. 1993. Field-Scale Numerical Modeling of Multiple Contact Miscible Processes Using Horizontal Wells in Heterogeneous Reservoirs. PhD dissertation. The University of Texas at Austin.
- Liu, J. 1993. High-Resolution Methods for Enhanced Oil Recovery Simulation. Ph.D. dissertation, The University of Texas at Austin.
- Liu, J., Delshad, M., Pope, G.A., and Sepehrnoori, K. 1994. Application of Higher Order Flux-Limited Methods in Compositional Simulations. *Transport in Porous Media.* **16** (1): 1-29.
- Lotfollahi M., Farajzadeh, R., Delshad, M., Varavei, A. J., Rossen, W.R. 2015. Comparison of Population balance and Implicit Texture Foam Models. Submitted to *J. Pet. Sci. Eng.*
- Lotfollahi, M., Varavei, A., Delshad, M., Farajzadeh, R., Pope, G. A. 2014. A Four-Phase Flow Model to Simulate Chemical EOR with Gas. Paper SPE 173322 presented at the SPE Reservoir Simulation Symposium, Houston, TX. 23-25 February.
- Lu, B. 2008. Iteratively Coupled Reservoir Simulation for Multiphase Flow in Porous Media. PhD dissertation. The University of Texas at Austin.
- Ma, K. Farajzadeh, R. Lopez-Salinas, J. L., Miller, C. A., Biswal, S. L. Hirasaki, G. L. 2014a. Non-uniqueness, Numerical Artifacts, and Parameter Sensitivity in Simulating Steady-State and Transient Foam Flow Through Porous Media. *Transport in Porous Media* **102** (3) 325-348.

- Ma, K., Lopez-Salinas, J. L., Puerto, M.C., Miller, C.A., Biswal, S.L., Hirasaki, G.J. 2013. Estimation of parameters for the simulation of foam flow through porous media. Part 1: the dry-out effect. *Energy Fuels*. **27** (5): 2363–2375.
- Ma, K., Ren, G., Mateen, K., Morel, D., and Cordelier, P., 2014b. Literature Review of Modeling Techniques for Foam Flow through Porous Media. Paper SPE 169104 presented at the SPE Improved Oil Recovery Symposium., Tulsa, OK, 12-16 April.
- Ma, Z.Y., Jing, F.J., Xu, X.M. and Sun, J.C. 1995. Simulation of black oil reservoir on distributed memory parallel computers and workstation cluster. Paper SPE 29937 presented at the International Meeting on Petroleum Engineering, Beijing, China. 14-17 November.
- Martinsen, H. A., and Vassenden, F. 1999. Foam Assisted Water Alternating Gas (FAWAG) Process on Snorre. Presented at the 10th European Symposium on Improved Oil Recovery, Brighton, UK. 18-20 August.
- Mohammadi, H. 2008. Mechanistic Modeling, Design, and Optimization of Alkaline/Surfactant/Polymer Flooding, PhD Dissertation, The University of Texas at Austin.
- Mohammadi, S. S., Coombe, D. A., Stevenson, V. M. 1993. Test of steam-foam process for mobility control in South-Casper Creek reservoir. *J. Can. Pet. Technol.* **32** (10), 49–54.
- Moncorgé, A., Patacchini, L., and de Loubens, R. 2012. Multi-Phase, Multi-Component Simulation Framework for Advanced Recovery Mechanisms. Paper SPE 161615 presented at the Abu Dhabi International Petroleum Exhibition and Conference, Abu Dhabi, UAE, 11-14 November.
- Moradi-Araghi, A., Johnston, E. L., Zornes, D. R., Harpole, K. J. 1997. Laboratory Evaluation of Surfactants for CO₂-Foam Applications at South Cowden Unit. Paper SPE 37218 presented at the SPE International Symposium on Oilfield Chemistry, Houston, TX, 18-21 February.
- Myers, T. J., and Radke, C. J. 2000. Transient Foam Displacement in the Presence of Residual Oil: Experiment and Simulation Using a Population-Balance Model. *Industrial & Engineering Chemistry Research* **39** (8): 2725-2741.
- Naderi Beni, A., Varavei, A., Delshad, M., Farajzadeh, E. 2013. Modeling Gas Solubility in Water for Foam Propagation in Porous Media. Paper SPE 163579 presented at the SPE Reservoir Symposium, Woodland, TX. 10-20 February.

- Nangacovié, H. L. M. A. 2012. Application of WAG and SWAG injection Techniques in Norne E-Segment. Msc project. Norwegian University of Science and Technology. NTNU-Trondheim.
- Nelson, R. C. 1983. The Effect of Live Crude on Phase Behavior and Oil-Recovery Efficiency of Surfactant Flooding Systems. *SPE J.* **23** (03): 501-510. SPE 10677-PA.
- Nelson, R.C. and Pope, G.A. 1978. Phase Relationships in Chemical Flooding. *SPE J.* **18** (05): 325-338. SPE 6773-PA.
- Nguyen, Q. P., Currie, P. K., Buijse, M., and Zitha, P. L. J., 2007. Mapping of Foam Mobility in Porous Media. *Journal of Petroleum Science and Engineering* **58** (1-2) 119-132.
- Nguyen, Q. P., Rossen, W. R., Zitha, P. L. J., and Currie, P. K., 2009. Determination of Gas Trapping With Foam Using X-Ray Computed Tomography and Effluent Analysis. *SPEJ* **14** (02) 222-236. SPE-94764-PA.
- Norvik, H. 1985. Fluid parameters for black oil simulators. SPE 14700.
- Osterloh, W. T., and Jante, M. J. 1992. Effects of Gas and Liquid Velocity on Steady-State Foam Flow at High Temperature. Paper SPE 24179 presented at the SPE/DOE EOR symposium, Tulsa, OK, April 22-24.
- Parker, J.C., Lenhard, R.J., and Kuppusamy, T. 1987. A Parametric Model for Constitutive Properties Governing Multiphase Flow in Porous Media. *Water Resour. Res.*, **23** (4), 618-624.
- Patzek, T. W., 1988. Description of Foam Flow in Porous Media by the Population Balance Approach, in D. Smith (ed.), *Surfactant-Based Mobility Control: Progress in Miscible-Flood Enhanced Oil Recovery*, American Chemical Society, Washington, DC, chapter 16, pp. 326–341.
- Patzek, T. W., and Myhill, N. A. 1989. Simulation of the Bishop Steam Foam Pilot. Paper SPE 18786 presented at SPE California Regional Meeting, Bakersfield, CA. 5-7 April.
- Peaceman, D.W. 1977. *Fundamentals of Numerical Reservoir Simulation*. Elsevier Scientific Publishing Co., Amsterdam.
- Peaceman, D.W., and Rachford, H.H. 1995. The numerical solution of parabolic and elliptic differential equations. *J. Soc. Ind. Appl. Math.* **3** (1):28-41.

- Persoff, P., Radke, C. J., Pruess, K., Benson, S. M., and Witherspoon, P. A., 1991. A Laboratory Investigation of Foam Flow in Sandstone at Elevated Pressure. *SPE Reservoir Engineering* **6** (03) 365-372. SPE-18781-PA.
- Pope, G. A., Lake, L.W., and F. G. Helfferich. 1978. Cation Exchange in Chemical Flooding: Part 1 -Basic Theory Without Dispersion, *SPE J* **18** (06): 418-434. SPE-6771-PA.
- Pope, G.A. and Nelson, R.C. 1978. A Chemical Flooding Compositional Simulator. *SPEJ*. **18** (05) 339-354. SPE-6725-PA.
- Pope, G.A., Wu, W., Narayanaswamy, G., Delshad, M., Sharma, M. M., Wang, P. 2000. Modeling Relative Permeability Effects in Gas-Condensate Reservoirs With a New Trapping Model. *SPE Reservoir Evaluation & Eng.* **3** (02): 171-178.
- Prouvost, L., Pope, G.A., and Rouse, B.A. 1985. Microemulsion Phase Behavior: A Thermodynamic Modeling of the Phase Partitioning of Amphiphilic Species. *SPE J.* **25** (05): 693 - 703. SPE 12586-PA.
- Prouvost, L., Pope, G.A., and Sepehrnoori, K. 1986. Modeling of Phase Behavior of Micellar Systems Used for EOR, *Surfactants in Solution*, 4, K. L. Mittal and P. Bothorel (eds.), Plenum Press.
- Prouvost, L., Satoh, T., Pope, G.A., and Sepehrnoori, K. 1984. A New Micellar Phase-Behavior Model for Simulating Systems With Up to Three Amphiphilic Species. Paper SPE 13031 presented at the 59th Annual Meeting of the Society of Petroleum Engineers, Houston, TX. 16-19 September.
- Pudugramam, V. S., Lotfollahi, M., Varavei, A., and Delshad, M. 2014. Field Scale Screening of CO₂ and Chemical Enhanced Oil Recovery. Presented at the 13th annual Carbon Capture, Utilization & Storage Conference. Pittsburg, PA, April 28-May 1.
- Puerto, M. C., and Reed, R. L. 1983. A Three-Parameter Representation of Surfactant/Oil Brine Interaction. *SPE J.* **23** (04): 669-682. SPE 10678-PA.
- Ramachandran, K. P., Gyani, O. N., Sur, S. 2010. Immiscible Hydrocarbon WAG: Laboratory to Field. Paper SPE 128848 presented at SPE Oil and Gas India Conference and Exhibition. Mumbai, India. 20-22 January.
- Ransohoff, T. C. and Radke, C. J., 1988. Mechanisms of Foam Generation in Glassbead Packs. *SPE Reservoir Engineering* **3** (2), 573–585. SPE-15441-PA.

- Reed, R.L. and Healy, R.N. 1977. Some Physico-Chemical Aspects of Microemulsion Flooding: A Review, Improved Oil recovery by Surfactant and Polymer Flooding, Shah, D.O. and Schechter, R.S., (eds.), Academic Press, New York.
- Roger, J. D., and Grigg, R.B. 2000. A Literature Analysis of the WAG Injectivity Abnormalities in the CO₂ Process. Paper SPE 59329 presented at the SPE/DOE Improved Oil Recovery Symposium. Tulsa, OK, 3-5 April.
- Roshanfekar, M., Johns, R. T., Pope, G., Britton, L., Linnemeyer, H., Britton, C., and Vyssotski, A. 2009. Effect of Pressure, Temperature, and Solution Gas on Oil Recovery from Surfactant Polymer Floods. Paper SPE 125095 presented at the SPE Annual Technical Conference and Exhibition, New Orleans, Louisiana, 4-7 October.
- Rossen, W. R. 1996. Foams in Enhanced Oil Recovery. In *Foams: Theory, Measurements and Applications*, ed. R. K. Prud'homme and S. Khan. New York: Marcel Dekker.
- Rossen, W. R., & Gauglitz, P. A., 1990. Percolation Theory of Creation and Mobilization of Foam in Porous Media. *A.I.Ch.E. Journal* **36** (8) 1176–1188.
- Rossen, W. R., and Boeije, C. S. 2013. Fitting foam simulation model parameters for SAG foam applications. Paper SPE 165282 presented at SPE Enhanced Oil Recovery Conference. Kuala Lumpur, Malaysia. 2-4 July.
- Rossen, W.R., Zeilinger, S.C., Shi, J.X., and Lim, M.T., 1999. Simplified Mechanistic Simulation of Foam Processes in Porous Media. *SPE J* **4** (03): 279-287. SPE-57678-PA.
- Saad, N. 1989. Field scale simulation of chemical flooding. PhD dissertation. The University of Texas at Austin.
- Sagi, A. R., Puerto, M., Bian, Y., Miller, C. A., Hirasaki, G. J., Salehi, M., Thomas, C. P., Kwan, J. T. 2013. Laboratory Studies for Surfactant Flood in Low-Temperature, Low-Salinity Fractured Carbonate Reservoir. Paper SPE 164062 presented at SPE International Symposium on Oilfield Chemistry, Woodlands, TX, 8-10 April.
- Salager, J. L., Bourrel, M., Schechter, R. S., and Wade, W. H. 1979b. Mixing Rules for Optimum Phase-Behavior Formulations of Surfactant/Oil/Water Systems. *SPE J.* **19** (5): 271-278. SPE 7584-PA.
- Salager, J. L., Morgan, J. C., Schechter, R. S., Wade, W. H., and Vasquez, E. 1979a. Optimum Formulation of Surfactant/Water/Oil Systems for Minimum Interfacial Tension or Phase Behavior. *SPE J.* **19** (2): 107-115. SPE 7054-PA.

- Sanchez, J. M., Schechter, R. S. and Monsalve, A. 1989. Surfactant Effects on the Two-Phase Flow of Steam-Water and Nitrogen-Water Through Permeable Media. *Journal of Petroleum Science and Engineering* **3** (1-2): 185-199.
- Sanderson, S. B., Stenby, E. H., and Solms, N. 2012. The Effect of Pressure on the Phase Behavior of Surfactant Systems: An Experimental Study. *Colloids and Surfaces A: Physicochemical and Engineering Aspects* **415**: 159-166.
- Satoh, T. 1984. Treatment of Phase Behavior and Associated Properties Used in a Micellar-Polymer Flood Simulator, M.S. thesis, The University of Texas at Austin.
- Schramm, L. L., Foams: Fundamentals and Applications in the Petroleum Industry. 1994. Vol. 242. Washington, DC: American Chemical Society.
- Skauge A., and Fortland P. 1990. Effect of Pressure and Temperature on the Phase Behavior of Microemulsions. *SPE Res. Eng.* **5** (4): 601-608. SPE 14932-PA.
- Skoreyko, F. A., Villavicencio, A. P., Prada, H. R., Nguyen, Q. P., 2012. Understanding Foam Flow With a New Foam EOR Model Developed From Laboratory and Field Data of the Naturally Fractured Cantarell Field. Paper SPE153942 presented at the 18th SPE Improved Oil Recovery Symposium, Tulsa, OK, 14-18 April.
- Southwick, J. G., Svec, Y., Chilek, G., and Shanin, G. T. 2012. Effect of Live Crude on Alkaline/Surfactant Polymer Formulations: Implications for Final Formulation Design. *SPE J.* **17** (02): 352-361. SPE 135357-PA.
- Spivak, A., and Dixon, T.N.1973. Simulation of gas-condensate reservoir. Paper SPE 4271 presented at SPE Symposium on Numerical Simulation of Reservoir Performance, Houston, TX. 11-12 January.
- Srivastava, M. 2010. Foam Assisted Low Interfacial Tension Enhanced Oil Recovery. PhD dissertation. The University of Texas at Austin.
- Srivastava, M., Zhang, J., Nguyen, Q. P., Pope, G. A. 2009., A Systematic Study of Alkali Surfactant Gas Injection as an Enhanced Oil Recovery Technique. Paper SPE 124752 presented at the SPE Annual Technical Conference and Exhibition, New Orleans, Louisiana, 4-7 October.
- Stone, H.L. 1973. Estimation of Three-Phase Relative Permeability and Residual Oil Data. *Journal of Canadian Petroleum Technology.* **12** (4): 53–61.
- Szlendak, S. M., Nguyen, N., and Nguyen, Q. P. 2013. Laboratory Investigation of Low-Tension-Gas Flooding for Improved Oil Recovery in Tight Formations. *SPE J.* **18** (05) 851-866. SPE 159841-PA.

- Tan, T.B. and Kaiogerakis, N. 1991. A fully implicit, three-dimensional, three-phase simulator with automatic history-matching capability. Paper SPE 21205 presented at the 11th SPE Symposium on Reservoir Simulation, Anaheim, CA. 17-20 February.
- Tanzil, D., Hirasaki, G. J., Miller, C. A. 2002. Conditions for Foam Generation in Homogeneous Porous Media. Paper SPE 75176 presented at the SPE/DOE Improved Oil Recovery Symposium, Tulsa, OK. 13-17 April.
- Trangenstein, J.A. and Bell, J.B. 1989. Mathematical structure of the black oil model for petroleum reservoir simulation. *SIAM Journal on App. Math.*, 49(3):749-783.
- Trouillaud, A., Patacchini, L., de Loubens, R., and Moncorge, A. 2014. Simulation of Surfactant Flooding in the Presence of Dissolved and Free Gas Accounting for the Dynamic Effect of Pressure and Oil Composition on Microemulsion Phase Behavior. Paper SPE 169148 presented at the SPE Improved Oil Recovery Symposium, Tulsa, Oklahoma, 12-16 April.
- van Genuchten, M.T. 1980. A Closed-Form Equation for Predicting the Hydraulic Conductivity of Unsaturated Soils, *Soil Science Society of America Journal*, **44**: 892-989.
- Vassenden, F. and Holt, T., 1998. Experimental Foundation for Relative Permeability Modeling of Foam. Paper SPE 39660 presented at the SPE/DOE Improved Oil Recovery Symposium, Tulsa, OK. 19–22 April.
- Vassenden, F., Ghaderi, A., and Solheim A. 1999. Foam Propagation on Semi-Reservoir Scale. *SPE Reservoir Eval. & Eng.* **2** (05) 436-441. SPE-58047-PA.
- Wang, L. 2006. MS Thesis. Alkali-Surfactant-Polymer Foams (ASPF): Laboratory Investigation of Displacement Mechanisms. University of Calgary, Calgary, Alberta, Canada.
- Watts, J.W. 1985. A compositional formulation of the pressure and saturation equations. *SPE Reservoir Engineering*. **1** (03) 243-252. SPE-12244-PA.
- Whitson, C.H., Silva, F. and Soride I. 1988. Simplified compositional formulation for modified black oil simulators. Paper SPE 18315 presented at 63rd Annual Technical Conference and Exhibition, Houston, TX. 2-5 October.
- Wong, T.W., Nutakki, R., and Aziz, K. 1987. A comparison of two approaches to compositional and black oil simulation. Paper SPE 15999 presented on 9th SPE symposium on reservoir simulation, San Antonio, TX. 1-4 February.

- Wu, X., Ogbe, D. O., Zhu, T., Khataniar, S. 2004. Critical Design Factors and Evaluation of Recovery Performance of Miscible Displacement and WAG Process. Presented at the Petroleum Society's 5th Canadian International Petroleum Conference (55th Annual Technical Meeting), Calgary, Alberta, Canada, June 8 – 10
- Xu, Q., and Rossen, W. R. 2003. Effective Viscosity of Foam in Periodically Constricted Tubes. *Colloids Surfaces A: Physicochem Eng. Aspects* **216** (1-3), 175-194.
- Young, L.C. and Stephenson, R.E. 1983. A generalized compositional approach for reservoir simulation. *SPEJ* **23** (05) 727-742. SPE-10516-PA.
- Zahoor, M. K., Derahman, M. N., Yunan, M. H. 2011. WAG Process Design-An Updated Review. *Brazilian Journal of Petroleum and Gas*. **5** (2) 109-121.
- Zhou, Z .H. and Rossen, W .R. 1995. Applying Fractional-Flow Theory to Foam Processes at the 'Limiting Capillary Pressure'. *SPE Adv. Technol.* **3** (01): 154-162. SPE-24180-PA.
- Zitha, P. L. J., 2006. A New Stochastic Bubble Population Model for Foam in Porous Media. Paper SPE 98976 presented at the SPE/DOE Symposium on Improved Oil Recover, Tulsa, OK, 22-26 April.